UNIVERSITAT POLITÈCNICA
DE CATALUNYA
BARCELONATECH

Quick assessment through analytical solutions of induced seismicity in geo-energy applications

Haiqing Wu

ADVERTIMENT La consulta d'aquesta tesi queda condicionada a l'acceptació de les següents condicions d'ús: La difusió d'aquesta tesi per mitjà del repositori institucional UPCommons (http://upcommons.upc.edu/tesis) i el repositori cooperatiu TDX (http://www.tdx.cat/) ha estat autoritzada pels titulars dels drets de propietat intel·lectual **únicament per a usos privats** emmarcats en activitats d'investigació i docència. No s'autoritza la seva reproducció amb finalitats de lucre ni la seva difusió i posada a disposició des d'un lloc aliè al servei UPCommons o TDX. No s'autoritza la presentació del seu contingut en una finestra o marc aliè a UPCommons (*framing*). Aquesta reserva de drets afecta tant al resum de presentació de la tesi com als seus continguts. En la utilització o cita de parts de la tesi és obligat indicar el nom de la persona autora.

ADVERTENCIA La consulta de esta tesis queda condicionada a la aceptación de las siguientes condiciones de uso: La difusión de esta tesis por medio del repositorio institucional UPCommons (http://upcommons.upc.edu/tesis) y el repositorio cooperativo TDR (http://www.tdx.cat/?locale-attribute=es) ha sido autorizada por los titulares de los derechos de propiedad intelectual **únicamente para usos privados enmarcados** en actividades de investigación y docencia. No se autoriza su reproducción con finalidades de lucro ni su difusión y puesta a disposición desde un sitio ajeno al servicio UPCommons No se autoriza la presentación de su contenido en una ventana o marco ajeno a UPCommons (*framing)*. Esta reserva de derechos afecta tanto al resumen de presentación de la tesis como a sus contenidos. En la utilización o cita de partes de la tesis es obligado indicar el nombre de la persona autora.

WARNING On having consulted this thesis you're accepting the following use conditions: Spreading this thesis by the institutional repository UPCommons (http://upcommons.upc.edu/tesis) and the cooperative repository TDX (http://www.tdx.cat/?locale- attribute=en) has been authorized by the titular of the intellectual property rights **only for private uses** placed in investigation and teaching activities. Reproduction with lucrative aims is not authorized neither its spreading nor availability from a site foreign to the UPCommons service. Introducing its content in a window or frame foreign to the UPCommons service is not authorized (framing). These rights affect to the presentation summary of the thesis as well as to its contents. In the using or citation of parts of the thesis it's obliged to indicate the name of the author.

Ph.D. Thesis

Quick assessment through analytical solutions of induced seismicity in geo-energy applications

By

Haiqing Wu

Hydrogeology Group (GHS)

Department of Civil and Environmental Engineering (DECA),
Universitat Politècnica de Catalunya (UPC)

Supervised by:

Maarten W. Saaltink

Víctor Vilarrasa Riaño

June, 2023

This thesis was funded by the Secretariat for Universities and Research of the Ministry of Business and Knowledge of the Government of Catalonia (AGAUR) and the European Social Fund through the “Grant for Universities and Research Centers for the Recruitment of New Research Personnel” (FI- 2019). Financial support was also provided by the Becas Santander Research Scholarship from the Universitat Politècnica de Catalunya (UPC) and the Santander Bank.

To my family

Abstract

Understanding the triggering processes and mechanisms of induced seismicity remains one of the most critical challenges in geo-energy applications. This Thesis aims at assessing (1) fault stability and induced seismicity potential under various geological, geometrical, and poromechanical conditions in the framework of poromechanics, and (2) poromechanical effects on the earthquake nucleation process.

First, we adopt the inclusion theory and Green's function to develop an analytical solution for stress variations due to pore pressure changes within the reservoir under plane strain conditions. The solution is valid for various fault offsets, dip angles, reservoir lengths, and permeable and impermeable faults. Fault stability analysis finds that (1) the induced seismicity potential of impermeable faults is always larger than that of permeable faults under any initial and injection conditions; (2) the slipping fault patch size increases with the offset for permeable faults, while it is independent of the offset for impermeable faults; and (3) an impermeable fault would rupture at the lower deviatoric stress and the smaller pressure buildup than a permeable one.

Second, we propose a closed-form solution for the poromechanical displacement with similar methods and conditions but in a half space relative to the previous stress solution, aiming at quickly estimating the ground uplift/subsidence. Results present that ground displacement increases with fault dip and decreases with increasing fault offset, in contrast, reservoir geometry shows a stronger effect than fault geometry. We compare the solution in a half space with that in a full space, showing that neglecting free surfaces underestimates the poroelastic displacement in the overburden. According, we recommend an index to assess the validity of full-space solutions. The specific condition is site-dependent and can be estimated by our solution.

Next, we apply the analytical solutions to analyze the triggering mechanisms of the Pohang M_w5.5 earthquake, which currently is the largest seismic event induced by any Enhanced Geothermal System. We make a comparative analysis on the relative likelihood of the existing in-situ stress state estimates for the Pohang site at depth, finding two likely oblique-slip patterns that can describe the triggering processes: a reverse-slip pattern with a strike-slip component (RS-S) and a strike-slip pattern with a reverse component (SS-R). We perform both deterministic and stochastic poromechanical analyses for both slip patterns, and then assess the induced seismicity potential. Two kinds of results provide three consistent evidences to support the RS-S pattern rather than the SS-R pattern. Results also highlight that (1) a small overpressure can trigger a damaging earthquake when preexisting faults are critically stressed at the initial state, and (2) we should devote more efforts to site characterization at the prior stage of projects.

Finally, we incorporate the analytical stress solution into the interfacial slip model of

cracks to simulate the nucleation process. Including poroelasticity drastically affects the quasi-static crack growth, revealing a wider range of slip regimes and reducing the expected magnitude of induced seismicity in some regimes. We generate maps of slip regime and earthquake magnitude with respect to a parametric space. The slip regime map comprises all the nucleation information: nucleation length, time, slip, and leading factors that include poroelasticity, slip weakening, and residual friction. The earthquake size map displays the moment magnitude associated with the ultimate nucleation of dynamic rupture in different slip regimes. Analyzing the two maps finds the favorable and unfavorable conditions as a function of rock properties, background stress, and injection parameters for deploying geo-energy applications. On the contrary, neglecting poroelastic effects cannot recognize many of such conditions.

Resumen

Comprender los procesos y mecanismos desencadenantes de la sismicidad inducida sigue siendo uno de los desafíos más críticos en las aplicaciones de geoenergía. Esta Tesis tiene como objetivo evaluar (1) la estabilidad de fallas y el potencial de sismicidad inducida bajo diversas condiciones geológicas, geométricas y poromecánicas en el marco de la poromecánica, y (2) los efectos poromecánicos en el proceso de nucleación sísmica.

Primero, adoptamos la teoría de inclusión y la función de Green para desarrollar una solución analítica para las variaciones de tensión debidas a los cambios de presión intersticial dentro del yacimiento bajo condiciones de deformación plana. La solución es válida para varias compensaciones de fallas, ángulos de buzamiento, longitudes de yacimientos y fallas permeables e impermeables. El análisis de estabilidad de fallas encuentra que (1) el potencial de sismicidad inducida de las fallas impermeables es siempre mayor que el de las fallas permeables bajo cualquier condición inicial y de inyección; (2) el tamaño del parche de falla deslizante aumenta con el desplazamiento de las fallas permeables, mientras que es independiente del desplazamiento de las fallas impermeables; y (3) una falla impermeable se rompería con el menor esfuerzo desviador y la menor acumulación de presión que una permeable.

En segundo lugar, proponemos una solución de forma cerrada para el desplazamiento poromecánico con métodos y condiciones similares pero en medio espacio en relación con la solución de tensión anterior, con el objetivo de estimar rápidamente el levantamiento/hundimiento del suelo. Los resultados muestran que el desplazamiento del suelo aumenta con el buzamiento de la falla y disminuye con el aumento del desplazamiento de la falla; en contraste, la geometría del yacimiento muestra un efecto más fuerte que la geometría de la falla. Comparamos la solución en un medio espacio con la de un espacio completo, mostrando que despreciar las superficies libres subestima el desplazamiento poroelástico en la sobrecarga. De acuerdo, recomendamos un índice para evaluar la validez de las soluciones de espacio completo. La condición específica depende del sitio y puede ser estimada por nuestra solución.

A continuación, aplicamos las soluciones analíticas para analizar los mecanismos desencadenantes del terremoto de Pohang Mw5.5, que actualmente es el evento sísmico más grande inducido por cualquier sistema geotérmico mejorado. Realizamos un análisis comparativo de la probabilidad relativa de las estimaciones del estado de tensión in situ existentes para el sitio de Pohang en profundidad, encontrando dos patrones probables de deslizamiento oblicuo que pueden describir los procesos desencadenantes: un patrón de deslizamiento inverso con un componente de deslizamiento de rumbo (RS-S) y un patrón strike-slip con componente inversa (SS-R). Realizamos análisis poromecánicos tanto deterministicos como estocásticos para ambos patrones de deslizamiento y luego evaluamos el potencial de sismicidad

inducida. Dos tipos de resultados proporcionan tres evidencias consistentes para apoyar el patrón RS-S en lugar del patrón SS-R. Los resultados también destacan que (1) una pequeña sobrepresión puede desencadenar un terremoto dañino cuando las fallas preexistentes están críticamente estresadas en el estado inicial, y (2) debemos dedicar más esfuerzos a la caracterización del sitio en la etapa previa de los proyectos.

Finalmente, incorporamos la solución de estrés analítico en el modelo de deslizamiento interfacial de grietas para simular el proceso de nucleación. La inclusión de la poroelasticidad afecta drásticamente el crecimiento de grietas cuasiestáticas, lo que revela una gama más amplia de regímenes de deslizamiento y reduce la magnitud esperada de la sismicidad inducida en algunos regímenes. Generamos mapas de régimen de deslizamiento y magnitud de terremotos con respecto a un espacio paramétrico. El mapa del régimen de deslizamiento comprende toda la información de nucleación: longitud de nucleación, tiempo, deslizamiento y factores principales que incluyen poroelasticidad, debilitamiento por deslizamiento y fricción residual. El mapa del tamaño del terremoto muestra la magnitud del momento asociado con la nucleación final de la ruptura dinámica en diferentes regímenes de deslizamiento. El análisis de los dos mapas encuentra las condiciones favorables y desfavorables en función de las propiedades de la roca, la tensión de fondo y los parámetros de inyección para implementar aplicaciones de geoenergía. Por el contrario, descuidar los efectos poroelásticos no puede reconocer muchas de tales condiciones.

Acknowledgements

Expressing gratitude usually is a shy thing for engineering students like me, leading to that I do not know what to say when I have to say something. But I would like to say a "Thanks" from my heart to many people who were involved in my work and my life during my PhD studies at this moment.

First, I would like to express my deepest gratitude to my supervisors, Dr. Victor Vilarrasa and Dr. Maarten Saaltink for giving me the chance to pursue a PhD degree at the UPC. Both of them help me a lot with my research work and my life in Barcelona. There are too many memories in my brain that they guide me how to do innovative research work, how to improve my professional writing style for academic publications, how to do presentations, and how to make international collaborations. It is really my pleasure to work with them.

Second, I would like to express my sincere gratitude to Dr. Francesco Parisio and Dr. Silvia de Simone for the fruitful discussion and their interest in my work. Both of them also show me how to improve my ability on literature review and professional writing during our collaborations. I really appreciated their insightful comments and constructive suggestions to my work.

I would also like to express my gratitude to all the people with whom I have worked during the past few years. An incomplete list includes: Iman R. Kivi, Dario Sciandra, Iman Vaezi, Auregan Boyet, Linus Walter, Sara Hanson-Hedgecock, Sebastià Olivella, Jesus Carrera, Jonny Rutqvist, Andrés Alcolea and Peter Meier.

I would like to thank some managing staff at the UPC who did me a favor with the paperwork, especially to Sílvia Aranda Gimó, Lluïsa Romanillos, Begoña Martínez, Teresa Garcia Tolosana and Mercè Tirado Pasanau. Their helps make my stay there comfortable.

I would like to thank some Chinese PhD candidates at the UPC, especially to Fei Song, Xiangbo Bu, Yufei Wang, Jingjing Wang, Ningning Zhang, Yunfeng Zhou, Hao Zeng and Jiangtao Lei. I am happy to stay with them to share our work and to enjoy the life in Barcelona.

Last but not least, I would like to give my special gratitude to all my family members: my parents, my brother and sisters, my wife (Xin Yang) and my kids (Zixuan Wu and Xianzhi Wu). I lived with my wife and my kids together during these years. Thanks Xin for her understanding and support. Thanks Zixuan and Xianzhi for their innocence and love. I love you forever!

List of Contents

1 Introduction 1

1.1 Background and motivation 1
1.2 Objectives and methodology 6
1.3 Thesis layout 8

2 Analytical solution to assess the induced seismicity potential of faults in pressurized and depleted reservoirs 11

2.1 Introduction 11
2.2 Analytical solution for stress changes around a fault crossing a pressurized/depleted reservoir 13
2.2.1 Problem formulation and assumptions 13
2.2.2 Analytical solution 14
2.2.3 Verification against numerical solution 17
2.3 Induced seismicity potential assessment 19
2.3.1 Coulomb failure stress (*CFS*) and Coulomb failure stress change (ΔCFS) 19
2.3.2 Slipping fault patch size 20
2.3.3 Properties of the base case scenario 21
2.4 Results 22
2.4.1 Effect of fault permeability in the base case scenario 22
2.4.2 Effect of fault offset and fault dip 26
2.4.3 Effect of initial stress and pore pressure changes 30
2.5 Discussion 34
2.6 Conclusions 36

3 Analytical solution to quickly assess ground displacement for a pressurized or depleted deep reservoir intersected by a fault in a half space 39

3.1 Introduction 39
3.2 Analytical solution for stress changes around a fault crossing a pressurized/depleted reservoir 42
3.2.1 Problem formulation and assumptions 42
3.2.2 Closed-form Solution 43
3.3 Verification against existing analytical solutions 45
3.3.1 Verification against Geertsma's solution 45
3.3.2 Verification against Segall's solution 47
3.4 Assessment of poroelastic displacement with a compartmentalized reservoir 49
3.4.1 Properties of the base-case scenario 49

3.4.2 Parametric space analysis on the geometric properties of geological model 50
3.5 Results 51
3.5.1 The role of fault permeability in the base case scenario 51
3.5.2 Effect of fault dip and fault offset on ground displacement 52
3.5.3 Effect of the reservoir geometry properties on ground displacement 53
3.6 Effects of traction-free surface on poroelastic displacement 55
3.6.1 A complete comparison of displacement in a half space and in a full space 55
3.6.2 Condition for neglecting the effects of free surface 57
3.7 Discussion 59
3.8 Conclusions 63

4 Stochastic poromechanical analysis of induced seismicity – application to the Pohang Mw5.5 earthquake 65

4.1 Introduction 65
4.2 Materials and Methods 67
4.2.1 Pohang setting 67
4.2.2 Stress transformation from the three dimensional (3D) principal stress space to the two dimensional (2D) fault plane of interest 69
4.2.3 Theis's solution for pore pressure diffusion 71
4.2.4 Analytical solution for stress variations induced by pore pressure changes 72
4.2.5 Coulomb failure stress and slipping fault patch size 74
4.2.6 Moment magnitude and Ohnaka's rupture nucleation model 74
4.2.7 Monte Carlo simulation procedure 75
4.2.8 Potential slip patterns and simulation strategy 75
4.3 Results 79
4.3.1 Likelihood of existing in-situ stress estimates and its effect on fault geometry 79
4.3.2 Fault stability at the instant of the mainshock 81
4.3.3 Effect of geological properties on induced seismicity potential 84
4.3.4 Probability distribution considering the uncertainty of geological properties 86
4.4 Discussion 90
4.5 Conclusions 92

5 Poroelastic effects on the nucleation process of dynamic fault rupture during fluid injection 95

5.1 Introduction 95
5.2 Nucleation process modeling during fluid injection 97
5.2.1 Interfacial slip model of cracks including poroelastic stress 97
5.2.2 Analytical solutions for pore pressure changes and poroelastic stress 100
5.2.3 Scaling and numerical solution 102
5.3 Results 105
5.3.1 Poroelastic effects on nucleation process 105

5.3.2 Characteristics of crack growth in different slip regimes 108
5.4 Moment magnitude estimate of injection-induced earthquakes associated with the ultimate nucleation in unstable slip regimes 114
5.5 Discussions 115
5.6 Conclusions 118

6 Conclusions 121

Appendices 125

A. Inclusion theory and induced stress 127
B. Surface integral of Green's function for stress 131
C. Induced stress on the fault plane 137
D. Supplementary Information for Chapter 2 141
E. Poroelastic displacement due to fluid injection/depletion in a half space 151
F. Closed-form integral solution of displacement function in a half space for two basic elements of inclusion: a rectangle and a triangle 155
G. Closed-form versions of Geertsma's solution and our solution for vertical displacement along the vertical reservoir center line 165
H. Closed-form version of Segall's solution and our solution for ground displacement 167
I. Approximate version of our integral solution for displacement function in a half space 169
J. Supplementary Information for Chapter 3 171
K. Supplementary Information for Chapter 5 177

References 185

1 Introduction

1.1 Background and motivation

Humanity is currently facing the significant challenge of decarbonizing the economy to mitigate climate change. The world primary energy demand will increase by 40% from 2009 to 2035 (IEA, 2011), with fossil fuels still providing most of the demand, which indicates a great number of greenhouse gas emissions. To effectively reduce these emissions, subsurface carbon-free alternatives are indispensable, such as geothermal energy exploitation, subsurface hydrogen storage and Carbon Capture, Utilization and Storage (CCUS). These geo-energy applications/technologies can contribute between 20 to 30 % of the total CO_2 emissions reduction (IEA, 2020). Thus, the potential of the subsurface is essential to achieve the goal of the COP21 Paris Agreement, i.e., limiting the global temperature increase below 2 ℃ above the pre-industrial levels.

However, the proliferating geo-energy projects have led to an increasing number of induced earthquakes all over the world (Figure 1.1, Foulger et al., 2018). These earthquakes can damage infrastructure and buildings, and even injure people. Some of these earthquakes have resulted in the cancellation of projects, as happened with the Deep Heat Mining Project in Basel, Switzerland (Haring et al, 2008; Deichmann and Giardini, 2009; Terakawa et al., 2012), the Castor underground gas storage project, in Spain (Del Potro 2015; Juanes et al., 2017; Villaseñor et al. 2020), and the Enhanced Geothermal System (EGS) project at Pohang, South Korea (Ellsworth et al., 2019; Grigoli et al., 2018; Lee et al., 2019). An interesting phenomenon in these three cases is that the largest earthquakes occurred after the stop of fluid injection, which represents a counterintuitive, yet typical, phenomenon for post-injection seismicity (Ge and Saar, 2022). The cancellation of such projects implies millionaire losses that have a negative impact on society. Furthermore, induced earthquakes generate nuisance and fear among the local population, giving rise to a negative public perception of geo-energy projects.

Induced damaging earthquakes have been observed in various fluid injection/depletion-related subsurface activities, such as conventional and unconventional hydrocarbon production, wastewater disposal, shale gas fracturing, geologic CO_2 storage (GCS), and geothermal energy exploitation (Figure 1.2, Bao and Eaton, 2016; Foulger et al., 2018; Grigoli et al., 2017; Kivi et al., 2023). During the past decade, the rate of induced earthquakes with magnitudes $M \geqslant 3$ has grown tenfold in Oklahoma (Ellsworth, 2013; Rubinstein and Mahani, 2015) and threefold in western Canada (Atkinson et al., 2020). The increase of seismic events in Oklahoma principally resulted from the large amount of wastewater reinjection (Shirzaei et al., 2016), while it is broadly attributed to hydraulic fracturing of low-permeability shales

in western Canada to exploit the unconventional oil and gas (Bao and Eaton, 2016). Hydraulic stimulation is also usually applied in deep geothermal energy exploitation to develop EGS (Evans et al., 2012). Several damaging earthquakes are believed to be involved in EGS projects, with the Pohang M_w5.5 earthquake being the largest one (Ellsworth et al., 2019). Although GCS is unlikely to induce a damaging seismic event as it usually operates in high-permeability sedimentary deformations (Juanes et al., 2012; Rutqvist et al., 2016; Vilarrasa and Carrera, 2015) and the vast majority of the recorded seismicity associated with CO_2 injection are lower than M2 (Cheng et al., 2023), eighteen M⩾3 earthquakes were recorded between 2006 and 2011 around the CO_2-enhanced oil recovery (CO_2-EOR) project site in Cogdell, United States (Gan and Frohlich, 2013), of which the maximum event of M4.4 occurred in 2011. Induced seismicity has become one of the most critical issues in these geo-energy activities (Ellsworth et al., 2016; Keranen and Weingarten, 2018; Rathnaweera et al., 2020; Schultz et al., 2020). Thus, minimizing the risk of inducing a damaging earthquake is a prerequisite for the sustainable development of geo-energy applications.

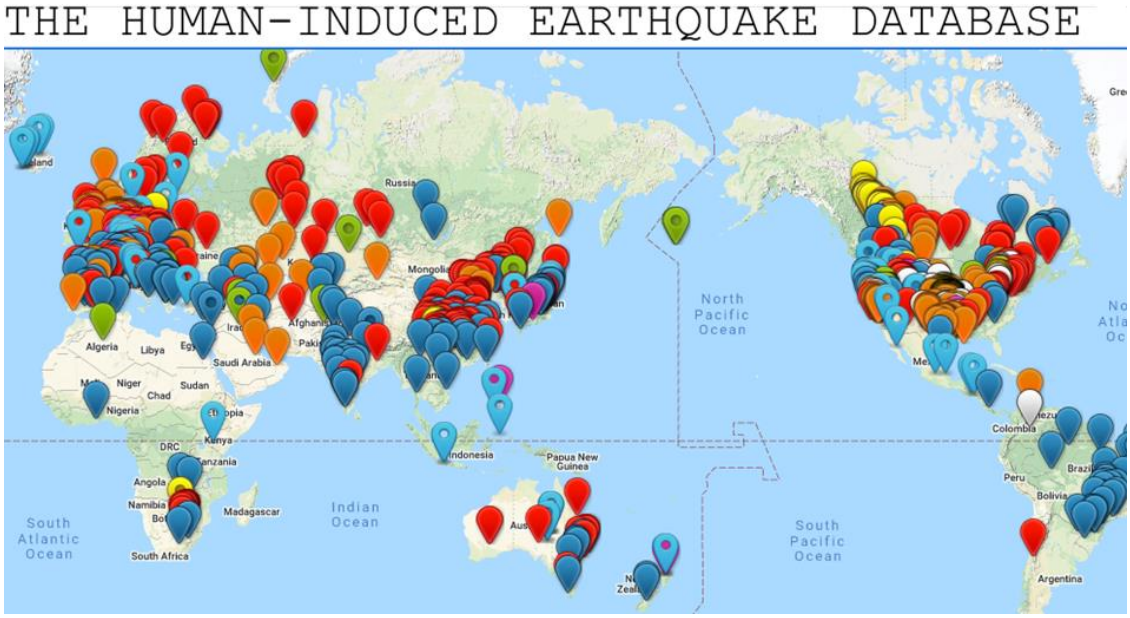

Figure 1.1: World map of seismicity induced by human activities (source: HiQuake database webpage-http://inducedearthquakes.org/). The balls are colored based on the type of human activities, with yellow for fracking, red for mining, dark blue for water reservoir impoundment, orange for conventional oil and gas, blue for geothermal, white for waste water disposal, green for nuclear explosions and magenta for research.

Yet, we currently remain unable to forecast and manage fluid-induced seismicity because of the limited characterization of project sites, the incomplete understanding of triggering mechanisms, and the insufficiency of real-time risk assessment tools (Cheng et al., 2023; Ge and Saar, 2022; Grigoli et al., 2017; Lee et al., 2019; Vilarrasa et al., 2022). The main tasks of site characterization are to detect the preexisting faults and large joints, to measure the thermo-hydro-mechanical (THM) properties of these weak zones, and to estimate the in-situ stress state at depth (Ben-Zion and Sammis, 2003). Risk assessments of induced seismicity can only be performed under a series of

simplifications and assumptions without enough site information, reducing the reliability and accuracy of assessments. Thus, several scholars have suggested devoting more efforts in site characterization at the prior stage of geo-energy projects (Chang et al., 2020; Chang and Yoon, 2021; Vilarrasa et al., 2022).

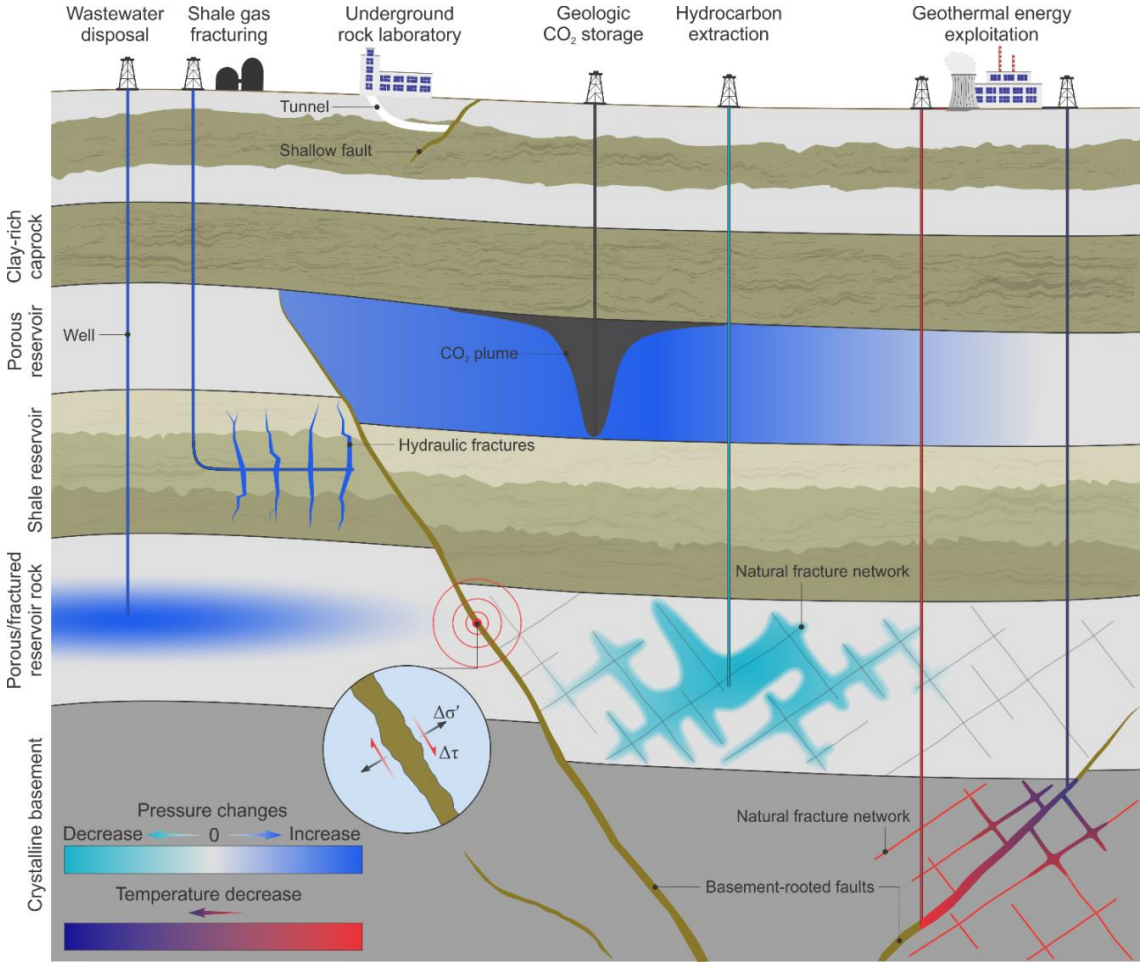

Figure 1.2: Schematic description of geo-energy applications associated with induced seismicity (Kivi et al., 2023).

Understanding the processes and mechanisms that induce seismicity is fundamental to assess the induced seismicity potential and to develop risk assessment tools. Considerable studies have been performed to this hot topic in recent years. These studies currently have reached a consensus in explaining fluid-induced seismicity in the framework of thermoporomechanics. This consensus is that fluid injection/depletion at depth leads to pore pressure diffusion and cooling effect in the aquifer (reservoir), which alter the in-situ stress state in the subsurface (Figure 1.2, De Simone et al., 2017; Rathnaweera et al., 2020; Vilarrasa et al., 2019). Once the THM perturbation is strong enough relative to the initial stress state, preexisting faults could be reactivated and the intact rocks may be fractured, releasing the elastic energy stored in the rock mass, and thus, inducing seismicity (Chang and Segall, 2016a, b; Rutqvist et al., 2008; Segall and Lu, 2015; Vilarrasa et al., 2019; Zbinden et al., 2017, 2020). Such fault reactivation and rock fracturing can also transfer stress to other critically stressed faults near or far away from the THM perturbed region (Brown and Ge, 2018;

Catalli et al., 2013, 2016; Ge and Saar, 2022), which may trigger a lower or larger magnitude earthquake, depending on the transferred stress and faulting state (King et al., 1994; Stein, 1999).

The preceding consensus indicates several triggering mechanisms of induced seismicity based on the Mohr-Coulomb failure criterion (Figure 1.3, Vilarrasa et al., 2019): (1) pore pressure diffusion, (2) poromechanical stress, (3) thermomechanical stress, and (4) stress transfer. The pressure build-up caused by fluid injection has originally been regarded as the basic principle of induced seismicity (Hubbert and Rubey, 1959; Healy et al., 1968; Raleigh et al., 1976; Pearson, 1981; Shapiro and Dinske, 2009) as it reduces the effective normal stress, and thus, brings the stress state closer to failure (Figure 1.3). This principle would give the impression that the higher the pressure build-up, the larger the number and magnitude of induced events. Indeed, the first attempt to mitigate induced seismicity was based on this idea. If the magnitude of an induced seismic event exceeded a given threshold, the injection rate was decreased in order to lower pressure build-up and thus, the frequency and magnitude of induced earthquakes (Langenbruch and Zoback, 2016; Zhang et al., 2013). However, this procedure has been proven unsuccessful in many cases (Bao and Eaton, 2016; Keranen and Weingarten, 2018). Especially, this principle cannot effectively explain the higher-magnitude post-injection seismicity than the earthquakes occurred during injection (De Simone et al., 2017; Segall and Lu, 2015; Vilarrasa et al., 2019), e.g., the cases of Basel, Castor, and Pohang, and the far-field (it means the non-pressurized region far away from injection wells) seismicity (Ge and Saar, 2022), e.g., the Fairview earthquake sequence in Oklahoma (Goebel et al., 2017).

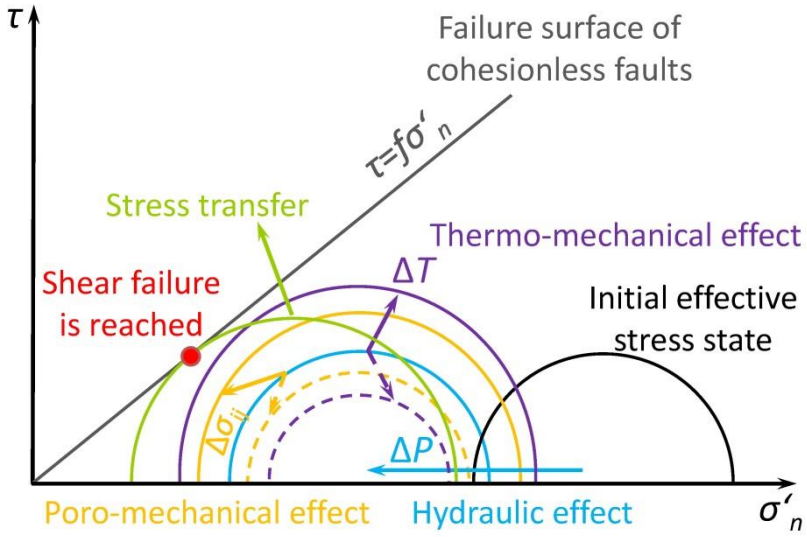

Figure 1.3: Schematic representation of thermo-hydro-mechanical (THM) coupling effects and the role of stress transfer on fault stability. Pressure buildup, Δp , decreases the effective normal stress and causes poromechanical stress that changes the size of the Mohr circle; cooling effect, ΔT , induces thermomechanical stress; stress transfer could be from one patch of the fault to other patches, and/or from one fault to surrounding faults.

Subsequently, the role of poromechanical response of geological media has been

noticed (Cocco and Rice, 2002; Rutqvist and Stephansson, 2003), analyzed in various geological settings and cases (Chang and Segall, 2016a, 2017; Deng et al., 2016; Fan et al., 2016; Jha and Juanes, 2014; Jansen et al., 2019; Juanes et al., 2016; Orlic and Wassing, 2013; Rutqvist et al., 2008; Vilarrasa et al., 2016; Zbinden et al., 2017, 2020), and even applied to explain the far field seismicity (Chang and Segall, 2016b; Fan et al., 2019; Goebel et al., 2017) and post-injection seismicity (Boyet et al., 2023; De Simone et al., 2017; Segall and Lu, 2015; Vilarrasa et al., 2021). The poromechanical stress caused by pressure buildup can affect a size larger than the pressurized region (Vilarrasa et al., 2016; Jansen et al., 2019), which is one of the causes for far field seismicity. The heterogeneity of formations can strengthen the poromechanical effect because of the stress concentration (Buijze et al., 2017). The poromechanical stress is non-uniform and may change from compression to tension in different fault patches (Jansen et al., 2019; Orlic and Wassing, 2013; Vilarrasa et al., 2016; Wu et al., 2021a). As a result, it can promote fault slip in some locations while inhibit slip in others (Figure 1.3). This non-uniformity can be used to analyze the hypocenter of earthquakes (Wu et al., 2021d). Thus, the poromechanical effect is fundamental both for explaining the triggering mechanisms and forecasting induced seismicity.

The cooling effect was mainly proposed to explain the induced seismicity associated with EGS projects (De Simone et al., 2013, 2017; Ghassemi et al., 2007; Jeanne et al., 2014; Kivi et al., 2022b; Majer et al., 2007) as it involves injecting cold fluid into the deep geothermal reservoirs and producing hot fluid from production wells (Figure 1.2). The distribution and properties of thermomechanical stress are similar to the ones of poromechanical stress (De Simone et al., 2017) because both the poromechanical and thermomechanical strains are the type of dilatational strain, i.e., expanding or contracting isotropically without shear component (McTigue, 1986; Segall, 1985; Segall and Fitzgerald, 1998; Soltanzadeh and Hawkees, 2008). Thus, the cooling effect can be treated as a similar mechanism to the poromechanical effect as long as the temperature difference between the injected fluid and target formations is big enough.

Stress transfer usually is the primary triggering mechanism of natural earthquakes (Feed, 2005; King et al., 1994; Stein, 1999; Toda et al., 2005, 2011). It has been used to explain the far field and post-injection seismicity recently (Boyet et al., 2023; Brown and Ge, 2018; Catalli et al., 2013, 2016; Ge and Saar, 2022; Yeo et al., 2020) because of its transferring nature and time lag effect. Shear-slip stress may transfer from one patch of the fault to other patches, and/or from one fault to other faults that are close to or far away from the reactivated fault. The previous four mechanisms can bring weak zones to failure individually or jointly, and a combination of multiple triggering mechanisms has been suggested to explain damaging earthquakes (Ge and Saar, 2022; Vilarrasa et al., 2022). Nonetheless, how they combine and work may change from one case to another, depending on the geological setting and injection/production management. In general, the pore pressure diffusion and poromechanical stress are more basical and ubiquitous for injection-induced seismicity than the others two mechanisms as the latter only plays an important role under certain conditions (Ge and Saar, 2022). Thus, a comprehensively poromechanical analysis

considering various geological, geometrical, and poromechanical conditions would be insightful to understand how the multiple triggering mechanisms work and to develop risk assessment tools.

The second problem of these THM mechanisms is that they overlook the nucleation process of earthquakes and the subsequent dynamic rupture propagation (Galis et al., 2017; Buijze et al., 2019; Wu et al., 2023a). Relevant results can only tell us if the fault is stable or not and how large is the unstable fault patch size when it is unstable, failing to provide any information about the stability of fault slip. The unstable fault patch size (Chang et al., 2020; Jansen et al., 2019) evaluated by these methods can only be regarded as a lower limit of the true value, failing to provide indications about the final size of the induced earthquakes. In contrast, existing studies including earthquake nucleation process have revealed several dominating mechanisms that control dynamic fault ruptures, such as (1) the nucleation and arrest of dynamic rupture (Garagash and Germanovich, 2012; Azad et al., 2017), (2) aseismic slip (Bhattacharya and Viesca, 2019; Eyre et al., 2019; Sáez et al., 2022; Jacquey and Viesca, 2023), (3) thermal pressurization (Viesca and Garagash, 2015), and (4) run-out distance (Garagash and Germanovich, 2012; Garagash, 2021). Relevant studies on natural earthquakes have shown the impact of the nucleation process on the physics of earthquakes (Ohnaka and Kuwahara, 1990; Ohnaka, 1992; Rubin and Ampuero, 2005; Ampuero and Rubin, 2008) and provided scaling laws linking the final earthquake magnitude with the critical size of nucleation zone (Ellsworth and Beroza, 1995; Ohnaka, 2000; Uenishi and Rice, 2003). Thus, quantifying the nucleation process is helpful to improve the estimates of induced earthquake magnitude. Yet, the preceding studies on nucleation process do not include the poromechanical effect on the background stress caused by pore pressure diffusion. As aforementioned, such poromechanical effect is known to be an essential mechanism controlling fault reactivation. Therefore, we believe that the poromechanical stress would significantly affect the nucleation process of fluid-induced earthquakes.

1.2 Objectives and methodology

This Thesis precisely aims at addressing the two key issues that are defined in Section 1.1, i.e., (I) fault stability and induced seismicity potential under various geological, geometrical, and poromechanical conditions in the framework of poromechanics, and (II) the poromechanical effect on the earthquake nucleation process. We divide the main objectives into four sub-objectives with details listed below.

Sub-objective (1): to develop an analytical solution for poromechanical stress due to reservoir pressurization or depletion. We assume a reservoir crossed by a fault that could be either permeable or impermeable with an arbitrary dip angle and offset. Changing the hydro-mechanical and geometrical parameters can represent different geological settings. We then use this solution and the Mohr-Coulomb failure criterion to assess fault stability and thus, induced seismicity potential in various parametric spaces.

Sub-objective (2): to develop an analytical solution for poromechanical displacement due to reservoir pressurization or depletion. We consider a similar scenario to the one adopted in the previous stress solution. We then use this solution to estimate the ground uplift or subsidence, aiming at gaining insights of reservoir and fault geometries and revealing some precursors of induced seismicity by analyzing surface deformation patterns.

Sub-objective (3): to apply the analytical solutions to analyze the triggering mechanisms of the Pohang M_w5.5 earthquake. Since the geological setting around the Pohang EGS site is highly uncertain, a statistical analysis is carried out with the help of analytical solutions. This analysis would show us which estimate of geological setting is the most likely one and how is the occurrence probability of this earthquake.

Sub-objective (4): to couple our poromechanical stress solution with the model that describes the earthquake nucleation process to analyze characteristics of crack growth in different slip regimes, including the non-uniformly poromechanical stress. We then apply the nucleation information to estimate the final earthquake magnitude under various conditions, which can promote the development of induced seismicity forecasting tools.

Sub-objectives (1) and (2) address the key issue I. Sub-objective (3) applies the obtained analytical solutions to a well-known earthquake, which permit considering poromechanical effects in uncertainty analysis. The last sub-objective deals with key issue II. The breakthrough of this Thesis will make a substantial advance in understanding the processes and mechanisms of induced seismicity, greatly promoting the development of induced seismicity forecasting tools, which will eventually enable the successful deployment of geo-energy applications.

To achieve such goals, a systematical methodology will be followed, which consists of four aspects: (1) reservoir pressurization/depletion, (2) geomechanics, (3) estimate of ground deformation, and (4) assessment of induced seismicity. Both analytical and numerical approaches are adopted to solve the physical problems.

Reservoir pressurization/depletion is the origin of subsequent stress variations, fault instability, ground deformation, and induced seismicity in the framework of poromechanics. Site characterization is the first step, i.e., giving an appropriate geological setting for modeling. To develop the analytical solutions shown in sub-objectives (1) and (2), necessary simplifications about the model geometry and hydro-mechanical properties have to be adopted (see details in Chapters 2 and 3). Subsequently, a uniform pore pressure change within the reservoir is assumed for base case studies. As for a practical application, we adopt existing analytical solutions to describe the non-uniform pressure changes.

Representing the poromechanical response due to reservoir pressurization/depletion is one part of geomechanics. The essence of this poromechanical problem is related to the following open questions: when the reservoir undergoes a change of size and shape caused by a dilatational loading, what are the induced stress and strain in the reservoir

and its surroundings? What would happen if there is a fault in the perturbed region? Would it be reactivated? Eshelby's inclusion theory (Eshelby, 1957) is a valid and useful method to formulate this problem. Thus, it is adopted to develop the analytical solutions. After solving the solutions, some verification against numerical solutions and other analytical solutions are presented before applications. In addition, geomechanics also give the initial (in-situ) stress state for fault stability analysis.

Applying the analytical displacement solution can directly estimate the ground deformation under various geological settings. By comparing with the monitoring data of ground deformation, if it is available, we can gain insights of reservoir and fault geometries and reveal some precursors of induced seismicity. In contrast, to assess the induced seismicity potential, a failure criterion is required in addition to the analytical stress solution. For the parametric space analysis of sub-objectives (1) and (2), and the statistical analysis of sub-objective (3), this Thesis applies the concept of Coulomb Failure Stress (*CFS*, King et al., 1994), a minor variation of the Mohr-Coulomb failure criterion, to assess fault stability and induced seismicity potential. As for the earthquake nucleation problem, i.e., the slip stability, of sub-objective (4), the interfacial slip model of cracks (Bilby and Eshelby, 1968; Uenishi and Rice, 2003) is applied, by coupling with our poromechanical stress solution, to characterize the nucleation process. A threshold of slip rate (Ohnaka and Kuwahara, 1990; Ohnaka, 1992) is adopted to judge if the quasi-static slip will transit to dynamic rupture or arrest. Finally, this Thesis uses Ohnaka's model (Ohnaka, 2000) to estimate the moment magnitude, aiming at establishing a link between the slipping fault patch size or nucleation size and the magnitude of induced earthquakes. All the relevant details will be shown in Chapters 2 and 5.

This Thesis mainly focuses on the analytical approach to develop closed-form solutions for the relevant poromechanical problems. Despite simplifications, the closed-form solutions are useful because they provide an instantaneous solution and serve to identify important scaling relationships that can give insights of the physical mechanisms that govern the problems. Numerical solutions are used for two purposes: on the one hand, for verifying the developed analytical solutions; on the other hand, for solving the singular integral equation that appears in characterizing the nucleation process, which usually cannot be solved analytically.

The objectives of this Thesis and the applied methodology require research in and crossing the borders between hydrogeology, geomechanics, geophysics, applied mathematics and seismology. This interdisciplinary approach is an innovative aspect with respect to previous efforts to understand, assess, and forecast induced seismicity, which should permit to advance at the frontiers of knowledge for managing induced seismicity.

1.3 Thesis layout

This Thesis is organized in six chapters, which coincide with papers already published in international scientific journals or in the process of peer review and presentations in

conferences, workshops, and seminars. Each chapter contains its own introduction and conclusions. The rest of the Thesis is structured as follows:

- Chapter 2 presents the closed-form solution developed for stress variations in response to injection into or pumping from a reservoir crossed by a fault that could be either permeable or impermeable with an arbitrary dip angle and offset. The solution is verified by comparing with both numerical and other analytical solutions. Applications of this solution under various geological settings illustrate the effects of fault permeability, fault geometry, initial stress state, and pore pressure changes on fault stability and induced seismicity potential. The contents of this Chapter have been published in the scientific journal *Journal of Geophysical Research: Solid Earth* (Wu et al., 2021a) and have been presented in several conferences (Wu and Vilarrasa, 2019; Wu et al., 2020b, 2020c, 2021b) and a seminar (Wu et al., 2020a).

- Chapter 3 describes the closed-form solution developed for displacement generated from reservoir pressurization/depletion by considering a similar geological setting to the one adopted in Chapter 2 but in a half space instead of the previous full space. This solution is verified by comparing with two analytical solutions. We then present the effects of fault permeability, fault and reservoir geometries, and ground surface on induced displacement, with special emphasis on ground displacement. According to the results with and without the free surface, we propose an index to assess the condition for neglecting free-surface effects. An intrinsic threshold of such index is found for calibrating the validity of full-space solutions. This Chapter has resulted in an article (Wu et al., 2023b), which is currently under review in a scientific journal.

- Chapter 4 deals with the uncertainty problem of geological properties for the Pohang M_w5.5 earthquake by a stochastic poromechanical analysis. Both the pore pressure diffusion and poromechanical response due to the cyclic fluid injection are represented by analytical solutions to perform the stochastic simulations for the uncertain estimates of in-situ stress and fault plane. The slipping fault patch size is quantitatively linked to the critical size of nucleation zone and thus, to the magnitude of induced seismicity. Relevant results show us the occurrence probability of this earthquake and the most likely estimate of the in-situ stress and fault plane. A parametric space analysis on the uncertain geological properties is also carried out to see which parameters are playing an essential role on induced seismicity. The contents of this Chapter have been presented in several conferences (Wu et al., 2021d, 2023d) and a seminar (Wu et al., 2021c) and will be submitted to a scientific journal (Wu et al., 2023c).

- Chapter 5 addresses the poromechanical effect on the nucleation process of earthquakes, aiming at filling the gap between earthquake nucleation and stress heterogeneity caused by poromechanical response to fluid injection. Both the pore pressure diffusion and poromechanical response due to fluid injection are represented by analytical solutions to couple with the interfacial slip model of

cracks. Results reveal additional slip regimes in addition to the ones found without considering the poromechanical stress, and the poromechanical effect on earthquake magnitude. The contents of this Chapter have been included in an article (Wu et al., 2023a), which is under review in a scientific journal, and have also been presented in a seminar (Wu et al., 2022).

- Chapter 6 summarizes the most insightful findings and conclusions of the Thesis.

In addition, some details for all the Chapters are uniformly included in Appendices. All the references are listed at the end of the Thesis.

2 Analytical solution to assess the induced seismicity potential of faults in pressurized and depleted reservoirs

2.1 Introduction

Induced seismicity has become a widespread issue as a result of the proliferation of geo-energy projects (Foulger et al., 2018). On the one hand, geothermal energy production and geologic carbon storage are essential technologies to reach zero or negative net carbon emissions. On the other hand, the increased energy demand is boosting other operations, such as seasonal natural gas storage, subsurface energy storage and disposal of wastewater from conventional and non-conventional oil and gas production. Injecting or pumping fluids at depth – a widespread practice in geo-energy operations – alters the in-situ stress field and may lead to fault rupture and induced seismicity (Ellsworth 2013; Buijze et al., 2017; Grigoli et al., 2018). In several cases, authorities have decided to cancel projects believed to be associated with large induced earthquakes and a non-exhaustive list includes the Deep Heat Mining Project in Basel, Switzerland (Haring et al, 2008; Deichmann and Giardini, 2009; Terakawa et al., 2012), the Castor natural storage project, Spain (Del Potro 2015; Juanes et al., 2017; Villaseñor et al. 2020), and the Enhanced Geothermal System (EGS) project at Pohang, South Korea (Grigoli et al., 2018; Lee et al., 2019; Ellsworth et al., 2019). To reduce the risks of induced seismicity and safely promote sustainable energy development, tools to predict and subsequently mitigate induced seismicity should be developed.

Despite the considerable advancements in understanding the triggering mechanisms of induced seismicity in recent years, forecast and mitigation of induced seismicity remains challenging and some fundamental questions remain open (Elsworth et al., 2016; Lee et al., 2019). Potential triggering mechanisms include pore pressure diffusion caused by single phase (Simpson et al., 1988; Shapiro and Dinske, 2009) and multi-phase flow (Zbinden et al., 2017), poroelastic and thermally-induced stress changes (Chang and Segall, 2016; Langenbruch and Zoback, 2016, De Simone et al., 2017) and strength weakening due to geochemical reactions (Rohmer et al., 2016; Vilarrasa et al., 2019). These mechanisms, separately or acting jointly, can lead to fault slip (Orlic et al., 2013; Orlic and Wassing, 2013; Van den Bogert, 2015; Lele et al., 2016; Rutqvist et al., 2016; Van Wees et al., 2017; Lehner, 2019) and nucleation of dynamic rupture (Garagash and Germanovich, 2012; Buijze et al., 2017, 2019; Galis et al., 2017, 2019) on different geological settings (Bourne and Oates, 2017; Haug et al., 2018), even at very large distances (Goebel et al., 2017).

Faults intersecting the injection/pumping formation undergo pore pressure and stress changes, affecting their stability. Pore pressure changes are controlled by the hydraulic properties of faults, which are highly variable, ranging from conductive faults to flow barriers (Caine et al., 1996). For example, low-permeable faults are present at the Snohvit CO_2 storage site, Norway (Chiaramonte et al., 2013; Hansen et al., 2013), at

Pohang EGS project, South Korea (Kim et al., 2018; Ellsworth et al., 2019) and at many compartmentalized reservoirs (e.g., Castelletto et al., 2013), and permeable faults are found at the Groningen gas field, the Netherlands (Van Wees et al., 2014; Jansen et al., 2019) and the Corinth rift, Greece (Geraud et al., 2006; Duverger et al., 2015). Stress changes arise when the reservoir deformation is restricted, as in the case of closed or compartmentalized reservoirs, and they are governed by the poromechanical properties of the rock – the stiffer the rock, the larger the induced stress – and by the fault offset, which generates an additional stress concentration (Buijze et al., 2017; Galis et al., 2017, 2019). Such generated stress could lead to an increase in induced earthquake frequency, as was observed in the Groningen gas field (Van Wees et al., 2014; NAM, 2016; Van Wees et al., 2017).

Numerical simulations can account for great physical and geometrical complexity, but the computational cost often prevents systematic explorations of the parametric space. Analytical methods offer an alternative to obtain fast estimations, but require more stringent hypotheses and simplifications on the geometry and physics of the problem when compared to numerical methods. Interestingly, their drawback turns into an advantage when the perspective is changed and the goal becomes a quick and efficient parametric space analysis, ultimately highlighting the factors controlling the problem. For the problem of reservoir pressurization/depletion, Eshelby's inclusion theory (Eshelby, 1957) is at the heart of several analytical solutions describing displacement, strain and stress fields in an infinite half-space with an elliptic inclusion (Segall, 1985, 1992; Segall and Fitzgerald, 1998). The theory was applied to study subsidence and induced seismicity (Segall, 1985; Segall et al., 1994; Segall, 1989), recognizing the influence of reservoir geometry and orientation (Soltanzadeh and Hawkees, 2008, 2009) and the importance of including the contribution of crack-tip resistance to fault strength (Wang et al. 2016). Existing analytical solutions either assume non-displaced faults (Segall, 1985, 1992; Segall and Fitzgerald, 1998; Soltanzadeh and Hawkees, 2008, 2009; Wang et al. 2016) or displaced but permeable faults (Jansen et al., 2019). No solution currently exists for low-permeable faults that cross the reservoir with an offset: the aim of our contribution is to fill this knowledge gap and analyze the difference in terms of fault stability between permeable and low-permeable faults crossing a pressurized/depleted reservoir for both non-displaced and displaced faults.

In this chapter, we propose an analytical solution for stress variations in response to injection/pumping into a reservoir crossed by a fault that could be either permeable or impermeable with offset ranging from zero to the reservoir thickness. Note that by stress variations we refer to total stress changes, whereas for the effective stress, we explicitly mention effective in our terminology. The structure of the chapter is as follows. In Section 2.2, we introduce the conceptual problem, develop the analytical solution and show its validation. In Section 2.3, we present the methods to assess fault stability and fault slip potential based on our solution for both permeable and impermeable faults. In Section 2.4, we illustrate the effect of fault permeability on fault stability and perform a systematical parametric space analysis of fault offset, fault dip, initial stress state and pressure change. Finally, we provide extended discussion of the

results and its principal implications in Section 2.5.

2.2 Analytical solution for stress changes around a fault crossing a pressurized/depleted reservoir

2.2.1 Problem formulation and assumptions

We evaluate the induced stress arising in a deep reservoir crossed by a displaced permeable or impermeable fault as a consequence of fluid injection or production. The reservoir is treated as an inclusion that is hydraulically disconnected from the overlying caprock and underlying bedrock (Figure 2.1). A displaced fault with an arbitrary dip angle θ crosses the whole reservoir and extends to the surrounding rock, dividing the entire domain into two parts: the left part is the hanging wall and the right part is the footwall for a normal fault (Jansen et al., 2019). A non-displaced fault is a particular case in which fault offset is zero. The fault offset, *ht*, is defined as $b - a$ (see Figure 2.1), and fault geometry is parametrized by four corner points (P1, P2, P3 and P4). The height (thickness) and width of the faulted reservoir are $a + b$ and $c + d$, respectively, where the width can be assumed as infinite by imposing $c = d = \infty$. The reservoir length is assumed as infinite in the out-of-plane direction.

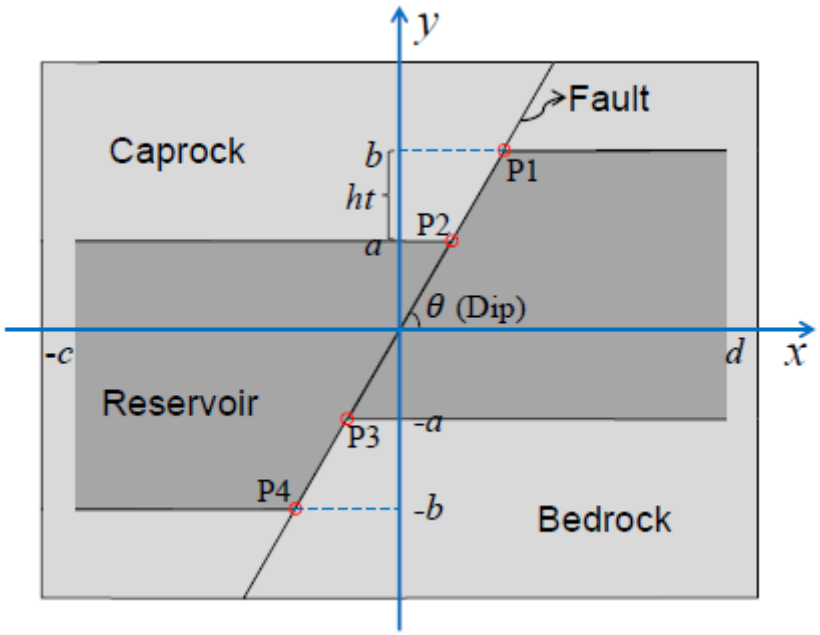

Figure 2.1: Geological model and its schematic geometry. Pore pressure changes within the reservoir in one or both sides of the fault depending on whether the fault is impermeable or permeable, respectively. The caprock and bedrock are assumed impermeable and thus, no pressure changes occur outside the reservoir.

We adopt the solid mechanics sign convention of stress and strain, i.e., negative normal components denote compression, and a positive shear stress is assumed to rotate the material element in the counterclockwise direction, which indicates that the left part of fault moves downward relative to the right part. For pore pressure, a negative pore

pressure change refers to production and a positive one to injection.

We apply the following hypotheses: i) the reservoir, assumed horizontal, elastic, homogeneous and isotropic, and its surroundings have identical stiffness but different permeability and porosity – the latter implies that flow and pressure changes take place exclusively within the reservoir –; ii) two-dimensional (2D) plane strain conditions apply based on the assumption that the reservoir extends infinitely in the out-of-plane direction; iii) quasi-steady-state uniform pore pressure changes occur in the reservoir as a consequence of injection/production, i.e., the transient effect of flow is neglected, iiii) reservoir depth is great enough so as the effect of the free surface can be neglected (Lehner, 2019).

2.2.2 Analytical solution

According to the inclusion theory (Eshelby, 1957; Mura, 1987; Rudnicki, 2011), pore pressure changes induce stress variation σ_{ij} in the reservoir as (see Appendix A for the full mathematical development)

$$\sigma_{ij}(x,y) = C\left[\iint_{\Omega} g_{ij}(x,y,\varsigma,\xi)d\Omega - \pi\delta_{ij}\delta_{\Omega}\right] = C\left[G_{ij}(x,y) - \pi\delta_{ij}\delta_{\Omega}\right], \tag{2.1}$$

$$C = \frac{(1-2\nu)\alpha\Delta p}{2\pi(1-\nu)}, \tag{2.2}$$

where Ω is the inclusion domain, g_{ij} and G_{ij} represent the Green's function for stress and its surface integral, respectively, x and y are the Cartesian coordinates, ς and ξ denote the coordinate values within the domain Ω, α is the Biot's coefficient, ν is the Poisson's ratio, and Δp is the pore pressure change. δ_{ij} is the Kronecker delta, which equals 1 if $i = j$ or 0 if $i \neq j$ and δ_{Ω} is the modified Kronecker delta, which equals 1 if $(x,y) \in \Omega$ or 0 if $(x,y) \notin \Omega$.

Green's function g_{ij} gives the magnitude of the stress in the i-th direction at point (x, y) in response to a body force in the j-th direction applied at point (ς, ξ) (see Equations (A17) to (A19)). To perform their integration over the inclusion domain as in Equation (2.1), we set the origin to coincide with the midpoint of the fault (Figure 2.1). The integration domain is different whether we are in the case of permeable or impermeable faults. For the former case, pore pressure changes within the reservoir on both sides of the fault. For the latter case, pore pressure only changes on the side of the fault where injection or depletion takes place. In the permeable case, the entire inclusion consists of two trapezoids (Figure 2.1), each of which can be divided into two subdomains to simplify the integration. Thus, we apply the superposition principle of integral to combine the solutions for a rectangular and a triangular domains, which returns (see Appendix B for the full derivation)

$$
\begin{aligned}
G_{xx}(x,y) &= -G_{yy}(x,y) \\
&= \operatorname{atan}\frac{y+b}{x+c} - \operatorname{atan}\frac{y-a}{x+c} + \operatorname{atan}\frac{y-b}{x-d} - \operatorname{atan}\frac{y+a}{x-d} \\
&\quad -\left[f_1(x,y,-b) - f_1(x,y,a) + f_1(x,y,b) - f_1(x,y,-a) \right]\sin^2\theta \\
&\quad -\frac{\sin\theta\cos\theta}{2}\ln\frac{f_2(x,y,-b)\,f_2(x,y,b)}{f_2(x,y,a)\,f_2(x,y,-a)} - \pi\delta_{\Omega}
\end{aligned}
\tag{2.3}
$$

$$
\begin{aligned}
G_{xy}(x,y) &= \left[f_1(x,y,-b) - f_1(x,y,a) + f_1(x,y,b) - f_1(x,y,-a) \right]\sin\theta\cos\theta \\
&\quad -\frac{\sin^2\theta}{2}\ln\frac{f_2(x,y,-b)\,f_2(x,y,b)}{f_2(x,y,a)\,f_2(x,y,-a)} + \frac{1}{2}\ln\frac{f_3(x+c,y+b)\,f_3(x-d,y-b)}{f_3(x+c,y-a)\,f_3(x-d,y+a)},
\end{aligned}
\tag{2.4}
$$

where functions f_1, f_2 and f_3 are

$$
f_1(x,y,\hat{y}) = \operatorname{atan}\frac{(x-\hat{y}\cot\theta)\cot\theta + (y-\hat{y})}{x - y\cot\theta},
\tag{2.5}
$$

$$
f_2(x,y,\hat{y}) = \left(x-\hat{y}\cot\theta\right)^2 + \left(y-\hat{y}\right)^2,
\tag{2.6}
$$

$$
f_3(x-\hat{x},y-\hat{y}) = (x-\hat{x})^2 + (y-\hat{y})^2,
\tag{2.7}
$$

where a, b, c, and d are the geometrical parameters shown in Figure 2.1. The last term $(-\pi\delta_{\Omega})$ in Equation (2.3) results from the solution of improper integral (Courant and John, 1989) because the Green's function for stress becomes unbounded for points (x, y) located in the inclusion domain. The corners of two trapezoidal domains are singularities for the solutions (Equations (2.3) and (2.4)) (see Appendix B). The vertical fault is a special case of inclined fault, which is obtained by setting $\theta = 90°$ (Equations (B21)-(B22)). And faults with no offset are also a special case in which $a = b$ (Equations (B23)-(B24)).

When substituting Equations (2.3) and (2.4) into Equation (2.1), we obtain the x-y planar solution for describing the distribution of induced stress in the pressurized or depleted reservoir and its surrounding rock. Our solution is consistent to the one developed by Jansen et al. (2019) for the case of a horizontal infinite reservoir crossed by a permeable fault. However, our current solution is also valid for any arbitrary reservoir width, with the solution for the infinite reservoir being a special case, i.e., $c = d = \infty$.

Fault stability and its likelihood of rupture depend on the distribution of the normal and tangential stress components along the fault plane. Thus, the above x-y planar solution along the fault plane needs to be transformed into the coordinate system placed on the fault and oriented along it. We apply the stress transformation with axis rotation (Equations (C4) and (C5)) to derive the closed expressions for such induced stress along an arbitrary fault plane with dip angle θ, which yields (see Appendix C for the full derivation)

$$\begin{aligned}\bar{\sigma}_n(y\cot\theta, y) = &-\frac{\pi}{2}\left[\operatorname{sgn}(y+b)-\operatorname{sgn}(y-a)+\operatorname{sgn}(y-b)-\operatorname{sgn}(y+a)\right]\sin^2\theta \\ &-\cos 2\theta\left(\operatorname{atan}\frac{y+b}{y\cot\theta+c}-\operatorname{atan}\frac{y-a}{y\cot\theta+c}+\operatorname{atan}\frac{y-b}{y\cot\theta-d}\right. \\ &\left.-\operatorname{atan}\frac{y+a}{y\cot\theta-d}-\pi\delta_\Omega\right)+\frac{\sin 2\theta}{4}\ln\frac{f_4(y,b)}{f_4(y,a)} \\ &-\frac{\sin 2\theta}{2}\ln\frac{f_3(y\cot\theta+c,y+b)\,f_3(y\cot\theta-d,y-b)}{f_3(y\cot\theta+c,y-a)\,f_3(y\cot\theta-d,y+a)}-\pi\delta_\Omega\end{aligned}, \tag{2.8}$$

$$\begin{aligned}\bar{\tau}(y\cot\theta, y) = &-\frac{\pi}{4}\left[\operatorname{sgn}(y+b)-\operatorname{sgn}(y-a)+\operatorname{sgn}(y-b)-\operatorname{sgn}(y+a)\right]\sin 2\theta \\ &+\sin 2\theta\left(\operatorname{atan}\frac{y+b}{y\cot\theta+c}-\operatorname{atan}\frac{y-a}{y\cot\theta+c}+\operatorname{atan}\frac{y-b}{y\cot\theta-d}\right. \\ &\left.-\operatorname{atan}\frac{y+a}{y\cot\theta-d}-\pi\delta_\Omega\right)-\frac{\sin^2\theta}{2}\ln\frac{f_4(y,b)}{f_4(y,a)} \\ &-\frac{\cos 2\theta}{2}\ln\frac{f_3(y\cot\theta+c,y+b)\,f_3(y\cot\theta-d,y-b)}{f_3(y\cot\theta+c,y-a)\,f_3(y\cot\theta-d,y+a)}\end{aligned}, \tag{2.9}$$

where $\sigma_n(y\cot\theta, y)$ and $\tau(y\cot\theta, y)$ are the induced normal and tangential stress components along the fault plane, respectively, they will be shorten into σ_n and τ for convenience hereafter. The stress components with an overbar denote the dimensionless stress components, which are normalized by the scaling parameter *C* (Equation (2.2)). The sgn(•) is the sign function defined as 1 if (•) > 0, 0 if (•) = 0 or -1 if (•) <0, and function f_4 is defined as

$$f_4(y,\hat{y}) = \left(y+\hat{y}\right)^2\left(y-\hat{y}\right)^2. \tag{2.10}$$

The four corners P1, P2, P3 and P4 on the fault plane are singularities of Equations (2.8) and (2.9) (Figure 2.1). With such general solution, one can easily find the solutions for the special cases of vertical faults (Equations (C8) and (C9)) and zero offset faults (Equations (C10) and (C11)). In particular, σ_n and τ just correspond to σ_{xx} and σ_{xy} for the case of vertical faults, respectively. In the above equations, the segment P1-P2 of the fault belongs to the inclusion, while the segment P3-P4 belongs to the surroundings (see Appendix C).

For an impermeable fault, we assume that the pore pressure change is restricted to the side of the fault where injection/production takes place, while pore pressure in the other side remains unaltered. Thus, the integration of the Green's function for stress only entails one part of the inclusion domain, i.e., one trapezoidal domain. Considering that fluid is injected into the left-hand side of the domain, such integrations are

$$
\begin{aligned}
G_{xx}(x,y) &= -G_{yy}(x,y) \\
&= \operatorname{atan}\frac{y+b}{x+c} - \operatorname{atan}\frac{y-a}{x+c} - \frac{\sin\theta\cos\theta}{2}\ln\frac{f_2(x,y,-b)}{f_2(x,y,a)}, \\
&\quad -\left[f_1(x,y,-b) - f_1(x,y,a)\right]\sin^2\theta - \pi\delta_\Omega
\end{aligned}
\tag{2.11}
$$

$$
\begin{aligned}
G_{xy}(x,y) &= \left[f_1(x,y,-b) - f_1(x,y,a)\right]\sin\theta\cos\theta \\
&\quad -\frac{\sin^2\theta}{2}\ln\frac{f_2(x,y,-b)}{f_2(x,y,a)} + \frac{1}{2}\ln\frac{f_3(x+c,y+b)}{f_3(x+c,y-a)},
\end{aligned}
\tag{2.12}
$$

and the dimensionless induced normal and tangential stress components along the fault plane are

$$
\begin{aligned}
\bar{\sigma}_n(y\cot\theta, y) &= -\cos 2\theta\left(\operatorname{atan}\frac{y+b}{y\cot\theta+c} - \operatorname{atan}\frac{y-a}{y\cot\theta+c} - \pi\delta_\Omega\right) \\
&\quad -\frac{\pi}{2}\left[\operatorname{sgn}(y+b) - \operatorname{sgn}(y-a)\right]\sin^2\theta + \frac{\sin 2\theta}{4}\ln\frac{(y+b)^2}{(y-a)^2}, \\
&\quad -\frac{\sin 2\theta}{2}\ln\frac{f_3(y\cot\theta+c, y+b)}{f_3(y\cot\theta+c, y-a)} - \pi\delta_\Omega
\end{aligned}
\tag{2.13}
$$

$$
\begin{aligned}
\bar{\tau}(y\cot\theta, y) &= \sin 2\theta\left(\operatorname{atan}\frac{y+b}{y\cot\theta+c} - \operatorname{atan}\frac{y-a}{y\cot\theta+c} - \pi\delta_\Omega\right) - \frac{\sin^2\theta}{2}\ln\frac{(y+b)^2}{(y-a)^2} \\
&\quad -\frac{\pi}{4}\left[\operatorname{sgn}(y+b) - \operatorname{sgn}(y-a)\right]\sin 2\theta - \frac{\cos 2\theta}{2}\ln\frac{f_3(y\cot\theta+c, y+b)}{f_3(y\cot\theta+c, y-a)}
\end{aligned}
\tag{2.14}
$$

.

The corners of the left-hand trapezoidal domains of the fault are singularities of Equations (2.11) and (2.12), and the corners P2 and P4 on the fault plane are singularities of Equations (2.13) and (2.14) (Figure 2.1). The whole impermeable fault belongs to the surroundings for fluid injection into the left-hand side of the fault because we apply the right limit, i.e., the limit that the argument approaches the fault from its right-hand side, as the value of the fault plane. Note that in Equation (2.11) the extra term originating from improper integral is always $-\pi\delta_\Omega$ because it depends only on the integrand (the limit of integration at improper points only depends on the integrand) and not on geometry. The solution is similar in the case of injection into the right-hand side of the fault. To avoid confusion or repetitions, in the following we will always consider the case of injection into the left-hand side as an example to represent the impermeable case.

2.2.3 Verification against numerical solution

To verify the accuracy and correctness of our analytical solution, we compare fluid injection-induced stress distribution along a permeable and an impermeable fault against numerical solutions. The numerical simulations are performed with the fully coupled finite element code CODE_BRIGHT (Olivella et al., 1994, 1996). The

geometry is shown in Figure 2.1. We adopt dimensions and rock properties as in Jansen et al. (2019) in order to also compare our results with theirs (Table 2.1). In the numerical simulations, we mimic the impermeable rock, i.e., caprock and bedrock, and the impermeable fault by assigning low values of intrinsic permeability, i.e., 10^{-18} m^2. We impose mechanical boundary conditions of zero normal displacement to the lateral and lower boundaries and an overburden of -70 MPa on the upper boundary, corresponding to a depth of 3.5 km. We assume that the initial stress state is isotropic. The magnitude of the initial stress and pressure is irrelevant because we are interested in the stress changes induced by pore pressure changes and both the hydraulic and the mechanical processes are linear. We impose a pressure buildup of 20 MPa in the reservoir, which is the entire reservoir in the case of permeable fault while half of it in the case of impermeable fault. We make sure that the size of the reservoir is large enough to minimize boundary effects.

Table 2.1: Geometrical parameters of the reservoir and rock properties adopted for the validation example.

Parameter	Physical meaning	Value	Unit
a		100	m
b	Geometrical parameters	200	m
c	(Refer to Figure 2.1)	2000	m
d		2000	m
θ	Fault dip	60	°
μ	Shear modulus	6500	MPa
ν	Poisson's ratio	0.15	-
α	Biot's coefficient	0.9	-
Δp	Pressure buildup	20	MPa

We compare the numerical and analytical results for a permeable and an impermeable fault (Figure 2.2). Further results are presented in Appendix D. The numerically computed induced stress on the fault plane is almost identical to the analytical one. Small discrepancies near the corners are a consequence of the existence of singularities for the analytical solution, which leads to an infinite stress, and of the discrete nature of the numerical solution. We also consider the case of vertical permeable fault crossing a horizontal infinite reservoir in order to compare our results with the ones of Jansen et al. (2019). Comparisons are shown in Appendix D and they exhibit a good agreement.

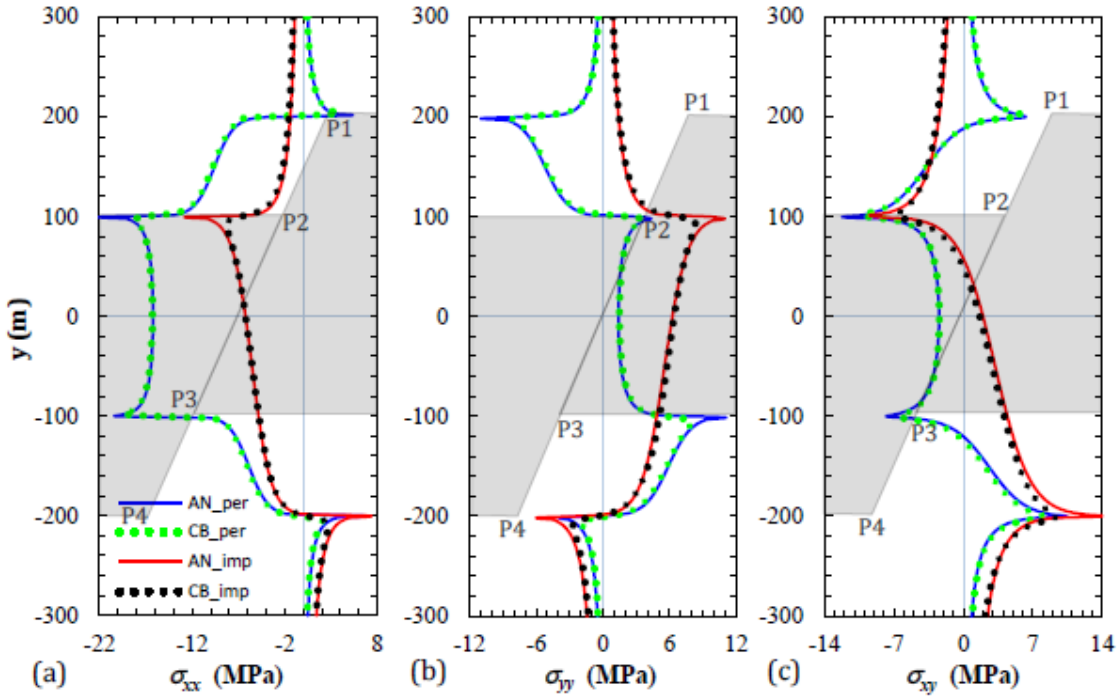

Figure 2.2: Comparison between analytically and numerically evaluated induced (a) horizontal, (b) vertical and (c) *x*-*y* planar shear stress components along the fault plane. Results along the fault are projected on the vertical axes *y*. The legend is shown in (a), indicating that solid lines represent the analytical results (AN) and dotted lines represent the numerical results with CODE_BRIGHT (CB), for both a permeable (per) and an impermeable (imp) fault. A schematic of the reservoir geometry, with the four corners, is indicated by the grey background.

2.3 Induced seismicity potential assessment

2.3.1 Coulomb failure stress (*CFS*) and Coulomb failure stress change (ΔCFS)

We assess the fault stability by means of the Coulomb Failure Stress (*CFS*) (King, 1994)

$$CFS = \left|\tau + \tau^0\right| + \eta_{st}\left(\sigma_n^{'} + \sigma_n^{'0}\right), \tag{2.15}$$

where η_{st} is static friction coefficient, superscript 0 represents the initial state and the superscript ' denotes effective stress. Here, the initial normal and tangential stress components on the fault plane are calculated also according to the stress transformation Equations (C4) and (C5). Shear stress always drives the fault to slip regardless it is positive or negative. The second term in right-hand side of Equation (2.15) denotes the fault slip resistance and increases as the effective normal stress becomes more compressive. A positive value of *CFS* indicates that slip is activated in the direction of the shear stress along the fault, i.e., a positive shear stress represents the normal slip

and a negative shear stress represents the reversed slip for a normal fault (Jha and Juanes 2014).

For the assessment of induced seismicity and to identify whether a portion of the fault becomes more or less stable, we use the Coulomb Failure Stress Change (ΔCFS)

$$\Delta CFS = \left|\tau + \tau^0\right| - \left|\tau^0\right| + \eta_{\mathrm{st}}\sigma_n^{'}, \tag{2.16}$$

A positive ΔCFS implies the induced stress is driving the fault toward failure and eventually co-seismic slip. *CFS* and ΔCFS can be normalized by the scaling parameter *C* (Equation (2.2))

$$CFS_{\mathrm{D}} = \left|\bar{\tau} + \frac{\tau^0}{C}\right| + \eta_{\mathrm{st}}\left(\bar{\sigma}_n + \frac{\alpha\Delta p}{C} + \frac{\sigma_n^0 + \alpha p^0}{C}\right), \tag{2.17}$$

$$\Delta CFS_{\mathrm{D}} = \left|\bar{\tau} + \tau^0 / C\right| - \left|\tau^0 / C\right| + \eta_{\mathrm{st}}\left(\bar{\sigma}_n + \alpha\Delta p / C\right), \tag{2.18}$$

where we make use of Equations (2.8) and (2.9) for permeable faults or Equations (2.13) and (2.14) for impermeable faults, and the subscript D denotes dimensionless variables. Here the dimensionless effective pore pressure change, i.e., the term $\alpha\Delta p/C$, is an initial physical property within the reservoir, which is independent of the process of integration. Thus, the segment P1 to P4 undergoes the same pore pressure change as the reservoir for permeable faults, and the segment P2 to P4 undergoes the same pore pressure change as the left-reservoir compartment for fluid injection into the left-hand side of the impermeable fault.

2.3.2 Slipping fault patch size

To quantitatively evaluate the fault slip potential, and thus, the induced seismicity potential, we define the slipping fault patch size as

$$S_i = \ell_i / \sin\theta, \tag{2.19}$$

where ℓ_i is a continuous interval in coordinate *y* with *CFS* > 0. The slipping area can be discontinuous, so more than one S_i may exist. We assume that the greatest magnitude of induced earthquakes is proportional to the maximum slipping fault patch size, defined as

$$S_{\max} = \max(S_i), \tag{2.20}$$

which can be expressed in dimensionless form as

$$S_{\mathrm{Dmax}} = S_{\max} / L_{\mathrm{s}} = \max(\ell_i) / (a+b), \tag{2.21}$$

where L_{s} is a characteristic length of fault, here assumed as the length of the fault intercepting the reservoir

$$L_s = (a+b)/\sin\theta\,. \tag{2.22}$$

Assuming that each grain is restricted by its surrounding grains, i.e., the existence of cohesion between grains, the fault will not slide until the maximum unstable patch reaches a threshold. We set $S_{\mathrm{Dmax}} = 0.01$ as the threshold of fault slip in this work, i.e., the fault is always regarded as stable for $S_{\mathrm{Dmax}} < 0.01$.

2.3.3 Properties of the base case scenario

We evaluate the stress variation and the fault stability as well as the fault slip potential for a pressurized reservoir whose properties are derived from laboratory measurements on Berea sandstone (Makhnenko et al., 2015; Vilarrasa et al., 2016) (Table 2.2). We assume the same geometrical model as in Section 2.3 (Figure 2.1 and Table 2.1), with the center of the reservoir at 3.5 km depth, and with the initial stress state (normal faulting stress regime) shown in Table 2.2.

To generalize the problem, we normalize the coordinate *y* and the fault offset by the reservoir thickness, and we scale the pressure buildup by the initial pore pressure, which yields the dimensionless variables

$$y_{\mathrm{D}} = y/(a+b)\,, \tag{2.23}$$

$$ht_{\mathrm{D}} = (b-a)/(a+b)\,, \tag{2.24}$$

$$\Delta p_{\mathrm{D}} = \Delta p / p^0\,. \tag{2.25}$$

Table 2.2: Properties of Berea sandstone and the initial stress state of the reservoir adopted for the failure potential analysis

Parameter	Physical meaning	Value	Unit
θ	Fault dip	60	°
ht_{D}	Dimensionless fault offset	1/3	-
μ	Shear modulus	4600	MPa
ν	Poisson's ratio	0.29	-
α	Biot's coefficient	0.7	-
Δp_{D}	Dimensionless pressure buildup	4/7	-
p^0	Initial pore pressure	35	MPa
σ_{yy}^0	Initial vertical stress	-70	MPa
k_0	Stress ratio of horizontal to vertical stress	0.6	-
σ_{xy}^0	Initial shear stress in the *x*-*y* plane	0	MPa
η_{st}	Static friction coefficient	0.6	-
C	Scaling parameter for stress (Equation (2.2))	1.318	MPa
CFS_{D}^0	Initial dimensionless *CFS* (Equation (2.17))	-1.954	-

We compare the results for the two scenarios of permeable and impermeable faults to

understand the influence of the hydraulic properties of faults on fault stability and fault slip potential. In addition to these base case scenarios, we perform a parametric space analyses to explore the effects of fault geometry, initial stress state and operational aspects. We compare in all cases the difference between permeable and impermeable faults.

2.4 Results

2.4.1 Effect of fault permeability in the base case scenario

We evaluate the dimensionless induced shear and normal stress components on the fault plane according to Equations (2.8) and (2.9) for a permeable fault as well as Equations (2.13) and (2.14) for an impermeable fault (Figure 2.3). For the permeable fault, the dimensionless induced stress is symmetrical with respect to $y_D = 0$, as it is reflected by Equations (2.8) and (2.9) when the geometric parameters $c = d$. Corner points are singular, such that the induced shear stress tends to $+\infty$ at P1 and P4, and to $-\infty$ at P2 and P3 (for representation purposes, the infinite shear stress is cut off to a finite value). The induced normal stress has a reverse behavior with respect to the induced shear stress (compare Figures 2.3a and 2.3b), i.e., it tends to $-\infty$ at P1 and P4, and to $+\infty$ at P2 and P3. The entire fault plane except for a tiny vicinity at corners P2 and P3 shows a negative induced normal stress implies the increase in slip resistance, which contributes to the fault stability.

Unlike the permeable case, the induced shear and normal stress components are not symmetrical with respect to $y_D = 0$ for the impermeable fault, but the feature of reverse behavior for shear and normal stress components still holds (compare Figures 2.3a and 2.3b). The induced shear and normal stress components tend to infinity at corners P2 and P4 as a consequence of injecting from the left-hand side. These stress singularities in both the permeable and impermeable faults correspond to the points of stress concentration. The infinite value is a theoretical consequence of the integration of the Green's function and it is unrealistic for faults in nature where the material will undergo nonlinear deformation bounding stress values. We also plot the initial shear and effective normal stress components as well as the pressure buildup in Figure 2.3 to identify the contribution of each term to fault slip.

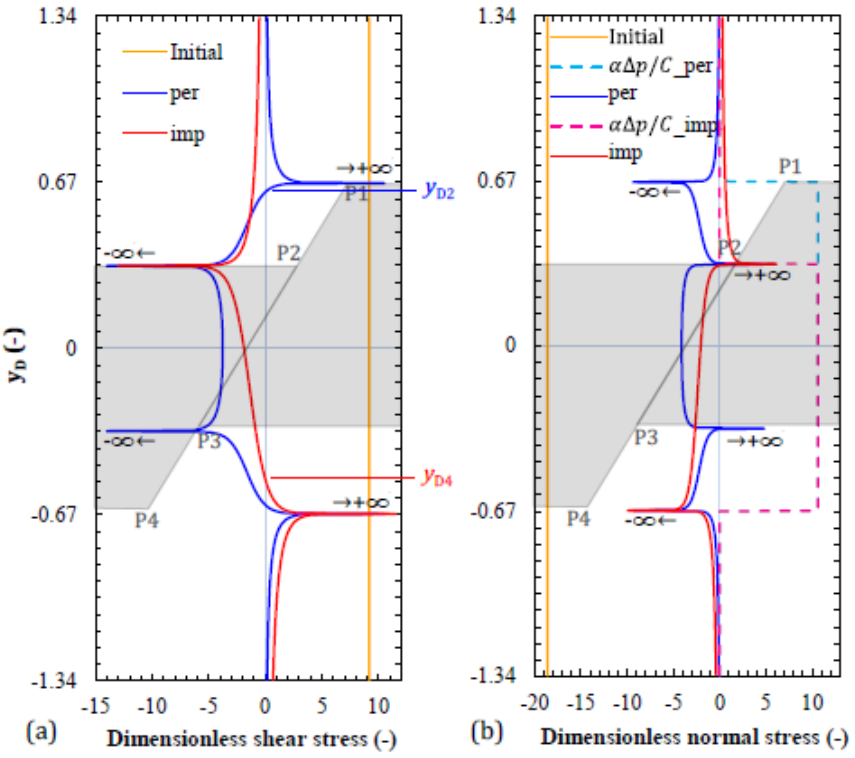

Figure 2.3: Dimensionless (a) shear and (b) normal stress components on the fault plane for the case of permeable (blue lines) and impermeable (red lines) fault. Dashed lines are the term of pressure buildup normalized by the scaling parameter *C*. Blue auxiliary line and label denote the zero point of $\bar{\tau}$ for a permeable fault, and the red ones for an impermeable fault. Results along the fault are projected on the vertical dimensionless axes y_D. A schematic of the reservoir geometry, with the four corners, is indicated by the grey background.

The dimensionless Coulomb Failure Stress change (ΔCFS_D, Equation (2.18)) along the fault plane, reflecting variations in the fault stability, remains symmetrical with respect to $y_D = 0$ for the permeable fault (Figure 2.4a) because the arithmetic operations of the symmetrical stress does not alter its symmetry. The stability of the permeable fault decreases everywhere, except for a small region close to the internal corners P2 and P3. Around the external corners, ΔCFS_D reaches its maximum value because of the stress concentration, which will likely induce fault slip locally. Conversely, the impermeable fault (Figure 2.4a) becomes more stable above the internal corner P2 and less stable below it. To determine the actual fault stability and assess whether failure conditions occur, CFS_D is computed as CFS_D^0 (Table 2.2) plus ΔCFS_D. It results that CFS_D has the same trend as ΔCFS_D (compare Figures 2.4a and 2.4b), but shifted by the magnitude of CFS_D^0. Therefore, the size of the fault that potentially undergoes failure ($CFS_D > 0$) is smaller than the one where stability decreases ($\Delta CFS_D > 0$).

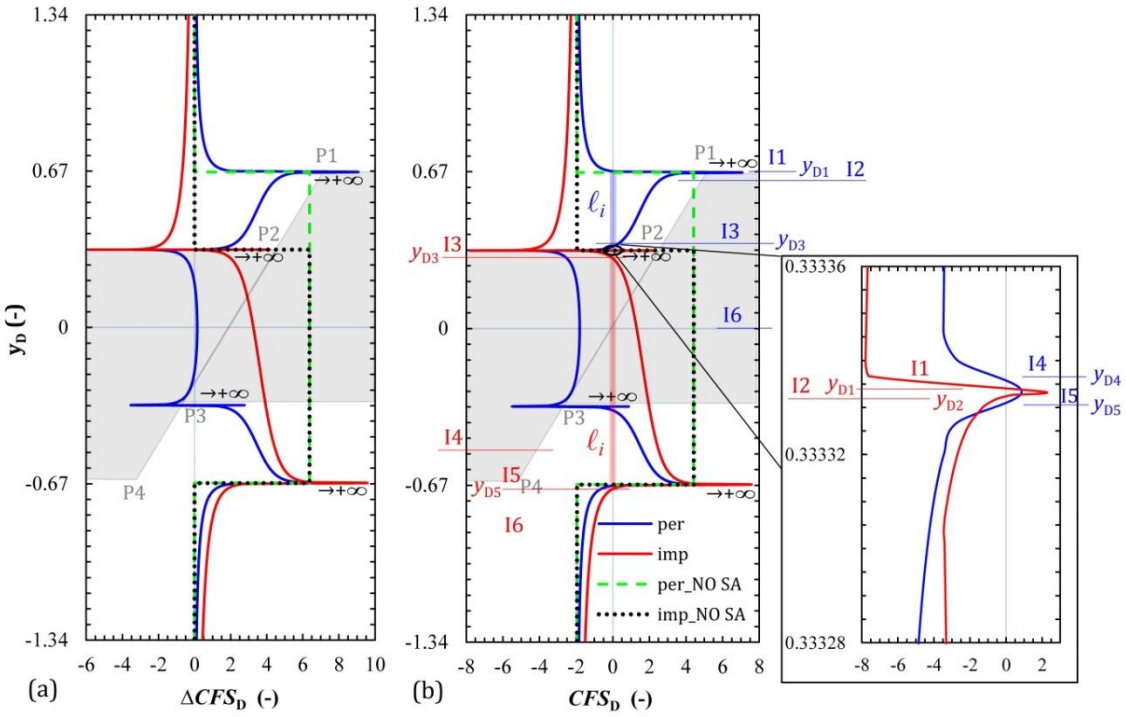

Figure 2.4: Dimensionless (a) Coulomb Failure Stress Change (ΔCFS_D) and (b) Coulomb Failure Stress (CFS_D) on the fault plane for the case of permeable (blue lines) and impermeable (red lines) faults. I*i* and y_{Di} are the sub-interval and zero point of CFS_D, respectively, in which the blue auxiliary lines and labels denote the ones for a permeable fault, and the red ones for an impermeable fault. Results along the fault are projected on the vertical dimensionless axes y_D. A schematic of the reservoir geometry, with the four corners, is indicated by the grey background. We also show the case of no stress arching (denoted by NO SA), i.e., stress changes induced by poromechanical effects are neglected. The legend is shown in (b).

To analyze the slip mechanism of permeable faults, given the symmetry of CFS_D, we divide the upper half part of the CFS_D curve into six sub-intervals (I1, I2, I3, I4, I5 and I6) by the four zero-points of CFS_D (y_{D1}, y_{D3}, y_{D4} and y_{D5}) and the zero point of $\bar{\tau}$ (y_{D2}, see Figure 2.3a) (blue symbols in Figures 2.3a and 2.4b). For impermeable faults, the whole CFS_D curve however is divided into six sub-intervals (I1, I2, I3, I4, I5 and I6) by the four zero points of CFS_D (y_{D1}, y_{D2}, y_{D3} and y_{D5}) and the zero point of $\bar{\tau}$ (y_{D4}, see Figure 2.3a) (red symbols in Figures 2.3a and 2.4b). Detailed fault state and mechanics for each sub-interval are shown in Table 2.3, in which the shear and normal stress components changes both belong to the fluid injection-induced poroelastic response. Overall, pore pressure buildup, which mainly results in the decrease of slip resistance, induce fault slip in the reservoir or make it less stable. The poroelastic response however represents a stabilizing effect on the fault within the reservoir except for a small vicinity around the corners because of the local stress concentration. While the poroelastic response has a small negative effect on fault stability both in the caprock and bedrock for permeable faults, it performs a positive effect on fault stability in the caprock but a negative effect in the bedrock for impermeable faults (Figure 2.4a).

Following such combined characteristics of pore pressure buildup and poroelastic

response, a permeable fault has four disconnected unstable patches (two normal slip patches and two reversed slip patches, Figure 2.4b), and an impermeable one has two unstable patches (one normal slip patch and one reversed slip patch, Figure 2.4b). The unstable patches of permeable faults, located between the external and internal corners (i.e., between P1 and P2 and between P3 and P4), are symmetric with respect to $y_D = 0$ and are separated by the stable central portion of the reservoir (between the internal corners P2 and P3). In contrast, practically the whole section of an impermeable fault located in the pressurized reservoir becomes unstable. In this case, while $S_{Dmax} = 0.32$ for the permeable fault, it reaches 0.99 for the impermeable case, so both of them slide but the slip size of the impermeable fault is more than 3 times the one for the permeable fault. Multiplying S_{Dmax} by the fault characteristic length (Equation (2.22)) yields the dimensional maximum slipping fault patch size, which is $S_{max} = 110.85$ m for the permeable case and $S_{max} = 342.95$ m for the impermeable case.

Table 2.3: Slip mechanism of permeable and impermeable faults in the base case scenario

Fault	Sub-interval	State (see Figure 2.4)	Mechanism (see Figure 2.3)
Permeable	I1	Less stable	Increase in shear stress
	I2	Normal slip	Increase both in shear stress and pore pressure
	I3	Normal slip	Increase in pore pressure
	I4	Stable	Decrease in shear stress
	I5	Reversed slip	Reversed increase in shear stress
	I6	Stable	Decrease in shear stress and increase in normal stress
Impermeable	I1	More stable	Decrease in shear stress
	I2	Reversed slip	Reversed increase in shear stress
	I3	Stable	Decrease in shear stress
	I4	Normal slip	Increase in pore pressure
	I5	Normal slip	Increase both in shear stress and pore pressure
	I6	Less stable	Increase in shear stress

For illustrative purposes, we include in Figure 2.4 the case in which the stress arching (Segall 1985; Rudnicki 2002; Soltanzadeh and Hawkees 2008) is neglected, i.e., stress changes both inside and outside the reservoir induced by poromechanical effects are neglected and the effective normal stress variation equals the pressure changes. Thus, only the pressure buildup in the reservoir induces the increase in *CFS*, i.e., $\Delta CFS = \eta_{st}\alpha\Delta p = 8.4$ MPa in the base case scenario, which is significantly larger than the ΔCFS for the case of including the stress arching, except for the infinite values at the corner points. Neglecting stress changes significantly overestimates the decrease in fault stability because the compression induced in the rock in response to reservoir expansion caused by pressurization is not taken into account. We will discuss this further in Section 5.

2.4.2 Effect of fault offset and fault dip

Fault offset affects differently permeable and impermeable faults (Figure 2.5). While fault stability significantly varies with offset for permeable faults (Figure 2.5a), impermeable faults undergo the same stability changes, but shifted, coinciding with the center of the pressurized/depleted reservoir (Figure 2.5b). For a permeable fault, ΔCFS_{D} slightly increases (stability decreases) within the reservoir and it is barely unaltered in the surrounding rock when the offset is equal to zero (Figure 2.5a). The stability-decreasing section increases proportionally to the fault offset and it concentrates at the external corners, where it tends to infinity. The section of the fault where the reservoir is juxtaposed on both sides of the fault presents a slight increase in stability. The size of this stabilized section decreases with fault offset, becoming negligible when the fault offset equals the reservoir thickness. In contrast, the size of the symmetric stability-decreasing sections between the internal and external corners of the reservoir increases with fault offset. Furthermore, both the stability of the caprock and the bedrock also slightly decreases. For an impermeable fault, the size of the stability-decreasing section, which is mainly constrained by the reservoir thickness, is independent of fault offset (Figure 2.5b), because the effect of stress concentration, which is controlled by the horizontal boundaries of the reservoir and the fault plane, is always the same for the impermeable fault regardless of its offset.

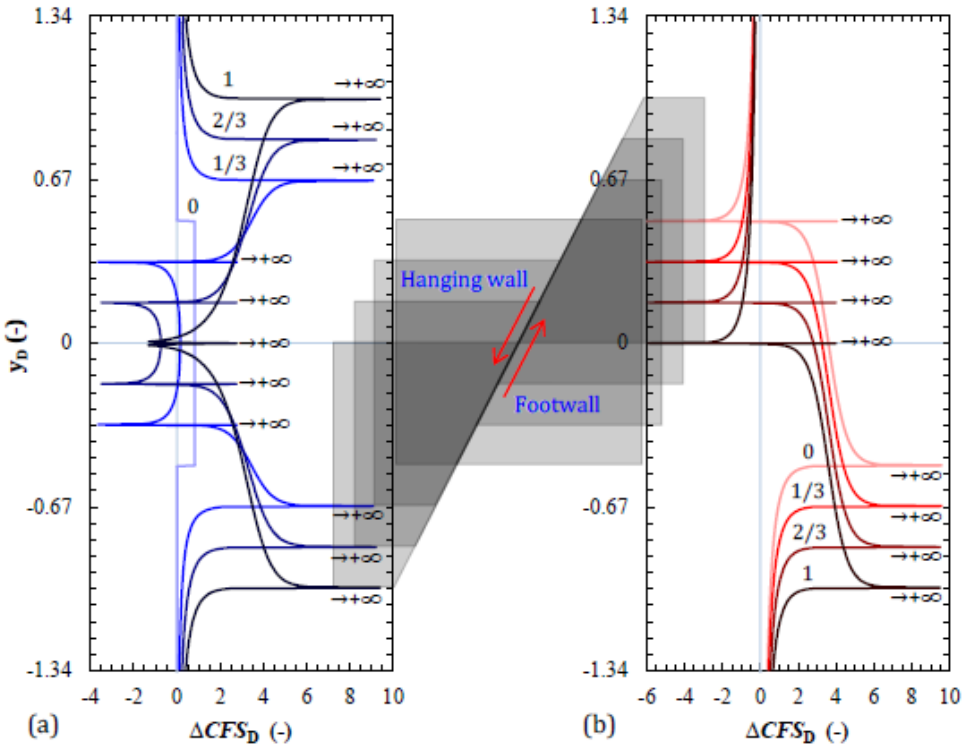

Figure 2.5: Dimensionless Coulomb Failure Stress Change (ΔCFS_{D}) on the fault plane for several dimensionless fault offsets for (a) permeable and (b) impermeable faults. The numbers on the curves denote the dimensionless fault offset. Results along the fault are projected on the vertical dimensionless axes y_D. The grey background indicates the position of the hanging and foot walls, which move simultaneously as the offset increases.

We analyze the impact of the fault dip, θ, (between 0°, horizontal fault, and 90°, vertical fault) on fault stability for both permeable and impermeable faults with no offset (Figure 2.6) and 1/3 of dimensionless offset (Figure 2.7). Figure 2.6a displays the schematic geometric model of no offset fault and the initial CFS_{D} as a function of the dip angle. The initial CFS_{D} shows that the fault is stable, with the most critical dip around 61°, as expected for a normal faulting stress regime with a fault friction coefficient of 0.6. As a result of reservoir pressurization, fault stability changes differ depending on the hydraulic nature of the fault.

For a permable fault, ΔCFS_{D} is constant in the reservoir for each value of the dip angle (Figure 2.6b). It exhibits the maximum value for $\theta = 0°$ (horizontal fault) and the minimum value for $\theta \approx 61°$ while it is close to zero in the surrounding rock for any value of the dip angle. For an impermeable fault, ΔCFS_{D} is not constant along the fault plane (see also Figure 2.5b), although its variation is only strongly relevant for $\theta > 45°$ (Figure 2.6c). Its maximum value is always located at the external corners (the horizontal boundary between the reservoir and its surrounding rock) because of the stress concentration (recall Figure 2.4a), especially for a high dip angle because the effect of stress concentration becomes maximum for the angle of corners at 90° (Ahmadi et al., 2012). ΔCFS_{D} in the caprock decreases for increasing dip angle except for $\theta > 85°$, being negative (more stable) in the range $31° < \theta < 85°$. ΔCFS_{D} increases with the dip angle in the bedrock and is positive (less stable) for $\theta > 31°$.

Note that to assess fault stability, ΔCFS_{D} for either a permeable or an impermeable fault have to be added to the initial CFS_{D}, which also changes with the dip angle (Figure 2.6a). The difference in ΔCFS_{D} between the permeable and impermeable faults is negative throughout the reservoir and baserock for almost all the dip angles, i.e., the impermeable fault is less stable, and positive over a small area located in the overlying caprock as a consequence of the left-hand side fluid injection (Figure 2.6d). A right-hand side injection would yield symmetrical results, with a positive difference located in the bedrock. Overall, an impermeable fault is more likely to be reactived than a permeable one when there is no offset.

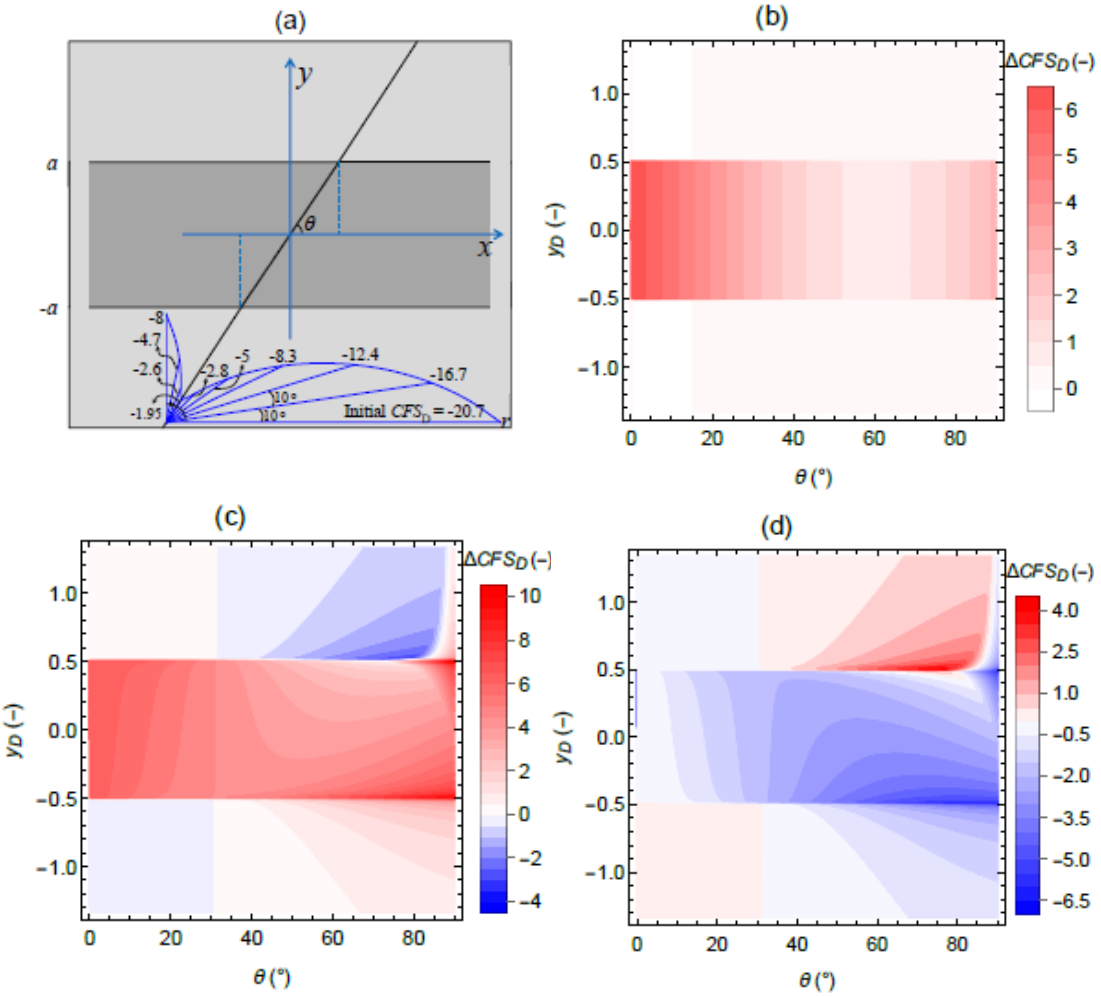

Figure 2.6: Fault stability changes along the fault plane as a function of the dip angle, θ, for the case of zero-offset fault. (a) Schematic geometry and CFS_{D}^{0} (shown in a polar coordinate system, the polar angle and diameter denote the fault dip angle and CFS_{D}^{0}, respectively), (b) ΔCFS_{D} for the permeable fault, (c) ΔCFS_{D} for the impermeable fault (for comparison purposes, (b) and (c) have the same color scale but the range of the legend is adapted to the values shown in each case) and (d) the difference between ΔCFS_{D} for the permeable and impermeable faults (i.e., (b)-(c)), where negative values indicate that the impermeable fault is less stable.

As for the case of 1/3 of dimensionless offset (Figure 2.7), CFS_{D}^{0} is the same as for the fault with no offset (compare Figures 2.6a and 2.7a). ΔCFS_{D} for a permeable fault is not constant along its plane and is symmetrical with respect to $y_{\mathrm{D}} = 0$ (Figure 2.7b). The fault has greater stability in the section between the internal corners P2 and P3, where the reservoir is juxtaposed on both sides of the fault, for $50° < \theta < 80°$ and lower stability for other dips. For an impermeable fault (Figure 2.7c), ΔCFS_{D} has the same distribution as for the case of no offset (Figure 2.6c), with the discontinuity shifted downward as a consequence of the downward shift of the boundary between the reservoir and the surrounding rock (recall Figure 2.5b). The difference in ΔCFS_{D} between the permeable and impermeable faults shows that for the section above the internal corner P2, the permeable fault is more unstable than the impermeable one, but the impermeable fault is less stable in the rest – a similar result to the zero-offset case

(Figure 2.7d).

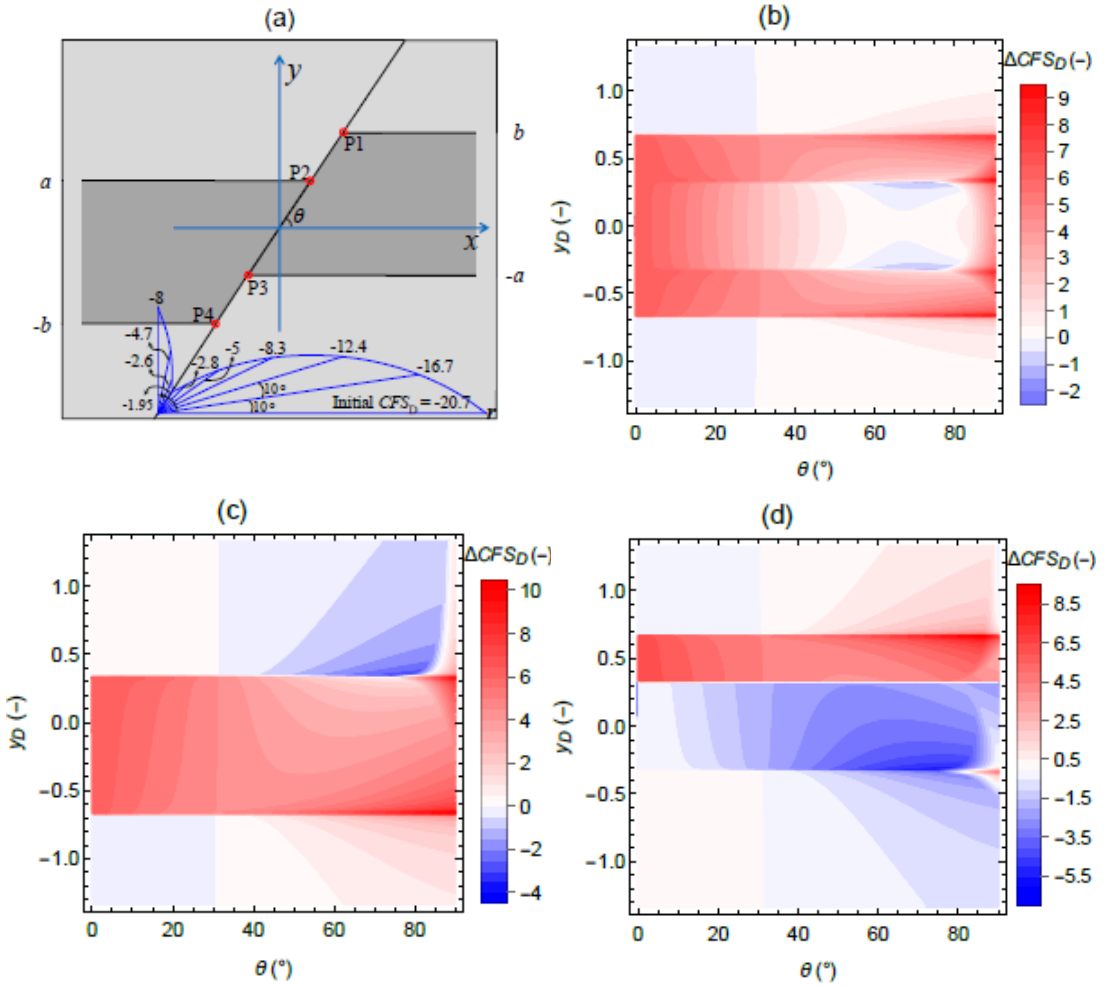

Figure 2.7: Fault stability changes along the fault plane as a function of the dip angle, θ, for the case with fault dimensionless offset equal to 1/3. (a) Schematic geometry and CFS_D^0 (shown in a polar coordinate system, the polar angle and diameter denote the fault dip angle and CFS_D^0, respectively), (b) ΔCFS_D for the permeable fault, (c) ΔCFS_D for the impermeable fault (for comparison purposes, (b) and (c) have the same color scale but the range of the legend is adapted to the values shown in each case) and (d) the difference between ΔCFS_D for the permeable and impermeable faults (i.e., (b)-(c)), where negative values indicate that the impermeable fault is less stable.

We present the fault slip potential as a function of the fault dip for several fault offsets while keeping the other parameters as the base case scenario, expressed in terms of the dimensionless maximum slipping fault patch size (S_{Dmax}), in Figure 2.8. For permeable faults, there is a clear onset value for fault dip ($\theta_o = 42$ º) corresponding to the threshold of fault slip, i.e., the fault undergoes slip for dip angles above the onset dip. Once $\theta > \theta_o$, S_{Dmax} increases rapidly and then gradually reaches its peak around $\theta_c = 56$ º, i.e., close to the critical dip angle for a normal faulting stress regime. The general trend of S_{Dmax} as well as the onset and critical fault dips for slip are almost independent of fault offset, but its maximum value (at $\theta = \theta_c$) increases with fault offset. According to our initial and injection conditions (Table 2.2), rupture does not occur when the

offset is zero. However, for more critical initial stress state or larger pressure buildup, failure would occur also in the case of zero offset as a consequence of pore pressure buildup (recall Figure 2.3). When the fault is close to be vertically oriented, there is an inflection point in S_{Dmax} that is barely visible for a small-offset (1/3) fault, but becomes more evident with larger offset. The occurrence of this inflection reflects that S_{Dmax} for reversed slip exceeds the one for normal slip, i.e., the reversed slip becomes the primary slip form. For impermeable faults, the effect of fault dip on S_{Dmax} is similar to the case of permeable fault, with an onset dip $\theta_o = 41.3°$ and a critical dip $\theta_c = 59.4°$, but no inflection is observed and the maximum value of S_{Dmax} is larger, approaching the reservoir thickness at the critical dip. The fault slip potential in impermeable faults is independent of the fault offset also because the effect of stress concentration is always the same regardless of its offset – a similar result to the fault stability (recall Figure5b).

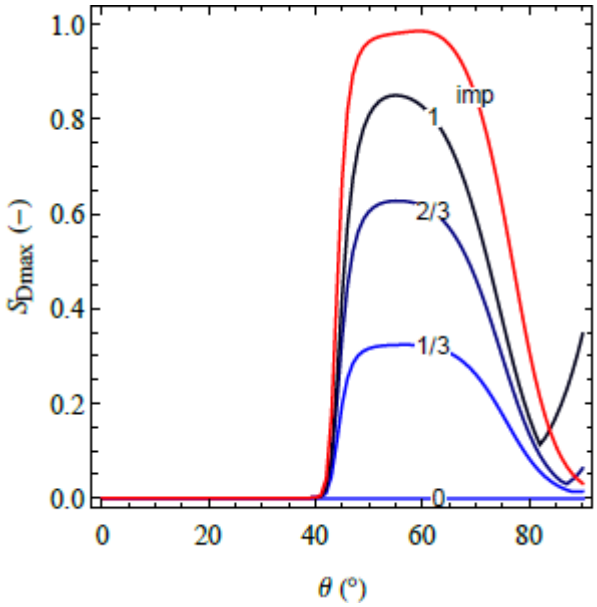

Figure 2.8: Dimensionless maximum slipping fault patch size (S_{Dmax}) as a function of fault dip for both permeable (blue color-scale lines) and impermeable faults (red line) and for several values of the dimensionless offset. The number on the blue lines denotes the dimensionless offset of permeable fault, and the results of different offsets for impermeable fault coincide in one line.

2.4.3 Effect of initial stress and pore pressure changes

The initial stress state determines the initial *CFS*, which significantly affects fault stability and the fault slip potential. We explore the influence of the initial stress state by applying different values of the horizontal to vertical stress ratio (k_0) while keeping the vertical stress constant (Figure 2.9). Given that we adopt a value of the static friction coefficient of 0.6, we set a minimum stress ratio of 0.563 to ensure that the initial conditions correspond to $CFS < 0$ (stable fault). We define a critical stress ratio k_0^c (marked by dots in Figure 2.9) which corresponds to the threshold of fault slip

(S_{Dmax} = 0.01), i.e., $k_0 > k_0^c$ implies a stable fault (negligible rupture size), and $k_0 < k_0^c$ a ruptured one for the applied pore pressure change. The dimensionless maximum slipping fault patch size increases with decreasing stress ratio for both the permeable and impermeable faults (Figure 2.9). In other words, the smaller the stress ratio, the larger the deviatoric stress and thus, the larger the slipping fault patch size. The rate of increase in S_{Dmax} with decreasing k_0 is not steady though and is controlled by the cusp-like shape of CFS_D (recall Figure 2.4b). The sharp increase in S_{Dmax}, when k_0 becomes lower than k_0^c, results from the progressive failure of the pressurized reservoir. Once the whole reservoir is in failure, the portion of the caprock or bedrock that undergoes failure increases slowly with k_0 decreasing (see Figure 2.4b). As the initial *CFS* approaches 0, the rupture size sharply increases because the asymptotic increase in ΔCFS_D within the caprock or bedrock is reached. The maximum rupture size coincides with the minimum in k_0, and for an impermeable fault in the base case scenario (only changing the stress ratio to its minimum) the rupture size is 3 times greater than the reservoir thickness ($S_{Dmax} \approx 3$). The rupture size is a lower bound because our model does not incorporate frictional strength weakening (Garagash and Germanovich, 2012; Buijze et al., 2017, 2019), and stress redistribution (Sacks et al., 1978; De Simone et al., 2017) associated with shear slip activation.

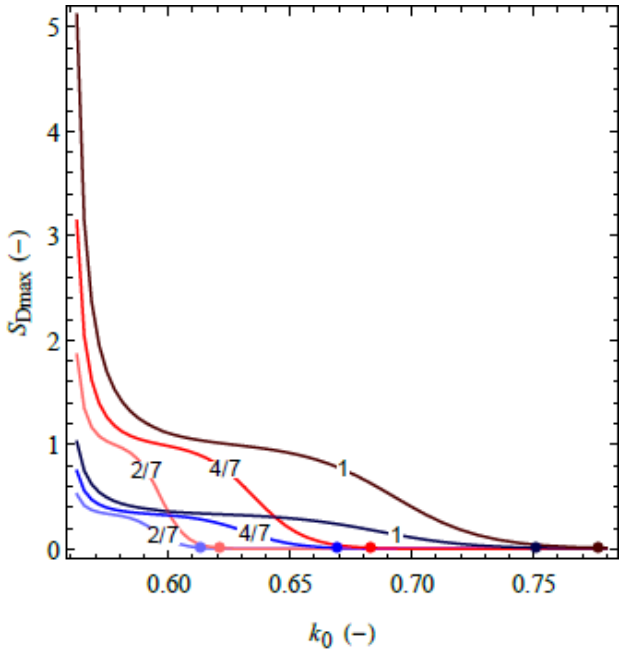

Figure 2.9: Dimensionless maximum slipping fault patch size (S_{Dmax}) as a function of the initial stress ratio for several pressure buildups. Dots represent the critical stress ratios. Blue and red color scales for curves and dots correspond to permeable and impermeable faults, respectively, and the number on the curves denotes the dimensionless pressure buildup.

The effect of operational aspects, expressed as pore pressure changes, is mainly controlled by the injected volume, injection rate and reservoir boundaries, i.e.,

compartmentalization, (Nordbotten et al., 2005; Mathias et al., 2009; Wu et al., 2016, 2018) and it affects the magnitude of induced earthquakes. Therefore, we further explore the (S_{Dmax}, k_0) space for different values of pressure buildup (Figures 2.9 and 2.10). We find that both S_{Dmax} and k_0^c (corresponding to the contour of $S_{Dmax} = 0.01$ in Figure 2.10) linearly increase with pressure buildup, with the highest increments of S_{Dmax} corresponding to the impermeable fault. The contour plots in S_{Dmax} with k_0 and Δp_D show that the rupture size and the critical stress ratio for an impermeable fault are larger than for a permeable one under any initial and injection conditions (Figure 2.10). Thus, impermeable faults would rupture at lower initial deviatoric stress and with larger earthquake magnitude. Generally, S_{Dmax} for an impermeable fault is 3 to 5 times greater than for a permeable one under a given k_0 and Δp_D.

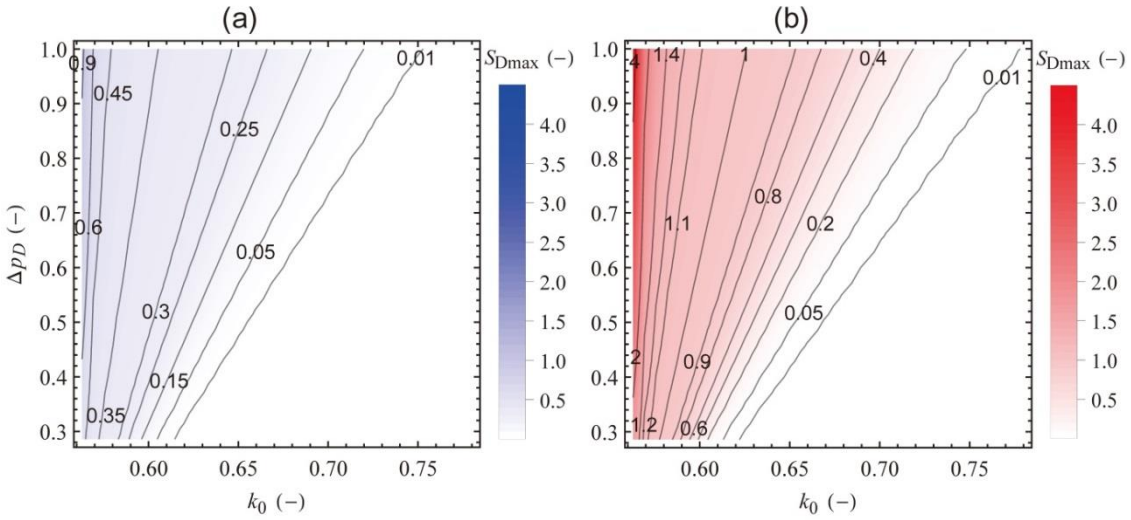

Figure 2.10: Dimensionless maximum slipping fault patch size (S_{Dmax}) as a function of the initial stress ratio and dimensionless pressure buildup for (a) permeable and (b) impermeable faults (for comparison purposes, both figures have the same color scale). The numbers on the contours denote the values of S_{Dmax}.

The previous analyses on fault dip show that the onset and critical dip angles (θ_o and θ_c) are barely related to the fault offset (Figure 2.8). Nonetheless, Equation (2.17) suggests that θ_o and θ_c depend upon the initial stress ratio k_0 and pressure buildup Δp_D. Such dependencies are the object of our next analyses. For a given pressure buildup (Table 2.2), while θ_o monotonically increases with the stress ratio, θ_c exhibits a more complex behavior (Figure 2.11a). θ_c evolution can be divided into three phases, with an increasing trend as k_0 increases, except for a decreasing branch in the mid-valued range of k_0. The differential θ_c - θ_o decreases with increasing k_0 and equals 0, i.e., the onset dip angle coincides with the critical dip angle, at k_0 = 0.674 (i.e., the critical stress ratio in this case) for a permeable fault and at k_0 = 0.694 for an impermeable fault. A direct consequence is that the range of dip angles favorable to slip is reduced for increasing k_0. For k_0 > 0.674 (0.694) the permeable (impermeable) fault is always stable regardless of its inclination (recall Figures 2.8 and 2.9). This means that geological sites with a higher in-situ stress ratio, i.e., lower initial deviatoric stress, are

intrinsically less prone to fluid injection-induced seismicity. The onset dip angle is smaller for impermeable faults than for permeable faults. Thus, the range of dip angles favorable to slip is larger for impermeable than for permeable faults, and its difference increases with k_0. The critical stress ratio corresponding to such critical fault dip is also greater for impermeable faults than for permeable ones, similar to the case for an arbitrary fault dip as shown in Figures 2.9 and 2.10. The difference in critical stress ratio between Figures 2.9 and 2.11 indicates that it increases with dip angle (only for $\theta_o < \theta < \theta_c$) and peaks at θ_c. Thus, the site characteristics significantly affect the results of the induced seismicity assessment.

In contrast, for a given k_0, the onset dip angle θ_o monotonically decreases with increasing dimensionless pressure buildup Δp_D, whereas θ_c decreases firstly and then increases with increasing Δp_D (Figure 2.11b). Thus, the differential θ_c - θ_o decreases with decreasing Δp_D and equals 0 at Δp_D = 0.213 (defined as the critical pressure buildup for this case) for a permeable fault and at Δp_D = 0.186 for an impermeable fault. Similarly, for Δp_D < 0.213 (0.186) the permeable (impermeable) fault is always stable regardless of its inclination. This means that a larger pressure buildup is necessary to induce seismicity, which can be translated into a value of maximum sustainable injection pressure (Rutqvist et al., 2007; Zhou et al., 2008; Bai et al., 2017) to minimize the risk of inducing seismicity. The main difference between permeable and impermeable faults is that the range of dip angles favorable to slip is larger for impermeable than for permeable faults, and the critical Δp_D related to θ_c - θ_o = 0 is smaller for impermeable than for permeable faults. It implies that an impermeable fault is more likely to induce seismicity in terms of pressure buildup and its maximum sustainable pressure is smaller compared with a permeable fault.

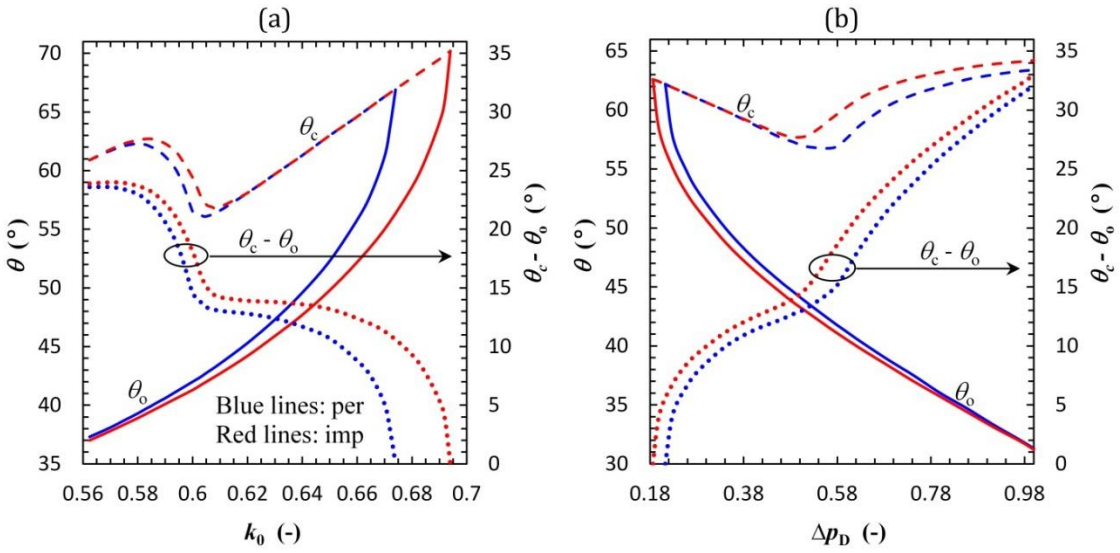

Figure 2.11: The onset and critical dip angles (θ_o and θ_c) for fault slip as a function of (a) the initial stress ratio with a dimensionless pressure buildup of 4/7 and (b) the dimensionless pressure buildup with a stress ratio of 0.6. The blue and red lines correspond to the permeable and impermeable faults, respectively. The solid and dashed lines denote θ_o and θ_c, respectively, while the dotted lines mean the difference between θ_c and θ_o.

2.5 Discussion

We present an analytical solution to assess fault stability changes (ΔCFS_{D}) as a result of reservoir pressurization/depletion. The results are shown in dimensionless form, which generalizes the problem with respect to the pore pressure change. All the stress components, ΔCFS and CFS are normalized by the scaling parameter C, which strongly depends on the Poisson's ratio (ν). C monotonically decreases with the increase of ν (Equation (2.2)). Fault stability is obtained by adding ΔCFS_{D} to the initial CFS_{D}, which depends on the initial stress state and pore pressure (Equation (2.17)). The variation in ν will change the final CFS_{D} and its zero points. An extra calculation shows that the magnitude of CFS_{D} and S_{Dmax} increases with increasing ν for both permeable and impermeable faults. Furthermore, the zero-offset permeable fault is stabilized when ν is lower than 0.24 for the case considered in Table 2.2, i.e., fault dip of $60°$ and pore pressure buildup of 20 MPa (it is destabilized for ν=0.29 in Figure 2.4a).

The analytical solution is a useful tool to quickly evaluate the induced seismicity potential of geo-energy projects. Injection control strategies of maximum sustainable pressure, which have been validated in CO_2 sequestration projects (Rutqvist et al., 2007; Zhou et al., 2008; Bai et al., 2017), could benefit from adding this solution in the decision-making process. A detailed site characterization is needed for its effective application, because the maximum rupture size, and thus, the magnitude of the induced earthquakes, not only depends on operational aspects, like pressure change, but also on the stress state and hydro-geomechanical characteristics of the fault, such as permeability, strength, offset and dip. For a given initial and injection conditions, the range of dip angles which may undergo failure can be defined, but knowing the hydraulic properties of faults is critical because all the parametric space analyses confirm the unfavorable effect in terms of induced seismicity potential of an impermeable fault, and an identical result can be predicted for fluid injection into the right-hand side of the fault (i.e., the footwall). In particular, low-permeable faults lead to larger rupture area at lower initial deviatoric stress and at smaller pressure changes (Figures 2.8-2.11). One factor for causing such unfavorable effect is that the differential deformation between the two sides of the impermeable fault distributes in the whole reservoir compartment, i.e., the segment P2-P4 for injection into the hanging wall or the segment P1-P3 for injection into the footwall, while the centered segment P2-P3 of a permeable fault always keeps the same deformation.

Pore pressure buildup arising from fluid injection reduces the slip resistance, and thus drives the fault toward failure (Shapiro and Dinske, 2009). The subsequent poroelastic response to adapt to such change tends to balance the system (Figure 2.3). However, the presence of the corners P1, P2, P3 and P4 (see Figure 2.1) results in a strong stress concentration (Buijze et al., 2017; Galis et al., 2019), leading to an excessive adjustment nearby the corners and fault sliding. Therefore, pore pressure buildup and stress concentration at the corners during reservoir pressurization are the main reasons of fault reactivation and induced seismicity when ignoring thermal effects and

geochemical reactions. Stress concentration is mainly controlled by the geometry of corners (Buijze et al., 2017), which changes with fault offset for permeable faults, but is independent of offset for impermeable faults, resulting in different fault stability patterns between permeable and impermeable faults (Figures 2.5-2.7).

Stress concentration not only highlights the effect of the hydraulic nature of faults, but also results in the occurrence of reversed slip at the internal corners P2 and P3 for normal faults with a normal faulting stress regime. In particular, reversed slip becomes the primary slip form for the permeable faults with a large dip angle and offset (Figure 2.8). In contrast, normal slip will occur and become the primary slip form for a small dip angle and permeable fault in thrust faults with a thrust faulting stress regime, i.e., $k_0 > 1$.

Regarding the criterion for fault slip, one option is to focus on points, i.e., when the stress state of one point reaches its failure conditions, e.g., $CFS > 0$, the fault slips. The disadvantage of such criterion is that the infinite induced stress at the corners leads to a misjudgment that even small amounts of injection will induce fault slip (Jansen et al., 2019). Another option consists in considering a minimum unstable patch, like the slipping fault patch size defined in this work. We have considered a threshold (0.01) for the dimensionless maximum slipping fault patch size, i.e., fault slip will not occur unless $S_{\mathrm{Dmax}} > 0.01$. Although further research is needed to determine how much the threshold should be, the parametric space analyses and the related conclusions that can be drawn from Section 4 are independent from the threshold value adopted.

Concerning fluid production, the results of ΔCFS_{D} are basically symmetrical to the ones of injection presented in this chapter and are easily obtained by a sign change, because the pressure change is included in the scaling parameter C. Thus, the change in fault stability is the opposite to the case of injection and, while fault slip firstly occurs at the external corners (P1 and P4) during reservoir pressurization, it firstly happens at the internal corners (P2 and P3) during reservoir depletion for both the permeable and impermeable faults (Jansen et al, 2019). The reverse effect may represent a potential method to control or mitigate induced seismicity: short-term production followed by an injection phase could improve the stability of the reservoir. Analogously, such an operation could be performed before decommissioning. Moreover, we also observe that the fault slip tendency in the case of production is much smaller than that in injection because ΔCFS_{D} is mainly negative (see Figure 2.4). Thus, the risk of induced seismicity in the case of injection is higher than that of production in a normal faulting stress regime like the one considered in this study.

Our analytical solution includes two limitations resulting from our simplifying assumptions to solve this complex problem: (i) we assume a linear elastic material, which is physically unrealistic for rock materials; in reality, a nonlinear elastic or inelastic deformation cannot be avoided during the reservoir pressurization/depletion; (ii) we assume a quasi-steady-state pore pressure change in the reservoir and neglect the transient effect of flow, so the calculated induced stress are still overestimated, particularly in the low-permeable fault zone because pore pressure will eventually

diffuse into the portion of the caprock and baserock in contact with the reservoir. Such limitations are worthy to be investigated further and complemented by more detailed numerical solutions.

Our analytical solution provides an accurate (Figure 2.2) and fast estimation of the stress variation in the reservoir and its surroundings, which takes into account the increase in stress due to the geological constraints to deformation. The stress variation, which is often called stress arching (Segall 1985; Rudnicki 2002; Soltanzadeh and Hawkees 2008), is positive within the reservoir in response to fluid injection. This means that the effective stress reduction is smaller than the pressure buildup (Figure 2.3). However, many engineering applications in subsurface energy-related projects neglect the stress arching in assessing fault stability and the effective stress reduction is assumed as equivalent to the pore pressure buildup during injection (e.g., Karvounis et al., 2014). For example, simplified models for CO_2 sequestration calculate the maximum sustainable pressure as the fracture pressure (Zhou et al., 2008; Mathias et al., 2009; Bandilla and Celia 2017), neglecting stress arching. We compare the slip tendency analysis estimated by means of our solution with the one estimated by neglecting the stress arching in Figure 2.4. Results show that ignoring the stress arching means overestimating the slip potential for both permeable and impermeable fault in a normal faulting stress regime. This implies an underestimation of the maximum sustainable pressure (i.e., injectivity).

2.6 Conclusions

In recent decades, the increasing interest in the subsurface as a source of carbon-free energy resources has led to an increasing number of induced earthquakes, with some of these earthquakes resulting in the cancellation of projects. To improve the prediction capability of induced seismicity, we have developed an analytical solution to compute the induced stress along both permeable and impermeable faults as a result of reservoir pressurization/depletion. The solution is based on the inclusion theory and has been validated by comparing it with a numerical solution. We have performed a comprehensive analysis on induced seismicity potential due to reservoir pressurization or depletion and obtained the following conclusions:

(1) The induced seismicity potential of impermeable faults is always larger than that of permeable faults under any initial and injection conditions. Generally, the maximum size of fault undergoing slip for the impermeable faults is 3 to 5 times greater than that for permeable ones under a given initial stress ratio and pressure buildup. Moreover, an impermeable fault would rupture at a higher stress ratio, i.e., less deviatoric stress, and at a smaller pressure buildup than a permeable one.

(2) Pore pressure buildup and stress concentration at the corners during reservoir pressurization/depletion are the main reasons of fault reactivation and induced seismicity. Stress concentration not only amplifies the effect of the hydraulic properties of faults, but also results in the occurrence of reversed slip at the

corners for normal faults with a normal faulting stress regime, and of normal slip for thrust faults with a thrust faulting stress regime.

(3) The slip potential of permeable faults resulting from reservoir pressurization/depletion increases with the fault offset because of the change in stress concentration, which implies that non-displaced permeable faults constitute a safer choice for site selection. In contrast, the offset has no impact on the slip potential of impermeable faults because the effect of stress concentration is always the same.

(4) For a given pressure buildup, the difference between the critical and onset dip angles, i.e., the range of dip angles favorable to slip, reduces for increasing the initial stress ratio and equals to zero at its critical stress ratio. This means that geological sites with a higher in-situ stress ratio (lower initial deviatoric stress) are intrinsically less prone to fluid injection-induced seismicity. This finding is useful for site selection in geo-energy projects.

(5) For a given stress ratio, the range of dip angles favorable to slip reduces for decreasing the pressure buildup and equals to zero at its critical pressure buildup as a larger pressure buildup is more likely to induce seismicity. Thus, the methodology of the maximum sustainable injection pressure to minimize the risk of inducing seismicity is feasible and should be available for designing and managing the injection parameters.

(6) The fault slip potential increases if we ignore the stress arching, i.e., assuming the effective stress reduction is equivalent to the pore pressure buildup during injection, for both permeable and impermeable faults in a normal faulting stress regime, which implies that the induced seismicity potential is overestimated and the maximum sustainable pressure is underestimated.

3 Analytical solution to quickly assess ground displacement for a pressurized or depleted deep reservoir intersected by a fault in a half space

3.1 Introduction

Ground deformation has been observed in various subsurface energy-related activities, such as exploitation of natural gas and oil (Bagheri-Gavkosh et al., 2021; Poland and Davis, 1969; Thienen-Visser and Fokker, 2017), reinjection of waste water (Loesch and Sagan, 2018; Shirzaei et al., 2016), geological carbon storage (Rinaldi and Rutqvist, 2013; Rutqvist et al., 2010), geothermal energy production (Araya and Biggs, 2020; Juncu et al., 2020, 2017), hydraulic fracturing (Eyre et al., 2022; Grigoli et al., 2018), subsurface energy storage (Teatini et al., 2011; Wang et al., 2022), among others. All these activities involve fluid injection/depletion at depth, which leads to pore pressure diffusion and thus, alters the in-situ stress equilibrium in the subsurface. As a consequence, a joint displacement/strain field accompanied with the stress variations in the perturbed region and its surroundings is generated (Jansen et al., 2019; Juncu et al., 2020; Shirzaei et al., 2016). Once the hydro-mechanical (HM) perturbation is strong enough relative to the initial stress state, preexisting faults may be reactivated and the intact rocks could be fractured, inducing seismicity (Rutqvist et al., 2008; Wu et al., 2021a; Zbinden et al., 2017, 2020). A rapid displacement/strain field is caused in the subsurface associated with such fault slip and rock fracturing (Deng et al., 2020; Juncu et al., 2020; Okada, 1985, 1992), which is usually evaluated by the dislocation theory (Segall, 2010; Steketee, 1958a,b). Deformation at the ground surface is of particular interest, because this is where most monitoring data is collected.

We distinguish the preceding two types of rock deformation as HM-induced and coseismic (a concept in seismology, Segall, 2010; Wright et al., 2013) deformation based on their different causes. HM-induced deformation is ubiquitous in all geo-energy projects while coseismic deformation only occurs in the case of reaching mechanical instability. Much more attention has been paid to the latter because of its high dependence with seismic events (Segall, 2010). Many analytical (Okada, 1985, and references therein; Okada, 1992; Pollitz, 1996) and numerical solutions (Dziewonski and Anderson, 1981; Grilli et al., 2013; Roering et al., 1997; Sun, 2014; Wang et al., 2006) developed based on the dislocation theory and for the natural earthquakes can be directly applied to estimate the coseismic deformation. These dislocation solutions, however, have no direct connection to the fluid-induced HM response, and thus, cannot be used to analyze the HM coupled processes and mechanisms of induced earthquakes. For such a purpose, one has to focus on the HM processes, including the HM-induced deformation. In the framework of HM coupling, stress analysis is often performed rather than deformation analysis in evaluating

earthquake triggering mechanisms because of its explicit relationship with rock failure criterions (Ge and Saar, 2022; Keranen and Weingarten, 2018). However, the deformation analysis has the advantage of direct comparison with the monitoring data of ground deformation. Both analyses, in reality, can be performed simultaneously, connected by constitutive laws between stress and strain, and thus, the stress analysis can be improved by incorporating the advantage of deformation analysis.

The HM-induced deformation interested by the geo-energy engineering community dates back to the 1920s due to the problem of land subsidence. For example, the Goose Creek field in Texas caused a ground subsidence of almost 1 m in eight years (Pratt and Johnson, 1926) as a result of reservoir compaction induced by oil and gas production (Fjær et al., 2008; Geertsma, 1973). More well-known cases afterwards include the Wilmington field in California (Gilluly and Grant, 1949), the Ekofisk and Valhall oil feild in the North Sea (Nagel, 2001), and the Groningen gas field in the Netherlands (Ketelaar et al., 2006; Thienen-Visser and Fokker, 2017). All these cases involved a noticeable subsidence after a few years of hydrocarbon exploitation. The uncertainty and complexity of geological conditions lead to a preference of addressing such a problem using analytical solutions, which require some simplifications, but are very useful for performing parametric space analysis (Fjær et al., 2008; Thienen-Visser and Fokker, 2017).

Existing (semi-)analytical solutions for HM-induced deformation are derived in general under the theory of linear poroelasticity (Detournay and Cheng, 1993; Wang, 2000). The most widely used analytical solution was proposed by Geertsma (Geertsma, 1973), on the basis of nuclei-of-strain as an analogy of thermoelastic strain (Mindlin and Cheng, 1950a,b), in the oil and gas industry field. This solution considers a uniform pore pressure change within a three dimensional (3D) disk-shaped reservoir in a half space (semi-infinite space). Segall (1992) extended Geertsma's solution to the case of non-uniform pore pressure changes as a given function within a general axisymmetric reservoir, while its application finally depends on numerical integration (Du and Olson, 2001; Segall et al., 1994). A similar extension has also been done by the principle of superposition (Jayeoba et al., 2019), leading to a closed-form solution for ground deformation. Another extension of Geertsma's solution aims at considering the elastic contrast between the reservoir and its surroundings (Mehrabian and Abousleiman, 2015). Although applying the perturbation theory leads to an explicit expression for displacement, the solution is still limited to the form of elliptic integral.

Apart from the line of Geertsma's solution, Segall (1985) derived a solution based on the inclusion theory (Eshelby, 1957), which considers a full HM-coupled problem under plane-strain conditions formulated by the primary variables of change in pore fluid content and displacement. Nonetheless, this approach cannot be solved analytically because of the non-uniform distribution of pore fluid content, and thus, its application either adopts numerical integration (Segall, 1985) or returns to the uniform change of pore fluid content (Segall, 1989). Also according to the inclusion theory, Jansen et al. (2019) developed a closed-form solution for a compartmentalized reservoir crossed by a permeable fault in a full space (infinite space). The preexisting

fault effects on the induced stress distribution and fault stability due to fluid injection have been investigated recently (Buijze et al., 2019, 2017; Galis et al., 2017; Jansen et al., 2019; Wu et al., 2021a). The stress changes caused by the presence of faults should have an impact on rock deformation. Fault permeability is highly variable, which strongly affects pore pressure changes inside the reservoir. Both permeable and low-permeable faults have been detected in geo-energy field sites (Chiaramonte et al., 2013; Géraud et al., 2006; Kim et al., 2018; Van Wees et al., 2014). Fault permeability plays an important role on fluid-induced seismicity (Vilarrasa et al., 2016; Wu et al., 2021a), while such a role on deformation remains open. One main drawback of Jansen et al. (2019) is that it neglects the effects of the traction-free surface on deformation, which could be a problem because an upward motion of the overburden can accommodate the vertical displacement (Richard et al., 1995; Rowan et al., 2004). Such free-surface effects have been well-known in geophysics and thus, a great number of solutions and models have been developed in a half space, while many others solutions were solved in a full space for the sake of simplification (Goodier, 1937; Jansen et al., 2019; Lehner, 2019; Robinson, 1951; Wu et al., 2021a). Providing a specific condition of neglecting the free-surface effects could make sense for the application of these full-space solutions. No solution exists for a reservoir compartmentalized by an offset fault in a half space. We aim at filling this gap and then focus on (1) analyzing the role of fault permeability on HM-induced deformation, and (2) presenting a systematical comparison between the solution in a half space and in a full space to find in which conditions the full-space solutions become valid.

We address this HM-coupled problem arising from reservoir pressurization/depletion by considering a horizontal reservoir offset by an intersecting fault that could be either permeable or impermeable with an arbitrary dip angle and offset in an elastic half space. We develop an analytical solution based on the theory of poroelasticity for analysis of poroelastic displacement. We organize the rest of the chapter as follows. In Section 3.2, we formulate the problem and propose a new closed-form solution for poroelastic displacement within the reservoir and its surroundings. Section 3.3 introduces some verification of the new closed-form solution against existing analytical solutions. We then describe the properties of our base-case study and the strategy for parametric space analysis in Section 3.4. Results are presented in Section 3.5 where we illustrate the role of fault permeability as well as the effect of fault and reservoir geometries on the poroelastic displacement with special emphasis on ground displacement. In Section 3.6, we show the effects of free surface on the displacement field. At the end, we provide an extended discussion of the results and its principal implications in Section 3.7, and our conclusions in Section 3.8. All the detailed theoretical and mathematical derivations are placed in Appendices E-F.

3.2 Analytical solution for stress changes around a fault crossing a pressurized/depleted reservoir

3.2.1 Problem formulation and assumptions

We focus on a compartmentalized reservoir that is crossed by a fault, which can be either permeable or impermeable and has an arbitrary dip angle θ and offset ht (Figure 3.1). ht is defined as $b - a$. The geological model is similar to the one in Wu et al. (2021a), but here we focus on the evaluation of poroelastic displacement, induced by injecting/pumping fluid into/from the reservoir, in a half space. The reservoir center at a depth of D below the ground surface is located at the cross point between the horizontal reservoir center line and the fault plane. We define the vertical line through the reservoir center as the vertical reservoir center line (but we do not mean that the lateral extents of the reservoir on both sides of the vertical center should be the same, i.e., c can be different from d). The height (thickness, h) and width (w) of the compartmentalized reservoir are $a + b$ and $c + d$, respectively, regardless of the fault offset. The reservoir width could be finite or infinite. The reservoir length is assumed as infinite in the out-of-plane direction as we formulate the problem in two dimensional (2D) plane-strain conditions. We locate the origin of the coordinate system at the cross point of the ground surface and the vertical reservoir center line. The positive direction for the y-axis points upwards, and all the previous geometric parameters shown in Figure 3.1 have a positive value.

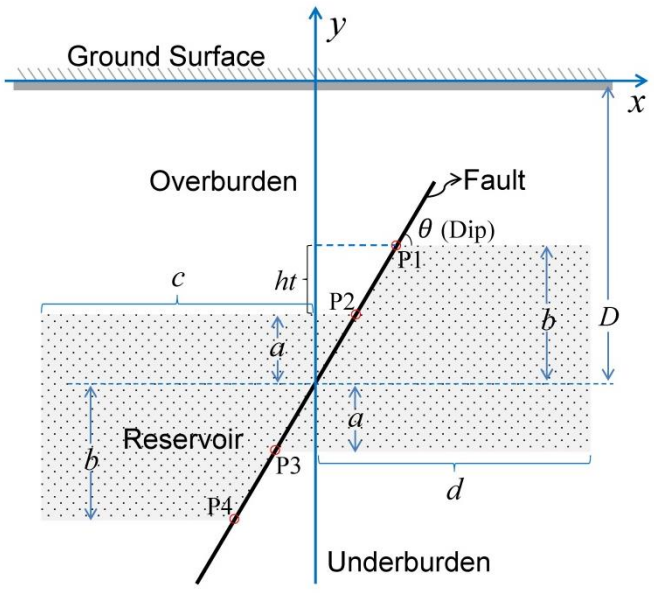

Figure 3.1: Geological model and its schematic geometry in a half space. Pore pressure changes within the reservoir in one or both sides of the fault depending on whether the fault is transversely impermeable (sealing) or permeable (non-sealing), respectively. The overburden and underburden are assumed impermeable and thus, no pressure changes outside the reservoir.

The infinite half space is assumed elastic, homogeneous, and isotropic in mechanics,

while the horizontal reservoir is much more permeable than its surroundings in hydraulics. The much higher permeability of the reservoir compared to that of confining layers implies that fluid diffusion and pressure changes occur exclusively within the reservoir during and after fluid injection or production. To solve the problem analytically, pressure changes in the reservoir are assumed uniform, which corresponds to the quasi-steady state after a long time of injection or production. It means that a uniform pore pressure change throughout the reservoir for the case of a permeable fault and limited to only one side of the fault for the case of an impermeable fault. The fault is simplified as a line without thickness and thus, its longitudinal permeability is neglected, excluding fluid flow along the fault and thus fluid leakage up through the caprock. By fault permeability, thus, we mean if the fault is transversely sealing or not, i.e., the sealing between the two sides of the fault.

3.2.2 Closed-form Solution

We formulate and solve the HM-coupled problem based on Green's function under point force (Mindlin, 1936; Segall, 2010) and Eshelby's inclusion theory (Eshelby, 1957). The poroelastic displacement tensor u_i inside and outside the reservoir is (see Appendix E for details on the derivation)

$$u_i(x,y)=\frac{(1-2\nu)\alpha\Delta p}{2\pi(1-\nu)\mu}\iint_{\Omega} g_i(x,y,\varsigma,\xi)d\Omega=\eta\frac{\Delta p}{\mu}\frac{G_i(x,y)}{\pi}, \tag{3.1}$$

where $\eta=\frac{\alpha(1-2\nu)}{2(1-\nu)}$ is the poroelastic coefficient (Detournay and Cheng, 1993), α and ν are Biot's coefficient and Poisson's ratio, respectively, Δp is the pore pressure change, μ is shear modulus, Ω is the inclusion domain, g_i and G_i represent displacement function tensor and its surface integral, respectively, x and y are the Cartesian coordinates, ς and ξ denote the coordinate values within the domain Ω.

The displacement function characterizes the displacement gradient at point (x, y) in response to a unit center of dilatation/contraction (Mindlin, 1936) at point source (ς, ξ) (Equations (E10) and (E11)). Its surface integral depends on the inclusion domain controlled by reservoir geometry and fault sealing. We have achieved the integration analytically, described in Appendix F, over a rectangular or a triangular inclusion. By superposing these closed-form expressions for the basic elements, one can obtain the integration over an arbitrary complex inclusion domain since a complex geometry can be combined by several elements of rectangle and triangle. Here, we study the setting shown in Figure 3.1 considering both permeable and impermeable faults for a demonstration.

For the case of an impermeable fault, pore pressure diffusion will be limited to the side of the fault where fluid injection/depletion occurs, and thus, the inclusion is a trapezoidal domain. Injecting fluid into the right-hand side of the fault corresponds to the right-type trapezoid inclusion formed by a triangle and a rectangle. We define the

result in this case as the right solution. Integrating the displacement function over such a domain gives

$$\begin{aligned} G_x^{\mathrm{Tra}}(x,y) &= \int_o^p \int_r^{(\varsigma-o)\tan\theta+r} g_x(x,y,\varsigma,\xi)d\xi d\varsigma + \int_p^q \int_r^s g_x(x,y,\varsigma,\xi)d\xi d\varsigma \\ &= G_x^{\mathrm{Tri,\,out}}(x,y) + G_x^{\mathrm{Rec,\,out}}(x,y) + \pi x\delta_\Omega \end{aligned}, \tag{3.2}$$

$$\begin{aligned} G_y^{\mathrm{Tra}}(x,y) &= \int_r^s \int_{(\xi-r)\cot\theta+o}^p g_y(x,y,\varsigma,\xi)d\varsigma d\xi + \int_r^s \int_p^q g_y(x,y,\varsigma,\xi)d\varsigma d\xi \\ &= G_y^{\mathrm{Tri,\,out}}(x,y) + G_y^{\mathrm{Rec,\,out}}(x,y) + \pi y\delta_\Omega \end{aligned}, \tag{3.3}$$

where δ_Ω is the modified Kronecker delta, which equals 1 if $(x,y) \in \Omega$ and 0 if $(x,y) \notin \Omega$. The last term in the right-hand side of Equations (3.2) and (3.3) result from the improper integral (Courant and John, 1989) for points located in the inclusion. The superscript out means that the points are located outside the inclusion and implies a standard integration. We use the abbreviation Tra, Tri, and Rec as superscripts meaning trapezoid, triangle, and rectangle, respectively, to represent the different inclusion domains (see Appendix B for the specific expressions of $G_i^{\mathrm{Tri,\,out}}(x,y)$ and $G_i^{\mathrm{Rec,\,out}}(x,y)$).

The upper and lower limits *o*, *p*, *q*, *r*, and *s* of integration, adopted for the general coordinates in Figure B1, have to be transformed into the specific coordinates in Figure 3.1 with the following relationships

$$o = -a\cot\theta, \quad p = b\cot\theta, \quad q = d, \quad r = -D-a, \quad s = -D+b. \tag{3.4}$$

When injecting fluid into the reservoir on the left-hand side of the fault, the inclusion domain becomes a left-type trapezoid formed by an inverted triangle and a rectangle. We refer to it as the left solution, which reads

$$\begin{aligned} G_x^{\mathrm{Tra}}(x,y) &= \int_l^p \int_r^s g_x(x,y,\varsigma,\xi)d\xi d\varsigma - \int_o^p \int_r^{(\varsigma-o)\tan\theta+r} g_x(x,y,\varsigma,\xi)d\xi d\varsigma \\ &= G_x^{\mathrm{Rec,\,out}}(x,y) - G_x^{\mathrm{Tri,\,out}}(x,y) + \pi x\delta_\Omega \end{aligned}, \tag{3.5}$$

$$\begin{aligned} G_y^{\mathrm{Tra}}(x,y) &= \int_r^s \int_l^p g_y(x,y,\varsigma,\xi)d\varsigma d\xi - \int_r^s \int_{(\xi-r)\cot\theta+o}^p g_y(x,y,\varsigma,\xi)d\varsigma d\xi \\ &= G_y^{\mathrm{Rec,\,out}}(x,y) - G_y^{\mathrm{Tri,\,out}}(x,y) + \pi y\delta_\Omega \end{aligned}. \tag{3.6}$$

The related transformation relationships of coordinate are

$$l = -c, \quad o = -b\cot\theta, \quad p = a\cot\theta, \quad r = -D-b, \quad s = -D+a. \tag{3.7}$$

Here, we consider the left-type trapezoid as the difference of a big rectangle minus a regular triangle in geometry, and thus, we update the *x* coordinate from *o*, *p*, *q*, to *l*, *o*, *p*. Note that this difference should be kept in mind when calling the specific expressions of $G_i^{\mathrm{Rec,\,out}}(x,y)$.

For the case of a permeable fault, pore pressure diffuses within the entire reservoir, implying an inclusion domain combined with a left-type and a right-type trapezoids. Summing both the left and right solutions gives the solution for a permeable fault. Note that the extra term associated with the improper integral is always πx for horizontal displacement and πy for vertical displacement for arbitrary inclusion geometries because a point can fall in only one location at one time.

All the corners of the inclusion domain are the singular points in the preceding three cases. For a vertical fault ($\theta = 90°$), $o = p = 0$ for both the left and right solutions, and then the integration over a triangular domain in Equations (3.2)-(3.6) gives zero. For a permeable fault with no offset in which $a = b$, the whole inclusion domain transforms into a simple rectangular one.

3.3 Verification against existing analytical solutions

3.3.1 Verification against Geertsma's solution

To verify the accuracy and correctness of our analytical solution for poroelastic displacement, we compare it with the well-known Geertsma's solution. Although Geertsma's solution is for a 3D axisymmetric geometry and our solution represents a 2D plane-strain geometry (Figure 3.2), they will be equivalent when the reservoir extends infinitely in the lateral direction. This comparison also aims at showing under which conditions a 3D model can be simplified into a 2D model.

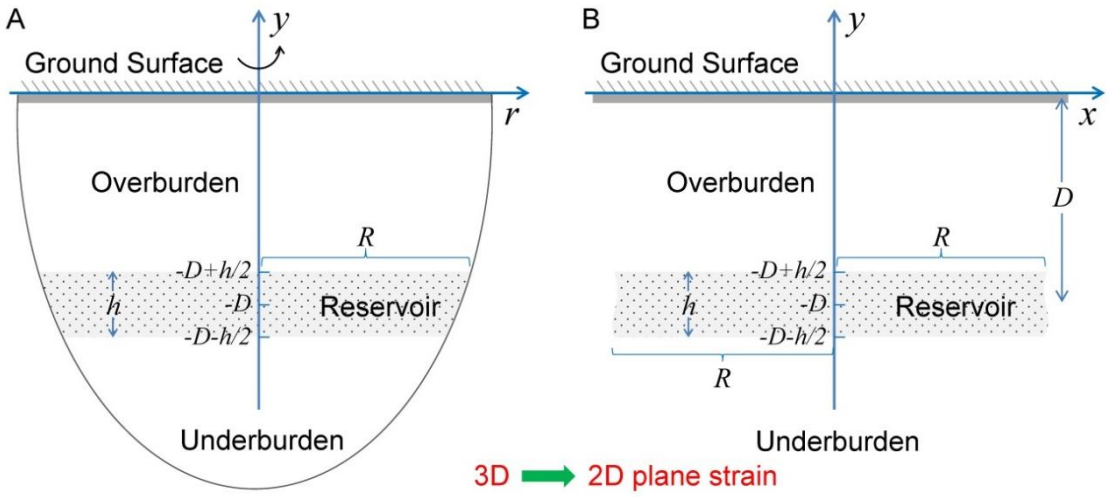

Figure 3.2: Schematic diagram of (A) 3D cylindrical model for Geertsma's solution and (B) 2D plane-strain model for the solution developed in this work in a half space. The reservoir is either finite or infinite in the horizontal direction, overlaied and underlaied by impermeable rock. The reserovir width is 2*R* for the 2D plane-strain model in this scenario.

In this verification example, we consider a uniform pore pressure buildup due to fluid injection of 10 MPa occurring in a 300-m thick cylindrical reservoir at a depth of 1 km. The reservoir thickness is relatively large, aiming at distinguishing the results of the

approximate and exact versions of Geertsma's solution (see Appendix G for details). The shear modulus and Poisson's ratio are assumed as 5 GPa and 0.25, respectively, for all the rocks inside and outside the reservoir. Biot's coefficient is considered as 1.

We first evaluate the vertical poroelastic displacement along the vertical reservoir center line by the two closed-form versions of Geertsma's solution and our plane-strain solution in this setting (Equations (G1)-(G3) in Appendix G) for three different reservoir widths (Figures 3.3A-3.3C). The approximate version of Geertsma's solution indeed can only provide accurate results for points outside the reservoir, which is identical to the exact version, and the exact version can also give accurate results for points inside the reservoir. It benchmarks the exact version of Geertsma's solution derived in this work. Our plane-strain solution is consistent with the exact version of Geertsma's solution for the reservoir width of 200 km. It means that such a reservoir can be regarded as a laterally infinite one and thus, both solutions become equivalent. For our solution in this scenario, the inclusion domain can be regarded as either an individual rectangle (Figure 3.2B) or a combination of two trapezoids crossed by a permeable fault with zero-offset (Figure 3.1). We carry out the evaluation for both cases and the related results are always identical to each other (Figures 3.3A-3.3C), verifying our integral solution for both rectangular and triangular inclusions as well as their superposition.

To further illustrate how the geometrical conditions characterize the infinite property of the reservoir, we calculate the ground displacement at the center $u_y(0, 0)$ as a function of reservoir width (w) under three different combinations of reservoir depth (D) and thickness (h) (Figures 3.3D-3.3F). More details for the other two combinations are shown in Figure J1. The difference of ground displacement between Geertsma's solution and our solution decreases with increasing w, and it becomes negligible when w approaches to a threshold. The ground displacement also tends to be a constant after reaching such threshold. The threshold of w is proportional to D (see Figures 3.3D and 3.3E) and is independent of h (see Figures 3.3D and 3.3F). It indicates that the ratio of reservoir width to depth (w/D) determines the infinite property of the reservoir. Our results show that the threshold of w/D could be about 50-100, in which the cylindrical reservoir tends to be laterally infinite and thus, a 3D model can be simplified into a 2D model.

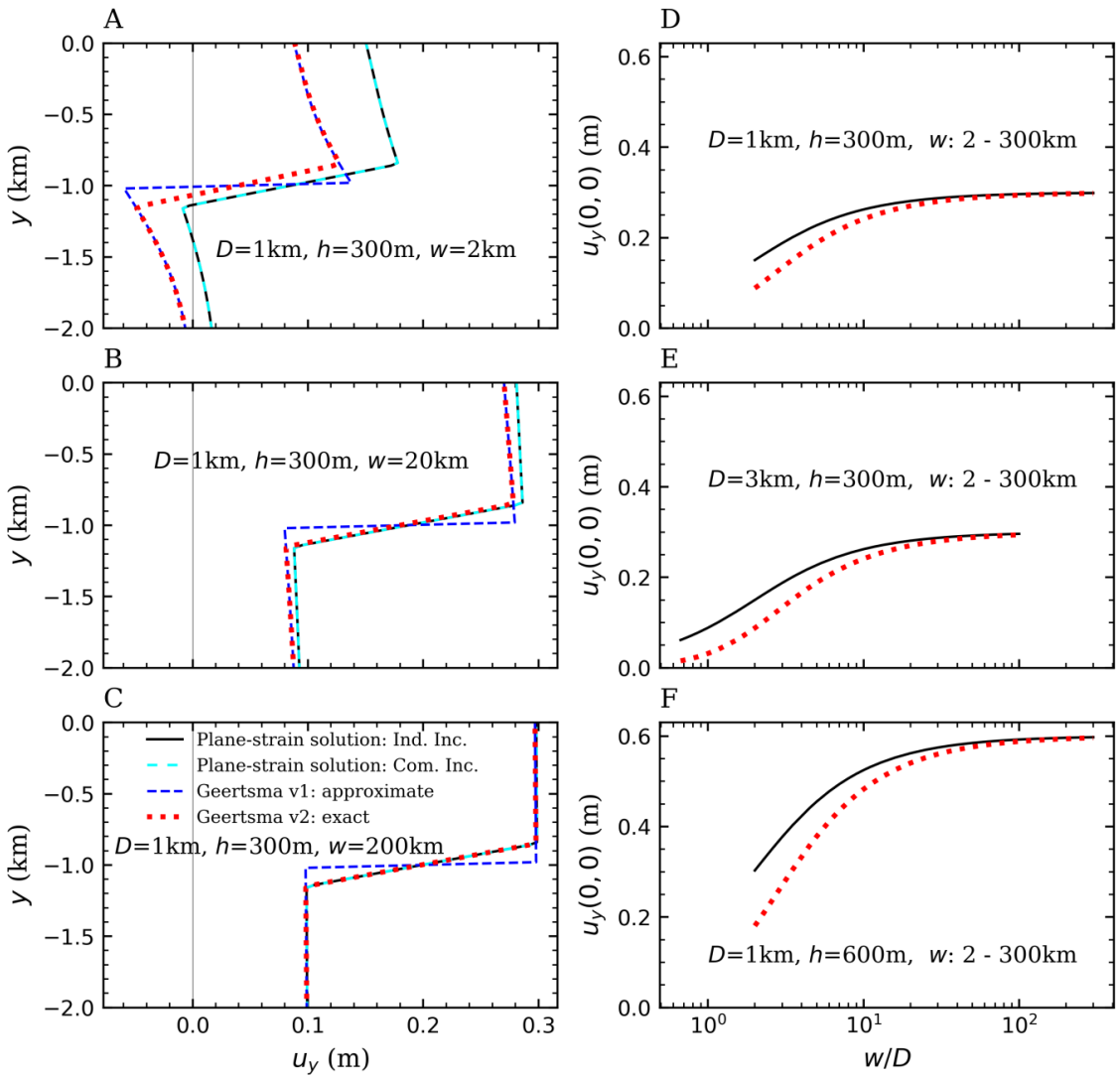

Figure 3.3: Comparison of vertical poroelastic displacement along the vertical reservoir center line (A, B, and C) and at the ground surface (D, E, and F) between Geertsma's solution and our plane-strain solution under various reservoir-geometric conditions. The legend is shown in (C), in which the black solid and cyan dashed lines represent our plane-strain solution evaluated, respectively, with an individual inclusion (Ind. Inc.) and a combined inclusion (combined by two trapezoidal domains, Com. Inc.), as well as blue dashed and red dotted lines denoting the approximate version (v1) and the exact version (v2) of Geertsma's solution, respectively. The ratio w/D changes as a function of w for a specific D in (D, E, and F).

3.3.2 Verification against Segall's solution

As mentioned in the Introduction, Segall (1985) derived a semi-analytical solution for displacement considering non-uniform changes of pore fluid content in the reservoir. Our solution can be regarded as a special case of Segall's solution in terms of pore pressure changes, whereas our solution can handle a more complicated reservoir geometry and is expressed in a closed form. A closed-form version of Segall's solution for ground displacement (Equations (H1) and (H2) in Appendix H) was developed by

assuming a uniform change of pore fluid content and a vertically concentrated compaction/dilatation at the horizontal reservoir center line instead of a distributed one throughout the reservoir (Segall, 1989). As a complementary verification, we here compare our solution with this approximate Segall's solution.

We adopt the same values as the ones applied in the verification against Geertsma's solution for all the geometrical and hydro-mechanical parameters to carry out this verification example with the only difference in reservoir thickness. The distribution of ground displacement between the two solutions displays an excellent consistency under the base case of h = 300 m (Figure 3.4). It verifies our solution again and also indicates that a reservoir thickness of 300 m is thin enough compared to a depth of 1 km, i.e., h/D = 0.3, which is the condition of vertically concentrated compaction/dilatation. When increasing the ratio h/D to 0.6, the comparison still matches well. Only small discrepancy occurs locally even for the case of h/D = 1. Since the approximate Segall's solution (Equations (H1) and (H2)) only differs from our solution (Equations (H3) and (H4)) in terms of the assumption of vertically concentrated compaction/dilatation. These comparisons imply that such an assumption is still acceptable for the case of h/D = 1 (in general, all the field cases in practical geo-energy projects meet this condition) in estimating the ground subsidence/uplift. Predictably, this assumption will not affect the estimate of displacement outside the reservoir (Figures 3.3A-3.3C) (Fjaer et al., 2008). We discuss this further in Section 3.7.

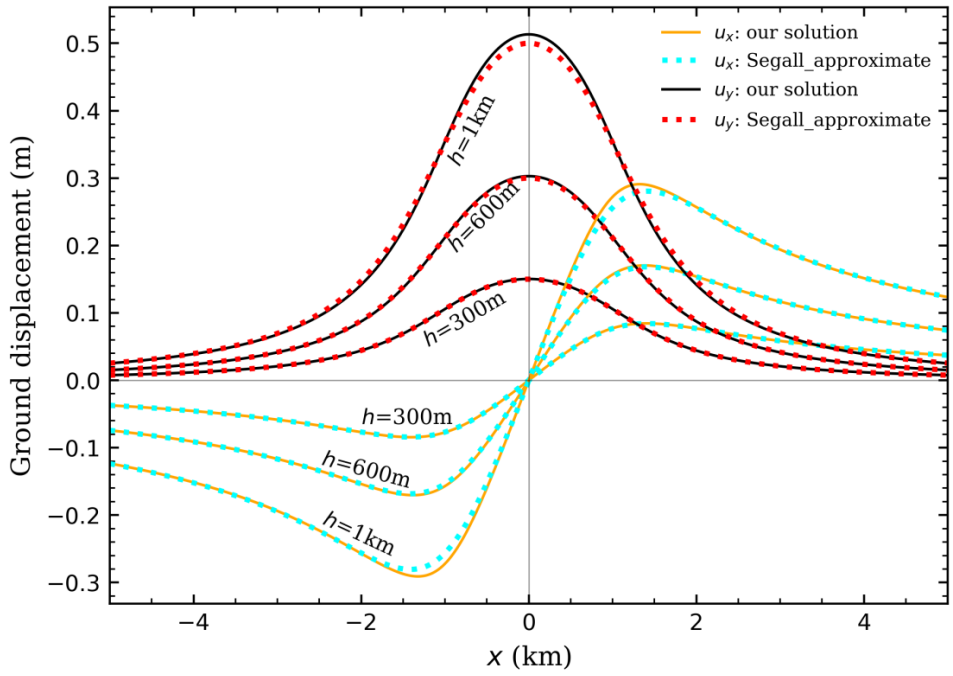

Figure 3.4: Comparison of ground displacement along the x-axis between our analytical solution and the approximate version of Segall's solution under three cases of reservoir thickness.

3.4 Assessment of poroelastic displacement with a compartmentalized reservoir

We now apply our analytical solution to assess the fluid-induced poroelastic displacement with a compartmentalized reservoir (Figure 3.1). The displacement is the product of poroelastic coefficient η, relative strength of pore pressure change to rock stiffness $\Delta p/\mu$, and reservoir geometry factor $G_i(x,y)/\pi$ (Equation 3.1). To generalize the analysis with respect to the HM parameters, we hereafter take the reservoir geometry factor as a scaled poroelastic displacement.

3.4.1 Properties of the base-case scenario

We first perform a base-case study to show the full distribution of poroelastic displacement in a 2D zone of interest due to fluid injection into a fault-displaced reservoir. We consider both permeable and impermeable faults, with injection into the reservoir on left-hand side of the fault as an example, to show the role of fault permeability. In the base-case scenario, we adopt a general value for all the geometric parameters and a typical value for the HM parameters (Table 3.1). Thus, the scaled value for displacement is 6×10^{-4} with these typical HM values. Multiplying the results shown in Section 3.5 with this scaled value immediately yields the non-scaled poroelastic displacement. Applying to a specific experimental or in-situ HM condition only needs to adapt this scaled value.

Table 3.1: Geometric parameters of the reservoir and rock properties adopted for the base case scenario.

Parameter	Physical meaning	Value	Unit
a	Geometric parameters (Refer to Figure 3.1)	50	m
b		150	m
c		1000	m
d		1000	m
D	Depth	2000	m
θ	Fault dip	60	°
μ	Shear modulus	5	GPa
ν	Poisson's ratio	0.25	-
α	Biot's coefficient	0.9	-
Δp	Pressure buildup	10	MPa
η	Poroelastic coefficient	0.3	-

3.4.2 Parametric space analysis on the geometric properties of geological model

We then carry out a parametric space analysis for the geometric properties of geological model and focus our analysis on ground displacement. Two kinds of geometric properties describe the subsurface conceptual model (Figure 3.1): fault geometry and reservoir geometry. A zero-thickness fault is represented by the fault dip and fault offset. Both of them have a strong effect on induced stress around the fault, and thus, the fault stability and the maximum size of slipping fault patch (Wu et al., 2021a). However, how they affect the ground displacement remains an open question, which will be analyzed in Section 3.5.2. The other geometric feature, i.e., reservoir geometry, is characterized by its thickness, width, and depth, which can strongly affect the magnitude of ground displacement. In particular, the larger the reservoir size and the shallower the depth, the larger the ground displacement. Dimensionless variables are more widely used when generalizing the problem. We thus use the aspect ratio $e = h/w$, the vertical depth ratio h/D, and the horizontal (lateral) depth ratio w/D in our analysis to quantify the effect of these reservoir geometry properties.

We evaluate these parametric space analyses on the basis of the previous base-case study, and change (1) the fault dip from 15 to 90° in increments of 15°, and the fault offset from 0 to 300 m in increments of 100m (Section 3.5.2), and (2) the reservoir thickness, width, and depth to half and double of the one in the base-case scenario (Section 3.5.3). The values of the dimensionless variables associated with varying the dimensional geometry properties are shown in Table 3.2. The quantitative analysis for both the dimensional and dimensionless reservoir geometry properties will be included in Section 3.5.3. All these analyses do not involve the HM parameters and thus, the scaled value for displacement remains the same as shown in Section 3.4.1.

Table 3.2: Values of the dimensional geometry parameters and the related ones of the dimensionless variables adopted for the parametric space analysis of reservoir geometry.

Dimensional parameter	Value	Dimensionless parameter		
		e	h/D	w/D
h (m)	100	0.05	0.05	
	200	0.1	0.1	1
	400	0.2	0.2	
w (km)	1	0.2		0.5
	2	0.1	0.1	1
	4	0.05		2
D (km)	1		0.2	2
	2	0.1	0.1	1
	4		0.05	0.5

3.5 Results

3.5.1 The role of fault permeability in the base case scenario

Reservoir pressurization leads to reservoir dilatation towards its surroundings. As a result, the scaled horizontal and vertical components of poroelastic displacement concentrate on the lateral and vertical boundaries of the pressurized region, respectively, and then decreasingly extend to their surroundings (Figure 3.5). A negative value of displacement implies a deformation towards the negative direction of the coordinate axes. Thus, the displacement is regarded as a big one as long as its absolute value is large.

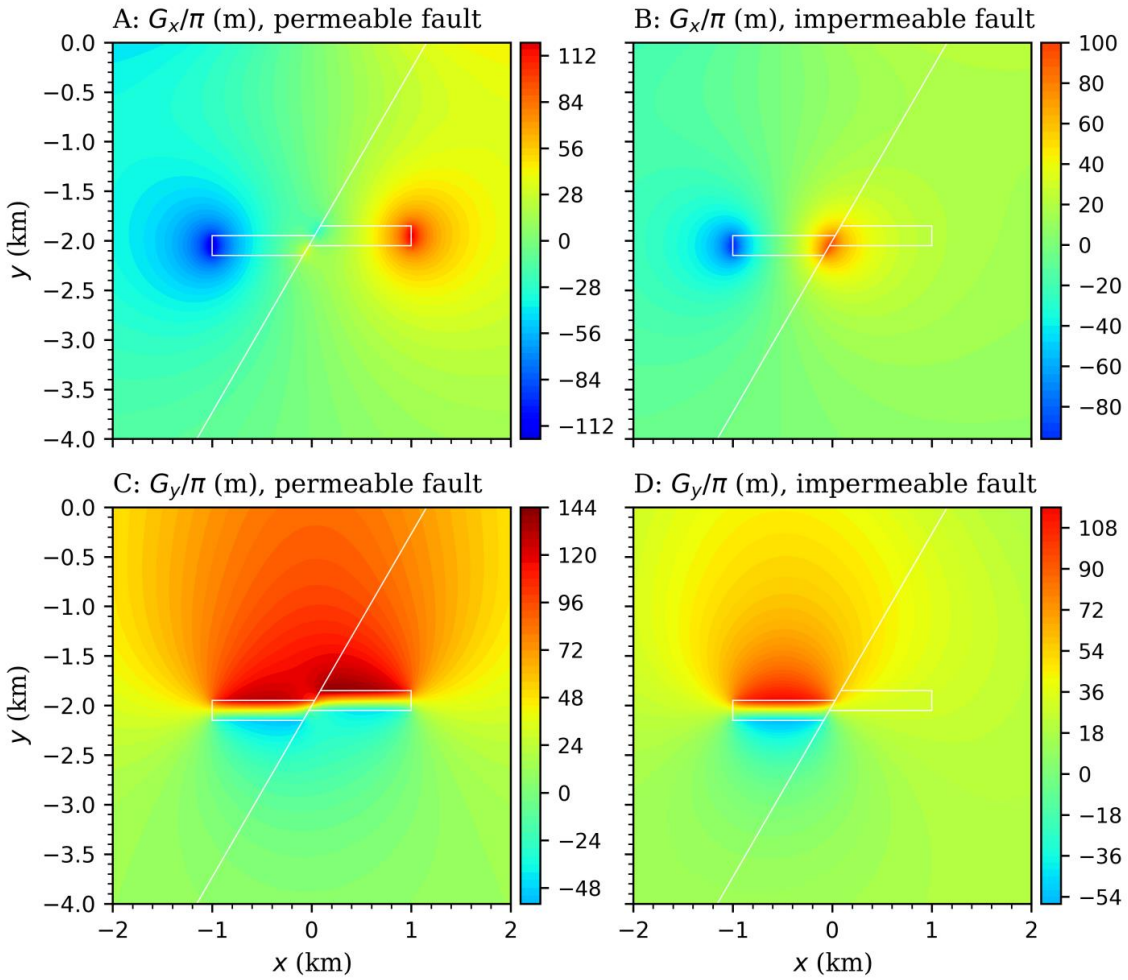

Figure 3.5: Horizontal (A and B) and vertical (C and D) components of the scaled poroelastic displacement for both cases of a permeable (A and C) and an impermeable (B and D) fault. Displacement is scaled by $\eta\Delta p / \mu$ with a value shown in Section 3.4.1. A, B, C, and D have the same color scale but the range of the legends is adapted to the values shown in each case. The reservoir geometry and the fault are indicated by the white lines.

Fault permeability has no impact on this primary feature of poroelastic displacement,

while some secondary differences are evident between the cases of permeable and impermeable faults. For a permeable fault, both the horizontal and vertical displacement components are almost symmetric with respect to $x = 0$, i.e., the vertical reservoir center line, only with small inconsistency around the symmetric axis because of fault offset (Figures 3.5A and 3.5C). Although such symmetry remains visible in the impermeable case, the symmetric axis shifts to the left for about half of the reservoir width, i.e., 500 m, being in consistency with the actual vertical center line of the pressurized reservoir (Figures 3.5B and 3.5D). The scaled displacement in the permeable-fault case is larger than the one in the impermeable-fault case because the pressurized reservoir size in the latter is half of the one in the former. Such a difference is more evident in the vertical component than in the horizontal component. Unlike the horizontal component, the vertical component is much larger in the overburden than in the underburden of the reservoir for both permeable and impermeable cases (Figures 3.5C and 3.5D). This asymmetry is due to the effects of the traction-free surface on the poroelastic displacement, which will be further discussed in Section 3.6.

3.5.2 Effect of fault dip and fault offset on ground displacement

Fault dip and fault offset show a similar effect on the distribution of ground displacement for both permeable and impermeable faults and they just slightly change the magnitude of ground displacement (Figure 3.6). The scaled ground displacement presents a similar symmetry to the full distribution of displacement shown in Figure 3.5. For a permeable fault, the maximum vertical ground displacement occurs around the center, while the maximum horizontal ground displacement occurs around two times the lateral reservoir boundaries. These maximum points shift to left 500 m for an impermeable fault, being in consistency with the symmetry shown in the full distribution of displacement between permeable and impermeable cases. Both the scaled horizontal and vertical ground displacement components in the permeable-fault case are about the double of the one in the impermeable-fault case because the pressurized reservoir size also doubles. The maximum of the vertical component is about two times the horizontal one in both permeable and impermeable cases.

These previous properties are basically independent of fault dip and fault offset. Only the symmetry is slightly affected by fault offset. In particular, ground displacement is exactly symmetric with respect to the center for a zero-offset fault, while it shows a slight deviation for these cases of a displaced fault (Figure 3.6D). The effect of fault geometry on ground displacement mainly affects its magnitude, with little changes to the spatial distribution. On the one hand, ground displacement increases as the fault inclination becomes stepper, and such an increment becomes less pronounced as fault dip increases (Figure 3.6A and 6B). On the other hand, ground displacement decreases with increasing fault offset and such a decrement is nearly proportional to the fault offset (Figure 3.6C and 6D). This effect is independent of fault permeability, and it is not very strong.

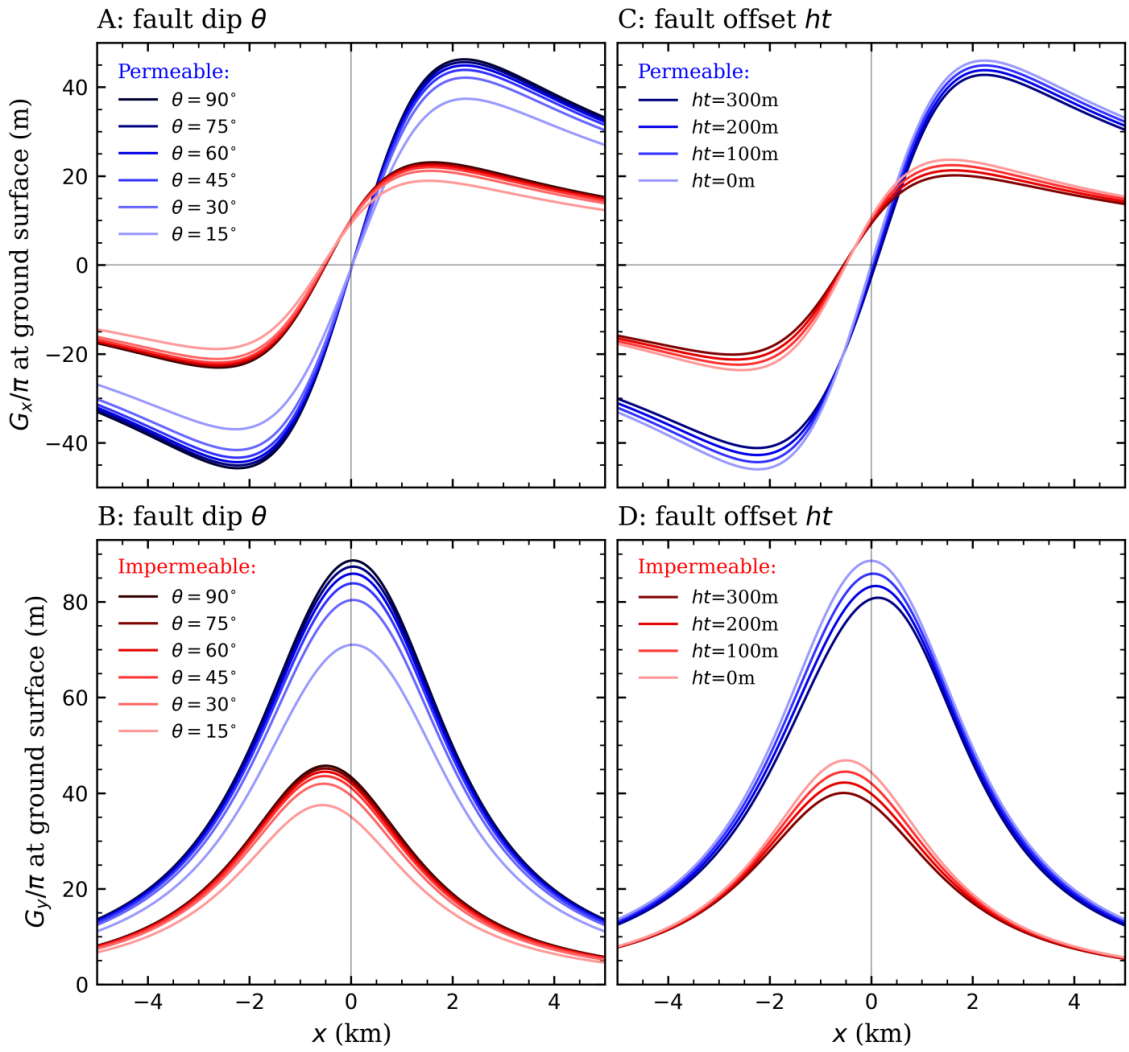

Figure 3.6: Horizontal (A and C) and vertical (B and D) components of the scaled ground displacement along the *x*-axis for both permeable (blue color-scale lines) and impermeable (red color-scale lines) faults under several values of fault dip (A and B) and fault offset (C and D). The fault offset in A and B is 100 m and the fault dip in C and D is 60°. The color-scale lines vary from light to dark, corresponding to fault dip changes from 15 to 90° with an increment of 15° and fault offset ranges from 0 to 300 m with an increment of 100 m. Displacement is scaled by $\eta\Delta p / \mu$ with a value shown in Section 3.4.1.

3.5.3 Effect of the reservoir geometry properties on ground displacement

The scaled ground displacement is proportional to the reservoir thickness and width, while it is inversely proportional to the reservoir depth (Figure 3.7). Such effect shows a similar strength among the three geometic properties and is independent of fault permeability, while it is much more evident than the one of fault geometry. Reservoir thickness almost does not affect the shape of displacement distribution: the maximum point of displacement always locates at the same position for different cases of thickness. In contrast, such a maximum point of horizontal displacement shifts outward

with increasing reservoir width because the reservoir expands with its width in lateral direction. As a result, the spatial distribution of ground displacement becomes gentler and wider with increasing reservoir width than increasing reservoir thickness. The maximum point shifts inward with decreasing reservoir depth, and thus, the spatial distribution of ground displacement concentrates towards the center (Figures 3.7A and 3.7B). Fault permeability only has an influence on the effect of reservoir width on the displacement distribution (Figures 3.7C and 3.7D) because the pressurized region only expands in the left-hand side direction for an impermeable fault.

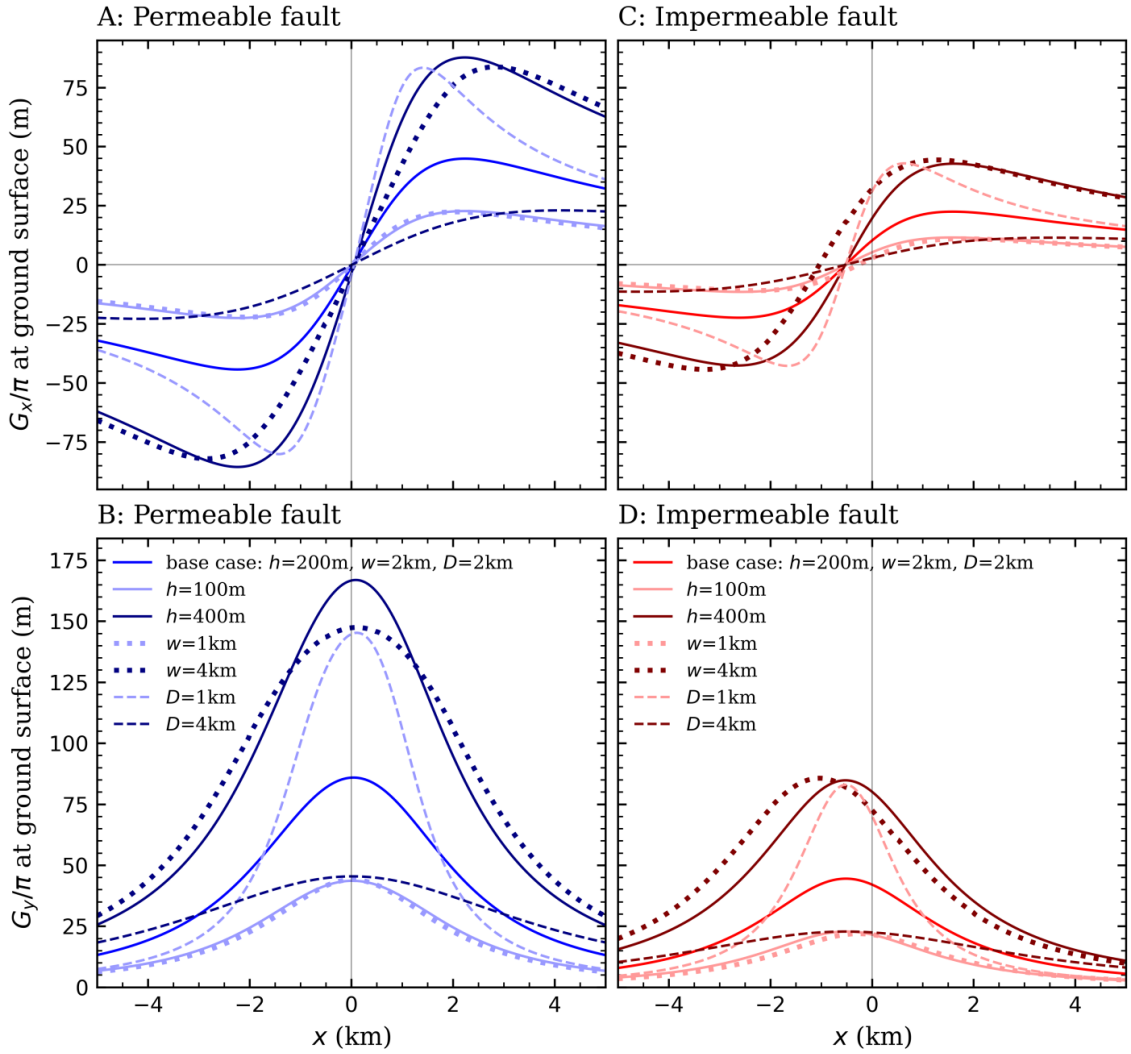

Figure 3.7: Horizontal (A and C) and vertical (B and D) components of the scaled ground displacement along the *x*-axis for both permeable (blue color-scale lines, A and B) and impermeable (red color-scale lines, C and D) faults under several values of reservoir thickness, width, and depth. The legends are shown in B and D. Displacement is scaled by $\eta\Delta p / \mu$ with a value shown in Section 3.4.1.

Figure 3.7 also reveals the intrinsical effect of the dimensionless aspect ratio and depth ratios of the reservoir. The cases of h = 100 m and w = 1 km correspond to two different aspect ratio (Table 3.2), while the related ground displacement is identical in

both cases. This means that the aspect ratio has no impact on the induced ground displacement. The cases of *h* ranging from 100 m to 400 m and *D* ranging from 4 km to 1 km correspond to the same increase of the vertical depth ratio (Table 3.2), in which the associated ground displacement presents a similar increasing trend. Thus, the ground displacement is proportional to the vertical depth ratio. The lateral depth ratio shows a similar behavior to the vertical one, which can be checked by the cases of different *w* and *D*. We conclude that the induced ground displacement is independent of the aspect ratio and is proportional to vertical and lateral depth ratios with a similar proportion, while fault permeability has no impact on such intrincial effect of reservoir geometry.

3.6 Effects of traction-free surface on poroelastic displacement

Earth ground as a typical traction-free surface has attracted much concern in rock mechanics and geophysics (Barla, 1972; Fu et al., 2015; Lehner, 2019; Pan et al., 1998; Strack and Verruijt, 2002; Verruijt, 1998; Verruijt and Booker, 1996). Although a great number of analytical and numerical models have been developed in a half space, a complete comparison between the solution in a half space and in a full space for a same problem is currently rare and the condition for neglecting the effects of the traction-free surface remains ambiguous because of the lack of quantitative analysis.

For our solution, the displacement function in a full space is a special case of the one in a half space, i.e., with only the first term in the right-hand side of Equations (E10) and (E11). Once the other terms in these equations are neglected, our analytical solution for poroelastic displacement transforms immediately into the version in a full space. Such a relationship provides a chance to systematically analyze the effects of traction-free surface on displacement and to show in which conditions the full-space solution becomes valid.

3.6.1 A complete comparison of displacement in a half space and in a full space

We adopt the case study in Section 3.4.1 as the base-case scenario to compare our analytical solution in a half space and in a full space. We first calculate the scaled displacement with and without free-surface effects as well as their difference for a permeable fault. The presence of free surfaces enhances the poroelastic displacement in the overburden for both horizontal and vertical components while declines the vertical component in the underburden (Figures 3.8 and Figure J2). The scaled displacement in a full space is symmetric with respect to the horizontal reservoir center line, which differs from the one in a half space (Figure J2). Such a difference is much more evident in the vertical component than in the horizontal one (Figure 3.8). The difference of horizontal displacement mainly focuses on the two small areas around the maximum point of horizontal ground displacement (Figures 3.6A and 3.8A). In contrast, the difference of vertical displacement is inversely proportional to the depth of the points and concentrates on the vertical reservoir center line (Figure 3.8B). The

maximum difference of both the horizontal and vertical components thus locates at the ground surface where the effects of free surface cause the largest difference.

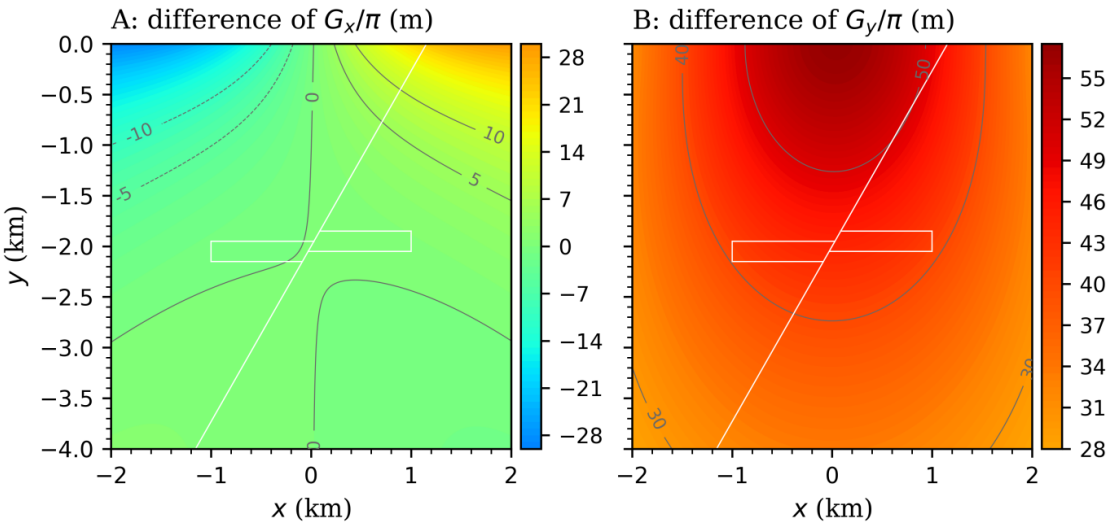

Figure 3.8: Difference of the scaled horizontal (A) and vertical (B) displacement components between the solution in a half space and in a full space for a permeable fault. Displacement is scaled by $\eta\Delta p / \mu$ with a value shown in Section 3.4.1. A and B have the same color scale but the range of the legends is adapted to the values shown in each case. The reservoir geometry and the fault are indicated by the white lines.

We then evaluate the previous difference at the ground surface for both horizontal and vertical components of the scaled poroelastic displacement under different reservoir geometries (Figure 3.9). The spatial distribution of such a difference is almost identical to the spatial distribution of ground displacement (Figures 3.7 and 3.9). The difference is also proportional to the reservoir thickness and width with a similar proportion coefficient, and thus, the vertical (h/D) and lateral (w/D) depth ratios. This similar proportion indicates that the effects of free surface can be neglected once the reservoir depth is big enough compared to both the reservoir thickness and width, while existing studies only pay attention to one dimension (Barla, 1972; Lehner, 2019; Soltanzadeh and Hawkes, 2008). The maximum difference in the vertical component is about two times the horizontal one, and this relationship basically is independent of reservoir geometry.

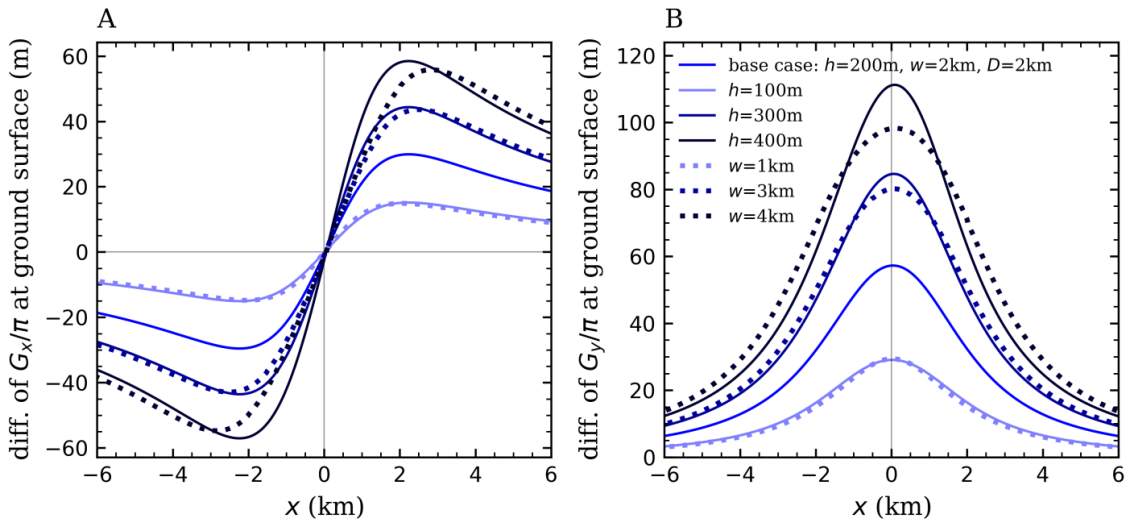

Figure 3.9: Difference of the scaled horizontal (A) and vertical (B) ground displacement components between the solution in a half space and in a full space for a permeable fault under several values of reservoir thickness and width. Displacement is scaled by $\eta\Delta p / \mu$ with a value shown in Section 3.4.1. The legend is shown in B.

3.6.2 Condition for neglecting the effects of free surface

We here perform a new example with a rectangular reservoir depth at 2 km to further identify the necessary condition for neglecting the effects of free surface. We consider three reservoir geometries with a comparative aspect ratio (e) as the three base-case scenarios and then vary either the reservoir width or thickness from 20 m to 3 km for each base scenario to see how the maximum difference of the scaled ground displacement in a half space and in a full space changes with the inverse of both w/D and h/D (Figures 3.10A-3.10C and J3A-J3C) as well as the inverse of wh/D^2 (Figures 3.10D-3.10F and J3D-J3F). We adopt the inverse of these dimensionless variables instead of themselves because that such difference is almost directly proportional to w/D and h/D (Figure 3.9), and that presenting the results in an inverse proportion is helpful to establish a threshold.

The inverse proportion of the previous maximum difference to the inverse of wh/D^2 with varying either w or h is definitely identical after a cutoff value of the inverse of wh/D^2 in all these base-case scenarios (Figures J3D-J3F and 3.10D-3.10F). Such a cutoff value is about 14 and 8 for the maximum difference of the vertical and horizontal displacement components, respectively (Figures J3D-J3F). Before this cutoff point (which means a big size of reservoir relative to its depth), the maximum difference increases faster with increasing h than w, indicating that the vertical depth ratio plays a stronger role on the free-surface effects than the lateral one. In contrast, these preceding features can be observed only in the base-case scenario of e = 1 (Figures J3B and 3.10B) when focusing on the inverse proportion to the inverse of w/D and h/D (Figures J3A-J3C and 3.10A-3.10C). It suggests that the inverse of wh/D^2 or

itself is a better index to represent the condition of neglecting the free-surface effects than the inverse of *w*/*D* and *h*/*D*.

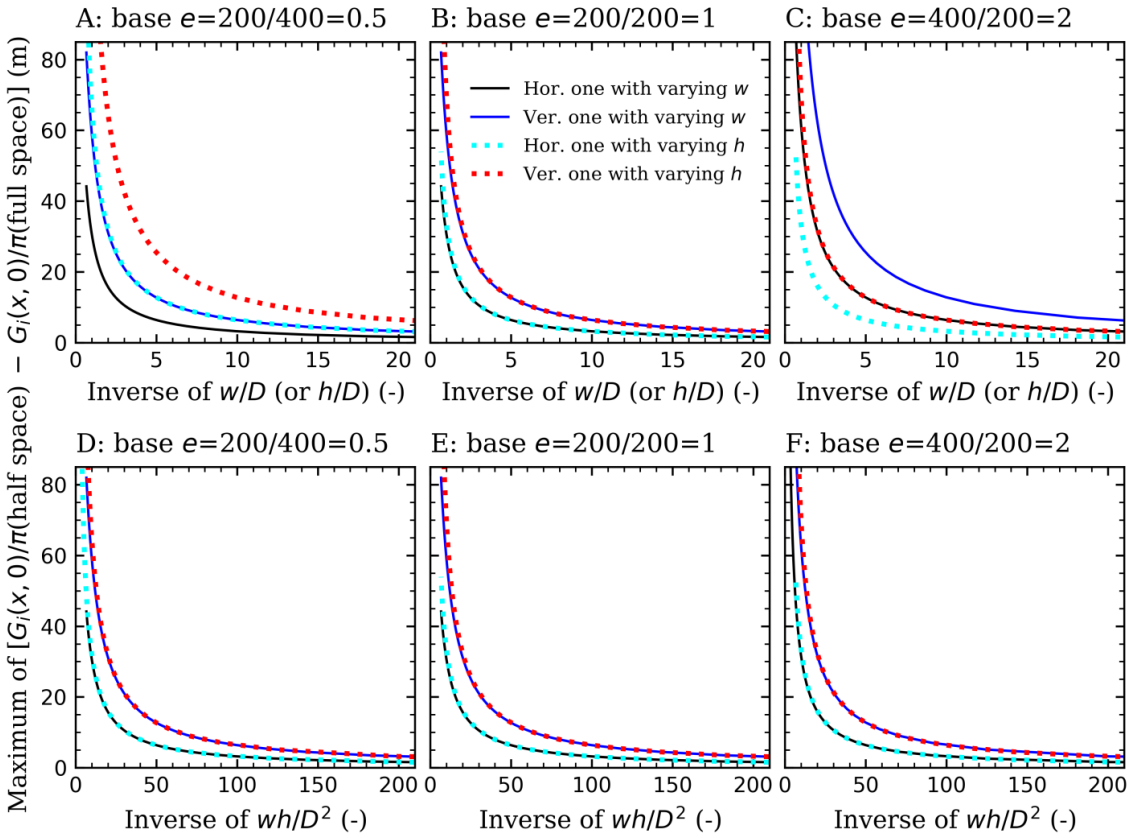

Figure 3.10: Maximum difference of the scaled horizontal (Hor.) and vertical (Ver.) ground displacement components between the solution in a half space and in a full space as a function of the inverse of *w*/*D* or *h*/*D* (Figures 3.10A-3.10C), and of the inverse of wh/D^2 (D, E, and F) for a rectangular reservoir with three comparative base values of aspect ratio *e*. Displacement is scaled by $\eta\Delta p / \mu$ with a value shown in Section 3.3.4.1. The legend is shown in B. The base values of reservoir thickness and width for each base-case scenario are included in the title of each subfigure. The axis value is limited to 21 for the inverse of *w*/*D* and *h*/*D*, to 210 for the inverse of wh/D^2, and to 85 m for the maximum difference, which aim at clearly showing the turning interval of these curves.

We discuss the condition in terms of the inverse of wh/D^2 for neglecting the free-surface effects in the turning interval where the decreasing rate of the maximum difference significantly declines from a large one to a small one. Such a turning interval locates in the right-hand side of the previous cutoff point (Figures 3.10D-3.10F), and the geological conditions in most of the practical geo-energy projects indeed are located in this turning interval (Kivi *et al.*, 2022, 2023). These inversely proportional curves between the maximum difference and the inverse of wh/D^2 display an intrinsic threshold for neglecting the free-surface effects because of their asymptotic property (Figures 3.10D-3.10F). This intrinsic threshold of the inverse of wh/D^2 could be about 50-100, i.e., 0.01-0.02 for wh/D^2 itself, when focusing on the

vertical ground displacement. The scaled maximum difference associated with such a threshold is about 14-7 m, corresponding to a non-scaled value of 8.4-4.2 mm with the HM parameters listed in Table 3.1. After this threshold, the maximum difference tends to zero asymptotically and thus, the full-space solutions become valid. We here propose a range for this intrinsic threshold instead of a specific value also because of the asymptotic property. It indicates the recognition that the specific condition for neglecting the free-surface effects can be different depending on the type of engineering projects, which depends on the field background and demands of each project. Our results (Figure 3.10) can provide a reference for each application.

3.7 Discussion

We present a new closed-form solution under 2D plane-strain conditions in a half space to estimate rock deformation within the reservoir and its surroundings resulting from reservoir pressurization/depletion due to various geo-energy related operations. With this solution, we elaborate (1) the role of fault permeability on poroelastic displacement (Figure 3.5), (2) the effect of fault and reservoir geometries on ground displacement (Figures 3.6 and 3.7), and (3) the effects of traction-free surface (Figures 3.8-9 and J2) as well as the condition for neglecting such a free surface (Figures 3.10 and J3). All the evaluated results are shown in a scaled form, which generalizes the problem and the associated conclusions with respect to the HM parameters. For the contrary scenario of fluid production, the scaled displacement shown in the previous cases of fluid injection remains the same, but the sign of scaled value changes. Unlike the unfavorable effect of an impermeable fault on induced seismicity potential (Wu et al., 2021a), the induced displacement is smaller in the case of an impermeable fault than a permeable one (Figures 3.5-3.7) because the pressurized reservoir size in the former is only half of the one in the latter. Although injecting the same amount of fluid into a smaller size of reservoir can finally lead to a higher pressure buildup, an overpressure in the impermeable-fault case below two times the one in the permeable-fault case cannot cause a same size of ground displacement as the permeable one (Figures 3.6 and 3.7). This indicates that cross-fault permeability (sealing) only plays a strong role on the spatial distribution of poroelastic displacement while its effect on displacement magnitude is small.

The poroelastic displacement is proportional to the hydraulic parameters and inversely proportional to shear modulus, while the relation to Poisson's ratio is more complicated. Once neglecting the effects of free surface, Poisson's ratio only exists in the poroelastic coefficient and thus, the displacement decreases with increasing Poisson's ratio but not linearly (Figures J4 and J5). We infer that the mechanical parameters have no impact on the spatial distribution of poroelastic displacement in a full space and only enlarge/minify its magnitude (Figures J2B, J2D, and J5). For an elastic half space, in contrast, the reservoir geometry factor also involves Poisson's ratio (Equations (F6), (F11), (F32), and (F43)) and it linearly decreases with increasing Poisson's ratio (Figure J6). The effect of Poisson's ratio on reservoir geometry factor mainly focuses on the ground surface and decreases with increasing reservoir depth

(Figure J6). Merging the effect of Poisson's ratio on poroelastic coefficient and on reservoir geometry factor yields the one on poroelastic displacement (Figure 3.11). The displacement still decreases with increasing Poisson's ratio and such a decrement increases with Poisson's ratio. This property is in agreement with the one of poroelastic coefficient and Poisson's ratio (Figure J4). However, the effect of Poisson's ratio on displacement primarily focuses on the reservoir boundaries and secondarily on the ground surface, unlike the one on reservoir geometry factor (Figure J6). We conclude that Poisson's ratio impacts both the spatial distribution of poroelastic displacement and its magnitude in a half space because the free-surface effects enhance such impact around the ground surface (Figure 3.8). The inverse relation between the poroelastic displacement and Poisson's ratio is retained in both full space and half space, mainly dominating by the relation between poroelastic coefficient and Poisson's ratio. This discussion is also valid for stress analysis (Wu et al., 2021a) and can be referred in considering the elastic contrast between the reservoir and its surroundings (Mehrabian and Abousleiman, 2015; Morita et al., 1989; Rudnicki, 1999, 2011).

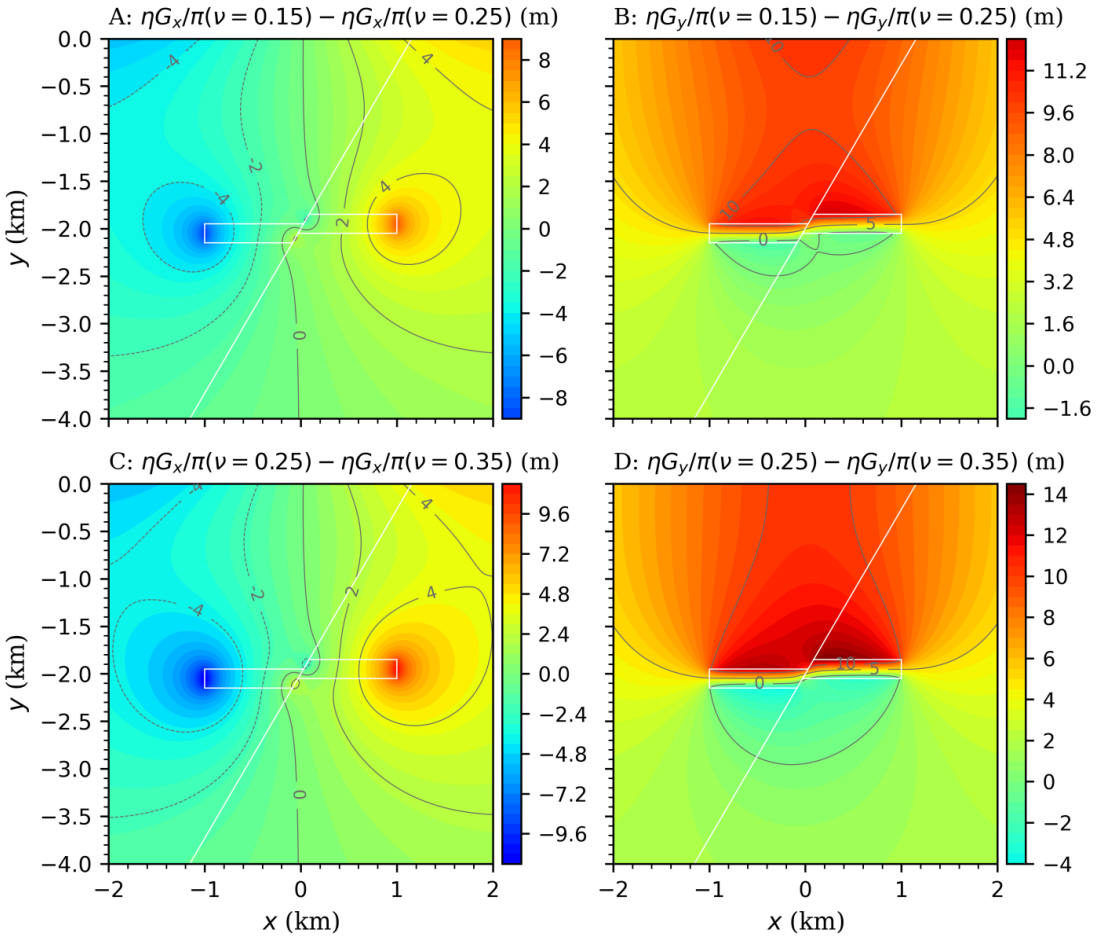

Figure 3.11: Difference of $\eta G_i / \pi$ between the cases of $\nu = 0.15$ and $\nu = 0.25$ (A and B), and between the cases of $\nu = 0.25$ and $\nu = 0.35$ (C and D) for a permeable fault in a half space. A, B, C, and D have the same color scale but the range of the legends is adapted to the values shown in each case. The reservoir geometry and the fault are indicated by the white lines. We take the base-case study in Section 3.4.1 as an example.

Several analytical solutions for poroelastic stress have already been proposed in a full space (Goodier, 1937; Jansen et al., 2019; Lehner, 2019; Soltanzadeh and Hawkes, 2008; Wu et al., 2021a), while their validity condition in terms of free-surface effects remain qualitative. Such a condition for stress analysis should be similar to our displacement analysis because of constitutive laws between stress and strain. From the perspective of stress analysis, Soltanzadeh and Hawkes (2008) proposed that the full-space solution is exactly accurate when the reservoir depth is five times greater than its lateral extent (i.e., $w/D < 0.2$ in our setting). This condition however omits the role of vertical depth ratio, which has a similar strength of impact on the free-surface effects (Figures 3.9 and 3.10). Lehner (2019) confirmed the availability of Goodier's stress solution (Goodier, 1937) for the Groningen gas field in which $w/D = 1$ and $h/D = 0.1$ in our setting. It indicates a scaled value of 60 m for the maximum error of vertical displacement (Figure 3.10) and 66 mm for the non-scaled one with the HM parameters of Groningen gas field (Jansen et al., 2019; Lehner, 2019). Such a reservoir geometry property locates in the left-hand side of the previous turning interval presented in Figure 3.10, and the non-scaled error exceeds 20% of the recorded subsidence in the Groningen gas field (Thienen-Visser and Fokker, 2017). It implies that the free-surface effects cannot be neglected for displacement analysis in this field and the full-space solutions are invalid. These different results between stress and displacement analyses indicate that the condition of neglecting the free-surface effects may be satisfied more easily for stress than for displacement because that stress is linked to the displacement gradient. Considering the proposal of Soltanzadeh and Hawkes (2008) and the case of Groningen gas field as well as the fact that reservoir thickness in general is smaller than depth, we recommend applying the inverse of $wh/D^2 \geq 10$, i.e., $wh/D^2 \leq 0.1$, as the condition of neglecting the free-surface effects on poroelastic stress (Figure 3.10).

Some of the main simplifying assumptions adopted to solve this HM-coupled problem analytically may hinder the generality of our solution and conclusions. In particular, non-linear elastic or inelastic rocks are physically more realistic than the assumption of linear elastic behavior (Doyle and Ericksen, 1956; Johnson and Rasolofosaon, 1996; Rivière et al., 2015; Scholz, 1968); and reservoirs commonly have a stiffness contrast with their surroundings (Bourne, 2003; Douma et al., 2019; Mehrabian and Abousleiman, 2015; Passey et al., 2010). The effects of these limitations in mechanics are worthy to be assessed by comparing the analytical with numerical solutions. Additionally, assuming a uniform pore pressure change within the reservoir may question the applicability of our solution in the early stage of fluid injection/production when the transient effect of pressure diffusion is evident (Crews and Cooper, 2014; Vilarrasa et al., 2010; Wu and Pruess, 2000). One can apply the principle of superposition to include this transient effect partially (Jayeoba et al., 2019).

Both approximate versions of Geertsma's solution (Geertsma, 1973) and Segall's solution (Segall, 1985) are derived by assuming a vertically concentrated compaction/dilatation at the horizontal reservoir center line (Fjær et al., 2008; Segall, 1989), which basically does not lose any accuracy in estimating displacement outside the reservoir (Figures 3.3 and 3.4). This assumption only requires that the ratio of

reservoir thickness to depth, i.e., h/D, is small enough (Segall, 1989). Almost all the field cases in practical geo-energy projects can meet such a condition (Kivi *et al.*, 2022, 2023) because the results remain acceptable even for the exaggerated case of $h/D = 1$ (Figure 3.4). However, both approximate solutions only consider a special location, which may limit their applications. These approximations have inspired us to simplify our exactly closed-form solution to an approximate version for an arbitrary position by adopting the vertically concentrated contraction/dilatation at the horizontal reservoir center (Appendix I). As an extension, we here compare the distribution of scaled poroelastic displacement evaluated by both our exact and approximate solutions in more detail as well as the difference between the two solutions in a 2D zone of interest (Figures 3.12 and J7). Results show that the approximate solution can provide accurate enough estimates for almost the whole interested zone outside the reservoir domain. For horizontal displacement, the relatively large scaled difference (e.g., > 1 m) only focuses on a small region around the lateral reservoir boundaries, and it concentrates on the entire reservoir as well as a small extension in the lateral surroundings for vertical displacement. We thus conclude that the approximate solution is preferable to assess the induced displacement in the surroundings, especially at the ground surface, because of its simplicity, and the exact one is recommended when the displacement inside the reservoir is of interest.

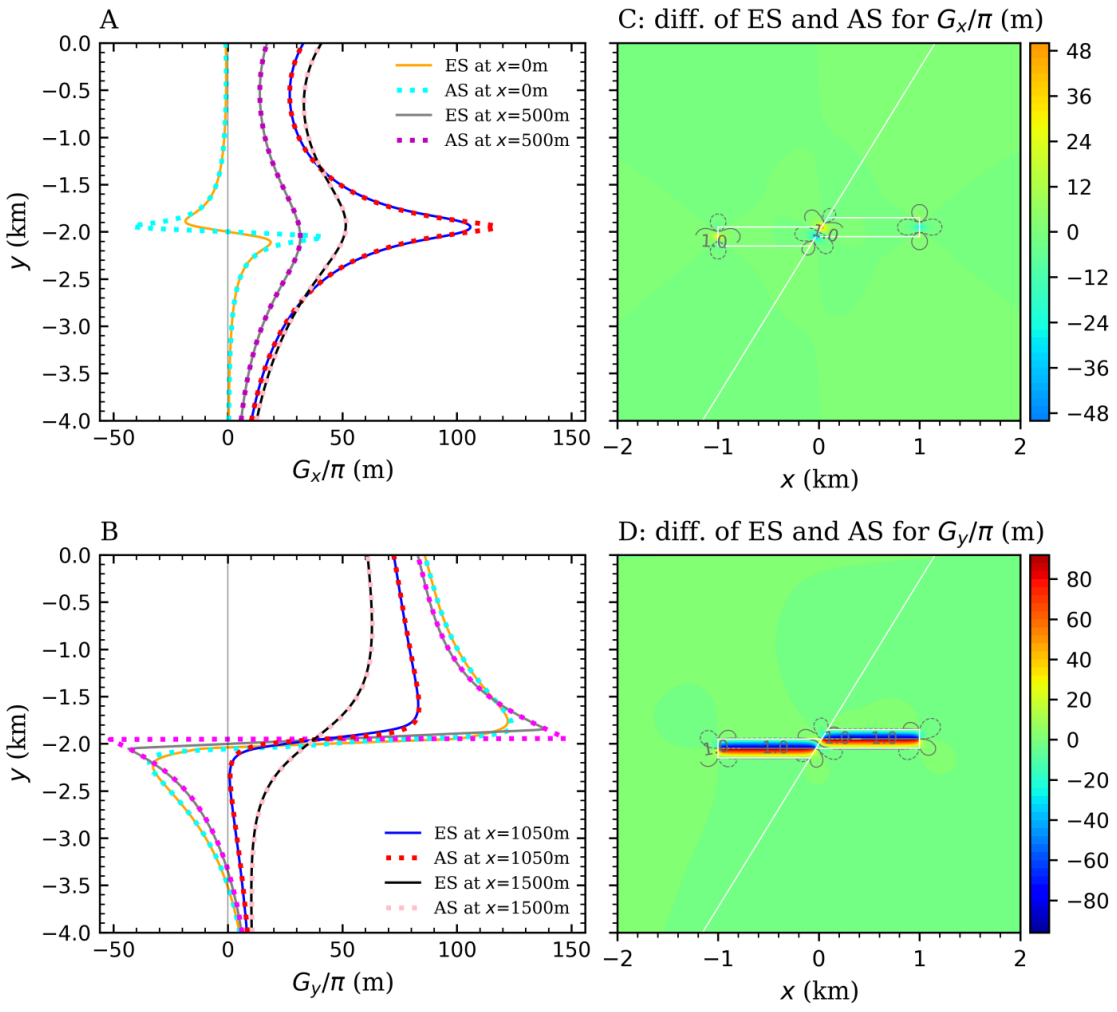

Figure 3.12: Comparison of scaled poroelastic displacement between our exact solution (ES) and approximate solution (AS) along the vertical direction for several fixed values of *x*-axis (A and B) as well as the difference between the two solutions for the zone of interest (C and D). C and D have the same color scale but the range of the legends is adapted to the values shown in each case. Displacement is scaled by $\eta\Delta p / \mu$ with a value shown in Section 3.4.1 (we take the base-case study in Section 3.4.1 as an example). The reservoir geometry and the fault are indicated by the white lines in C and D.

Our analytical solution is a useful tool to quickly evaluate the ground uplift/subsidence for geo-energy projects during their full lifetime. It makes the comprehensive parametric space analysis with respect to the geological properties of subsurface, such as fault permeability and sealing, reservoir and fault geometries, and rock strength, become feasible and executable. These comparisons can optimize the geological exploration strategy and numerical modeling (Rutqvist et al., 2010) in geo-energy applications. Superposing our solution to the existing dislocation solutions, for example, Okada's solution (Okada, 1985, 1992), for the coseismic deformation can shed a light on the transformation process from HM perturbation to fault reactivation or rock fracturing. It is helpful to build a link between the ground deformation and the seismological parameters of induced earthquakes (Lemoine et al., 2020; Ricco et al., 2019; Rudziński et al., 2019). This link may reveal some new precursors of fluid-induced seismicity and thus, can be used to predict and manage induced seismic events. At the same time, taking into account our solution in the decision-making process could also contribute to injection pressure management (Bai et al., 2017; Rutqvist et al., 2007). Besides, the distribution of horizontal and vertical displacement components displays some similar properties to the problem of ground fissures (Budhu, 2011; Jachens and Holzer, 1982; Lee et al., 1996; Peng et al., 2016) and land subsidence (Bagheri-Gavkosh et al., 2021; Galloway and Burbey, 2011; Ortiz-Zamora and Ortega-Guerrero, 2010), respectively, arising from groundwater production, which opens a new window for the application of our solution.

3.8 Conclusions

We develop a closed-form solution in a half space for evaluating the poroelastic displacement in the subsurface due to fluid injection or extraction in displaced reservoirs. It is a useful tool to quickly estimate the ground uplift/subsidence for subsurface energy-related projects. We derive the solution on the basis of inclusion theory and half-space Green's function. The solution has been verified by comparing it with Geertsma's solution and Segall's solution. We also provide an approximate version of our solution for the sake of simplification in applying our solution. We draw the following conclusions from evaluating the poroelastic displacement under various geological conditions:

- Fault permeability only plays a strong role on the spatial distribution of poroelastic displacement while its effect on displacement magnitude is small. The

displacement is smaller in the case of an impermeable fault than a permeable one because the impermeable fault restricts the pore fluid diffusion in the reservoir.

- The vertical component of ground displacement concentrates on the point projected to the vertical reservoir center, while the horizontal component symmetrically focuses on two points located outward the lateral reservoir boundaries. These distribution properties shift uniformly with the vertical center of the actual pressurized/depleted reservoir. Both fault dip and fault offset basically have no impact on the spatial distribution except for the offset slightly affecting its symmetry. Reservoir thickness does not affect this spatial distribution neither, while it uniformly compresses towards the center with decreasing either reservoir width or depth, especially the latter.

- Ground displacement increases with increasing fault dip, while it decreases with increasing fault offset. This effect on displacement magnitude is not so evident. In contrast, reservoir geometry shows a stronger effect than fault geometry. The ground displacement increases with reservoir thickness and width, and decreases for deeper reservoirs, i.e., displacement is proportional to the vertical (h/D) and lateral (w/D) depth ratios.

- Free-surface effects can enhance the poroelastic displacement in the overburden. We propose applying the product of the lateral and vertical depth ratios, i.e., wh/D^2, or its inverse as an index to assess the condition for neglecting the free-surface effects. The inverse proportion between the maximum error of full-space solutions and the inverse of wh/D^2 displays an intrinsic threshold for such a condition. This threshold may range from 50 to 100 for the inverse of wh/D^2, i.e., 0.01-0.02 for wh/D^2 itself, in displacement analysis. A specific value depends on the field background and the demands of engineering projects, and can be estimated based on our solution. Free-surface effects is smaller on stress than on displacement, we thus suggest applying $wh/D^2 \leq 0.1$ as a general condition for neglecting such effects on induced stress.

- The poroelastic displacement decreases with increasing Poisson's ratio in both full space and half space, dominating by the relation between poroelastic coefficient and Poisson's ratio. Poisson's ratio also has an impact on the spatial distribution of displacement in a half space because the free surface enhances the displacement non-uniformly with the strongest effect at the ground surface.

- Increasing the lateral depth ratio of the reservoir to 50-100 indicates an infinite reservoir in the lateral direction and thus, 3D models can be simplified into 2D models.

- We justify the assumption of vertically concentrated contraction/dilatation at the horizontal reservoir center. The approximate solution based on this assumption is preferable to assess the induced displacement in the surroundings, especially the ground displacement, and the exact solution is recommended when the displacement inside the reservoir is of interest.

4 Stochastic poromechanical analysis of induced seismicity – application to the Pohang M_w5.5 earthquake

4.1 Introduction

The Pohang M_w5.5 earthquake is the largest seismic event induced by any Enhanced Geothermal System (EGS) project (Ellsworth et al., 2019; Kim et al., 2018; Korean Government Commission (KGC, hereafter), 2019) and occurred approximately two months after hydraulic stimulation was completed. Although surface rupture did not occur, other superficial manifestations were recorded, such as significant coseismic surface deformations (Grigoli et al., 2018; Song and Lee, 2019), ground cracks, retaining wall deformations and soil liquefactions (Choi et al., 2019; Kang et al., 2019). The epicenter of the earthquake was located near the EGS project site (Ellsworth et al., 2019; Kim et al., 2018; Yeo et al., 2020), with the hypocenter corresponding to the depth of the injection wells (Ellsworth et al., 2019; Kim et al., 2018). It is now commonly accepted that the earthquake was induced by high-pressure hydraulic stimulation in the injection well PX-2, which activated a low-permeability fault (Ellsworth et al., 2019; Kim et al., 2018; Lee et al., 2019), whereas some of the specifics regarding the triggering mechanisms remain object of a scientific debate and contrasting hypotheses have been formulated.

The Overseas Research Advisory Committee (ORAC) concluded that the overpressure caused by fluid injection reactivated a critically stressed fault, which, in turn, released the stored elastic strain energy as the Pohang earthquake (Ellsworth et al., 2019; KGC, 2019). Lim et al. (2020) studied the effect of hydraulic diffusivity on the timing delay between the injection and the earthquake. Chang et al. (2020) and Wassing et al. (2021) argued that the poroelastic stress also played a significant role, especially in the case of the low-permeability fault that induced the earthquake, which requires coupled hydro-mechanical (HM) approaches to assess the triggering mechanisms. Yeo et al. (2020) proposed that the earthquake interactions, i.e., the static stress transfer from the previous induced seismicity, made a greater contribution on the earthquake nucleation than the pore pressure buildup. Geochemical effects in terms of fault corrosion have also been proposed as a triggering mechanism (Westaway and Burnside, 2019). Thus, multiple triggering mechanisms (Ge and Saar, 2022; Vilarrasa et al., 2021, 2022) driven by a combination of coupled thermo-hydro-mechanical-chemical processes likely induced the M_w5.5 earthquake.

The aforementioned studies on the Pohang earthquake present three limitations. First, most of the hydraulic and HM assessments focused only on fault stability (Chang et al., 2020; Ellsworth et al., 2019; KGC, 2019; Lim et al., 2020; Yeo et al., 2020; Wassing et al., 2021), while no scaling relationship between the final evaluated results (pore pressure buildup, transferred Coulomb static stress, poroelastic stress changes, and

Coulomb failure stress) and the earthquake magnitude has been established. Only knowledge on the activated mechanisms is available, while quantitative assessment of the earthquake magnitude and the risk of its occurrence has not been attempted. Second, all previous research assumed that the reactivated fault was initially very critical to failure and that any perturbation of larger than the general threshold, i.e., 0.01 MPa (King et al., 1994; Reasenberg and Simpson, 1992), could induce an earthquake (KGC, 2019) in Pohang EGS site, with estimates ranging from 0.05 to 0.3 MPa. Based on the focal mechanism solutions, Terakawa et al. (2020) estimated an overpressure of 8 ± 3 MPa in the source region of the mainshock, arguing that the fault could not have been so critical to failure conditions. Otherwise, small perturbations like tidal stress variations (0.001-0.01 MPa, Emter, 1997) would have been sufficient to trigger an earthquake of similar magnitude. Third, the uncertainty of the in-situ stress and the fault geometry was highlighted by several equally likely estimates (Tables 4.1 and 4.2) based on existing geological, seismological and geodetic analyses, and that present a wide range of proposed values (see Section 4.2.1 for details). Existing HM simulations (Lim et al., 2020; Chang et al., 2020; Wassing et al., 2021) adopted a deterministic approach, choosing one individual estimate to carry out their evaluations. No comprehensive analysis has been reported to compare the relative likelihood of these estimates and to show which estimate would provide the best fit. These reported evidences highlight that there was a wide uncertainty on the initial state of the fault, itself a function of the in-situ state of stress, the fault geometry and rock properties (Jaeger et al., 2007): we believe an uncertainty analysis can provide a quantitative estimate for the induced seismicity risk of the Pohang EGS site.

Monte Carlo simulation is a classic approach for such purpose of uncertainty (stochastic) analysis (Harrison, 2010; Raychaudhuri, 2008), which has already been applied in various geological hazard assessments. Original applications usually adopt the Monte Carlo method to analyze the earthquake recurrence parameters and sample earthquakes by following the probability distributions (Bourne et al., 2015; Gischig et al., 2013; Parsons, 2008). Later studies include that applying this method to estimate in-situ stress and rock properties according to field and laboratory data (Bhattacharya and Viesca, 2019; Kruszewski et al., 2021; Van den Ende et al., 2020), and to perform coupled HM simulations (Masoudian et al., 2019; Plúa et al., 2021; Raziperchikolaee and Mishra, 2020; Reyes Canales and Van der Baan, 2021; Zhang et al., 2021). Most of these HM simulations used the Monte Carlo method to generate a heterogeneous distribution of rock properties in the whole simulation domain and then simulated the coupled HM problem with heterogeneity of rock properties. To best of our knowledge, extremely few publications, e.g., Masoudian et al. (2019), carried out a full HM simulation for each realization of the Monte Carlo simulation. However, the number of both realizations and numerical elements adopted in Masoudian et al. (2019) is very limited (only about one thousand) because of the computational cost. Numerically evaluating the coupled HM process for every realization of Monte Carlo simulations indeed is a technical challenge for the current computational ability. Alternatively, we can simplify the evaluations of the coupled HM process by analytical solutions, which may greatly promote the development of stochastic poromechanical analysis.

This contribution aims at studying analytically the processes of pore pressure diffusion and poroelastic responses due to the cyclic fluid injection in Pohang EGS project and at evaluating the fault stability and induced seismicity potential with the range of proposed fault geometries and in-situ stress states to find which estimate is the best. We first make a deterministic analysis to show how the analytical solutions work and if it is possible to explain the Pohang earthquake. We also perform a parametric space analysis on the uncertain geological properties to see what parameters are playing an essential role on induced seismicity. Subsequently, we carry out Monte Carlo simulations that include multiple stochastic variables for this poromechanical problem, and then statistically estimate the probability of inducing the Pohang earthquake based on the stochastic simulation results. To realize the quantitative risk assessment, we combine the slipping fault patch size with the rupture nucleation model to build a link between the fault stability analysis and the magnitude of induced seismicity.

4.2 Materials and Methods

4.2.1 Pohang setting

The Pohang EGS project was deployed to produce geothermal energy in the granitic formation around 4.2 km depth, aiming at mitigating the issue of energy deficiency in Korea (Kim et al., 2018; KGC, 2019). The project site is one of the highest heat-flow areas in Korea (Lee et al., 2015), and is located within the Pohang basin that is surrounded by the Yangsan fault system and the Ulsan fault system (Grigoli et al., 2018). The former involves many N- or NNE-striking strike-slip faults, while the latter includes many typically NNE- to NNW-striking reverse faults (KGC, 2019). The previous earthquakes associated with these faults almost have no effect on fault stability in the area of the EGS project site (Grigoli et al., 2018; Ellsworth et al., 2019). Five hydraulic stimulations were conducted at the wells PX-1 and PX-2, which were drilled to a depth of 4215 m and 4348 m, respectively (KGC, 2019). Several publications have presented the recorded injection data and the related seismic events (Kim et al., 2018; KGC, 2019; Ellsworth et al., 2019; Yeo et al., 2020).

There are three independent evidences confirming that the mature fault associated with the Pohang earthquake intersects the injection well PX-2 at the depth of ~3.8 km (Lee et al., 2019; KGC, 2019; Ellsworth et al., 2019). However, the fault geometry (strike and dip angle) is uncertain. Eight estimates of the fault plane associated with the induced seismicity at the Pohang EGS site have been derived based on the focal mechanism, InSAR analysis and moment tensor analysis with the recorded seismic events (Table 4.1, Ellsworth et al., 2019; Grigoli et al., 2018). The reversed solutions (FP7 and FP8) with the recorded data show that the related fault is northwest-dipping (Grigoli et al., 2018), which means the alternative solutions (FP2 and FP4) of focal mechanism could not be a likely option. The fault strike of FP1, FP3, FP7 and FP8 is consistent with the one of FP5 instead of FP6 indicates that the mainshock is induced by the hydraulic stimulations in PX-2. Thus, five estimates (FP1, FP3, FP5, FP7 and

FP8) of the fault plane are the potential ones linked to the mainshock, and can be divided into two classes based on their difference in fault strike and dip angle. FP1, FP3 and FP5 show a relatively low dip angle with an almost same strike, while FP7 and FP8 present a higher dip angle with a similar strike. The former may correspond to the dip-slip fault and the latter probably is the strike-slip fault (Jaeger et al., 2007). The likely estimates of fault plane show a similarity with the previous quaternary faulting nearby the border of the Pohang basin, which may imply that there are two different fault slip patterns to explain the Pohang earthquake.

Table 4.1: Estimates of fault plane that is related to the induced seismicity at the Pohang EGS site (Ellsworth et al., 2019; Grigoli et al., 2018)

Number	Strike (°)	Dip (°)	Physical description
FP1	214	51	Northwest-dipping nodal plane (FP1) and its alternative one (FP2) of the mainshock focal mechanism from first-motion analysis
FP2	343	52	
FP3	215	58	Northwest-dipping nodal plane (FP3) and its alternative one (FP4) of M_w 3.2 event
FP4	339	48	
FP5	214	43	Plane of PX-2 seismicity
FP6	180	62	Plane of PX-1 seismicity
FP7	225	75	Mainshock fault plane from InSAR analysis (FP7), and from moment tensor analysis (FP8)
FP8	221	66	

Regarding the in-situ stress for the Pohang EGS site at depth, only the vertical stress component σ_v is determined, which is 106 MPa and is evaluated from the dipole sonic logging at 4.2 km of the PX-2 borehole (Park et al., 2017, 2020; KGC, 2019). Although the azimuth of the maximum horizontal principal stress σ_H is also derived from the logging data, it has a high uncertainty of ~30% because of the anisotropy features (KGC, 2019). Accordingly, σ_H and the minimum horizontal principal stress σ_h are estimated and thus, several in-situ stress tensors are proposed under different assumptions and methods (Table 4.2, Kim et al., 2017; Park et al., 2017; Soh et al., 2018; KGC, 2019; Castilla et al., 2019; Westaway and Burnside, 2019; Bethmann et al., 2019), in which, the one that was derived from the shallow depth of the EXP-1 well (Kim et al., 2017) has been extended to the depth of 4.2 km (Farkas et al., 2021). These estimates present a wide range of proposed values. Three (IS7, IS8, and IS9) of them are estimated by the source data that was measured in the sedimentary rock. These three estimates basically are not suitable for the stress state of the crystalline rock.

We define a maximum deviatoric stress ratio to make a first-order assessment on the proposed stress tensors, that is

$$DSR_{\max} = \frac{\sigma_1 - \sigma_3}{\sigma_1 + \sigma_3 - 2\alpha p^0}, \tag{4.1}$$

where σ_1 and σ_3 are the greatest and the least principal stress components, respectively, α is Biot's coefficient, p^0 is the initial pore pressure. The value of $DSR_{\max}$ for all these estimates is included in Table 4.2.

In fault stability analysis, a critical fault means that $DSR_{max} \approx \mathrm{Sin}\Theta$ based on the three dimensional linear Mohr circle diagram, in which Θ is the friction angle of the fault. Laboratory tests on the core samples of PX-2 shows that Θ is ~26.6° ($\mathrm{Sin}\Theta = 0.45$), which corresponds to a static friction coefficient of ~0.5 (Park et al., 2017; Kwon et al, 2019). Thus, with the assumption of a completely hydrostatic pore pressure (Ellsworth et al., 2019), we can exclude the estimates IS7, IS8, and IS9 because the value of DSR_{max} for these estimates is too small relative to $\mathrm{Sin}\Theta$. It would not result in misjudgment even for a smaller value of α because DSR_{max} decreases with α. The estimates with $DSR_{max} > \mathrm{Sin}\Theta$ imply a supercritical fault, while they cannot be excluded as DSR_{max} decreases with α. Thus, we have six potential estimates for the in-situ stress. Note that we did not exclude the estimates IS3 to IS5, although the value of DSR_{max} are also smaller than 0.45, because only two samples are tested for the friction angle of fault (Kwon et al, 2019), which may remain uncertain. We will make a deeper comparison among the six estimates to show their relative likelihood later.

Table 4.2: Estimates of the in-situ stress state at the depth of ~4.2 km for the Pohang EGS site. RF and SS mean the reverse faulting and strike-slip faulting regimes, respectively. Sedi and Crys denote the stress state is estimated by the source data that was measured in the sedimentary rock and the crystalline rock, respectively. DSR_{max} is the maximum deviatoric stress ratio defined in this work (Equation (4.1)).

Number	Azimuth of σ_H (°)	σ_H (MPa)	σ_h (MPa)	σ_v (MPa)	Regime	Measured rock type	DSR_{max}	Reference
IS1	N77±23	243	120	106	RF	Crys	0.517	Korean Government Commission (2019)
IS2	N74	203	93	106	SS	Crys	0.519	
IS3	N100	198	107	107	SS/RF	Crys	0.412	Castilla et al. (2019)
IS4	N100	168	95	107	SS	Crys	0.408	
IS5	N111	200	120	110	RF	Crys	0.398	Westaway and Burnside (2019)
IS6	N75	256	87	111	SS	Crys	0.653	Soh et al. (2018)
IS7	N130-136E	138	86	107	SS	Sedi	0.37	Kim et al. (2017)
IS8	N65-130E	115-138	81-105	110	SS	Sedi	≤0.357	Park et al. (2017)
IS9	N100E	133-153	89-119	107	SS/RF	Crys & Sedi	≤0.329	Bethmann et al. (2019)

4.2.2 Stress transformation from the three dimensional (3D) principal stress space to the two dimensional (2D) fault plane of interest

The in-situ stress is a tensor in 3D (Table 4.2). We need to transform the 3D principal stress to the 2D fault plane to couple with the 2D analytical hydromechanical solutions. Here we propose a new method for such purpose, i.e., continuously applying the 2D

coordinate transformation formula twice, instead of the 3D coordinate transformation (Peška and Zoback, 1995; Fan et al., 2016). The following is the 2D coordinate transformation formula from the *x*-*y* plane to an arbitrary *x*'-*y*' plane

$$\sigma_{x'x'} = \frac{\sigma_{xx} + \sigma_{yy}}{2} + \frac{\sigma_{xx} - \sigma_{yy}}{2}\cos(2A_{xx'} + \pi) + \sigma_{xy}\sin(2A_{xx'} + \pi), \tag{4.2}$$

$$\sigma_{x'y'} = -\frac{\sigma_{xx} - \sigma_{yy}}{2}\sin(2A_{xx'} + \pi) + \sigma_{xy}\cos(2A_{xx'} + \pi), \tag{4.3}$$

where $A_{xx'}$ is the angle between the original axis *x* and the new axis *x*'.

The idea is that we first transform the two horizontal principal stress components (σ_H and σ_h) to the vertical plane along the fault strike direction based on Equations (4.2) and (4.3), i.e., obtaining σ_{n1} and τ_1 (Figure 4.1A), and then transform the evaluated σ_{n1} and the vertical principal stress component (σ_v) to the inclined fault plane, i.e., obtaining σ_{n2} and τ_2 (Figure 4.1A). The angle $A_{xx'}$ equals azimuth – (strike – 180°), i.e., the angle between the fault strike and the azimuth of σ_H, and fault dip θ in the first and second coordinate transformations, respectively. Thus, the initial normal and shear stress components on the fault plane are

$$\sigma_n^0 = \sigma_{n2}, \tag{4.4}$$

$$\left|\tau^0\right| = \sqrt{(\tau_1 \sin\theta)^2 + \tau_2^2}, \tag{4.5}$$

where superscript 0 represents the initial state, and τ_1 should be projected on the inclined fault plane from its original vertical plane before the module operation.
After fluid injection, to evaluate the shear stress on the fault plane in the final state, the induced shear stress τ should be added only to τ_2 (Figure 4.1C), such that

$$\left|\tau^{\mathrm{f}}\right| = \sqrt{(\tau_1 \sin\theta)^2 + (\tau_2 + \tau)^2}. \tag{4.6}$$

The above stress transformation method has three essential advantages: (1) the shear stress direction on the fault plane is clear; (2) provide a more convenient approach to couple with the induced shear stress; and (3) we do not need to find the angles between the normal direction of the fault plane and the original principal stress coordinate.

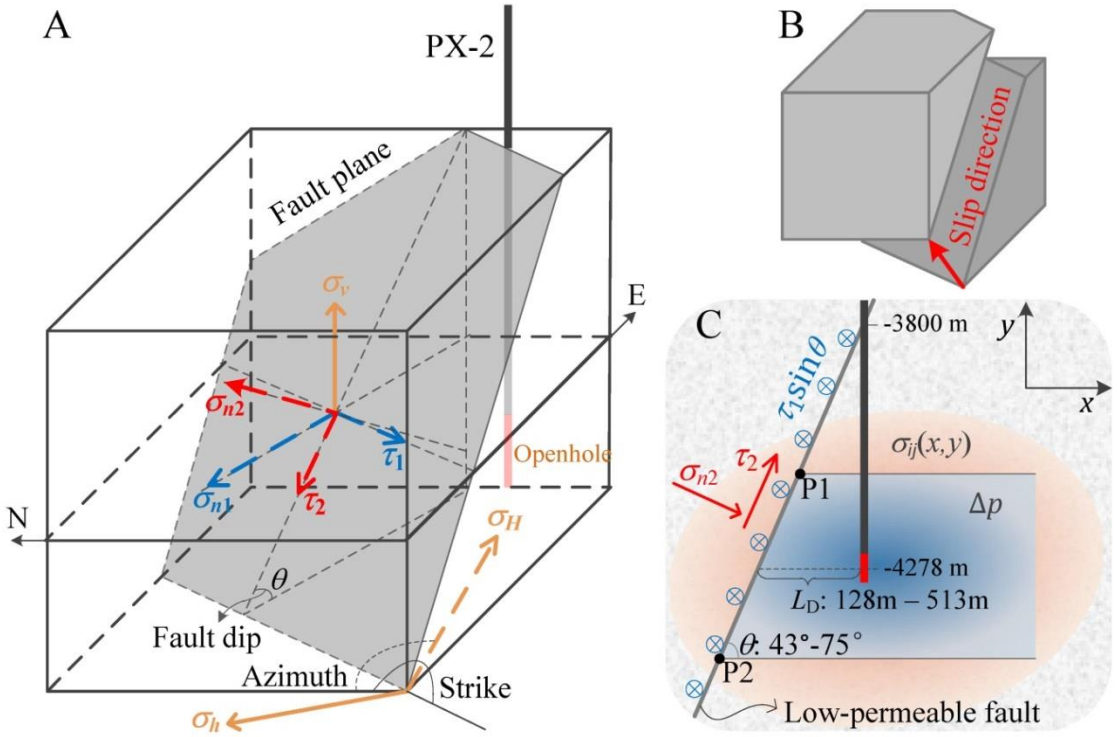

Figure 4.1: Schematic of (A) three dimensional (3D) geological model and its in-situ stress state, (B) oblique slip model along the fault plane, and (C) simplified two dimensional (2D) projection perpendicular to the fault strike. σ_v , σ_H , σ_h are the vertical principal stress, the maximum horizontal principal stress, and the minimum horizontal principal stress, respectively. σ_{n1} and τ_1 are the normal and shear stress components acting on the vertical plane along the fault strike direction, respectively, which are transformed from σ_H and σ_h. σ_{n2} and τ_2 are the normal and shear stress components acting on the inclined fault plane, respectively, which are transformed from σ_{n1} and σ_v. The module between τ_2 and the projection of τ_1 on the fault plane is the total shear stress at the initial state. All the stress components marked in (A) indicate the negative direction as we adopt the sign convention of geomechanics, i.e., positive for compression, which implies that the potential slip direction of the hanging wall is the one shown in (B). The positive direction of stress components along the fault plane is shown in (C), where blue ⊗ means the inward direction of the out-of-plane. The pore pressure and stress changes induced by fluid injection are also included in (C). L_D is the distance between the fault and the well PX-2, which is calculated based on the fault dip θ.

4.2.3 Theis's solution for pore pressure diffusion

For the typical cyclic injection, the fluid injection-induced pore pressure changes in an infinite homogenous and isotropic aquifer can be obtained by the superposition principle based on Theis's solution (Theis, 1935)

$$\Delta p = \sum_{i=1}^{n} \frac{Q_i - Q_{i-1}}{4\pi\lambda h} W(u_i), \tag{4.7}$$

$$u_i = \frac{\phi c_t r^2}{4\lambda(t - t_{i-1})}, \tag{4.8}$$

where Δp is the pore pressure change (positive value implies injection), Q is the volumetric injection rate, h is the aquifer thickness, λ is mobility defined as the ratio of permeability to fluid viscosity $\lambda = k/\varphi$, $W(u)$ is the Theis well function, ϕ is the rock porosity, c_t is the total compressibility of pore and fluid, r and t are the radial distance and the injection time, respectively. The subscript i means the i^{th} period of injection with constant injection rate Q_i, t_i corresponds to the instant of injection rate changing, and $t_0 = 0$ s, $Q_0 = 0$ m^3/s.

Regarding the evaluation of Theis well function, the series expansion is usually applied in the field of groundwater, it is however only available for small u (Barry et al., 2000; Tseng and Lee, 1998). In particular, the famous approximation of Cooper and Jacob (1946) can provide a good estimate only for $u < 0.01$. When evaluating the spatial distribution of pore pressure changes at the instant of the mainshock, the argument u may exceed the previous thresholds of series expansion for some values of the radial distance. Thus, we apply an analytical approximation (Barry et al., 2000)

$$W(u) = \frac{\exp(-u)\ln[1 + \frac{G}{u} - \frac{1-G}{(m+bu)^2}]}{G + (1-G)\exp(\frac{-u}{1-G})}, \tag{4.9}$$

where $G = \exp(-\gamma)$, $b = \sqrt{\frac{2(1-G)}{G(2-G)}}$, $m = \frac{1}{1+u\sqrt{u}} + \frac{m_\infty q}{1+q}$, $q = \frac{20}{47} u^{\sqrt{\frac{31}{26}}}$,

$m_\infty = \frac{(1-G)(G^2 - 6G + 1)}{3G(2 - G^2)b}$, and $\gamma = 0.5772156649015328606$ is the Euler constant.

Equation (4.9) is valid for the whole range of the argument $u > 0$ and is sufficiently accurate for data analysis in hydrological applications (Barry et al., 2000).

Logging data shows that the low-permeable fault core is surrounded by high-permeable damage zones (KGC, 2019; Ellsworth et al., 2019; Yeo et al., 2020), implying that the low-permeable fault remains permeable along its longitudinal direction and thus, the overpressure can dissipate along the fault. As a result, the blocking effect of the transversely low-permeable fault on the pore pressure diffusion can be neglected.

4.2.4 Analytical solution for stress variations induced by pore pressure changes

We apply the 2D analytical solution presented in Chapter 2 and Wu et al. (2021a) to evaluate the poromechanical stress induced by pore pressure changes. Theis's solution gives a radial distribution of overpressure around the injection well after fluid injection.

We cut the 2D cross-section that is overlapped with the projection in Figure 4.1C to couple with our 2D stress solution. The mean pore pressure change averaged over the 2D pressurized region is defined by

$$\Delta p_{\mathrm{m}} = \frac{1}{A}\int_A \Delta p dA = \sum_{i=1}^{n} \Delta p_i \cdot \Delta p_i h dr \Big/ \sum_{i=1}^{n} \Delta p_i h dr\,, \tag{4.10}$$

where A is the area, that is weighted by the pore pressure changes, of the pressurized region. We evaluate the mean pore pressure change by technically dividing the entire pressurized region into finite rectangular micro-segments, the area of each micro-segment is $\Delta p_i h dr$.

Our stress solution is a useful tool and can be applied in both the cases of permeable and impermeable faults with an arbitrary fault offset and dip angle θ. The spatial location of the low-permeable fault and the injection well PX-2 just constitutes the case of fluid injection into the right-hand side of a low-permeable fault. Once the pore pressure diffusion reaches the fault, the pressurized region will be limited by the fault and finally transforms into a trapezoidal inclusion domain (Figure 4.1C), which leads to (Wu et al., 2021a)

$$\begin{aligned}\sigma_{xx} = -\frac{(1-2\nu)\alpha\Delta p_{\mathrm{m}}}{2\pi(1-\nu)}\Bigg\{&\operatorname{atan}\frac{y-y_2}{x-d} - \operatorname{atan}\frac{y-y_1}{x-d} - \left[f_1(x,y,y_2) - f_1(x,y,y_1)\right]\sin^2\theta \\ &- \frac{\sin\theta\cos\theta}{2}\ln\frac{f_2(x,y,y_2)}{f_2(x,y,y_1)} - 2\pi\delta_\Omega\Bigg\}\end{aligned}, \tag{4.11}$$

$$\sigma_{yy} = \sigma_{xx} + \frac{(1-2\nu)\alpha\Delta p_{\mathrm{m}}}{(1-\nu)}\delta_\Omega\,, \tag{4.12}$$

$$\begin{aligned}\sigma_{xy} = -\frac{(1-2\nu)\alpha\Delta p_{\mathrm{m}}}{2\pi(1-\nu)}\Bigg\{&\left[f_1(x,y,y_2) - f_1(x,y,y_1)\right]\sin\theta\cos\theta \\ &- \frac{\sin^2\theta}{2}\ln\frac{f_2(x,y,y_2)}{f_2(x,y,y_1)} + \frac{1}{2}\ln\frac{f_3(x-d,y-y_2)}{f_3(x-d,y-y_1)}\Bigg\}\end{aligned}, \tag{4.13}$$

where σ_{ij} is the stress component along the direction j and acting on the surface i, x and y are the Cartesian coordinates, y_1 and y_2 denote the bottom and top boundaries of the trapezoidal inclusion domain Ω, respectively, d is the length of the pressurized region that can be measured at the vertical center of the pressurized region for a trapezoidal domain, α and ν are Biot's coefficient and Poisson's ratio, respectively. δ_Ω is the modified Kronecker delta, which equals 1 if $(x,y) \in \Omega$ or 0 if $(x,y) \notin \Omega$, and functions f_1, f_2 and f_3 are

$$f_1(x,y,\hat{y}) = \operatorname{atan}\frac{(x-\hat{y}\cot\theta)\cot\theta + (y-\hat{y})}{x - y\cot\theta}\,, \tag{4.14}$$

$$f_2(x,y,\hat{y}) = \left(x-\hat{y}\cot\theta\right)^2 + \left(y-\hat{y}\right)^2\,, \tag{4.15}$$

$$f_3(x-\hat{x}, y-\hat{y}) = (x-\hat{x})^2 + (y-\hat{y})^2 . \tag{4.16}$$

With these induced stress components in *x*-*y* plane, one can obtain the normal and shear stress components on the fault plane by applying the coordinate transformation formula (Equations (4.2) and (4.3)). Note that the induced shear stress should be added to the component of initial shear stress that is perpendicular to the fault strike (Equation (4.6)), i.e., τ_2 in Figure 4.1.

4.2.5 Coulomb failure stress and slipping fault patch size

Once the normal and shear stress components on the fault plane are obtained, we adopt the Coulomb Failure Stress (*CFS*) (King, 1994) and Coulomb Failure Stress Change (ΔCFS) to evaluate fault stability and its change

$$CFS = \left|\tau^{\mathrm{f}}\right| - f_{\mathrm{st}}\left(\sigma_n^{'} + \sigma_n^{'0}\right), \tag{4.17}$$

$$\Delta CFS = \left|\tau^{\mathrm{f}}\right| - \left|\tau^{0}\right| - f_{\mathrm{st}}\sigma_n^{'}, \tag{4.18}$$

where f_{st} is static friction coefficient, and the normal stress with a superscript $'$ means the effective normal stress including Biot's effect, i.e., $\sigma_n'^0 = \sigma_n^0 - \alpha p^0$ and $\sigma_n' = \sigma_n - \alpha \Delta p_{\mathrm{FP}}$, where Δp_{FP} is the overpressure on the fault plane.

In further, we apply the maximum slipping fault patch size (Chapter 2, Wu et al., 2021a) to assess the induced seismicity potential based on the final *CFS* distribution along the fault plane

$$S_{\max} = \max(\ell_i)/\sin\theta, \tag{4.19}$$

where l_i is a continuous interval in coordinate *y* with *CFS* > 0.

4.2.6 Moment magnitude and Ohnaka's rupture nucleation model

The moment magnitude (M_{w}) is the best measure of earthquake size for moderate to large earthquakes, which is defined based on the seismic moment (M_0 in N m) as (Kanamori 1977; Hanks and Kanamori 1979)

$$M_{\mathrm{w}} = \frac{2}{3}\lg M_0 - 6.07 . \tag{4.20}$$

The seismic moment can be evaluated on the basis of Ohnaka's rupture nucleation model (Ohnaka, 2000) to link to the quasi-static simulations. Ohnaka's model is a theoretical scaling relation between the seismic moment and the critical size ($2L_{\mathrm{c}}$) of the nucleation zone

$$M_0 = k_{\mathrm{NL}}(2L_{\mathrm{c}})^3, \tag{4.21}$$

where k_{NL} is the scaling parameter. We assume $k_{NL} = 10^9$, which is a typical and theoretical value with a few assumptions and laboratory-based observations, which also match well with the seismological data (Ohnaka, 2000, 2013). The maximum slipping fault patch size (Equation (4.19)) can be regarded as an approximate estimate of the critical size of the nucleation zone since both them are defined under the quasi-static and shear frictional equilibrium conditions.

4.2.7 Monte Carlo simulation procedure

The initial state of the fault evaluated with the random value of the stochastic variables could range from very stable (a relatively small negative value of CFS^0) to unstable ($CFS^0 > 0$) state during Monte Carlo simulations. An initially very stable fault will not slip, while an initially unstable fault is already in failure, both two types of extreme cases are unrealistic for Pohang EGS site and should be discarded. Thus, we redraw the samples when the value of CFS^0 falls out a reasonable range. To ensure the reliability of the Monte Carlo simulations, we adopt the following procedure for each simulation:

(1) Do one realization: generate the random value for all the stochastic variables according to the adopted distribution and then check if CFS^0 falls in a reasonable range: if so, evaluate the poroelastic stress, final *CFS*, and the maximum slipping fault patch size S_{max} (Equation (4.19)) in order; if not so, discard this sample and redraw it again.

(2) Compute the mean and the standard deviation of S_{max}, and plot them against the number of realizations. One can finish the simulation once the plot reaches a stationary state as it is not necessary to do more realizations. Otherwise, repeat the steps (1) and (2) to do another realization.

(3) Check if all the stochastic variables still follow the adopted distribution: if so, end the simulation procedure and the result is available; if not so, which means the adopted distribution is not available for the current problem, use another distribution for the stochastic variables that did not follow the previous distribution and then repeat steps (1) to (3) to do another simulation.

The applied convergence criterion in step (2) is that the relative error of both the mean and the standard derivation of S_{max} is less than 2×10^{-5} (0.2%) in this work.

4.2.8 Potential slip patterns and simulation strategy

The potential estimates of in-situ stress are either a reverse or a strike-slip stress faulting regime (Table 4.2). Transforming the 3D principle stress to the fault plane (Section 4.2.2) shows that the shear stress component on the likely fault plane aligns neither with the dip direction nor with the strike direction, but forms an angle with each of the directions regardless of the stress regimes (Figure 4.1A). An oblique slip occurs in such situation, with a displacement vector directed upward and to one side of the fault (Figure 4.1B). The primary slip component of this oblique slip is a reverse slip

for the reverse stress regime and is a strike slip for the strike-slip stress regime, just corresponding to the two type estimates of the fault: the dip-slip fault (FP1, FP3 and FP5) and the strike-slip fault (FP7 and FP8). Thus, we propose two oblique-slip patterns to analyze the problem of induced seismicity in Pohang: a reverse-slip-dominated pattern with a strike-slip component (RS-S pattern), which involves a reverse fault (e.g., FP1, FP3 or FP5) being in a reverse stress faulting regime (e.g., IS1); and a strike-slip-dominated pattern with a reverse component (SS-R pattern), which considers a strike-slip fault (e.g., FP7 or FP8) being in a strike-slip stress faulting regime (e.g., IS2). We further take the mean value of fault geometry of FP1, FP3 and FP5 as the base fault plane of RS-S pattern, and of FP7 and FP8 as the base fault plane of SS-R pattern, i.e., the geometry of the base fault plane is 214.5°/50.5° in the RS-S pattern and 223°/70.5° in the SS-R pattern.

Before performing the deterministic and probabilistic analyses for the purposes of this work, we first make an attempt to constraint the plausible range of the in-situ stress. We assess stability of the different characteristics of the fault, based on the linear Mohr-Coulomb criterion, for each of the proposed in-situ stress states (Table 4.2). We adopt the laboratory test value (0.5, Kwon et al., 2019) for the static friction coefficient and a value of 0.79 for Biot's coefficient (Chang et al., 2020; Chang and Yoon, 2021) as the reference value of our stability analysis. We follow the stress transformation formula shown in Section 4.2.2 to transform the 3D principal stress to the 2D fault plane. We further analyze the effect of in-situ stress on the fault geometry given that the natural faults arose in the subsurface present different geometrical properties in different stress faulting regimes. We show the results by Mohr circle diagrams (Figure 4.2), which suggest that the estimates IS1 and IS2 are the two most likely in-situ stress states (Section 4.3.1).

We do a deterministic analysis for the base fault plane of the two slip patterns in the second step. We apply Theis's solution to evaluate the spatiotemporal pore pressure evolution during and after the hydraulic stimulations in PX-2 (Section 4.2.3). We simplify the three hydraulic stimulations in PX-2 as five continuous injection periods (Table 4.3), i.e., a typical stepwise injection with five cycles, where the mean injection rates are calculated from the public recorded data (Yeo et al., 2020). We take the recorded temporal injection pressure (Yeo et al., 2020) as the in-put data and then try to match the simulated pore pressure changes at the bottom hole with the in-put data by varying the thickness of the aquifer. Thus, the radial distribution of pore pressure changes at the instant of the mainshock is the pressurized region that is related to the mainshock. With the size and mean pore pressure change of this pressurized region as well as the overpressure on the fault, we compute the poromechanical stress along the fault (Section 4.2.4, Wu et al., 2021a), and evaluate the fault stability (Section 4.2.5). Table 4.4 includes all the involved hydraulic and mechanical parameters.

Table 4.3: Injection information of the five injection periods in well PX-2 (Yeo et al., 2020)

Number of cycle	Start date	End date	Duration (Day)	Mean injection rate (L/s)	Injection/Shut-in
1	29/01/2016	05/02/2016	8	1.87	Injection
	06/02/2016	10/02/2016	5	0	Shut-in
2	11/02/2016	18/02/2016	8	1.12	Injection
	19/02/2016	15/03/2017	391	0	Shut-in
3	16/03/2017	18/03/2017	3	0.15	Injection
	19/03/2017	24/03/2017	6	0	Shut-in
4	25/03/2017	14/04/2017	21	1.7	Injection
	15/04/2017	29/08/2017	137	0	Shut-in
5	30/08/2017	18/09/2017	20	1.59	Injection
	19/09/2017	15/11/2017	58	0	Shut-in

Table 4.4: Hydraulic and mechanical parameters of the reservoir in the Pohang EGS site

Parameter	Physical meaning	Value	Unit	References
ϕ	Rock porosity	0.05	-	Kwon et al. (2019)
k	Intrinsic permeability	5	μD	Park et al. (2017); Hofmann et al. (2019); Yeo et al. (2020)
φ	Fluid viscosity	0.2	mPa s	Hofmann et al. (2019); Yeo et al. (2020)
c_t	Total compressibility	9E-10	Pa^{-1}	Hofmann et al. (2019); Yeo et al. (2020)
r_w	Radius of well PX-2	0.108	m	Hofmann et al. (2019)
μ	Shear modulus	13.8	GPa	Kwon et al. (2019)
ν	Poisson's ratio	0.21	-	
p^0	Initial pore pressure	42	MPa	Korean Government Commission (2019)
α	Biot's coefficient	0.79	-	Chang et al. (2020); Chang & Yoon (2021)
f_{st}	Static friction coefficient	0.5	-	Kwon et al. (2019)

We then perform a parametric space analysis to analyze the effect of in-situ stress state (σ_H, σ_h, and azimuth), fault geometry (θ) and rock properties (α, f_{st}) on induced seismicity (fault slip) in the third step as these six parameters are the main uncertain properties in Pohang. We do not consider the vertical stress because it already has a deterministic and credible value (Table 4.2). We disregard the fault strike because that the critically-stressed orientation of a fault is controlled by the angle azimuth – (strike – 180°) (Figure 4.2, Section 4.2.2), and thus analyzing one of them is enough. For these six parameters, we vary their value 10% above and below relative to the one of the base fault plane in each of the two slip patterns.

Last, we carry out the Monte Carlo simulations (Section 4.2.7) to address the uncertainty problem of geological setting and to statistically assess the probability of inducing a specific magnitude of an earthquake for the two slip patterns. We apply the pressurized regions evaluated in Section 4.3.2. We take the sex geological properties that are included in the third step as the stochastic variables. We assume all the stochastic variables follow a normal distribution, the related characteristic values are shown in Table 4.5. In particular, the uncertainty of the in-situ stress is 5% above and below each estimate. The dip angle ranges from the one of FP5 to FP3 for the RS-S pattern, and ranges from the one of FP8 to FP7 for the SS-R pattern. The upper limit of Biot's coefficient is 0.8, as adopted in Chang et al. (2020). Existing experiments on granite find that Biot's coefficient decreases with increasing the Terzaghi effective stress (Makhnenko and Labuz, 2016), and several cases that are close to 0.5 have been reported (Bernabe, 1986; Detournay and Cheng, 1993). Thus, we adopt 0.5 as its lower limit given the high in-situ stress. We take the test value of the static friction coefficient as its mean value and 10% above and below the mean value for its uncertainty. Both slip patterns have the same limits for the variables α and f_{st}. With the minimum and maximum of these variables, we solve the mean value as (maximum + minimum)/2 and derive the standard derivation (STD) as (maximum – mean)/3 at 99.74% of confidence.

After the Monte Carlo simulations, we calculate the earthquake magnitude (Section 4.2.6) based on the value of S_{max} for all the realizations and then statistically analyze the probability distribution of the moment magnitude M_w.

Table 4.5: Stochastic variables and their characteristic values for the reverse-slip-dominated pattern with a strike-slip component (RS-S pattern) and for the strike-slip-dominated pattern with a reverse component (SS-R pattern). Both slip patterns adopt the same values for Biot's coefficient and static friction coefficient. The different values for the SS-R pattern are filled in the parentheses.

Parameter	Physical meaning	Minimum	Maximum	Mean	STD	Unit
σ_H	The maximum horizontal principal stress	230.85 (192.85)	255.15 (213.15)	243 (203)	4.05 (3.4)	MPa
σ_h	The minimum horizontal principal stress	114 (88.35)	126 (97.65)	120 (93)	2.0 (1.55)	MPa
Azimuth	Azimuth of σ_H	N73.15 (N70.3)	N80.85 (N77.7)	N77 (N74)	1.28 (1.23)	°
θ	Fault dip	43 (66)	58 (75)	50.5 (70.5)	2.5 (1.5)	°
α	Biot's coefficient	0.5	0.8	0.65	0.05	-
f_{st}	Static friction coefficient	0.45	0.55	0.5	0.017	-

4.3 Results

4.3.1 Likelihood of existing in-situ stress estimates and its effect on fault geometry

Stability analysis of preexisting faults at the initial state can quantify the likelihood of in-situ stress estimates. Such analysis for each of the potential in-situ stress states (Table 4.2) for the Pohang EGS site shows that all the likely estimates of fault plane are much more critically oriented in the stress states IS1 and IS2 than in IS3, IS4 and IS5 with the reference value of 0.5 for the static friction coefficient f_{st}, and 0.79 for Biot's coefficient α, but are much less critical than in IS6 (Figures 4.2A to 4.2F). $f_{st} \geq 0.78$ is necessary for initial stability in IS6 under the reference value of α, and even $\alpha = 0$ cannot reach initial stability under the reference value of f_{st} (Figure 4.2F), which implies that IS6 is a highly unlikely stress state. Assuming that the crust is generally in a state of incipient frictional failure (Townend and Zoback, 2000; Zoback, 2010; Zoback and Gorelick, 2012), especially stiff crystalline rock (Vilarrasa and Carrera, 2015), i.e., in a critically stressed state, the initial stress state should be close to failure conditions for the most critically-oriented plane. However, even for $\alpha = 1$, IS3, IS4 and IS5 are not critically stressed for the reference value of f_{st}. Although f_{st} ~0.4 (i.e., decreasing ~20% the reference value) could lead the crust to be critically stressed with the reference value of α, only one likely estimate (FP5) of fault plane is critically oriented in IS3 and IS5, and no one is critically oriented in IS4 (Figures 4.2C to 4.2E). These two inconsistencies make IS3, IS4 and IS5 not feasible estimates of the stress state. For the cases of IS1 and IS2, while some of the likely fault planes exceed the critical state under the reference values, varying either ~10% above the reference value of f_{st} or ~30% below the reference value of α can make the crust and all the likely estimates of fault plane being both initially stable and critically (or near critically) stressed (Figures 4.2A to 4.2B). We conclude from the previous analyses that the IS1 and IS2 are the two most likely in-situ stress states and, thus, will be applied in the following risk assessment.

Faulting regime also significantly affects the geometrical properties of faults. Faults are prone to slip with a low dip angle in a reverse faulting regime (e.g., IS1), and with a high dip angle in a strike-slip faulting regime (e.g., IS2, Figures 4.2G and 4.2H, Jaeger et al., 2007; Zoback, 2010; Vilarrasa et al., 2013). This theoretical results explain why the likely estimates FP1, FP3 and FP5 are more critical than FP7 and FP8 in the stress state IS1 (Figure 4.2A), while it becomes the opposite in IS2 (Figure 4.2B). The inclined fault with a low dip angle ($\leq(\pi/2\text{-atan } f_{st})/2 = 32°$ for $f_{st} = 0.5$) in the reverse regime is in the most critical orientation when the fault strike is perpendicular to the maximum horizontal principal stress direction (i.e., azimuth), and the most critical fault dip decreases with increasing f_{st} (Figure 4.2G). Vertical dipping faults are the most critical ones in a strike-slip regime, with the most critically-oriented direction when the angle azimuth $-$ (strike $-$ 180°) equals ($\pi/2$-atan f_{st})/2, i.e., 32° for $f_{st} = 0.5$. The angle increases not only with decreasing f_{st}, but also with decreasing the fault dip (Figure 4.2H). Comparing Figures 4.2G and 4.2H shows that the most critical dipping

angle of the most critically-oriented reverse faults and the most critical orientation of the vertical dipping strike-slip faults present the same correlation with the static friction coefficient, which is (π/2-atan f_{st})/2.

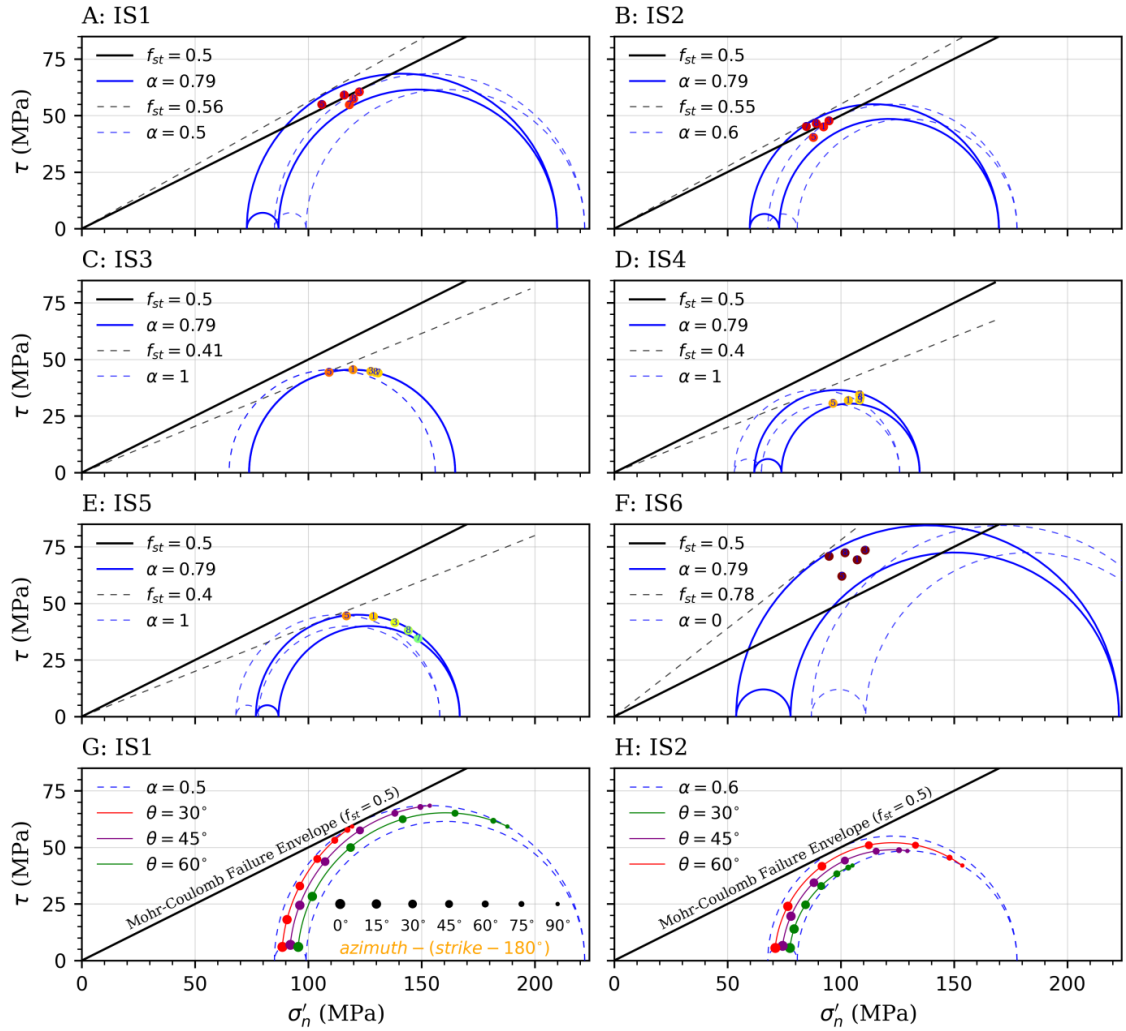

Figure 4.2: Mohr-Coulomb diagram calculated with the in-situ stress states (A) IS1, (B) IS2, (C) IS3, (D) IS4, (E) IS5, (F) IS6, (G) the reverse faulting regime (IS1) and (H) the strike-slip faulting regime (IS2). The black solid and dashed lines are the Mohr-Coulomb failure envelopes under different values, as shown in the legends, of the static friction coefficient f_{st}. The blue solid and dashed half circles represent the Mohr circles with different values of Biot's coefficient α. The solid lines and half circles represent the cases with the reference value (Section 4.2.8) of f_{st} and α. The other values of both f_{st} and α are derived by making the crust just being in the critical stressed state with changing either f_{st} or α for each of the in-situ stress states, in which changing α may not form a critical state and thus, the case with its maximum or minimum is presented. The colored dots with numbers denote the five potential fault planes (Section 4.2.1), which are plotted based on the solved shear and effective normal stress components (Section 4.2.4) and colored based on the initial Coulomb failure stress (Section 4.2.5). The curves with seven size-scaled points in (G) and (H) are the trajectory of three planes with the dip angle of 30 º, 45 ºand 60 ºvarying the orientation from perpendicular to parallel with respect to the maximum horizontal stress direction (azimuth). The size of points is plotted based on the angle azimuth – (strike – 180°), as shown in (G).

4.3.2 Fault stability at the instant of the mainshock

With the adopted injection information (Table 4.3) and hydraulic parameters (Table 4.4), an aquifer thickness of ~750 m makes a relatively well estimate of the temporal pore pressure evolution at the bottom hole compared with the recorded data (Figure 4.3). The radial distributions of pore pressure changes at the instant of the mainshock for both RS-S and SS-R patterns follow an identical spatial trace (Figure 4.4) because the blocking effect of the transversely low permeability of the fault has been cancelled out by its longitudinally high permeability, as assumed (Section 4.2.3). Although the pressurized region evaluated with Theis's solution extends infinite in radial direction, we propose a new estimate, i.e., the one that corresponds to the situation that the mean pore pressure change reaches a stationary point, for the radius of influence (R_{max}). As a consequence, R_{max} is ~586 m in this scenario and the pore pressure change at such location is ~0.01 MPa. Summing L_D and R_{max} gives the length of the pressurized region, which is ~980 m for the RS-S pattern and ~755 m for the SS-R pattern. It means a pressurized region that expands isotropically from source point, agreeing with existing numerical simulations (KGC, 2019; Yeo et al., 2020; Wassing et al., 2021). The related mean pore pressure change (Δp_m) of the pressurized region is 1.85 MPa for the former and 1.97 MPa for the latter (Figure 4.4). The pore pressure change on the fault (Δp_{FP}) for the RS-S and SS-R patterns are 0.06 MPa and 0.7 MPa, respectively, being consistent with the numerical solutions of Ellsworth et al. (2019), Lim et al. (2020), Yeo et al. (2020) and Wassing et al. (2021). The pressure changes near the bottom hole are also similar to the ones of Wassing et al. (2021). Thus, the hydraulic results (Figure 4.4) could be reasonable and available for the following mechanical assessment.

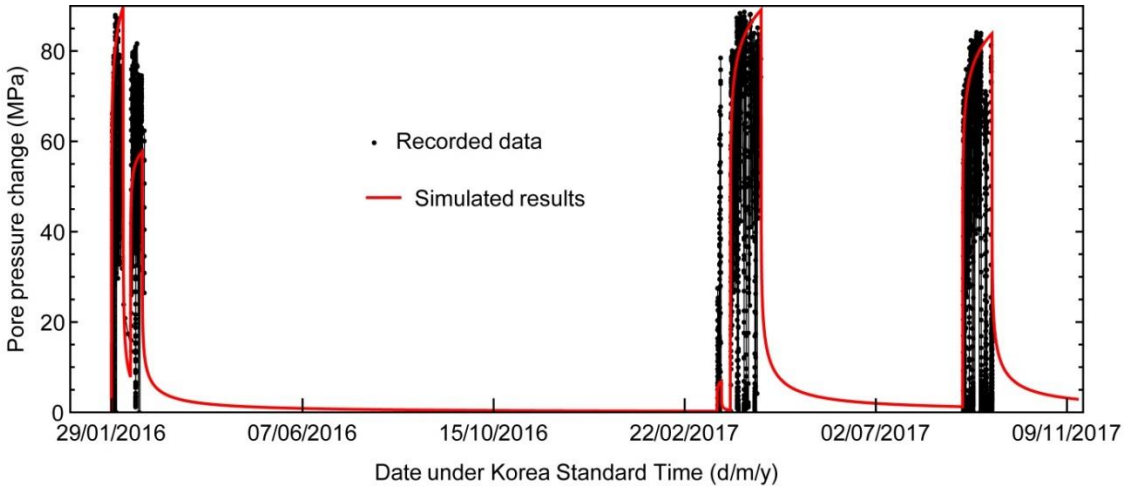

Figure 4.3: Comparison between the simulated temporal pore pressure evolution at the bottom hole of PX-2 and the recorded injection pressure from the beginning of the first hydraulic stimulation to the instance of the mainshock. The recorded data is referred from Yeo et al. (2020)

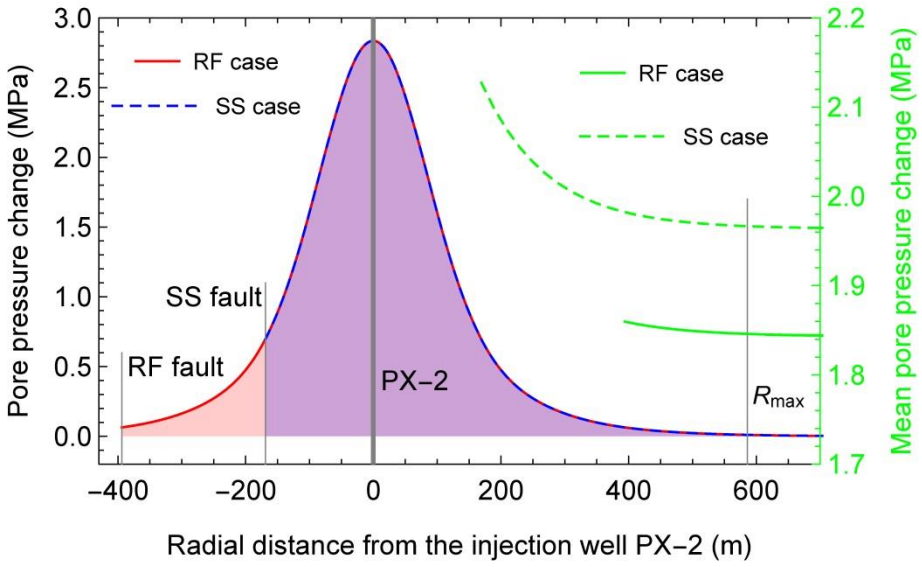

Figure 4.4: Spatial distributions of pore pressure changes at the instant of the mainshock for both RS-S and SS-R patterns. The mean pore pressure change of the pressurized region as a function of the radius of influence is also included. The distance between the fault and the injection well PX-2 is 394 m for the RS-S pattern and 169 m for the SS-R pattern as the fault dip is 50.5° in the RS-S pattern and 70.5° in the SS-R pattern.

We then analytically evaluate the poroelastic stress (Section 4.2.4, Figure 4.5) along the base fault for both slip patterns with the mean overpressure of the pressurized region, and assess the fault stability change (Section 4.2.5, Figure 4.6) with the overpressure on the fault. Two smaller values of Biot's coefficient α than its reference value are adopted here to reach initial stability. Values of the initial Coulomb Failure Stress (CFS^0) show that the fault of the SS-R pattern is closer to instability than the one of the RS-S pattern at the initial state regardless of α. The Coulomb Failure Stress Change (ΔCFS) along the fault plane shows a similar destabilized fault patch for the two base faults: the patch is centered at the bottom cross-point (P2 in Figure 4.1C) between the fault and the pressurized region, and extends along both below and above directions. The center of this destabilized fault patch, i.e., the most critical point close to instability, locates at a depth of 4.65 km, being consistent with the hypocenter of the mainshock (Kim et al., 2018). We compute a larger increase of ΔCFS toward instability for the fault of the RS-S pattern than the one of the SS-R pattern, which means that the RS-S pattern is more sensitive to the pore pressure perturbation than the SS-R pattern despite the overpressure on the fault being one order of magnitude larger in the latter than in the former. The difference is a consequence of fault dip, since the induced shear stress on the fault plane decreases and the corresponding normal stress increases proportionally to the dip angle (Figure 4.5).

ΔCFS is almost the same in Figures 4.6A and 4.6B because the difference of the two adopted values of α is only ~3%, whereas the differences in CFS^0 have reached 24% and 88% for the RS-S and SS-R patterns, respectively. The dramatic distinction between the initial pore pressure and the overpressure results in the different effect of α

on CFS^0 and ΔCFS. Adding CFS^0 to ΔCFS obtains the final state of the fault at the instant of the mainshock. For the scenario of $\alpha = 0.65$ (Figure 4.6A), the fault of both slip patterns is stable because the initial state is far away from failure conditions. For the scenario of $\alpha = 0.67$ (Figure 4.6B), the fault of the SS-R pattern is in failure, while the one of the RS-S pattern remains stable. We can further calculate the slipping fault patch size and the magnitude of corresponding earthquake, implying that the applied methods and workflow is valid to explain the Pohang earthquake.

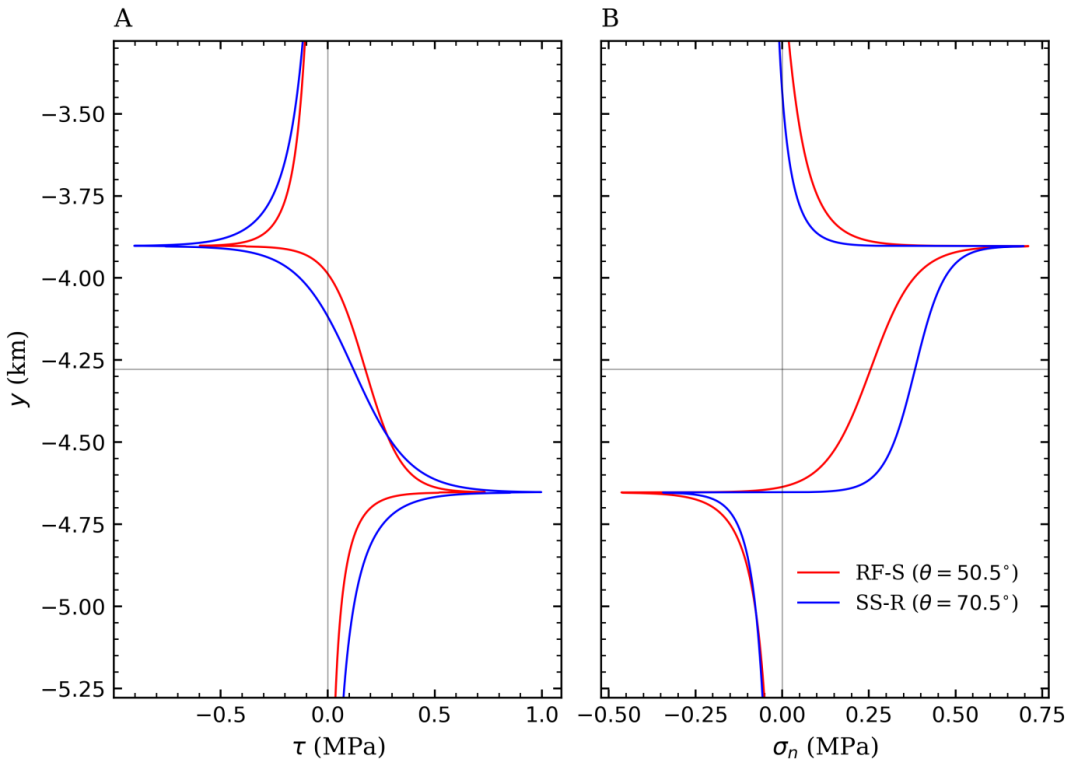

Figure 4.5: Induced (A) shear and (B) normal stress components along the base fault plane for both RF-S and SS-R patterns. The fault dip for each pattern is included in the legend, which is shown in (B). The depth of injection center is indicated by the horizontal gray line as a background.

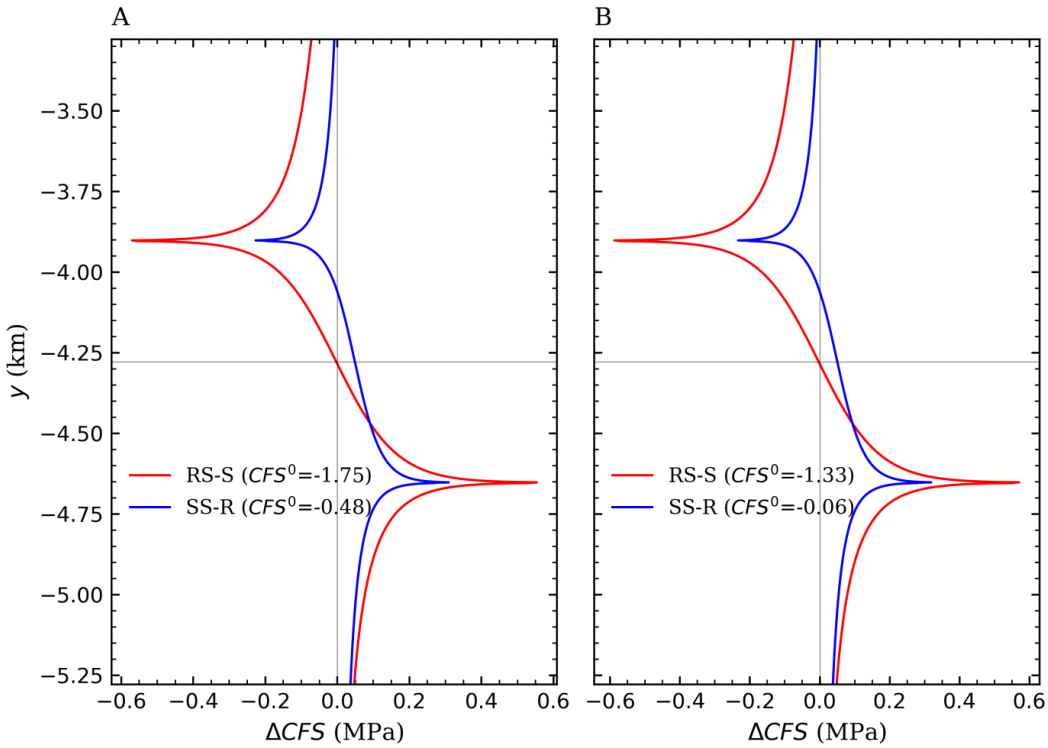

Figure 4.6: Coulomb Failure Stress Change (Δ*CFS*) of the base fault for both the RS-S and SS-R patterns with (A) $\alpha = 0.65$ and (B) $\alpha = 0.67$. The initial *CFS* (CFS^0) for each pattern is included in the legend. Fault dip is 50.5° in the RS-S pattern and 70.5° in the SS-R pattern. The depth of injection center is indicated by the horizontal gray line as a background.

4.3.3 Effect of geological properties on induced seismicity potential

We adopt the size of the pressurized region evaluated in Section 4.3.2 but increase the pore pressure changes to fivefold the original ones, aiming at clearly displaying the global effect of these parameters on fault slip. We take 0.65 as the base value of α for its parametric space analysis with considering the results shown in Figure 4.6. The base scenario, that is applying the base value for all the uncertain geological properties, leads to a fault patch centered at the cross-point P2 being unstable for both patterns. Thus, increasing or decreasing each of the uncertain parameters indicates either an increase or a decrease of the slipping fault patch size. For the RS-S pattern, CFS^0 and the maximum slipping fault patch size (S_{max}) are proportional to α, the maximum horizontal principal stress (σ_H), are inversely proportional to f_{st}, the minimum horizontal principal stress (σ_h) and the fault dip θ, and increase firstly and then decrease with increasing the azimuth of σ_H (Figures 4.7A and 4.7B). The steeper the line, the larger the effect, which means that the relative importance of the effect of these parameters on CFS^0 and S_{max} is $\sigma_H > f_{st} > \sigma_h > \alpha >$ azimuth/$\theta >$ θ/azimuth. The relative importance of the azimuth and θ depends on the relative state of fault dipping and fault orientation (Figures 4.2G and 4.2H).

All the parameters present a similar effect on CFS^0 and S_{max} in the SS-R pattern except

for the fault dip, which is opposite (Figures 4.7C and 4.7D). Such difference is a consequence of the different most critical dipping angle between the reverse and the strike-slip faults (Figures 4.2G and 4.2H). Similarly, the relative importance of the effect of these parameters on CFS^0 and S_{max} in the SS-R pattern is $\sigma_h > \sigma_H > f_{st} > \alpha >$ azimuth/$\theta >$ θ/azimuth. σ_h is the intermediate principal stress in the RS-S pattern, while it is the least principal stress in the SS-R pattern, which results in the different relative importance between σ_h and σ_H because the intermediate principal stress generally has a smaller effect on fault stability compared with the greatest and the least principal stress components (Jaeger et al., 2007; Zoback, 2010).

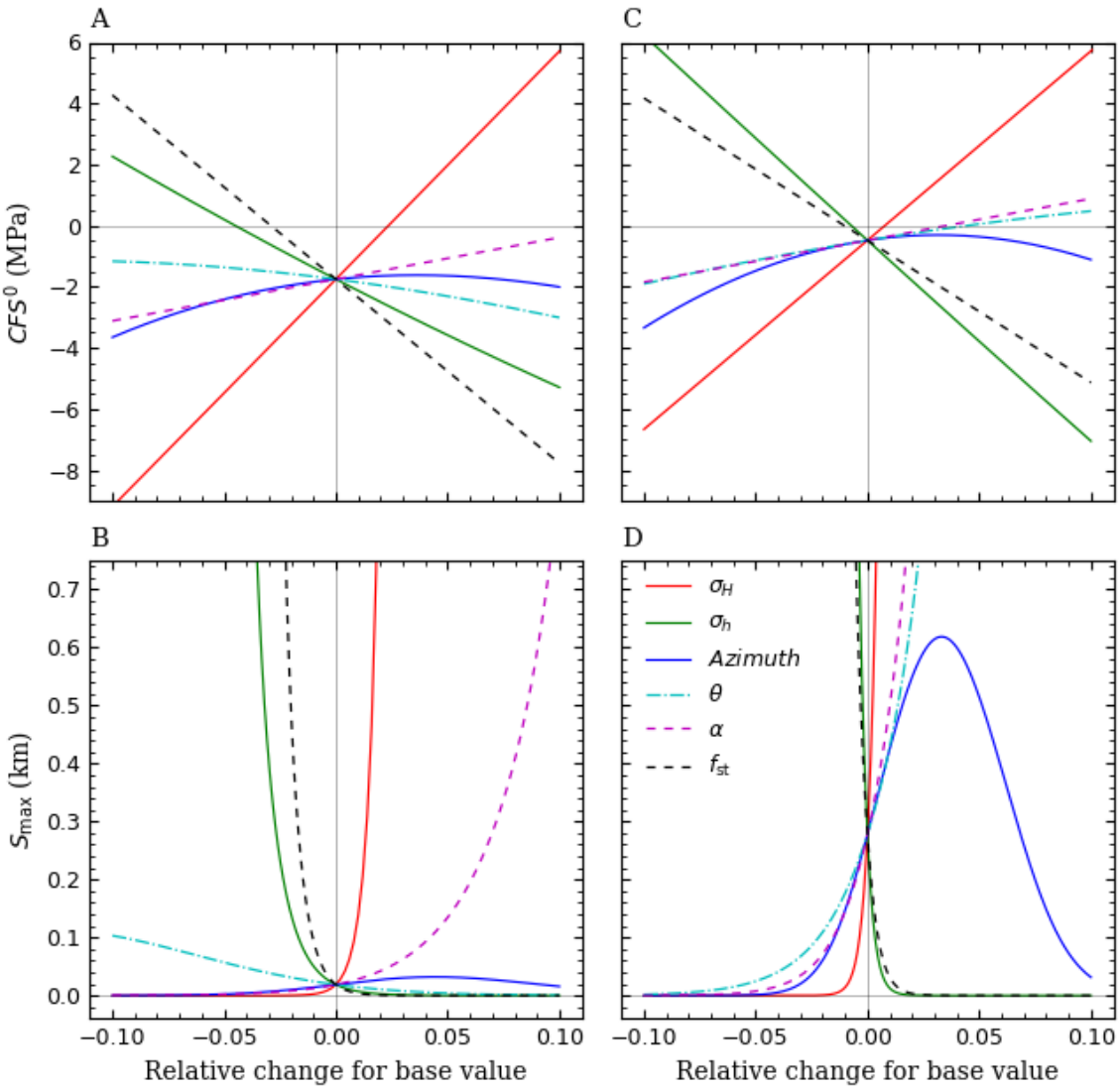

Figure 4.7: (A) the initial CFS (CFS^0) and (B) the maximum slipping fault patch size (S_{max}) of the base fault in the RS-S pattern, (C) CFS^0 and (D) S_{max} of the base fault in the SS-R pattern, as a function of the relative change for the base value of the in-situ stress state (σ_H, σ_h, azimuth), fault dip (θ) and rock properties (α, f_{st}). The base value of α is 0.65 in this simulation. The intersecting point of all the curves in each of the slip patterns corresponds to the result of the base fault with the given base value for all the geological properties.

A typical S_{max} curve in Figure 4.7B and 7D, like the one of σ_H can be divided into two

segments based on its changing rate (slow or sharp), which correspond to the initiation stage of fault slip around the cross-point P2 and its subsequent asymptotic failure stage, respectively (Figure 4.6, Wu et al., 2021a). Comparison between the RS-S and SS-R patterns also shows that a more critical fault at the initial state is more sensitive with changing the geological properties than a less critical fault, because the asymptotic failure is easier to be induced in the former than in the latter. In conclusion, the magnitude of in-situ stress and the static friction coefficient are playing a more significant role in inducing a seismic event than Biot's coefficient and the fault geometry.

4.3.4 Probability distribution considering the uncertainty of geological properties

We now analyze the final state of the fault under various geological settings (Section 4.2.8) for both slip patterns. We restrict CFS^0 in the range of -0.61 MPa to -0.05 MPa for the RS-S pattern and of -0.27 MPa to -0.05 MPa for the SS-R pattern during the Monte Carlo simulations (Figure 4.8) to limit the magnitude of induced seismicity in a range that agrees with the recorded seismic events (Kim et al., 2018; Yeo et al., 2020) in Pohang. In particular, the lower limits of CFS^0 corresponds to the earthquake size of M_w-1, and the upper limits restricts the earthquake size is less than M_w6.0 (Figure 4.11). The Monte Carlo simulations converge after ~25000 realizations (Figure 4.9). For each of the simulations, the randomly generated values of all the stochastic variables still follow the normal distribution (Figure 4.10) although we redraw the samples when the value of CFS^0 falls out the restricted range, confirming the reliability of the simulated results.

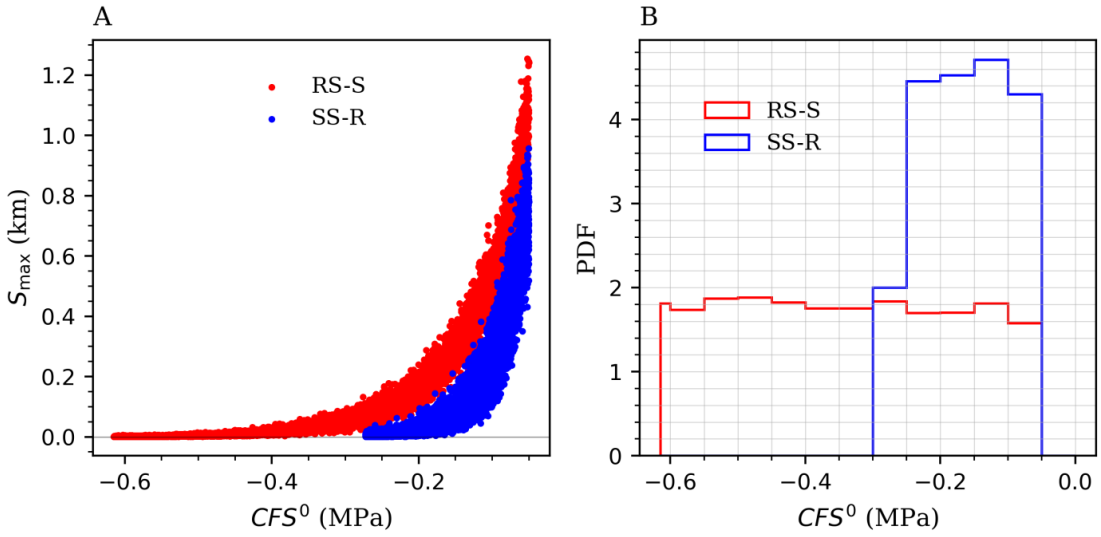

Figure 4.8: (A) The maximum slipping fault patch size (S_{max}) as a function of the initial *CFS* (CFS^0) and (B) probability density function (PDF) of CFS^0 for both RF-S and SS-R patterns

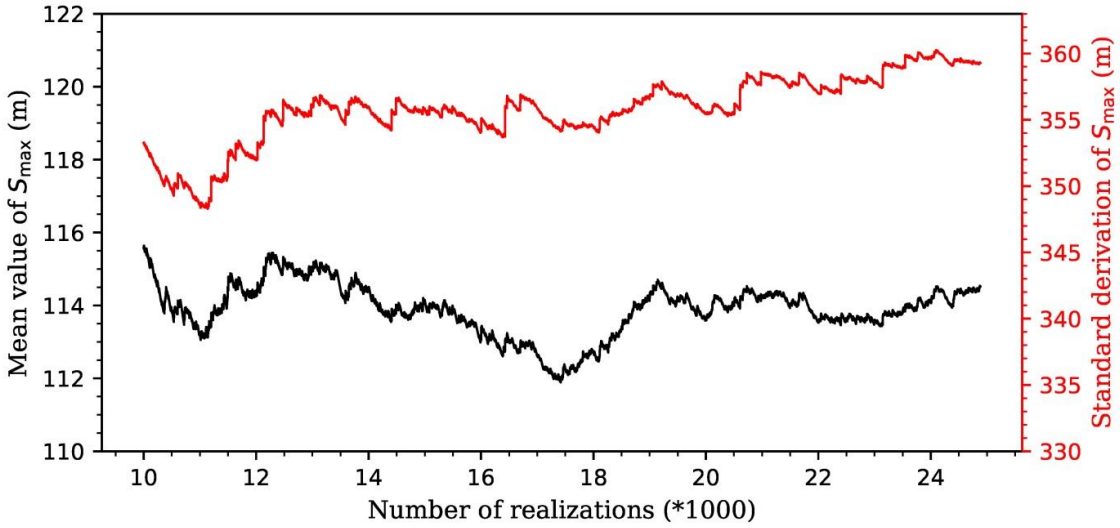

Figure 4.9: Mean and standard derivation of S_{max} against the number of realizations for the reverse-slip-dominated pattern with a strike-slip component (RS-S pattern)

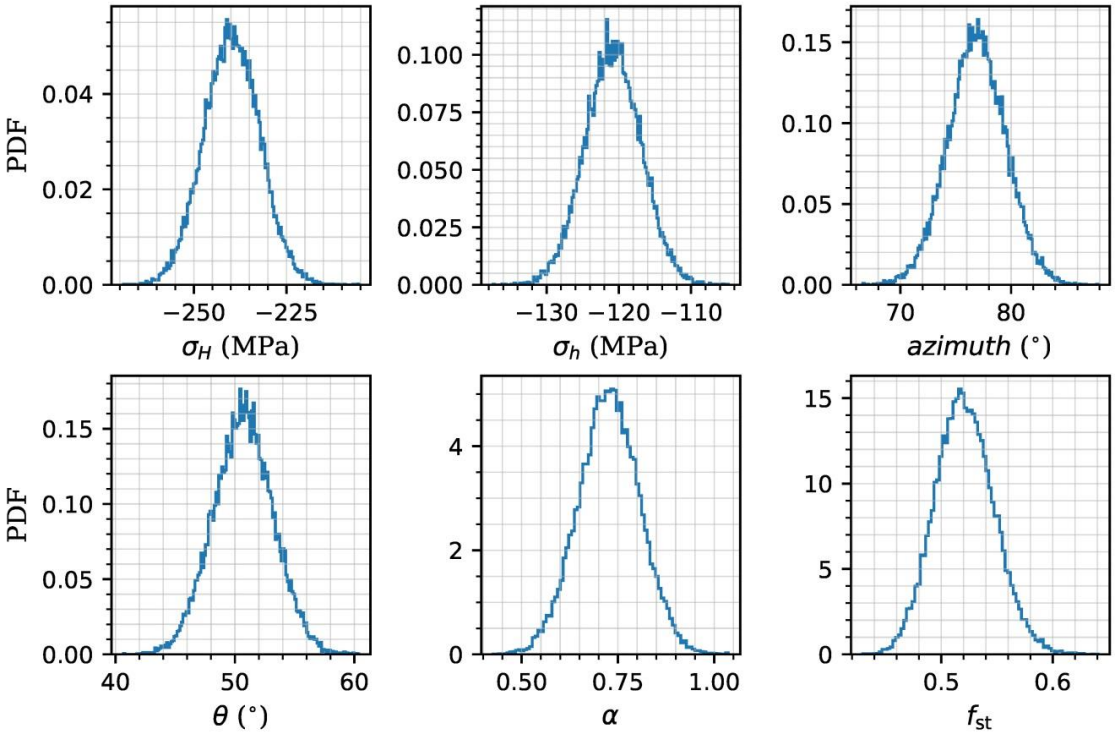

Figure 4.10: Probability density function (PDF) of all these stochastic variables after Monte Carlo simulation for the reverse-slip-dominated pattern with a strike-slip component (RS-S pattern). The thickness of pressurized region is 755 m.

We then present the probability distribution for the results of Monte Carlo simulations (Figure 4.11). In general, the complementary cumulative distribution function (CCDF) of the earthquake magnitude for the RS-S pattern is very similar to that for the SS-R pattern as we apply different ranges of CFS^0 to limit the simulated earthquake magnitude agree with the recorded events. Some small differences still can be observed. Simulated seismicity mainly falls in the center range of $2.0 < M_w < 5.5$ in the SS-R pattern, while the distribution of seismicity in the RS-S pattern is more dispersed

(Figure 4.11A). As a result, the probability of inducing an earthquake with $M_w < 5.0$ is a little larger in the SS-R pattern than in the RS-S pattern, while it becomes opposite for inducing a $M_w > 5.5$ earthquake (Figure 4.11B). For example, the probability of inducing a $M_w > 3.0$ earthquake and a $M_w > 5.5$ earthquake is ~49% and ~6.4% for the RS-S pattern, respectively, and ~59% and ~4.7% for the SS-R pattern, respectively. The probability density for $M_w < 2.0$ is always lager in the RS-S pattern than in the SS-R pattern. The majority of recorded seismicity in Pohang is smaller than M_w2.0 (Kim et al., 2018; Yeo et al., 2020), which means that the RS-S pattern may be more consistent with the magnitude-frequency relationship of earthquakes occurred in Pohang.

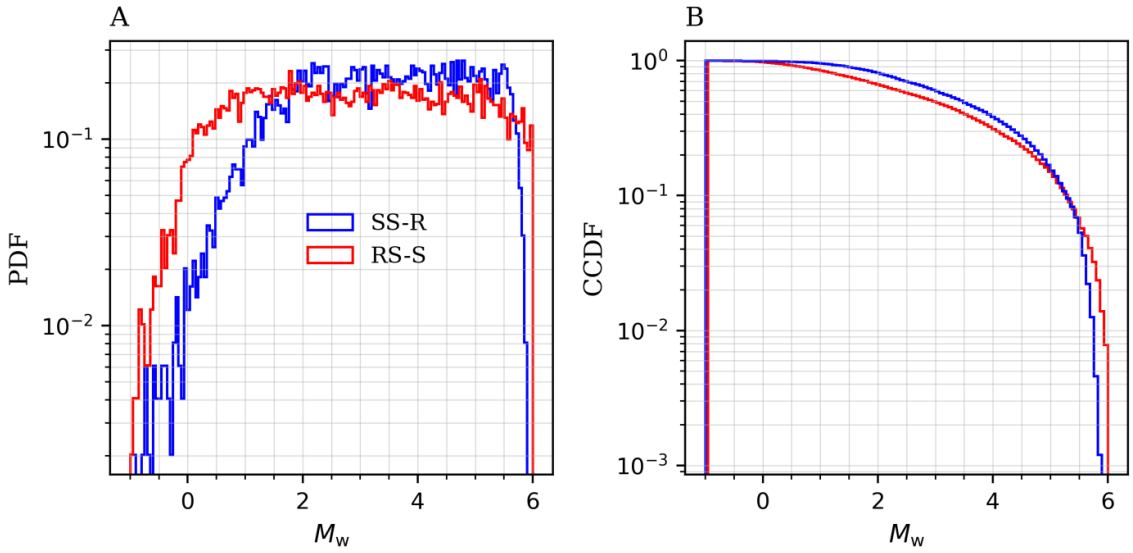

Figure 4.11: (A) Probability density function (PDF) and (B) complementary cumulative distribution function (CCDF) of the moment magnitude (M_w) of induced seismicity for both RS-S and SS-R patterns

Once the poromechanical perturbation cause the fault to slide, the quasi-static fault slip develops with different characteristics under different rock properties, initial stress, and loading conditions. The slip regime map (Azad et al., 2017; Ciardo and Lecampion, 2019; Garagash and Germanovich, 2012) provides a useful approach to qualitatively judge whether the slip is stable or not and how the slip evolves in a certain condition. For each of the Monte Carlo simulations, we have a great number of realizations and each realization represents a different initial condition. Thus, we put all of these realizations into the slip regime map with respect to the normalized understress $(\tau_p - \tau^0)/\tau_p$ and effective overpressure $\alpha\Delta p/\sigma_n'^0$ to see which initial conditions are in favor of the fault slip, where $\tau_p = f_{st}\sigma_n'^0$ denotes the peak strength of the fault, and Biot's coefficient is included relative to the initial map shown in Garagash and Germanovich (2012).

All of these realizations for both slip patterns locate at the left-bottom corner of the slip regime map (Figure 4.12). For the RS-S pattern, a part of realizations belong to the limiting case of critically stressed fault (Garagash and Germanovich, 2012), which lead

to damaging earthquakes; another part of realizations belong to the limiting case of marginally pressurized fault (Garagash and Germanovich, 2012), which result in microseismicity (Figure 4.12A). In contrast, for the SS-R pattern, there are a part of realizations that are belong to the limiting case of critically stressed fault, while no realization corresponds to the limiting case of marginally pressurized fault (Figure 4.12B). The distribution of realizations in the slip regime map colored by CFS^0 also presents the similar characteristics to that of the previous one colored by M_w (Figure 4.13). Such consistency between the two distributions indicates a clear threshold of CFS^0 to judge if the fault is critically stressed under initial conditions. This threshold is about -0.1 MPa for the Pohang EGS site. For such critically stressed fault with a value of $CFS^0 > -0.1$, a small pore pressure perturbation can induce a damaging earthquake.

In addition, Figure 4.12 also shows that the earthquake magnitude associated with a critically stressed fault is mainly controlled by the normalized understress, while it is independent of the normalized effective overpressure. This implies that site selection is more important than injection management: we should devote more efforts to find suitable sites without critically stressed faults to deploy geo-energy projects.

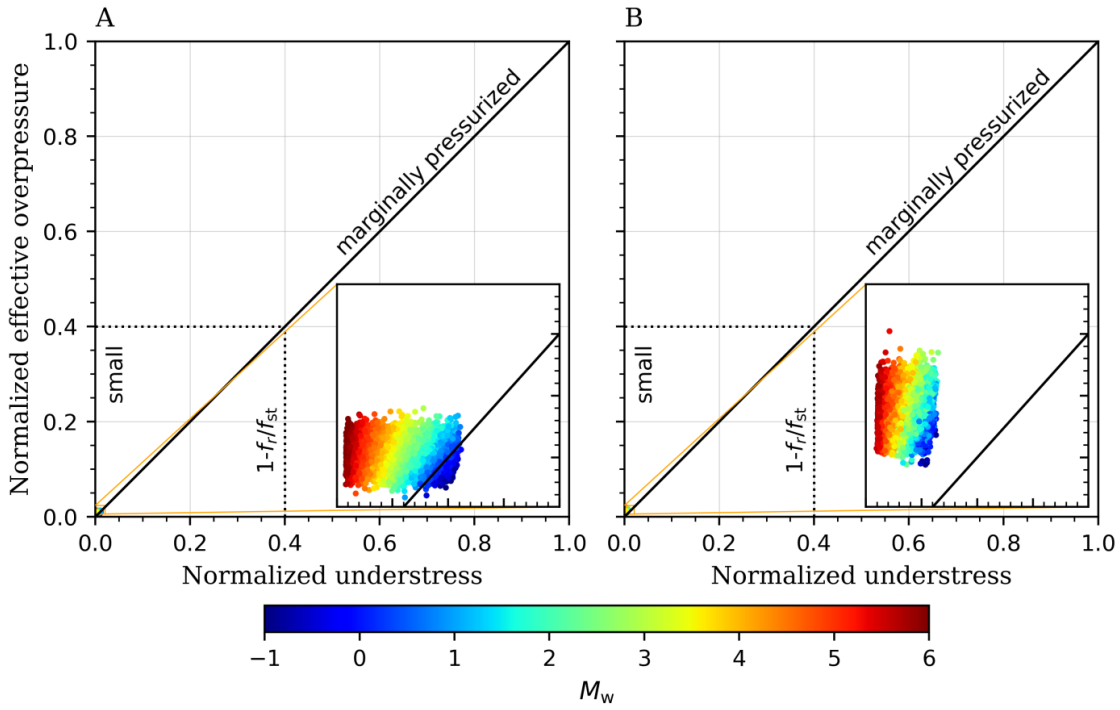

Figure 4.12: Distribution of all the realizations of the Monte Carlo simulation in the slip regime map with respect to the normalized understress and effective overpressure with f_r/f_{st} = 0.6 for (A) the RS-S pattern and (B) the SS-R pattern. One point means one realization, which is located according to its normalized understress and effective overpressure, and colored according to its moment magnitude (M_w). f_r is the residual friction coefficient. The normalized understress and effective overpressure of the zoom in part range from 0 to 0.02 and from 0.006 to 0.024, respectively.

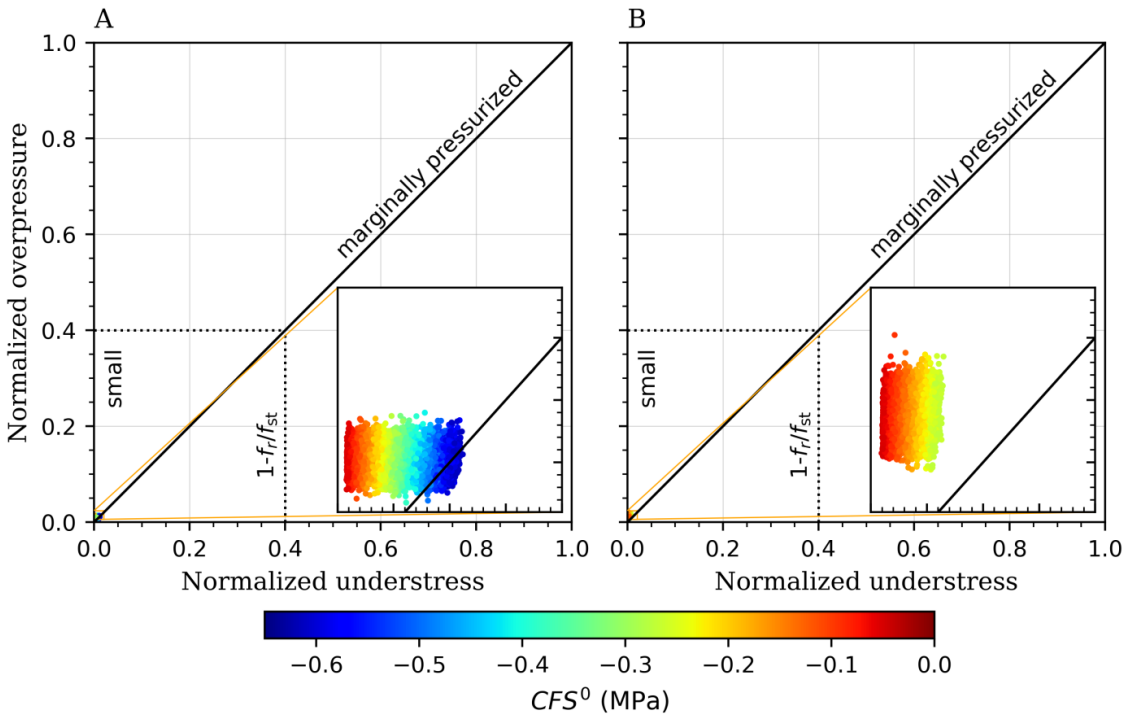

Figure 4.13: Distribution of all the realizations of the Monte Carlo simulation in the slip regime map with respect to the normalized understress and effective overpressure with f_r/f_{st} = 0.6 for (A) the RF-S pattern and (B) the SS-R pattern. One point means one realization, which is located according to its normalized understress and effective overpressure, and colored according to its initial *CFS* (CFS^0). f_r is the residual friction coefficient. The normalized understress and effective overpressure of the zoom in part range from 0 to 0.02 and from 0.006 to 0.024, respectively.

4.4 Discussion

The qualitative fault stability analysis excludes the unlikely and low likely in-situ stress states for the Pohang EGS site, which finds that the most two likely stress states are IS1 and IS2 (Figure 4.2). These two stress states just correspond to the characteristics of the potential estimates of fault plane. Thus, we propose two oblique-slip patterns to simulate the processes and mechanisms of the induced seismic events. The simulated results show us three evidences to conclude that the RS-S pattern is closer to the actual scenario than the SS-R pattern: (1) the RS-S pattern is more prone to slip as a result of poromechanical perturbation than the SS-R pattern despite both the fault being more stable at the initial state and the overpressure on the fault being one order of magnitude larger in the latter than in the former (Figure 4.6); (2) the relatively higher probability density for $M_w < 2.0$ in the RS-S pattern than in the SS-R pattern (Figure 4.11) indicates that the RS-S pattern may matches better with the fact that the majority of recorded seismicity is smaller than M_w2.0 (Ellsworth et al., 2019; Kim et al., 2018; Yeo et al., 2020); and (3) the a little larger of probability for inducing a $M_w > 5.5$ earthquake in the RS-S pattern than in the SS-R pattern (Figure 4.11). In addition, this conclusion is consistent with the indications obtained from the

ground surface deformation (Choi et al., 2019) and the focal mechanism solutions of the aftershocks (Kim et al; 2018; Kim et al., 2020). Thus, the most likely triggering mechanism for the Pohang earthquake is the reactivation (with an oblique slip) of a critically stressed reverse fault with a relatively low dip angle due to the pore pressure buildup in the injection formation and its subsequent poromechanical response. It means that the most likely estimate of in-situ stress and fault plane are IS1 and FP5, respectively.

During Monte Carlo simulations, restricting CFS^0 of all the realizations be lower than -0.05 MPa limits the earthquake magnitude be less than M_w6.0 for both slip patterns (Figures 4.8 and 4.11). It means that the initial state of the fault linked to the largest earthquake is not so critical as assumed in the existing studies (Chang et al., 2020; Ellsworth et al., 2019; KGC, 2019; Lim et al., 2020; Yeo et al., 2020; Wassing et al., 2021), otherwise, earthquakes with $M_w > 7.0$ may have been triggered in Pohang. Our stochastic analysis shows that the initial state of the fault may range from -0.61 MPa to -0.05 Mpa (Figure 4.8), if adopting CFS^0 as a judging index. For such range of CFS^0, the fault could be subcritically to critically stressed. We find a threshold to judge if the fault is critically stressed by analyzing the distribution characteristics of all the realizations in the slip regime map (Garagash and Germanovich, 2012). This threshold is site dependent and is -0.1 MPa (Figures 4.12 and 4.13) for the Pohang EGS site.

The two slip patterns proposed in this work have a small difference in explaining the seismicity. For the RS-S pattern, the main factor that induces microseismicity is the poroelastic effect caused by pore pressure diffusion, while both the overpressure and the poroelastic stress have a similar effect for the SS-R pattern (Figures 4.5, 4.6, 4.11 and 4.13). In contrast, the initially critical state of the stressed fault is the primary factor that induces a damaging earthquake for both slip patterns, while the external stimulation just is a fuse (Figures 4.11 and 4.13). Thus, a small pore pressure perturbation can trigger damaging earthquakes when the preexisting faults are critically stressed at the initial state. These observations also justify the existing consensus (Evans et al., 2012; Juanes et al., 2012; Rutqvist et al., 2016; van der Baan, 2021; Vilarrasa and Carrera, 2015) that fluid-induced seismicity in general is limited to microseismicity and geo-energy projects are unlikely to directly induce damaging earthquakes, which usually belong to the triggered seismicity (McGarr et al., 2002). Thus, the Pohang M_w5.5 earthquake is a typical triggered seismicity, explaining why all the existing scaling laws fail to link the earthquake magnitude to the total injected volume (Galis et al., 2017; McGarr, 2014; Van der Elst et al., 2016; Woo et al., 2019). Pressure management (Rutqvist et al., 2007; Bai et al., 2017) and the cyclic soft stimulation scheme (Zang et al., 2013, Zang et al., 2019; Hofmann et al., 2019; Ji et al., 2021) may not be valid for the triggered seismicity linked to a critically stressed fault at the initial state. Thus, we should devote more efforts in site characterization at the prior stage of geo-energy projects, as also suggested by other related publications (Chang et al., 2020; Chang and Yoon, 2021; Vilarrasa et al., 2022)

We neglect the effect of tensile hydraulic fracturing on the pore pressure and stress changes, while such area should be limited in the range of 100 m away from the well

PX-2 (Lim et al., 2020; Yoo, 2018; Yoo et al., 2021; Wassing et al., 2021) and thus, such effect on the induced seismicity potential also should be limited. We do not consider the effect of nucleation process on the slipping fault patch size, and such effect can increase the final slipping patch size. However, the normalized understress of all the realizations is very small (< 0.012, Figure 4.12), indicating a very short nucleation process and a relatively small slip dislocation (Garagash and Germanovich, 2012). Thus, the contribution of nucleation process on the earthquake magnitude may be limited for the Pohang case. We do not include the Coulomb stress transfer as the history earthquakes almost have no effect on the induced seismicity in Pohang (Grigoli et al., 2018; Ellsworth et al., 2019). It does not matter the credibility of risk assessment before fluid injection. As for the mainshock, the foreshocks may have an effect on its occurrence, in particular, the M_w3.2 seismic event occurred in April 15, 2017, which transferred a Coulomb stress of ~0.13 MPa to the fault (Yeo et al., 2020). It is not a big contribution compared with the poroelastic stress (Figures 4.5 and 4.6) that is evaluated in this work. In any way, the probability of ~6.4% for the mainshock is a conservative estimate.

Analytical solutions provide the opportunity to conveniently perform the parametric space analysis, which shows that the magnitude of in-situ stress and the friction coefficient are playing a more significant role in inducing a seismic event than Biot's coefficient and the fault geometry (Figure 4.7). We take the former as the preliminary variables, and the latter as the secondary variables. With changing the preliminary variables, the state of a fault can be dramatically different. An initially non-critical fault with the given preliminary variables would not become critical regardless of the secondary variables (Figures 4.2 and 4.7). It implies that we can adopt the most critical fault geometry (Figures 4.2G and 4.2H) and Biot's coefficient to do a conservative risk assessment for site selection when there is no much available data.

The Monte Carlo simulations also strongly depend on the closed form solutions. Otherwise, it is almost incredible to perform a poromechanical coupled simulation with simultaneously considering multiple stochastic variables for a great number of realizations (Masoudian et al., 2019; Reyes Canales and Van der Baan, 2021; Zhang et al., 2021). We then can statistically evaluate the probability (risk) of inducing a specific magnitude of earthquake as well as the other statistical values. Thus, we suggest that taking the methodology applied in this work as a routinely option for risk assessment during the whole lifetime of geo-energy projects, as required by KGC (2019) and Lee et al. (2019) to successfully proceed these projects in future. The projects have to be suspended until we can exclude the potential risk, once the evaluating probability of inducing a $M_w > 3.0$ earthquake at any stage reaches a specific threshold. Our work will be useful to improve safety of geo-energy applications.

4.5 Conclusions

The high uncertainty of geological setting at the Pohang EGS site leads to the debate about triggering mechanisms of the Pohang M_w5.5 earthquake. We make a relatively

complete workflow that includes geological setting analysis, poromechanical coupled process modeling, failure criterion, and earthquake magnitude estimate to simulate the triggering processes of the mainshock and to narrow the potential estimates of uncertain geological properties for this site.

We do a comparative analysis for the existing estimates of in-situ stress based on the Mohr-Coulomb criterion, finding two likely oblique-slip patterns that can be used to analyze the triggering mechanisms: a reverse-slip-dominated pattern with a strike-slip component (RS-S pattern) and a strike-slip-dominated pattern with a reverse component (SS-R pattern). We then perform both deterministic and stochastic poromechanical analyses, relevant results present three evidences that support the RS-S pattern rather than the SS-R pattern. It implies that the pore pressure buildup in the injection formation and the subsequent poromechanical response reactivate the critically stressed reverse fault with a low dip angle (relative to the other estimates for fault geometry), triggering the mainshock. Our stochastic analysis also reveals a clear threshold of the initial *CFS* to judge if the fault is critically stressed or not. This threshold is site dependent and is -0.1 MPa for the Pohang EGS site.

In addition, results also highlight that (1) the magnitude of in-situ stress and the friction coefficient play a more significant role on fault stability and induced seismicity potential than Biot's coefficient and fault geometry; (2) a small overpressure can trigger a damaging earthquake when preexisting faults are critically stressed at the initial state; and (3) we should devote more efforts to site characterization at the prior stage of projects.

5 Poroelastic effects on the nucleation process of dynamic fault rupture during fluid injection

5.1 Introduction

Induced seismicity is a complex and limiting factor in many geo-energy applications (Foulger et al., 2018; Kivi et al., 2023): as we speak, our ability to anticipate damaging events is limited to non-existent. Understanding the triggering processes and mechanisms, which form the basis of reliable forecasting tools for managing induced earthquakes, is one of the most critical challenges in the geo-energy community (Ellsworth et al., 2016; Keranen and Weingarten, 2018; Rathnaweera et al., 2020; Schultz et al., 2020; Ge and Saar, 2022). Injecting fluid into geological formations is usually carried out in geo-energy harvesting, with the potential to cause thermo-hydro-mechanical perturbations in the subsurface (De Simone et al., 2017; Vilarrasa et al., 2019; Rathnaweera et al., 2020). Such perturbations may lead pre-existing faults to slip (reactivation), and, if the nucleation process grows further with an increase in slip rate, the slip may transit to a dynamic rupture (wave propagation) and manifest as a (micro-)seismic shock (Ripperger et al., 2007; Galis et al., 2017; Buijze et al., 2019).

The potential mechanisms leading to fault reactivation during and after fluid injection have been extensively studied under quasi-static conditions, while the dynamic processes have often been overlooked (Healy et al., 1968; Simpson et al., 1988; Langenbruch and Zoback, 2016; Rohmer et al., 2016; Kang et al., 2019; Rathnaweera et al., 2020, and references therein). These analyses mainly focus on the assessment of fault stability usually evaluated by means of Coulomb Failure Stress (*CFS*; King et al., 1994), slip tendency (Morris et al., 1996; Lisle and Srivastava, 2004), mobilized friction coefficient (Kokusho et al., 2009) or angle (Vilarrasa et al., 2016), and shear capacity utilization (Buijze et al., 2017), all of which are minor variations of the Mohr-Coulomb failure criterion. Results have highlighted the conditions that govern fault stability (Fan et al., 2016; Vilarrasa et al., 2016; Buijze et al., 2017; Jansen et al., 2019), its triggering mechanisms (Chang and Segall, 2016; Grigoli et al., 2018; Chang et al., 2020; Vilarrasa et al., 2021), and the size of the unstable fault patch (Chang et al., 2020; Wu et al., 2021a). The quasi-static Mohr-Coulomb based methods fail to describe crack growth as they do not consider the slip-weakening process (Rice and Ruina, 1983; Rice et al., 2005). As a consequence, the unstable fault patch size evaluated by these methods can only be regarded as a lower limit of the true value, failing to provide indications about the final size of the induced earthquakes.

In contrast, studies including dynamic processes have shed light on several dominating mechanisms that control dynamic fault ruptures, such as (1) the nucleation and arrest of dynamic rupture (Garagash and Germanovich, 2012; Azad et al., 2017), (2) aseismic

slip (Bhattacharya and Viesca, 2019; Eyre et al., 2019; Sáez et al., 2022; Jacquey and Viesca, 2023), (3) thermal pressurization (Viesca and Garagash, 2015), and (4) run-out distance (Garagash and Germanovich, 2012; Garagash, 2021). Following the method of Uenishi and Rice (2003), Garagash and Germanovich (2012) found the conditions for nucleating dynamic rupture and its arrest on a pressurized fault due to fluid injection, and theoretically distinguished the two slip regimes of slip-weakening faults: unstable and ultimately stable sliding, based on the different ultimate states of dynamic fault rupture. Although their work was done under quasi-static conditions, the findings are in agreement with the results of elastodynamic simulations (Gischig, 2015; Piris Casasnovas, 2022). Later extensions have taken into account the opening fractures (Azad et al., 2017) and the effects of dilatancy (Ciardo and Lecampion, 2019) and injection rate ramp-up (Ciardo and Rinaldi, 2022) on the nucleation and arrest of dynamic rupture. The unstable slip regime implies a seismic slip and is followed by an unabated dynamic rupture, and the ultimately stable slip regime indicates an aseismic slip, although a self-arrested seismic event remains possible during the nucleation process (Garagash and Germanovich, 2012). Here the aseismic slip remains a slip-weakening frictional behavior. It differs from the original one used in seismology, which refers to the slip-strengthening behavior (Byerlee and Brace, 1968; Scholz et al., 1969; Cornet, 2016) and thus, implies that no seismicity occurs by itself. We term this slip-weakening aseismic slip as the second-type aseismic slip to avoid confusion. Nonetheless, both types of aseismic slip may trigger an earthquake further away from the unstable fault by stress transfer (Wei et al., 2015; Eyre et al., 2019; Vilarrasa et al., 2021; Sáez et al., 2022) or because the injection-induced aseismic slipping fault patch can grow larger and quicker than the pressurized region (Guglielmi et al., 2015; Galis et al., 2017; Bhattacharya and Viesca, 2019; Cappa et al., 2019). Once the slip transits to the dynamic rupture, thermal pressurization can cause dynamic strength weakening on faults, becoming the leading mechanism controlling high-slip rate earthquakes (Garagash and Germanovich, 2012; Viesca and Garagash, 2015). A long run-out distance can facilitate the dynamic weakening mechanisms (Garagash, 2021). All these previous mechanisms originate from the nucleation process as a result of the fast increase in slip rate. Studies applied on natural earthquakes have shown the impact of the nucleation process on the physics of earthquakes (Ohnaka and Kuwahara, 1990; Ohnaka, 1992; Rubin and Ampuero, 2005; Ampuero and Rubin, 2008) and provided scaling laws linking the final earthquake magnitude with the critical nucleation size (Ellsworth and Beroza, 1995; Ohnaka, 2000; Uenishi and Rice, 2003). Thus, quantifying the nucleation process is helpful to improve the estimates of induced earthquake magnitude, promoting the development of induced seismicity forecasting tools.

The nucleation process characterizes the development of quasi-static crack growth, i.e., the transient evolution from initial fault slip into fully-formed dynamic rupture (Ohnaka and Kuwahara, 1990; Ohnaka, 1992). This process can be simulated by the interfacial slip model of cracks (Bilby and Eshelby, 1968; Rice, 1980; Uenishi and Rice, 2003). Applying such model requires to solve analytically or numerically the singular integral equations (Muskhelishvili, 1953). The analytical method can only

solve the simplest problem of eigenvalues (Uenishi and Rice, 2003), and thus the numerical solution has been applied more frequently thanks to its versatile nature (e.g., Garagash and Germanovich, 2012; Viesca and Garagash, 2015, 2018). Coupling the interfacial slip model with a reservoir modeling tool remains a technical challenge that has not yet been solved because of the high computational cost. Existing studies do not include poroelastic effects on the background stress induced by pore pressure diffusion. Yet, the poromechanical response of geological media to fluid injection is known to be an essential mechanism controlling fault reactivation (Fan et al., 2016; Kang et al., 2019; Rathnaweera et al., 2020; Chang et al., 2020; Vilarrasa et al., 2021; Wu et al., 2021a, and references therein). Poroelasticity is likely to play an important role on the earthquake nucleation process, by causing a heterogeneous stress distribution along the fault.

The goal of this study is to fill this gap by taking into account the stress heterogeneity and analyzing the characteristics of crack growth in different slip regimes by including poroelastic effects in the interfacial slip model of cracks. We couple the interfacial slip model to a hydro-mechanical analytical solution (Wu et al., 2021a) of poroelastic stress and pressure changes during fluid injection. In Section 5.2, we introduce the interfacial slip model of cracks, develop the model to include the poroelastic stress, and present the analytical solution of pore pressure changes and poroelastic stress for the scenario of constant-rate injection into a fault zone. We then normalize the developed model in its dimensionless form and describe the numerical method adopted to solve the singular integral equations. In Section 5.3, we show the results of our simulations and illustrate the role of poroelasticity on the nucleation process and the slip regimes. In Section 5.4, we estimate the moment magnitude of earthquakes for the unstable slip regimes based on the ultimate nucleation length. Section 5.5 includes an extended discussion on the obtained results and their implications for the forecasting of injection-induced seismicity. Finally, we conclude that injecting fluid at low rates into faults with background shear stress above the residual friction only induces microseismicity, while injection into faults with background shear stress below the residual friction results in a long run-out distance that has a potential risk of triggering damaging earthquakes. This finding cannot be revealed when the poroelastic effects are neglected.

5.2 Nucleation process modeling during fluid injection

5.2.1 Interfacial slip model of cracks including poroelastic stress

In the framework of poromechanical analysis, fluid injection at depth leads to pore pressure changes $\Delta p(x,t)$, which alters the initial background stress in the geological formations (Figure 5.1; Chang and Segall, 2016; Wu et al., 2021a). A preexisting fault starts to slowly slide once the hydro-mechanical perturbation causes the fault to break the quasi-static elastic equilibrium condition. The slip results in both a shear stress drop and a frictional strength drop (Rice et al., 2005) along the slipping fault patch due

to slip-weakening mechanism. The former hinders crack growth, while the latter, in turn, promotes sliding. Slip weakening results in a new frictional equilibrium, which may be broken again by the further hydro-mechanical perturbation, and thus, the crack gradually grows before reaching dynamic ruptures (Bilby and Eshelby, 1968; Rice, 1980; Garagash and Germanovich, 2012). That is the essence of the quasi-static crack growth of slip-weakening faults due to fluid injection, which has been simulated by the interfacial slip model of cracks assuming a uniform stress field without considering the injection-induced stress variations (Garagash and Germanovich, 2012). Here, we develop the interfacial slip model, following the line of Garagash and Germanovich (2012), but incorporating the poroelastic stress into the frictional equilibrium equation. To do so, first, we update the shear stress $\tau(x)$ inside the slipping fault patch as the difference between the background shear stress (loading) τ^{b} summed with the tangential poroelastic stress component $\Delta\tau(x,t)$, and the stress drop caused by fault slip $\delta(x)$,

$$\tau(x) = \tau^{\mathrm{b}} + \Delta\tau(x,t) - \frac{\mu^*}{2\pi}\int_{-a}^{a} \frac{d\delta(s)/ds}{x-s} ds\,, \tag{5.1}$$

where $\mu^* = \mu$ for mode III and $\mu^* = \mu/(1-\nu)$ for mode II, μ is the shear modulus, ν is Poisson's ratio, a is the crack (slipping fault patch) half-length, x and t denote the spatial and temporal variables, respectively, and $1/(x\text{-}s)$ is a simple Cauchy-type kernel of singular integral (Erdogan et al, 1973). A symmetrical crack is analyzed in this work.

Second, we add the normal poroelastic stress component $\Delta\sigma(x,t)$ to the fault in evaluating the frictional shear strength $\tau_{\mathrm{s}}(x)$,

$$\tau_{\mathrm{s}}(x) = [f_{\mathrm{p}} - w\delta(x)][\sigma_0' - \alpha\Delta p(x,t) + \Delta\sigma(x,t)], \quad 0 \le \delta(x) < \delta_{\mathrm{w}}\,, \tag{5.2}$$

where α is Biot's coefficient, f_{p} is the static friction coefficient, which linearly decreases with the slip by a rate of w. Hence, $\delta_{\mathrm{w}} = f_{\mathrm{p}}/w$ means the slip-weakening scale. The shear strength reaches its peak value at the initial state, i.e., $\tau_{\mathrm{p}} = f_{\mathrm{p}}\sigma_0'$, where $\sigma_0' = \sigma_0 - \alpha p_0$ denotes the initial effective normal stress and p_0 the initial pore pressure. The simplified linear slip-weakening friction law is applied in this work instead of the laboratory-derived rate-and-state friction (Marone, 1998). This simplification is valid in describing the post-failure strength of granite and carbonate under triaxial compression conditions (Wawersik and Brace, 1971; Wawersik and Fairhurst, 1970; Wong, 1982) and is appropriate in studying the earthquake nucleation process (Uenishi and Rice, 2003; Rubin and Ampuero, 2005; Ampuero and Rubin, 2008; Garagash and Germanovich, 2012). A positive value of pressure change and normal stress implies injection and compression, respectively. The time-dependence of the slip, crack length, and stress drop implicitly depends on the pore pressure changes and poroelastic stress that are expressed explicitly as functions of time.

Since the shear stress at the crack tip is bounded and continuous, the following constraint has to be met along the crack,

$$\int_{-a}^{a} \frac{\tau(x)-\tau^{\mathrm{b}}-\Delta\tau(x,t)}{\sqrt{a^2-x^2}}dx=0\,. \tag{5.3}$$

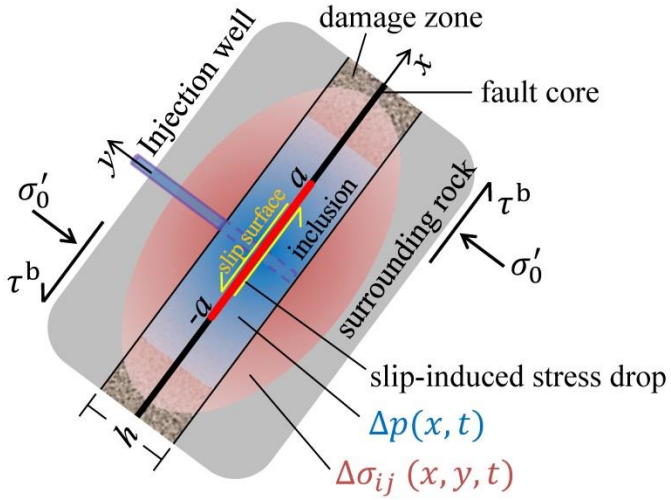

Figure 5.1: Schematic diagram of a slipping fault patch (crack mode II or III) due to fluid injection into the fault zone that consists of fault core and damage zone. Pore fluid/pressure diffuses exclusively within the fault zone. Slip occurs along the fault core. The fault is uniformly loaded at the initial stress state. The crack length may be limited inside or extend to outside the hydro-mechanical perturbation. This diagram only depicts the former case.

Equating Equations (5.1) and (5.2) gives the elastic equilibrium equation including poroelastic stress for modeling the nucleation process,

$$\frac{\tau^{\mathrm{b}}+\Delta\tau(x,t)}{\tau_{\mathrm{p}}}-\frac{\mu^{*}}{2\pi\tau_{\mathrm{p}}}\int_{-a}^{a}\frac{d\delta(s)/ds}{x-s}ds=\left[1-\frac{\delta(x)}{\delta_{\mathrm{w}}}\right]\left[1-\frac{\alpha\Delta p(x,t)-\Delta\sigma(x,t)}{\sigma_0'}\right]. \tag{5.4}$$

The pore pressure changes and poroelastic stress are expressed by a general form, indicating that the equilibrium equation is available for all scenarios of injection. The right hand-side of Equation (5.4) expresses the shear strength variations inside the slipping fault patch, including the factors of overpressure, poroelastic effects, and slip-weakening effects. We divide Equation (5.4) into four cases to compare the role of each factor: case A only considers the factor of overpressure, case B adds poroelastic effects to case A, case C adds slip-weakening effects to case A, and case D (Equation (5.4)) includes all the three factors (see details in Appendix K). We take cases C and D as the main cases of our simulations, aiming at analyzing the role of poroelastic effects on the nucleation process (case D), with case C being the one analyzed in Garagash and Germanovich (2012).

The unlimited slip-weakening law of friction coefficient applied in the previous derivations implies an implicit assumption that the slip is small enough during the nucleation process. This assumption is, in general, difficult to meet in practice.

Residual friction may affect the slip of cracks, and the crack length when the frictional shear strength reduces to its residual limit (Garagash and Germanovich, 2012). For a limited slip-weakening law, the final equilibrium equation for case D changes to

$$\frac{\tau^{\mathrm{b}}+\Delta\tau(x,t)}{\tau_{\mathrm{p}}}-\frac{\mu^{*}}{2\pi\tau_{\mathrm{p}}}\int_{-a}^{a}\frac{\frac{d\delta(s)}{ds}}{x-s}ds=\begin{cases}\left[1-\frac{\delta(x)}{\delta_{\mathrm{w}}}\right]\left[1-\frac{\alpha\Delta p(x,t)-\Delta\sigma(x,t)}{\sigma_0'}\right], & \delta(x)<\delta_{\mathrm{r}}\\ \frac{f_{\mathrm{r}}}{f_{\mathrm{p}}}\left[1-\frac{\alpha\Delta p(x,t)-\Delta\sigma(x,t)}{\sigma_0'}\right], & \delta(x)\geq\delta_{\mathrm{r}}\end{cases}, \quad (5.5)$$

where f_{r} is the residual friction coefficient, and $\delta_{\mathrm{r}}=(1-f_{\mathrm{r}}/f_{\mathrm{p}})\delta_{\mathrm{w}}$ is the slip associated with f_{r}.

5.2.2 Analytical solutions for pore pressure changes and poroelastic stress

We consider the scenario of injection into the fault zone with negligible permeability along the fault thickness direction (*y*-axis in Figure 5.1) at a constant volumetric rate. We apply analytical solutions to specify the general form of pore pressure changes and poroelastic stress shown in Equations (5.4) and (5.5). In this scenario, fluid diffuses axisymmetrically with respect to the injection well in the plane of *x* and out-of-plane direction. Such an axisymmetric pore pressure diffusion can be evaluated by the Theis well solution (Theis, 1935)

$$\Delta p(x,t)=\frac{Q\eta}{4\pi\kappa h}W(\xi^{2}), \quad (5.6)$$

where Q is the volumetric injection rate, h is the fault thickness, κ and η are the intrinsic permeability and fluid viscosity, respectively, and $W(\xi^2)$ is the Theis well function. The spatiotemporal variable is $\xi=x/\sqrt{4D_{\mathrm{h}}t}$ if $x\geq r_{\mathrm{well}}$, and $\xi=r_{\mathrm{well}}/\sqrt{4D_{\mathrm{h}}t}$ if $x<r_{\mathrm{well}}$, where D_{h} is the hydraulic diffusivity, and r_{well} is the radius of injection well.

We then apply the plane-strain assumption to analytically calculate the stress variations caused by pore pressure changes. For a two-dimensional cross-section model perpendicular to the out-of-plane direction (Figure 5.1), the pressurized region can be regarded as a rectangular inclusion with respect to the whole geological media (Eshelby, 1957; Wu et al., 2021a). As a consequence, the analytical stress solution of Wu et al. (2021a) can be used to evaluate the induced poroelastic stress $\Delta\sigma_{ij}$ along the fault

$$\Delta\sigma_{ij}(x,y,t)=-\frac{(1-2\nu)\alpha\Delta p_{\mathrm{m}}(t)}{2\pi(1-\nu)}\left[G_{ij}(x,y)-\pi\delta_{ij}\delta_{\Omega}\right], \quad (5.7)$$

where Ω is the inclusion domain, G_{ij} represents the surface integral of stress Green's

function (see details in Appendix K), Δp_{m} denotes the mean value of pore pressure changes within the inclusion, δ_{ij} is the Kronecker delta, and δ_{Ω} is the modified Kronecker delta (Wu et al., 2021a). The minus in the right hand-side of Equation (5.7) results from the adopted sign convention of normal stress, assumed here as the geomechanics convention, i.e., positive for compression. Coordinate y equals zero along the fault plane. For the three components of poroleastic stress, $\Delta\sigma_{xx}$ is parallel to the fault plane (Figure 5.1), which has no impact on the shear failure of fault, and $\Delta\sigma_{xy}$ is always zero along the whole fault plane (Figures K2A and K2B). We thus only need to consider $\Delta\sigma_{yy}$, which acts as a normal stress on the fault, i.e., $\Delta\sigma(x,t)$ in Equation (5.2).

Theis's solution (Equation (5.6)) gives a nonlinear distribution of pore pressure changes. Directly adopting the mean value of this non-uniform pore pressure changes to evaluate the poroelastic stress would lead to an unrealistic jump at the lateral boundaries of the pressurized region (Figures K2C and K2D). Hence, we divide the whole pressurized region into m sub-inclusions (Figure 5.2). In particular, the k^{th} sub-inclusion is overlapped with the $(k-1)^{\text{th}}$ one in space, and the former has a smaller size than the latter in x dimension. As a consequence, the pressure change of the $(k-1)^{\text{th}}$ sub-inclusion has to be subtracted from the one of the k^{th} sub-inclusion in evaluating the poroelastic stress of the k^{th} sub-inclusion as

$$\Delta\sigma_{yy}^{k}(x,0,t)=-\frac{\alpha(1-2\nu)}{2\pi(1-\nu)}\left[G_{yy}^{k}(x,0)-\pi\delta_{\Omega}\right]\left[\Delta p(x^{k},t)-\Delta p(x^{k-1},t)\right], \tag{5.8}$$

where $\Delta p(x^{0},t)=0$, superscript k means the k^{th} sub-inclusion, and

$$G_{yy}^{k}(x,0)=\operatorname{atan}\frac{x-x_1^{k}}{-y_1}-\operatorname{atan}\frac{x-x_2^{k}}{-y_1}-\operatorname{atan}\frac{x-x_1^{k}}{-y_2}+\operatorname{atan}\frac{x-x_2^{k}}{-y_2}, \tag{5.9}$$

where x_1^{k}, x_2^{k}, y_1, and y_2 are the left, right, bottom, and top boundaries of the k^{th} sub-inclusion, respectively. All the sub-inclusions have the same bottom and top boundaries, i.e., $y_1=-h/2$ and $y_2=h/2$, as the fault thickness is uniform.

We finally superpose the induced poroelastic stress of each sub-inclusion to compute the total one as

$$\Delta\sigma_{yy}(x,0,t)=\sum_{k=1}^{m}\Delta\sigma_{yy}^{k}(x,0,t). \tag{5.10}$$

This meshing method implies that we are actually dividing the overpressure instead of the pressurized region (Figure 5.2), and then taking the region that corresponds to the k^{th} sub-overpressure as the k^{th} sub-inclusion. Meshing in this way facilitates the application of the poroelastic stress solution (Equation (5.7)) because all the sub-inclusions are centralized at the injection well, i.e., (0, 0). Otherwise, the value of x has to be updated to the center of sub-inclusion when applying Equation (5.7) for each sub-inclusion.

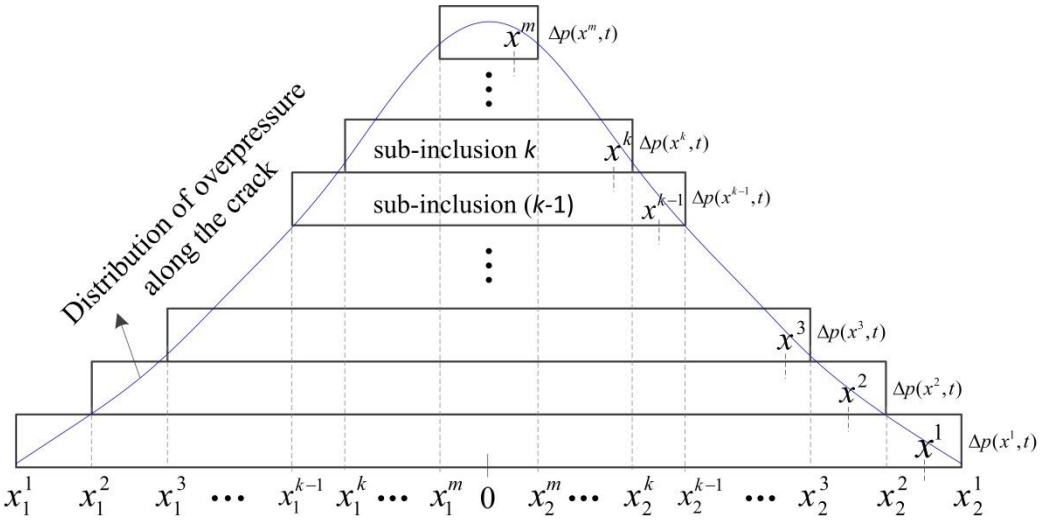

Figure 5.2: Schematic diagram of dividing the whole pressurized region into *m* sub-inclusions. The k^{th} sub-inclusion is overlapped with the $(k-1)^{\text{th}}$ one in space, the former has a smaller size than the latter in the *x* dimension. All sub-inclusions have the same height (*y* dimension) as the fault thickness is uniform.

5.2.3 Scaling and numerical solution

We introduce the following dimensionless variables to describe the above model in a more compact form and to solve the problem by a general method. $a_{\mathrm{w}} = \delta_{\mathrm{w}}\mu^*/\tau_{\mathrm{p}}$ denotes the characteristic patch length, which only depends on the rock properties and the in-situ stress around the fault. The crack half-length and slip are normalized by a_{w} and δ_{w}, respectively, i.e., $\bar{a} = a/a_{\mathrm{w}}$ and $\bar{\delta} = \delta/\delta_{\mathrm{w}}$. The spatial and temporal variables are scaled as $\bar{x} = x/a$ ($\bar{s} = s/a$ as well) and $\bar{t} = 4D_{\mathrm{h}}t/a_{\mathrm{w}}^2$, respectively. The tangential and normal stress components are normalized by τ_{p} and σ_0', respectively, i.e., $\bar{\tau}^{\mathrm{b}} = \tau^{\mathrm{b}}/\tau_{\mathrm{p}}$, $\Delta\bar{\tau} = \Delta\tau/\tau_{\mathrm{p}}$, $\Delta\bar{\sigma} = \Delta\sigma/\sigma_0'$, and $\Delta\bar{p} = \Delta p/\sigma_0'$. Taking Equation (5.4) as an example, its dimensionless form is

$$-\frac{1}{2\pi\bar{a}}\int_{-1}^{1}\frac{d\bar{\delta}(\bar{s})/d\bar{s}}{\bar{x}-\bar{s}}d\bar{s} = 1-\bar{\tau}^{\mathrm{b}} - \left[1-\bar{\delta}(\bar{x})\right]\left[\alpha\Delta\bar{p}(\bar{x},\bar{t}) - \Delta\bar{\sigma}(\bar{x},\bar{t})\right] - \bar{\delta}(\bar{x}), \qquad (5.11)$$

where $\bar{\delta}(\bar{x})$ ranges from 0 to 1 for unlimited slip-weakening law.

To specify the dimensionless form of pore pressure changes and poroelastic stress, we define the characteristic volumetric injection rate and the characteristic aspect ratio of the fault as $Q_{\mathrm{w}} = \kappa\sigma_0' a_{\mathrm{w}}/\eta$ and $A_{\mathrm{c}} = h/a_{\mathrm{w}}$, respectively. We then have

$$\Delta\bar{p}(\bar{x},\bar{t}) = \frac{Q}{Q_{\mathrm{w}}}\frac{1}{4\pi A_{\mathrm{c}}}W(\xi^2), \qquad (5.12)$$

$$\Delta\bar{\sigma}(\bar{x},\bar{t})=\frac{\Delta\sigma_{yy}(\bar{x},0,\bar{t})}{\sigma_0'}=-\frac{\alpha(1-2\nu)}{2\pi(1-\nu)}\sum_{k=1}^{m}\left[G_{yy}^{k}(\bar{x},0)-\pi\delta_{\Omega}\right]\left[\Delta\bar{p}(\bar{x}^{k},\bar{t})-\Delta\bar{p}(\bar{x}^{k-1},\bar{t})\right], \quad (5.13)$$

where Q/Q_{w} can be regarded as a normalized volumetric injection rate, ξ can be further expressed as $\bar{x}\bar{a}/\sqrt{\bar{t}}$ if $\bar{x}\geq r_{\mathrm{well}}/a_w/\bar{a}$, and as $r_{\mathrm{well}}/a_w/\sqrt{\bar{t}}$ if $\bar{x}<r_{\mathrm{well}}/a_w/\bar{a}$. Lateral boundaries of each sub-inclusion are also scaled by the crack half-length, i.e., $\bar{x}_1^k=x_1^k/a$ and $\bar{x}_2^k=x_2^k/a$, while the bottom and top boundaries are scaled by the characteristic patch length, i.e., $\bar{y}_1=y_1/a_{\mathrm{w}}=-A_{\mathrm{c}}/2$ and $\bar{y}_2=A_{\mathrm{c}}/2$. Hence, $\mathrm{G}_{yy}^{k}(\bar{x},0)$ can be rewritten as

$$G_{yy}^{k}(\bar{x},0)=\operatorname{atan}\frac{2(\bar{x}-\bar{x}_1^k)\bar{a}}{A_c}-\operatorname{atan}\frac{2(\bar{x}-\bar{x}_2^k)\bar{a}}{A_c}-\operatorname{atan}\frac{2(\bar{x}-\bar{x}_1^k)\bar{a}}{-A_c}+\operatorname{atan}\frac{2(\bar{x}-\bar{x}_2^k)\bar{a}}{-A_c}, \quad (5.14)$$

where the normalized left boundaries of sub-inclusions range from -1 to 0, and the right ones range from 1 to 0. We define them as

$$\bar{x}_1^k=-\frac{m+1-k}{m},\quad \bar{x}_2^k=\frac{m+1-k}{m},\quad \bar{x}^k=\frac{m+0.5-k}{m},\quad k=1,2,\cdots,m. \quad (5.15)$$

The locations of $\bar{x}_1^k$ and $\bar{x}_2^k$ are symmetrical with respect to the crack center (x=0). We can take an arbitrary value between $\bar{x}_1^k$ and $\bar{x}_1^{k+1}$ as $\bar{x}^k$ to evaluate the pressure change of the k^{th} sub-inclusion when the distance between $\bar{x}_1^k$ and $\bar{x}_1^{k+1}$ is small enough, i.e., m is big enough. As an example, we here adopt the midpoint. To recognize that if the point $\bar{x}$ is located in the k^{th} sub-inclusions or not, we have

$$\begin{aligned}&\bar{x}_1^k\leq\bar{x}\leq\bar{x}_2^k,\quad \textit{inside}\\ &|\bar{x}|>\bar{x}_2^k,\quad \textit{outside}\end{aligned}. \quad (5.16)$$

Equations (5.4), (5.5), and (5.11) are the first group of singular integral equations, which have often been solved by numerical methods (Muskhelishvili, 1953; Erdogan and Gupta, 1972; Erdogan et al, 1973). Applications show that the Gauss-Chebyshev quadrature is reliable in ensuring a high-order of convergence and in achieving an acceptable computational efficiency (Erdogan et al, 1973; Viesca and Garagash, 2018; Viesca, 2021). Thus, we apply the Gauss-Chebyshev quadrature to solve these equations instead of the ones applied in Garagash and Germanovich (2012). Separating the normalized crack length by a set of collection point $\bar{x}_i$ and a set of Gauss-integral point $\bar{s}_j$ for the term in the left-hand side of Equation (5.11), we have

$$-\frac{1}{2\pi\bar{a}}\sum_{j=1}^{n}w_j\frac{F(\bar{s}_j)}{\bar{x}_i-\bar{s}_j}=1-\bar{\tau}^{\mathrm{b}}-\left[1-\bar{\delta}(\bar{x}_i)\right]\left[\alpha\Delta\bar{p}(\bar{x}_i,\bar{t})-\Delta\bar{\sigma}(\bar{x}_i,\bar{t})\right]-\bar{\delta}(\bar{x}_i), \quad (5.17)$$

where

$$\bar{x}_i=\cos\left(\frac{i-0.5}{n+1}\pi\right),\quad i=1,2,\cdots,n+1, \quad (5.18)$$

$$\bar{s}_j = \cos\left(\frac{j\pi}{n+1}\right), \quad j = 1, 2, \cdots, n, \tag{5.19}$$

$$w_j = \frac{1-\bar{s}_j^2}{n+1}\pi. \tag{5.20}$$

We then integrate the slip gradient from one of the crack tips to $\bar{x}_i$ to evaluate the normalized slip at $\bar{x}_i$, which reads (Erdogan et al, 1973; Viesca and Garagash, 2018)

$$\bar{\delta}(\bar{x}_i) - \bar{\delta}(-1) = \sum_{l=0}^{n-1}\sum_{j=1}^{n} B_{lj} F(\bar{s}_j)[\Phi_l(\bar{x}_i) - \Phi_l(-1)], \tag{5.21}$$

where

$$B_{lj} = \frac{2\sin(\theta_j)\sin((l+1)\theta_j)}{n+1}, \qquad \theta_j = \arccos(\bar{s}_j) = \frac{j\pi}{n+1}, \tag{5.22}$$

$$\Phi_l(\bar{x}_i) = \frac{1}{2}\left[\frac{\sin(l\theta_i)}{l} - \frac{\sin((l+2)\theta_i)}{l+2}\right], \qquad \theta_i = \arccos(\bar{x}_i) = \frac{i-0.5}{n+1}\pi. \tag{5.23}$$

Updating the continuous $\bar{x}$ by the discrete points $\bar{x}_i$ in Equations (5.12) and (5.13) and then substituting them into Equation (5.17), we obtain the complete equation. It is a set of strong nonlinear equations because the normalized slip is a function of the unknowns $F(\bar{s}_j)$ and both the pressure changes and poroelastic stress are also involved in the unknown $\bar{a}$. We adopt the Newton-Simpson method to solve the unknowns after giving the normalized background loading $\tau^{\mathrm{b}}/\tau_{\mathrm{P}}$, injection rate Q/Q_{w}, and injection time $\bar{t}$. Once solving the unknowns, one can calculate the distribution of normalized slip, shear stress, overpressure, and poroelastic stress along the crack. Note that the collection points $\bar{x}_i$ range from -1 to 1 with increasing *i* from 1 to n+1 (Equation (5.18)), which means that there is at least one $\bar{x}_i$ that will be located inside the injection well during numerical calculations. Recognizing this point is essential to achieve the convergence and stability of numerical algorithms. The above solving method has been benchmarked against the results of Garagash and Germanovich (2012), with details shown in Appendix K.

Some basic parameters have to be given when applying the aforementioned model to solve a specific problem. We adopt $\alpha = 0.7$, $\nu = 0.25$, $f_{\mathrm{r}}/f_{\mathrm{p}} = 0.6$, r_{well} = 0.108 m, h = 10 m, $a_{\mathrm{w}} = 20$ m in the subsequent simulations. The value of r_{well} corresponds to a standard wellbore diameter in the industry. The value of h and a_{w} is in the order of field scale (Ben-Zion and Sammis, 2003; Uenishi and Rice, 2003).

5.3 Results

5.3.1 Poroelastic effects on nucleation process

We first evaluate the normalized crack half-length and the normalized slip at the crack center (x=0), i.e., the peak slip, as functions of the square root of normalized time $\sqrt{\bar{t}}$ for cases without (case C) and with (case D) poroleastic effects (Figure 5.3). We here consider an unlimited slip-weakening law under the normalized volumetric injection rate of 0.9 and various values (0.9, 0.85, 0.8, 0.75, 0.7, 0.65, and 0.6) of the normalized background shear stress. Each evolution curve of both the crack half-length and peak slip with injection time consists of two parts: the solid and dashed parts correspond to the quasi-static crack growth under physically meaningful advance and meaningless reversal of the pore pressure diffusion, respectively. The demarcation point from meaningful advance to meaningless reversal, i.e., the point with vertical slope, of each curve means the instability of quasi-static crack growth, i.e., the nucleation of dynamic rupture. This point is referred as the nucleation point, and thus the corresponding quantities are the nucleation time t_c, nucleation half-length a_c, and nucleation fault patch. Beyond the nucleation point, the crack propagates dynamically, which does not follow the quasi-static equilibrium (Uenishi and Rice, 2003). These characteristics in case C are similar with the ones of Garagash and Germanovich (2012), while all the nucleation time, nucleation length, and the peak slip at the nucleation instants are inversely proportional to the background loading in case C (Figure 5.3A and 5.3B). The differences can be attributed to the different injection scenarios, i.e., injection with a constant injection pressure in Garagash and Germanovich (2012) and a constant injection rate in this study.

When including poroelastic effects, the quasi-static crack growth drastically changes (Figures 3C and 3D). There are two nucleation points of dynamic rupture for the relatively small values of background loading (0.65 and 0.6) as a result of the superposition of poroelastic and slip-weakening effects. We define the first one as the poroelasticity-dominated nucleation (PE-nucleation) point and the second one as the slip-weakening-dominated nucleation (SW-nucleation) point for clarity in the description. The definitions imply the dominant factor leading to the nucleation, which is recognized by comparing Figure 5.3 with the results (Figure K3) of cases A and B. The episode between points N_p and Ar (see Figure 5.3) represents the self-arrested dynamic rupture propagation and its distance is defined as the run-out distance (Garagash and Germanovich, 2012). After the point Ar, the dynamic rupture returns to quasi-static fault slip until the SW-nucleation. The crack half-length and peak slip associated with the PE-nucleation are much smaller than the ones of the SW-nucleation, and these characteristic crack sizes at the latter nucleation instant in case D are smaller than the ones in case C. The smaller size indicates that the initial dynamic rupture nucleated by poroelasticity releases a small part of the accumulated elastic energy

during injection (fault loading), which reduces the crack size at the SW-nucleation instant. The evolution of quasi-static crack growth in case D for these relatively small background loadings presents an initial PE-nucleation with a small crack size and then immediately propagates from points N_p to Ar, followed by an arrest and a final SW-nucleation with a larger crack size. In contrast, the crack growth in case C only displays the SW-nucleation of dynamic rupture without arrest.

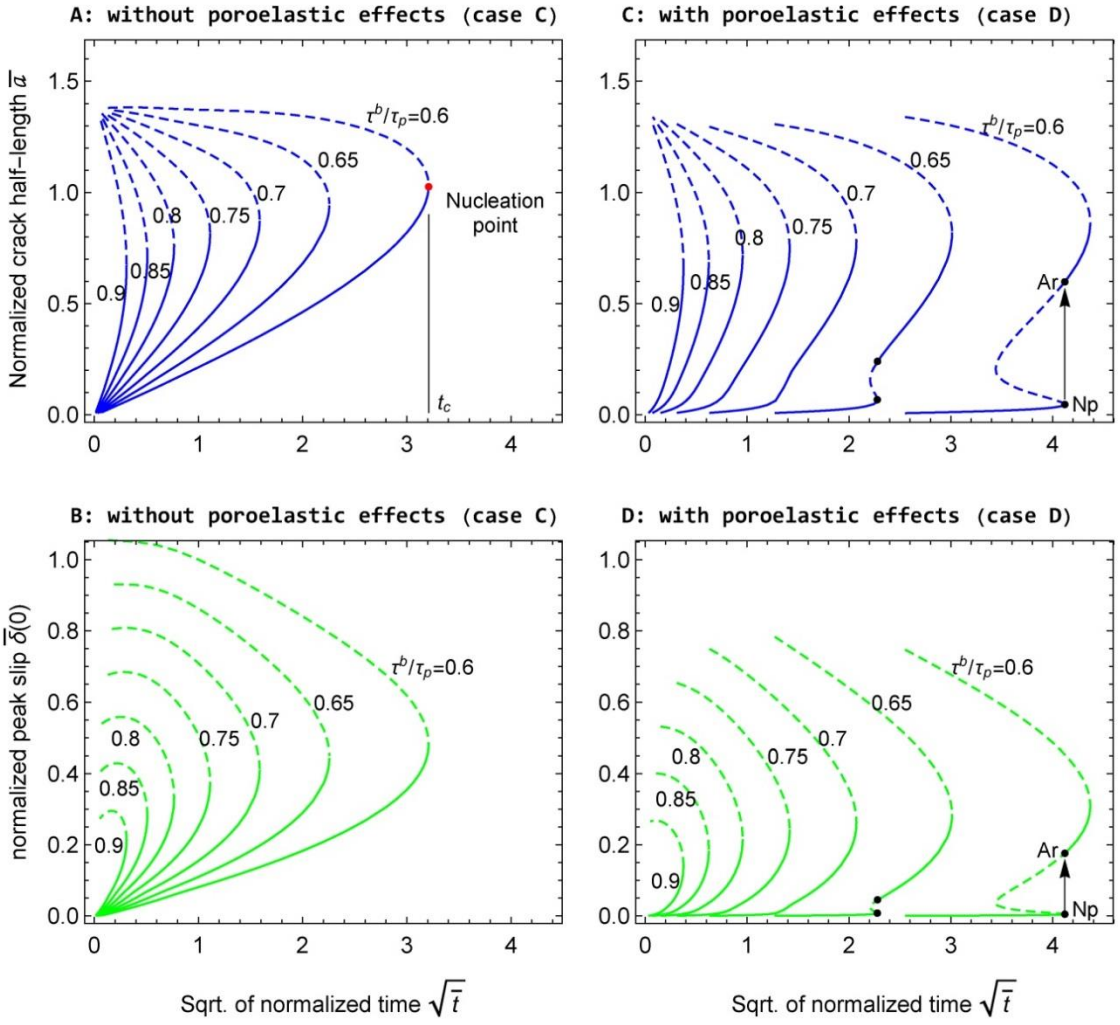

Figure 5.3: Evolution of the normalized crack half-length (A and C) and the normalized peak slip (i.e., the slip at the crack center) (B and D) with an unlimited slip-weakening law under the normalized volumetric injection rate of 0.9 and various values of the background shear stress. (A) and (B) correspond to the case C (without poroelastic effects), and (C) and (D) correspond to the case D (with poroelastic effects). Solid and dashed parts of the lines correspond to the crack growth under physically meaningful advance and meaningless reversal of the pore pressure diffusion, respectively.

For the relatively large background loading, although poroelasticity does not cause nucleation, the crack size at the SW-nucleation instant is still smaller in case D than in case C. The crack growth is reduced by poroelastic effects because the poroelastic normal stress neutralizes part of injection-induced overpressure (Figure 5.4B) and, thus, reduces the slip (Figure 5.4A) and shear stress drop (Figures 4C and 4D). In addition,

the slip starts later in case D than in case C, implying that poroelastic effects can delay the onset of quasi-static fault slip. The SW-nucleation time is larger in case D than in case C for arbitrary background shear loading, which means that poroelastic effects can also delay the ultimate instability time of the quasi-static crack growth.

Crack length and slip are much bigger in case C than in case D under the specific conditions of $Q/Q_{\mathrm{w}} = 0.9$, $\tau^{\mathrm{b}}/\tau_{\mathrm{P}} = 0.75$, and $\sqrt{\bar{t}} = 1$ (Figure 5.4A), indicating again that poroelasticity is indispensable in accurately analyzing crack growth. The distribution of normalized effective overpressure in case C is identical to the one in case D (Figure 5.4B), benchmarking our simulations (model derivations, solving algorithm, code programing, processing, etc.). The smoothness of the poroelastic stress distribution and the shear stress distribution (Figures 4B-4D) validates the proposed superposition method in evaluating the poroelastic stress (Equations (5.15)-(5.17)). The difference between the background shear loading and the shear stress along the crack shows the shear stress drop, and the difference between the initial shear strength and the shear stress also means the shear strength drop as the shear stress equals the strength along the slipping fault patch (Figures 4C-4D). It implies that the difference between the normalized strength and stress drops equals $(\tau_{\mathrm{P}} - \tau^{\mathrm{b}})/\tau_{\mathrm{P}}$, which is a constant along the crack for a homogeneous fault initially loaded by a uniform stress field. This constant indicates the maximum bearing capacity of the fault and can be defined as the normalized fault understress. Its value ranges from 0 to 1, the lower and upper limits correspond to a critically stressed fault and a stress-free fault at the initial state, respectively (Gischig, 2015).

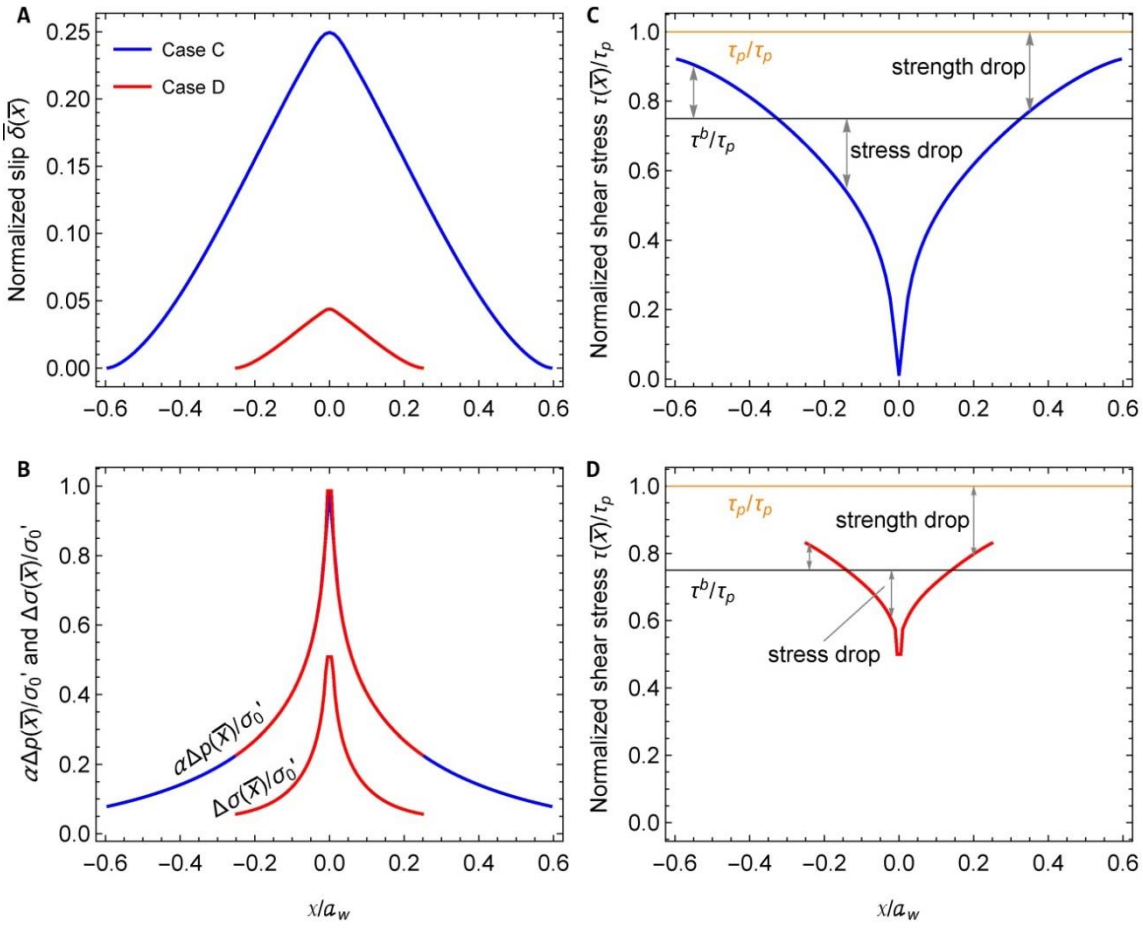

Figure 5.4: Distribution of the normalized (A) slip, (B) effective overpressure and poroelastic stress for both cases C (blue lines) and D (red lines), and shear stress along the crack for (C) case C and (D) case D with an unlimited slip-weakening law under the normalized volumetric injection rate of 0.9 and normalized loading of 0.75 at the instant of the square root of normalized time equals 1.

5.3.2 Characteristics of crack growth in different slip regimes

In Section 5.3.1, some of the normalized peak slips at the nucleation point exceed 0.4 (Figure 5.3), which in general cannot be regarded as a small enough value. Such values indicate that the residual friction may affect the nucleation of dynamic rupture and its possible arrest, i.e., slip regime. Hereafter, we apply the model with a residual friction in case D (Equation (5.5)) to investigate the change of the slip regime with respect to the normalized fault understress $(\tau_{\mathrm{P}} - \tau^{\mathrm{b}})/\tau_{\mathrm{P}}$ and volumetric injection rate Q/Q_{w}. This normalized space represents different hydro-mechanical properties, background stress and injection conditions.

We display the results as a map of the different slip regimes (Figure 5.5). The black line (the first-class boundary) divides the map into two parts. In the left-hand side part, the background shear loading is larger than the residual friction of the fault at ambient conditions, which finally leads to an unstable slip (US). The quasi-static fault slip will

transform to the unabated dynamic rupture with one or more nucleation points (Figure 5.6). On the contrary, the slip is ultimately stable (SS) in the right-hand side part as its shear loading is smaller than the residual friction (Figure 5.7). The two gray lines (the second-class boundary) divide the map into three sub-domains by the dominant factors of nucleation. The nucleation in the bottom and top sub-domains are dominated by the poroelastic and slip-weakening effects, respectively, while the intermediate sub-domain is controlled by both of them. The SW-nucleation can be affected by the residual friction or not, whose boundary is the blue line (the third-class boundary). Above this boundary, such nucleation is delayed in the US and removed in the SS, and it is not affected below this boundary. For the latter case, when the slip weakening of a local slipping patch around the crack center is completed (the friction coefficient reaches its residual value), a new re-nucleation point is generated in the US. The new re-nucleation could be physically meaningful or meaningless, which is separated by the brown line. As a consequence, the map is divided into nine different slip regimes by the previous three types of boundaries. The properties of each slip regime are characterized by its typical evolution of the normalized crack half-length and peak slip (Figures 6 and 7), with details listed below.

US-1: poroelasticity-dominated unstable slip regime. As shown by A1 and A2 in Figures 6A and 6B, there is only one physically meaningful nucleation point of dynamic rupture, which is caused by poroelastic effects (the slip is very small at these conditions and thus the slip-weakening effects can be neglected). With increasing injection rate, a physically meaningless re-nucleation point induced by slip-weakening effects appears during the reversal of pore pressure diffusion. The re-nucleation time t_{c2} is smaller than the initial nucleation time t_{c1}.

US-2: double factors-dominated unstable slip regime. With increasing the injection rate further, t_{c2} becomes larger than t_{c1}, leading to a physically meaningful re-nucleation point (B in Figures 6A and 6B). Poroelasticity dominates the initial nucleation and slip-weakening effects dominate the re-nucleation. Fault slip in this regime has a run-out distance that is relatively short.

US-3: slip-weakening-dominated unstable slip regime, in which, poroelasticity does not lead to nucleation and the only nucleation is induced by slip-weakening effects (C1 and C2 in Figures 6A and 6B). The residual friction has no impact on the evolution of crack growth in this regime.

US-4: slip-weakening-dominated unstable slip regime with a residual friction-delayed nucleation point. The unique SW-nucleation is affected by the residual friction because the normalized peak slip exceeds its residual value (0.4 in this case) before the nucleation time, and thus the residual friction delays the nucleation (D in Figures 6C and 6D).

US-5: this regime is a cut from the regimes US-1, US-2 and US-3, and, thus, it includes three sub-regimes. There is a new physically meaningful re-nucleation point caused by the ending of slip weakening of a local slipping fault patch in addition to the PE-nucleation and SW-nucleation (E, F and G in Figures 6C and 6D). The new

re-nucleation is strongly related to the residual friction; we define it as the residual friction-dominated nucleation (RF-nucleation). The corresponding local fault patch is defined as the mature slip-weakening patch, and its half-length is x_c. The run-out distance before the RF-nucleation in this regime could range from a short one to a long one, which increases with decreasing the injection rate.

SS-4: slip-weakening-dominated ultimately stable slip regime without nucleation of dynamic rupture. Since the ending of slip weakening occurs before the nucleation time, the nucleation is removed, and thus, the fault slip is always stable (H in Figures 7A and 7B).

SS-3: slip-weakening-dominated ultimately stable slip regime with one nucleation point. The unique SW-nucleation is not affected by the residual friction, the dynamic rupture however arrests by itself, because the background loading is smaller than the residual friction, with a negligible run-out distance (I in Figures 7A and 7B).

SS-2: double factors-dominated ultimately stable slip regime with two nucleation points (SS-2a) or one nucleation point (SS-2b). Nucleation and re-nucleation in sub-regime SS-2a are dominated by the poroelastic and slip-weakening effects, respectively, which are not affected by the residual friction and are followed by the arrest of dynamic rupture (J in Figures 7A and 7B). Sub-regime SS-2b would be exactly the same as SS-2a if there was no residual friction. The residual friction however removes the SW-nucleation of SS-2b, and thus it has only one nucleation point (K in Figures 7C and 7D). After the dynamic rupture arresting, the quasi-static fault slip is then dominated by slip-weakening effects. The run-out distance in this regime is relatively short.

SS-1: poroelasticity-dominated ultimately stable slip regime with one nucleation point, which can be divided into two sub-regimes (SS-1a and SS-1b) by the dashed part of the third boundary. The unique meaningful PE-nucleation ultimately arrests by itself. The re-nucleation in both AS-1a and AS-1b would be meaningless if there were no residual friction, and it is removed by the residual friction in SS-1b (L in Figures 7C and 7D), while it is not affected by the residual friction in SS-1a (M in Figures 7C and 7D). The run-out distance in this regime is relatively long, which increases with decreasing the injection rate.

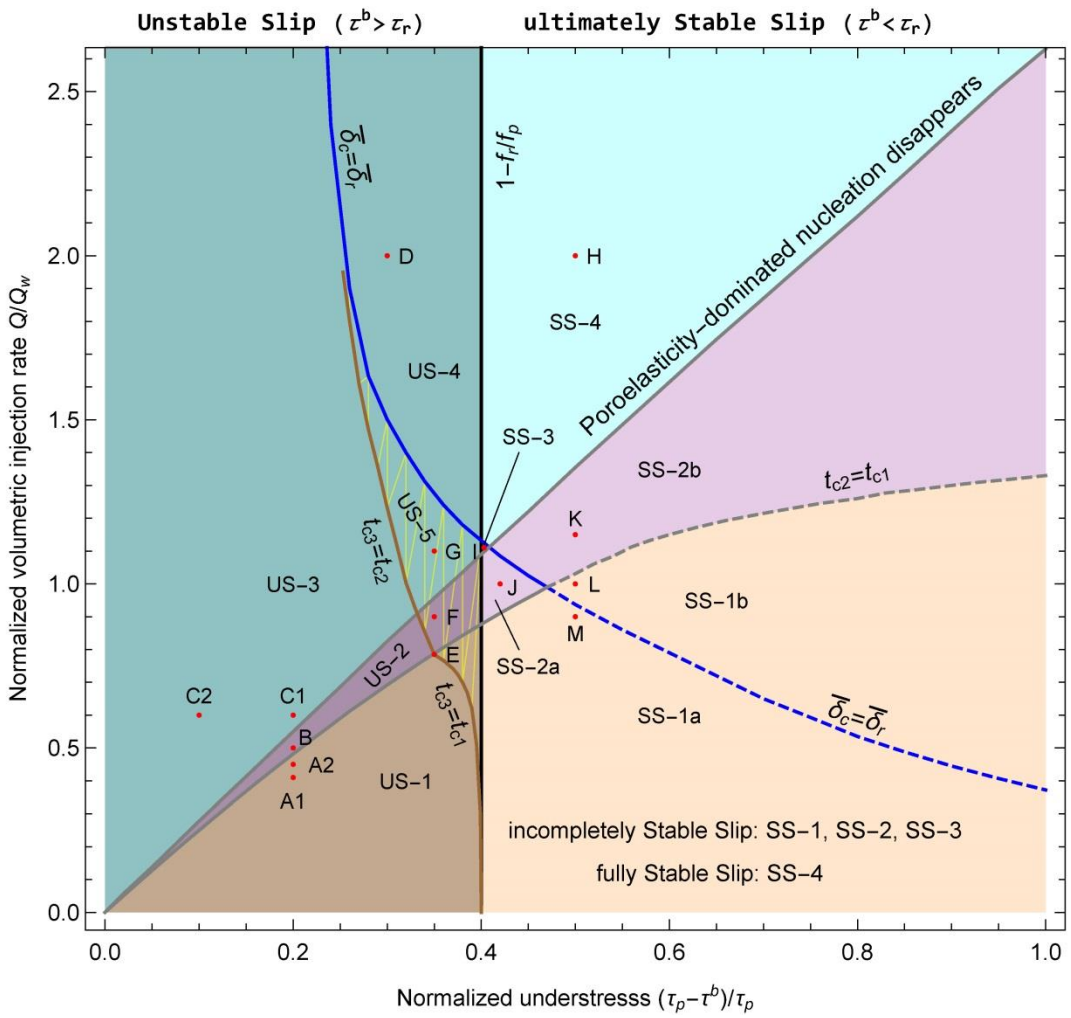

Figure 5.5: Map of slip regimes under case D (considering pore pressure changes and both poroelastic and slip-weakening effects) in the normalized space of fault understress and volumetric injection rate. The black line separates the map as unstable slip (US) and ultimately stable slip (SS) regimes. The two gray lines divide the map into three sub-domains by the dominant factors of nucleation. The blue line separates the map where the nucleation/re-nucleation is and is not affected by the residual friction f_r, respectively. The gray and blue lines are evaluated from the solution with an unlimited slip-weakening law, i.e., without f_r. The brown line cuts out a sub-regime that indicates that the new re-nucleation, caused by the ending of slip-weakening of a local patch, is and is not physically meaningful, respectively, which is evaluated with the limited slip-weakening law $f_r/f_p = 0.6$. US-1: poroelasticity-dominated unstable slip regime; US-2: double factors-dominated unstable slip regime; US-3: slip-weakening-dominated unstable slip regime; US-4: slip-weakening-dominated unstable slip regime with a residual friction-delayed nucleation point; US-5: cut from the regimes US-1, US-2 and US-3, with a second re-nucleation point; SS-4: slip-weakening-dominated ultimately stable slip regime without nucleation; SS-3: slip-weakening-dominated ultimately stable slip regime with one nucleation point; SS-2: double factors-dominated ultimately stable slip regime with two nucleation points (SS-2a) or one nucleation point (SS-2b); SS-1: poroelasticity-dominated ultimately stable slip regime with one nucleation point, includes two sub-regimes (SS-1a and SS-1b).

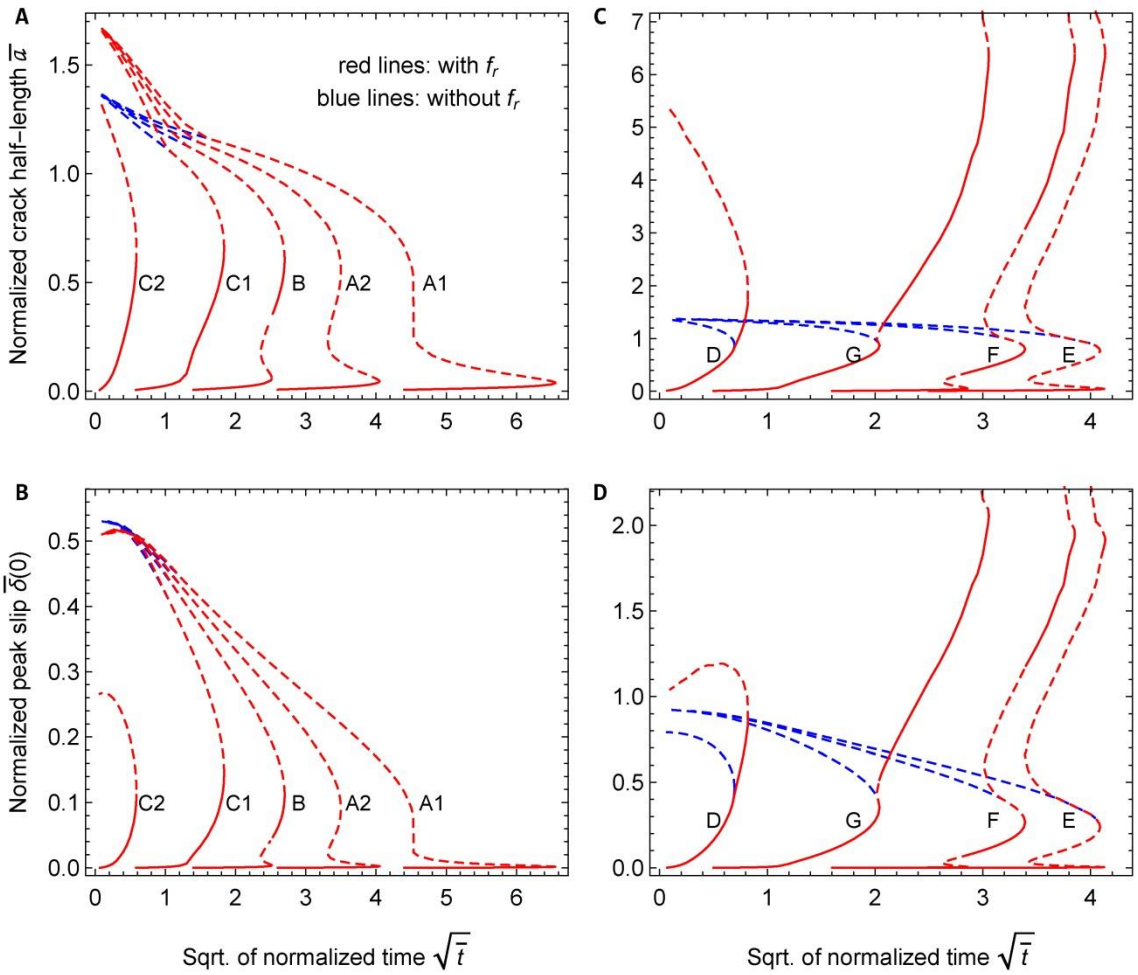

Figure 5.6: Typical evolution of the normalized crack half-length (A and C) and peak slip (B and D) for case D with (red lines) and without (blue lines) the residual friction in unstable slip regimes. Solid and dashed parts of the lines correspond to the crack growth under physically meaningful advance and meaningless reversal of the pore pressure diffusion, respectively. The location of points A1-G is shown in Figure 5.5.

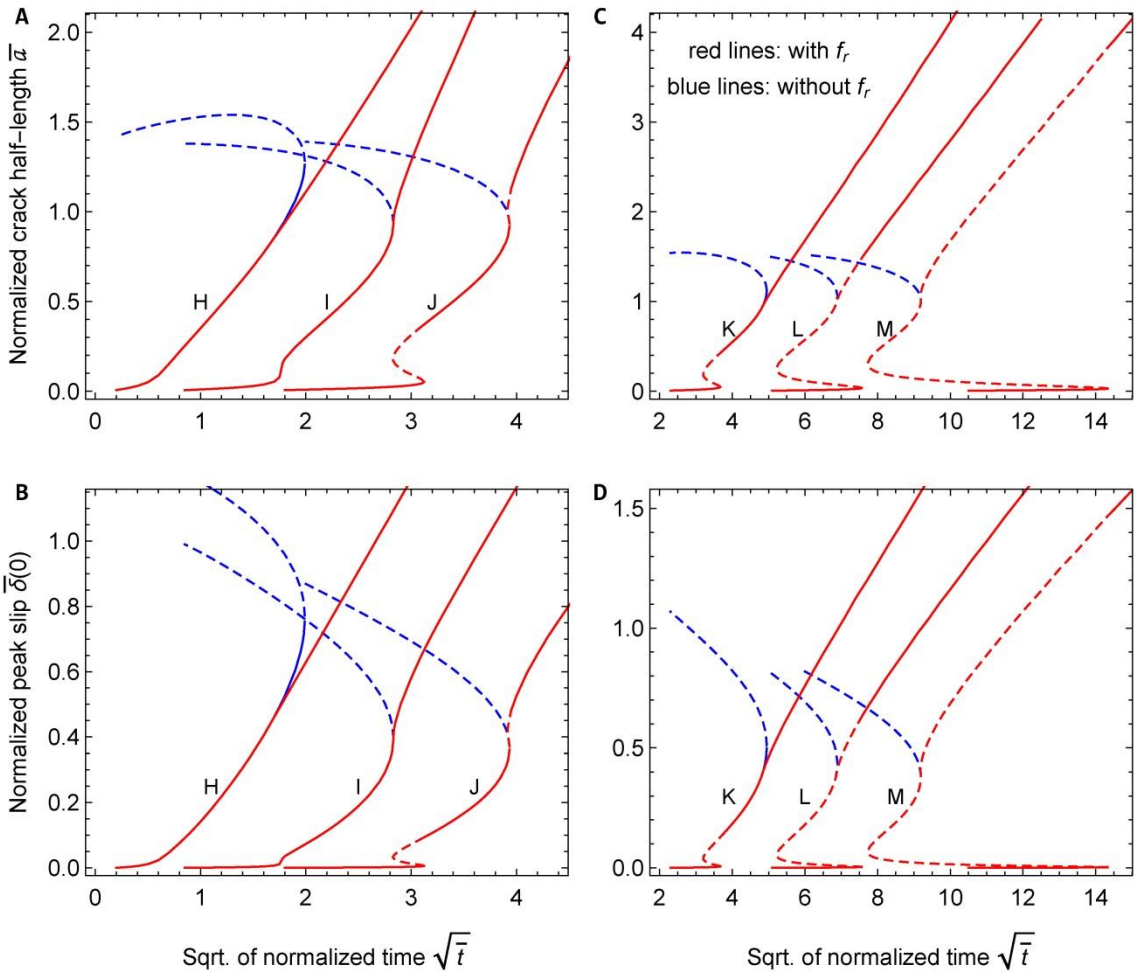

Figure 5.7: Typical evolution of the normalized crack half-length (A and C) and peak slip (B and D) for case D with (red lines) and without (blue lines) the residual friction in ultimately stable slip regimes. Solid and dashed parts of the lines correspond to the crack growth under physically meaningful advance and meaningless reversal of the pore pressure diffusion, respectively. The location of points H-M is shown in Figure 5.5.

The residual friction of faults differentiates the quasi-static fault slip into unstable and ultimately stable slip regimes. We further distinguish the latter as the incompletely stable (e.g., SS-1, SS-2, and SS-3) and fully stable (e.g., SS-4) slip regimes since a dynamic rupture can still nucleate in SS-1, SS-2, and SS-3 before the ultimately stable state. The dynamic ruptures nucleated in the incompletely stable slip regime (most of them are dominated by poroelasticity) always arrest by themselves, implying self-arrested seismic events. The dominant factor leading to nucleation changes from poroelastic to slip-weakening effects as the injection rate increases. The residual friction never affects the PE-nucleation because the related slip is very small, while it may affect the SW-nucleation. As a comparison, we also plot a similar map for case C (Figures K4 and K5), which only displays the slip regimes US-3, US-4, US-5, SS-3, and SS-4 because it does not consider the injection-induced poroelastic effects. Including poroelastic effects reveals new additional slip regimes in the normalized space of fault understress and volumetric injection rate.

5.4 Moment magnitude estimate of injection-induced earthquakes associated with the ultimate nucleation in unstable slip regimes

The slip regime map provides all the nucleation information under different conditions. With this map, we now apply the moment magnitude (M_w) and Ohnaka's model (Ohnaka, 2000) to quantitatively estimate the earthquake size and to specify to what extent poroelasticity reduces it. The moment magnitude is defined from the seismic moment (M_0 in N·m) as (Kanamori 1977; Hanks and Kanamori 1979)

$$M_w = \frac{2}{3}\lg M_0 - 6.07 . \tag{5.24}$$

To evaluate the seismic moment, Ohnaka (2000) derived a theoretical scaling relation between the seismic moment and the critical size of nucleation zone that corresponds to our nucleation length ($2a_c$) in the framework of fracture mechanics

$$M_0 = k_{NL}(2a_c)^3 , \tag{5.25}$$

where k_{NL} is the scaling parameter. $k_{NL} = 10^9$ is a typical and theoretical value with a few assumptions and laboratory-based observations, which also provides a good match with seismological data (Ohnaka, 2000, 2013).

We calculate the magnitude of earthquakes associated with the ultimate nucleation of dynamic rupture in unstable slip regimes (US). The results are incorporated into the slip regime map, leading to a similar map of moment magnitude of injection-induced earthquakes (Figure 5.8). The latter map is divided into three sub-regions with the same boundaries as in the former map. In the bottom sub-region, i.e., the region of US-1, the earthquake size is smaller than M_w 0.7 because the crack size associated with the PE-nucleation is very small (Figures 3 and 6). Once exceeding the boundary of US-1, the earthquake size immediately increases with a noticeable jump. In the left sub-region, i.e., the region of US-2 and US-3, the earthquake size is linked to the SW-nucleation and ranges from M_w 2.6 to M_w 3.6. It increases very slowly with respect to both the fault understress and injection rate. However, in the top-right sub-region, i.e., the region of US-4 and US-5, the earthquake size significantly increases with the fault understress. In contrast, the magnitude barely increases with the injection rate because the ultimate nucleation in US-4 and US-5 is controlled by the ending of slip weakening, i.e., the residual friction. At these ultimate nucleation points, the size of mature slip-weakening patch is proportional to the fault understress and is independent of the injection rate (Figure K6). The maximum earthquake size of the third sub-region exceeds M_w 7. The induced seismicity in these three sub-regions can be classified as micro-seismicity, felt earthquake, and moderate to large earthquake, respectively, and is dominated by the PE-nucleation, SW-nucleation, and RF-nucleation, respectively. Thus, adding poroelastic effects cuts out a space from the region dominated by slip-weakening effects (Figures 5 and S4) and the magnitude of induced seismicity in such space (US-1) is reduced from the felt level to the micro-seismic level by poroelasticity. The magnitude of self-arrested earthquakes in the incompletely stable slip regime (SS-1, SS-2, and SS-3) and whether the rock properties, background

loading and injection conditions located in each slip regime are appropriate to deploy geo-energy projects are discussed in Section 5.5.

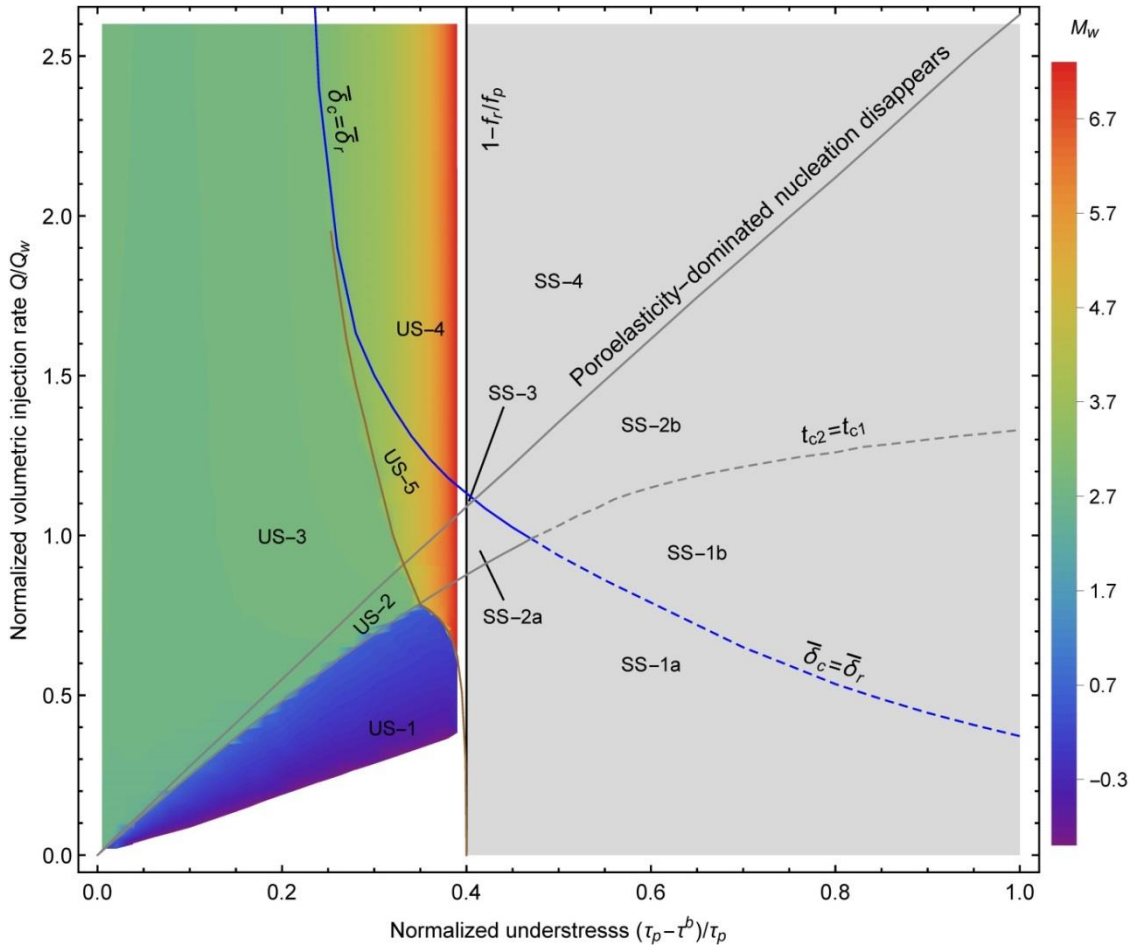

Figure 5.8: Map of moment magnitude of injection-induced earthquakes when considering pore pressure changes and both poroelasticity and slip-weakening effects (case D) in the normalized space of fault understress and volumetric injection rate. The previous three types of boundaries as well as the abbreviation of each slip regime shown in Figure 5.5 are also plotted here in the background for comparison. We do not evaluate the magnitude of earthquakes in the blank area of SS-1 as it is smaller than -1. The region of ultimately stable slip regimes is colored by a gray background without any implications to earthquake size.

5.5 Discussions

The interfacial slip model of cracks is a development of Mohr-Coulomb failure criterion by considering the slip-dependent shear stress and strength variations (Equations (5.1) and (5.2)), and thus, it can describe the earthquake nucleation process. Injection-induced quasi-static slip along the faults with slip-independent frictional properties never transits to dynamic ruptures (Figure K3; Rice, 1983; Rice and Ruina, 1983). For slip-weakening faults, the transition to the ultimate dynamic rupture depends on the relative size between the background shear loading and the residual friction of the faults at ambient conditions (Figures K4 and K5; Garagash and Germanovich, 2012; Azad et al., 2017; Ciardo and Lecampion, 2019). Although adding

poroelastic effects does not alter the previous transition condition, the detailed evolution of crack growth significantly changes (Figures 3, 6 and 7), revealing a wider range of slip regimes (compare Figures 5 and K4) and reducing the magnitude of earthquakes in some slip regimes (Figure 5.8).

Poroelasticity can partly neutralize the injection-induced overpressure (Figure 5.4B) under any conditions of the slip regime map and nucleate a dynamic rupture in the whole lower triangle of the slip regime map (Figure 5.5). As a consequence, the quasi-static crack growth presents several typical slip regimes under different rock properties, background stress and injection conditions (Figures 6 and 7). For the conditions in the poroelasticity-dominated unstable slip regime (US-1), the unique nucleation of dynamic rupture is dominated by poroelastic effects, while the subsequent slip-weakening effects are prevented as the slip is very limited. The very small nucleation length (Figure 5.6) in this regime restricts the corresponding seismicity to the micro-size level (Figure 5.8). The microseismicity partly releases the accumulated elastic energy of rock mass, hindering future damaging events. A similar phenomenon has also been observed in natural seismicity, in which the nucleation of parts of the San Andreas fault inhibited subsequent large earthquakes (Neely et al., 2023). Thus, the conditions of US-1 should be sought for geo-energy applications because the small magnitudes will permit an effective management of induced seismicity.

A similar crack growth can also be found in the poroelasticity-dominated incompletely stable slip regime (SS-1), however, the small background loading permits to build a high overpressure along a large fault patch before nucleation. As a result, once the dynamic rupture is nucleated by poroelastic effects, it can immediately propagate to a large size with a long run-out distance (exceeding 3.5 and 1.5 normalized crack half-length for SS-1a and SS-1b, respectively, in Figure 5.7). During such rupture propagation, the long run-out distance may coexist with a near sonic velocity (Ohnaka and Kuwahara, 1990; Ohnaka, 1992), which could activate the dynamic thermal pressurization and flash heating (Rice et al., 2006; Garagash and Germanovich, 2012; Garagash, 2021) and then induce a damaging earthquake (Viesca and Garagash, 2015; Bhattacharya and Viesca, 2019; Eyre et al., 2019). Thus, although the earthquake size associated with the unique PE-nucleation in SS-1 is similar to the one in US-1, the potential risk of inducing a damaging earthquake by the long run-out distance cannot be overlooked for the conditions in SS-1.

In the unstable slip regimes US-2 and US-3, slip-weakening effects break the constraint of poroelastic effects because of a fast increase in slip rate (Figure 5.6) and dominate the ultimate nucleation, leading to the earthquakes in a felt-size level (Figure 5.8). Similar size of seismicity to US-2 and US-3 can also occur in the incompletely stable slip regimes SS-2a and SS-3 because of the similarity of ultimate nucleation length between the former and the latter (Figures 6 and 7). Deploying geo-energy projects under these conditions needs to pay more attention and further assessment to avoid a negative public perception of projects. In contrast, as the SW-nucleation in SS-2b is removed by the residual friction, dynamic rupture can only be nucleated by

poroelastic effects (Figure 5.7), resulting in microseismicity that is similar to the one in US-1. Furthermore, the fast slip-weakening effects in SS-4 suppress the nucleation of poroelasticity (Figure 5.7), leading the slip to be fully stable. Hence, the conditions in both SS-2b and SS-4 are favorable for geo-energy projects.

As for the unstable slip regimes US-4 and US-5, the ultimate RF-nucleation can cause to a damaging earthquake, explicitly overruling the feasibility of deploying geo-energy projects. Our results and the preceding analysis focus on the mechanical stability and the potential risk of induced seismicity, while the injectivity (Bai et al., 2017; Hoteit et al., 2019) of sites is not considered. Thus, the volume capacity and the maximum allowable injection rate (Bachu et al., 2007) have to be assessed in each application. The limited injectivity of potential sites may reduce the range of SS-2b and SS-4 shown in Figure 5.8, while it could be negligible for US-1 because the injection rate is relatively low.

The run-out problem also exists in slip regimes US-5, US-2, SS-2, and SS-3, while its distance is limited, because the dynamic rupture has already arrested before reaching the mature slip-weakening state, except the one in US-5 (Figures 6 and 7). US-5 shows a similar size of run-out distance to SS-1, and thus, the earthquake size may be even larger than the estimate shown in Figure 5.8 when considering the previous dynamic-weakening effects. The longest run-out distance occurs when the crack directly runs from the PE-nucleation (almost no slip-weakening state) to the mature slip-weakening state, i.e., the shear stress instantly drops from a peak value to the residual value. Neglecting poroelastic effects cannot find this longest run-out distance (Figure K5). The heterogeneity of fault gouge and the roughness of fault plane (Power et al., 1987; Ohnaka, 1996; Ben-Zion and Sammis, 2003) may inhibit the long run-out distance. Further research on this topic is needed.

Our quasi-static simulation shows that the dynamic rupture associated with the ultimate nucleation in the unstable slip regimes is unabated once it is nucleated as we assume a homogenous fault zone with an infinite size in the longitudinal direction. However, such unabated dynamic rupture does not mean a runaway rupture (Galis, et al., 2017). In reality, the frictional properties of fault zone are nonuniform (Ohnaka, 1996; Ben-Zion and Sammis, 2003) and the fault size is limited (Alian et al., 2019; Galis, et al., 2019). Thus, whether such unabated dynamic rupture eventually transits to the self-arrested or runaway rupture should be further studied in the framework of elastodynamics with a finite fault size (Ripperger et al., 2007; Galis, et al., 2017, 2019). The nonuniformity of fault friction could be taken into account by incorporating stochastic simulations (Nguyen et al., 2015).

The slip increases very slowly during the poroelasticity-dominated crack growth, even for the instants close to the PE-nucleation (Figures 6 and 7). It indicates that the dynamic rupture nucleated by poroelasticity may probably be a slow slip event (Peng and Gomberg, 2010; Segall et al., 2010; Eyre et al., 2022). Thus, including poroelastic effects provides potential information and chance to analyzing the triggering mechanisms of slow slip events. Further research on this point is recommended by

referring to the evolution of slip rate during crack growth shown in Dublanchet (2019).

The residual friction coefficient f_r affects the first-class (between the unstable and ultimately stable slip regimes) and third-class (nucleation is or is not affected by f_r) boundaries of slip regime map (Figure 5.5). Reducing f_r will lead to a change in both boundaries: the former will shift to the right and the latter will move upwards. As a result, the SS-3 may either expand or shrink, eventually disappearing and forming a new double-factors-dominated unstable slip regime with a simultaneous residual friction-delayed re-nucleation point. The SS-2 changes similarly. These changes, however, do not affect the previous nucleation process, and thus the new additional slip regimes hold, only the size of slip regimes varies.

The injection-induced stress variations have, in turn, an undrained effect on the pore pressure, which is ignored here since the pore fluid is more compressible than the rock mass. In contrast, the slip-induced pressure drop due to dilatant mechanism (Rudnicki and Chen, 1988; Segall and Rice, 1995; Segall et al., 2010; Ciardo and Lecampion, 2019) may be more visible (Cocco and Rice, 2002; Vilarrasa et al., 2021). Slip-induced pressure drop can neutralize a part of injection-induced overpressure along the slipping fault patch, which is similar to the poroelastic effects. As a result, the second-class boundary of slip regime map (Figure 5.5) would move upwards. This movement implies that the allowable injection rate would be larger than the one in the current results for deploying geo-energy projects. Evaluating such pressure drop involves assessing the slip-induced porosity and permeability changes of fault gouge (Segall and Rice, 1995; Garagash and Rudnicki, 2003) as well as the dilatant effects (Ciardo and Lecampion, 2019), which is recommended for future research.

The slip-regime map delimits the slip regimes as a function of the understress and the injection rate. In geo-energy applications, we can control the injection rate, but the understress is fault dependent. This dependency implies that in order to design safe injection schemes, subsurface characterization is key to quantify the stress state and fault characteristics (Ben-Zion and Sammis, 2003; Vilarrasa et al., 2022). The slip-regime map can be used as a decision-making tool to minimize the risk of inducing earthquakes that might end up with project cancellation. This substantial advance in the frontiers of knowledge of the mechanisms that induce seismicity when considering poroelasticity opens up a promising pathway in the development of reliable induced-seismicity forecasting.

5.6 Conclusions

Earthquake nucleation process, which characterizes the intermediate evolution phase between the initial fault reactivation and the final dynamic rupture propagation, is of physical fundament in understanding both natural and induced earthquakes. We incorporate the poroelastic stress resulting from pore fluid diffusion into the interfacial slip model of cracks to study the nucleation process due to fluid injection. Including poroelastic effects in the rock mass drastically affects the nucleation process of fault rupture, which reveals new additional slip regimes and reduces the magnitude of

related earthquakes in some slip regimes.

The nature of injection-induced poroelastic response inside the slipping fault patch tends to resist the pressure buildup, and thus reduces the slip and shear stress drop along the crack. As a result, the initiation of both the quasi-static fault slip and ultimately dynamic rupture are delayed, and the crack size associated with the SW-nucleation is reduced. Such reduction in crack size is more visible once poroelastic effects can nucleate a dynamic rupture because the poroelasticity-nucleated dynamic rupture partly releases the stored elastic energy by means of microseismicity. The self-arrested dynamic rupture (existing in some slip regimes, i.e., certain conditions) can cause the crack to run out during the entire nucleation process. When the crack directly runs from the PE-nucleation to the mature slip-weakening state that is controlled by the residual friction, a long run-out distance occurs, resulting in a potential risk of triggering damaging earthquakes. In conclusion, our results recommend deploying geo-energy applications under the rock properties, background loading and injection conditions that correspond to the slip regimes US-1, SS-2b, and SS-4, excluding the conditions in US-4, US-5, and SS-1, and making a further assessment for the conditions in SS-2a, SS-3, US-2, and US-3, according to the induced seismicity potential and the seismic magnitude. On the contrary, if the poroelastic effects are neglected, not only the favorable conditions in US-1and SS-2b are lost, but also the unfavorable conditions in SS-1 cannot be recognized, which may significantly impede the successful deployment of geo-energy projects.

We also point out some interesting topics connected to our current results, such as simulating the dynamic rupture propagation after nucleation, heterogeneity in frictional properties along the fault, slow slip event, slip-induced pressure drop. The developed interfacial slip model including poroelastic effects can provide valuable fundaments and insights for the suggested future investigations on these topics. This model is useful to develop effective forecasting methodologies of injection-induced seismicity.

6 Conclusions

This Thesis addresses two poromechanical coupling issues related to fluid-induced seismicity to enable the successful deployment of geo-energy applications. Relevant results make a substantial advance in understanding the processes and mechanisms of induced seismicity, greatly promoting the development of risk assessment forecasting tools. The main conclusions of this Thesis are summarized below.

Analytical approach is useful for understanding and forecasting induced seismicity because it provides an instantaneous solution and serves to identify important scaling relationships that can give insights of the triggering mechanisms. We propose two closed-form solutions for the poromechanical stress and displacement, respectively, due to reservoir pressurization/ depletion. The solutions are derived based on the inclusion theory and Green's function under plane strain conditions. The solutions can be used for various geological settings in which a reservoir compartmentalized by an intersecting fault that could be either permeable or impermeable with an arbitrary dip angle and offset. For problems with a non-uniform pore pressure changes in the reservoir, both solutions are also available by applying the principle of superposition. With these solutions in hand, we can quickly evaluate the poromechanical stress along the fault and the ground uplift/subsidence, and thus, the slipping fault patch size and induced seismicity potential as well as the magnitude of earthquakes. We can also perform various parametric space, uncertainty, and stochastic analyses for cases with a high uncertain geological setting, like the Pohang M_w5.5 earthquake. Incorporating the poromechanical stress solution into the interfacial slip model of cracks allows further to take into account stress heterogeneities and geological features in a reservoir for the initial fault slip, nucleation process, and the initiation of dynamic rupture propagation. Applying this interfacial slip model including poromechanical stress greatly improves the estimate of earthquake magnitude. Thus, these physics-based analytical solutions and models developed in this Thesis represent a powerful tool for site selection, estimating land uplift/subsidence, gaining insights of reservoir and fault geometries, revealing precursors of induced seismicity, and supporting decision making during the full lifetime of geo-energy projects.

When the geological setting with faults intersecting reservoirs undergoes poromechanical response to fluid injection, the induced poromechanical stress concentrates along the fault plane, especially around the cross-points among the reservoir, surrounding, and fault because of the stress concentration effect. Poromechanical stress can stabilize the fault patch that is intersected with the reservoir, but destabilize some other patches. As a consequence, the fault may be reactivated locally, resulting in slipping fault patches and increasing induced seismicity potential. The maximum slipping fault patch size of an impermeable fault is 3 to 5 times larger than that of a permeable fault. Thus, the induced seismicity potential, and thus, the earthquake magnitude if earthquakes occur, is larger for impermeable than for

permeable faults. The slipping fault patch size increases with fault offset for permeable faults, is independent of the offset for impermeable faults, and increases with the initial deviatoric stress for both permeable and impermeable faults, implying that non-offset permeable faults and low initial deviatoric stress constitute a safer choice for site selection. Neglecting the poromechanical coupling effects, i.e., assuming the effective stress reduction is equivalent to the overpressure, will significantly misjudge fault stability and induced seismicity potential.

Unlike the distribution of poromechanical stress, the poromechanical displacement concentrates on the boundaries of the pressurized reservoir, i.e., reservoir pressurization leads to reservoir dilatation towards its surroundings. Also, unlike the unfavorable effect of impermeable faults on induced seismicity potential, fault permeability mainly impacts the spatial distribution of displacement while its effect on displacement magnitude is small. Ground displacement increases with fault dip, decreases with increasing fault offset, and is proportional to the vertical and lateral depth ratios, defined as the ratios of reservoir thickness (h) and width (w) to reservoir depth (D), respectively. Furthermore, reservoir geometry shows a stronger effect than fault geometry on displacement. The vertical component of ground displacement concentrates on the point projected to the vertical reservoir center, and the horizontal component symmetrically focuses on locations outward the lateral reservoir boundaries. The fault dip, offset, and reservoir thickness basically have no impact on this spatial distribution except for the offset slightly affecting its symmetry. The maximum vertical displacement is the double of the horizontal one regardless of fault permeability, fault and reservoir geometries, and mechanical parameters. Neglecting the free surface underestimates the poromechanical displacement in the overburden. The validity of full-space solutions can be assessed with the product of the lateral and vertical depth ratios, i.e., wh/D^2, which become valid when wh/D^2 decreases to an intrinsic threshold. This threshold may range from 0.01 to 0.02 for displacement, and its specific value depends on the field background and demands of projects, but can be estimated based on our solution. The threshold is larger for stress than for displacement, and $wh/D^2 \leq 0.1$ is recommended for induced stress.

The high uncertainty of geological setting at the Pohang EGS site leads to the debate about triggering mechanisms of the Pohang M_w5.5 earthquake. We make a comparative analysis for the existing estimates of in-situ stress based on the Mohr-Coulomb criterion, finding two likely oblique-slip faulting patterns that can be used to analyze this earthquake: a reverse-slip-dominated pattern with a strike-slip component (RS-S) and a strike-slip-dominated pattern with a reverse component (SS-R). Deterministic analysis presents that the RS-S pattern is more prone to slip as a result of poromechanical perturbation than the SS-R pattern despite both the fault being more stable at the initial state and the overpressure on the fault being one order of magnitude larger in the latter than in the former. Probabilistic assessment shows a higher probability of inducing earthquakes with a magnitude of $M_w > 5.5$ in the RS-S pattern than in the SS-R pattern. The relatively higher probability density for $M_w < 2.0$ in the RS-S pattern than in the SS-R pattern indicates that the RS-S pattern may matches

better with the fact that the majority of recorded seismicity is smaller than M_w2.0. These three observations suggest that the RS-S pattern is closer to the actual scenario of the Pohang case than the SS-R pattern, which means that the most likely in-situ stress and fault plane are IS1 and FP5, respectively, i.e., a reverse fault with a relative low-dip angle being in a 3D reverse faulting stress regime. The stochastic analysis reveals a clear threshold of the initial *CFS* to judge if the fault is critically stressed or not. This threshold is site dependent and is -0.1 MPa for the Pohang EGS site. In addition, results also highlight that (1) the magnitude of in-situ stress and the friction coefficient are playing a more significant role in inducing a seismic event than Biot's coefficient and fault geometry; (2) a small overpressure can induce a damaging earthquake when preexisting faults are critically stressed at the initial state; and (3) we should devote more efforts to site characterization at the prior stage of projects.

Earthquake nucleation process characterizes the intermediate evolution phase between the initial fault reactivation and the final dynamic rupture propagation. Including poromechanical effects in the rock mass drastically affects the nucleation process, revealing a wider range of slip regimes and reducing the expected magnitude of induced seismicity in some slip regimes. In detail, the poromechanical response to pore pressure diffusion within a longitudinally permeable fault zone tends to resist the pressure buildup and thus, reduces the slip and shear stress drop along the slipping fault patch (crack). As a result, the initiation of both the quasi-static fault slip and ultimately dynamic rupture are delayed, and the crack size associated with the slip-weakening-dominated nucleation is reduced. Such reduction in crack size is more visible once poromechanical effects can nucleate a dynamic rupture because the poroelasticity-nucleated dynamic rupture partly releases the stored elastic energy by means of microseismicity. The self-arrested dynamic rupture (existing in some slip regimes, i.e., certain conditions) can cause the crack to run out during the entire nucleation process. When the crack directly runs from the poroelasticity-dominated nucleation to the mature slip-weakening state that is controlled by the residual friction, a long run-out distance occurs, resulting in a potential risk of triggering damaging earthquakes. We generate maps of slip regime and earthquake magnitude with respect to the normalized fault understress and volumetric injection rate. The map is divided into five unstable (US) and four ultimately stable (SS) slip regimes, with some of them including two sub-regimes, based on the different characteristics of nucleation process. The two maps recommend deploying geo-energy applications under the rock properties, background loading and injection conditions that correspond to the slip regimes US-1, SS-2b, and SS-4, excluding the conditions in US-4, US-5, and SS-1, and making a further assessment for the conditions in SS-2a, SS-3, US-2, and US-3. On the contrary, if the poromechanical effects are neglected, not only the favorable conditions in US-1and SS-2b are lost, but also the unfavorable conditions in SS-1 cannot be recognized, which may significantly impede the successful deployment of geo-energy projects.

Appendices

A. Inclusion theory and induced stress

The fundamental concept of the inclusion theory lies on a series of imaginary steps involving cutting, transforming and restoring the inclusion itself (Eshelby, 1957; Mura, 1987; Rudnicki, 2011). In the last step, restoring the inclusion to its original shape and size, i.e., with zero strain, corresponds to the application of a stress field $\boldsymbol{\sigma}^*$ (eigenstress) inside the inclusion, to neutralize the volumetric eigenstrain $\boldsymbol{\varepsilon}^*$ that it would undergo if unbounded, and of simultaneous a body force $\mathbf{f}$ (restoring force) over the entire matrix, to keep the stress equilibrium (Rudnicki, 2011; Jansen et al., 2019). For the case of uniform pore pressure change inside the inclusion, Δp, then

$$\mathbf{f}(x,y,z) = -\alpha \Delta p \mathbf{n}_{\boldsymbol{\Gamma}}(x,y,z), \tag{A1}$$

where the vector $\mathbf{f}$ has three components in the coordinate directions for three-dimensional (3D) problem, $\mathbf{n}_{\boldsymbol{\Gamma}}$ is the unit normal vector pointing outward from the boundary (Γ) of the inclusion, x, y and z are the Cartesian coordinates, and α is Biot's coefficient. The term $-\alpha\Delta p$ indicates the normal eigenstress for the 3D scenario.

Affected by the opposite restoring force, a displacement field $u_i(x,y,z)$ is provoked in the inclusion and its surrounding rock

$$u_i(x,y,z) = \alpha \Delta p \iint_{\Gamma} \tilde{\mathbf{g}}_i(x,y,z,\varsigma,\xi,\psi) \cdot \mathbf{n}_{\boldsymbol{\Gamma}}(\varsigma,\xi,\psi)\, d\Gamma, \tag{A2}$$

where,

$$\tilde{\mathbf{g}}_i(x,y,z,\varsigma,\xi,\psi) = \left[\tilde{\mathrm{g}}_{ix}(x,y,z,\varsigma,\xi,\psi), \tilde{\mathrm{g}}_{iy}(x,y,z,\varsigma,\xi,\psi), \tilde{\mathrm{g}}_{iz}(x,y,z,\varsigma,\xi,\psi)\right]^T, \tag{A3}$$

and $\tilde{\mathrm{g}}_{ij}(x,y,z,\varsigma,\xi,\psi)$ is the Green's function describing the displacement at any point (x,y,z) under a unit body force at point (ς,ξ,ψ), ς,ξ,ψ are the coordinate values on Γ, subscripts i and j are free indexes with $i, j \in (x,y,z)$ in the 3D Cartesian space.

For an infinite elastic unbounded domain, the $\tilde{\mathrm{g}}_{ij}(x,y,z,\varsigma,\xi,\psi)$ can be expressed as (Love, 1944; Mura, 1987)

$$\tilde{\mathrm{g}}_{ij}(x,y,z,\varsigma,\xi,\psi) = \frac{\delta_{ij}}{4\pi\mu\tilde{R}} - \frac{1}{16\pi\mu(1-\nu)} \frac{\partial^2}{\partial x_i \partial x_j} \tilde{R}, \tag{A4}$$

where μ and ν are the shear modulus and Poisson's ratio, respectively, δ_{ij} is the Kronecker delta, which equals 1 if $i = j$ or 0 if $i \neq j$, and

$$\tilde{R}^2 = (x-\varsigma)^2 + (y-\xi)^2 + (z-\psi)^2 . \tag{A5}$$

Equation (A2) is a standard surface integral and can be transformed into a volume integral by applying the Gauss's divergence theorem

$$u_i(x,y,z) = \alpha\Delta p \iiint_\Omega \nabla \cdot \tilde{\mathbf{g}}_i(x,y,z,\varsigma,\xi,\psi)\, d\Omega , \tag{A6}$$

where Ω means the inclusion volume. Note that now ς,ξ,ψ in Equation (A6) denote the coordinate values in the domain Ω.

Under the assumption of plane strain, integrating Equation (A4) along the out-of-plane dimension (z) yields (Mura, 1987; Jansen et al., 2019)

$$\tilde{\mathrm{g}}_{ij}(x,y,\varsigma,\xi) = \frac{1}{8\pi\mu(1-\nu)}\left[\frac{\bar{x}_i \cdot \bar{x}_j}{R^2} - (3-4\nu)\delta_{ij}\ln R\right] \qquad i,j \in (x,y), \tag{A7}$$

where,

$$\bar{x}_i = |x-\varsigma| \text{ or } |y-\xi| , \tag{A8}$$

$$R^2 = (x-\varsigma)^2 + (y-\xi)^2 . \tag{A9}$$

Equation (A6) can be simplified into

$$u_i(x,y) = \alpha\Delta p \iint_\Omega \frac{\partial \tilde{g}_{ix}}{\partial\varsigma} + \frac{\partial \tilde{g}_{iy}}{\partial\zeta} d\Omega = D\iint_\Omega g_i(x,y,\varsigma,\xi) d\Omega , \tag{A10}$$

where $g_i(x,y,\varsigma,\xi)$ is

$$g_x(x,y,\varsigma,\xi) = \frac{x-\varsigma}{2R^2} , \tag{A11}$$

$$g_y(x,y,\varsigma,\xi) = \frac{y-\xi}{2R^2} , \tag{A12}$$

and *D* is a dimensionless scaling parameter

$$D = \frac{(1-2\nu)\alpha\Delta p}{2\pi(1-\nu)\mu} = \frac{(1+\nu)\alpha\Delta p}{3\pi(1-\nu)K} , \tag{A13}$$

where *K* is the bulk modulus.

For an isotropic linear elastic material, the Hooke's equation relating the stress σ_{ij} to the strain ε_{ij} tensor is

$$\sigma_{ij} = 2\mu\varepsilon_{ij} + \frac{2\mu\nu}{1-2\nu}\delta_{ij}\varepsilon_{kk} , \tag{A14}$$

where ε_{kk} is the volumetric strain and ε_{ij} equals the symmetric part of the displacement gradient

$$\varepsilon_{ij} = \frac{1}{2}\left(\frac{\partial u_i}{\partial x_j} + \frac{\partial u_j}{\partial x_i}\right). \tag{A15}$$

Substituting Equation (A10) into Equation (A15), and taking the results into Equation (A14), yields the expression of the stress field in the whole matrix induced by the restoring force **f**

$$\sigma_{ij}(x, y) = C\iint_{\Omega} g_{ij}(x, y, \varsigma, \xi) d\Omega, \tag{A16}$$

where $C = \mu D$ is a scaling parameter and $g_{ij}(x, y, \varsigma, \xi)$ is the Green's function for stress at (x, y) given a unit point force at (ς, ξ)

$$g_{xx}(x, y, \varsigma, \xi) = 2\frac{\partial g_x}{\partial x} = \frac{(y-\xi)^2 - (x-\varsigma)^2}{R^4}, \tag{A17}$$

$$g_{yy}(x, y, \varsigma, \xi) = 2\frac{\partial g_y}{\partial y} = \frac{(x-\varsigma)^2 - (y-\xi)^2}{R^4}, \tag{A18}$$

$$g_{xy}(x, y, \varsigma, \xi) = 2\frac{\partial g_x}{\partial y} = -2\frac{(x-\varsigma)(y-\xi)}{R^4}. \tag{A19}$$

For the inclusion, the stress field however is also affected by the eigenstress resulting from the application of the surface traction to bring the inclusion back to its initial configuration (Eshelby, 1957). Since the surface traction depends on the geometry of the inclusion, such eigenstress is different with the one of 3D scenario for the case of plane strain problem. Regarding that the eigenstrain is a pure dilatational strain, only the normal components of eigenstress has a finite value (Eshelby, 1957; Soltanzadeh and Hawkees, 2008), thus

$$\sigma_{ij}(x, y) = C\iint_{\Omega} g_{ij}(x, y, \varsigma, \xi) d\Omega + \sigma^* \delta_{ij} \delta_{\Omega} = CG_{ij}(x, y) + \sigma^* \delta_{ij} \delta_{\Omega}, \tag{A20}$$

where $G_{ij}(x, y)$ denotes the surface integral of Green's function $g_{ij}(x, y, \varsigma, \xi)$, δ_{Ω} is the modified Kronecker delta

$$\delta_{\Omega} = \begin{cases} 1 & \text{if} \quad (x, y) \in \Omega \\ 0 & \text{if} \quad (x, y) \notin \Omega \end{cases}. \tag{A21}$$

From the perspective of stress arching effect, the induced stress field caused by pore pressure change in the inclusion can be described as (Soltanzadeh and Hawkees, 2008)

$$\sigma_{ij} = -\gamma_{ij} \alpha \Delta p, \tag{A22}$$

where γ_{ij} is the normalized stress arching ratio, which depends on the geometry of the inclusion. The minus means that injection corresponds to compression.

For the ellipsoidal inclusions, the stress and strain fields are uniform for all points inside the inclusion (Eshelby, 1957; Rudnicki, 1999). And for the case in which the inclusion extends infinite in one direction (implying that we can apply the plane strain assumption), such as the elliptic cylindrical inclusion, the sum of the stress arching ratio in the other two directions is a constant (Soltanzadeh and Hawkees, 2008; Soltanzadeh, 2009)

$$\gamma_{xx} + \gamma_{yy} = \frac{(1-2\nu)}{1-\nu}. \tag{A23}$$

According to Equations (A20) to (A23), we find

$$C\left[G_{xx}(x,y) + G_{yy}(x,y)\right] + 2\sigma^* = -\frac{1-2\nu}{1-\nu}\alpha\Delta p\,. \tag{A24}$$

Given that $g_{xx}(x,y,\varsigma,\xi) = -g_{yy}(x,y,\varsigma,\xi)$ (Equations (A17) and (A18)), thus

$$\sigma^* = -\frac{1-2\nu}{2(1-\nu)}\alpha\Delta p\,. \tag{A25}$$

Although Equation (A25) is derived for an elliptic cylindrical inclusion, it is valid for all the geometric inclusions that can be regarded as plane strain problem, because the inclusion only undergoes a pure dilatational deformation. Introducing Equation (A25) into Equation (A20) we obtain the final expression of the induced stress tensor both in the inclusion and its surrounding rock, as given in Equation (2.1). All the variables/parameters adopted in this Appendix will keep the same physical meaning when we use them in the following Appendices B-D.

B. Surface integral of Green's function for stress

In this appendix, we solve the surface integrals of Equation (2.1). The entire inclusion is divided into two trapezoids by the fault. The surface integral of one function over a trapezoid can be regarded as the sum of the integrations over a triangle and a rectangle (Figure B1). The integrand function is the Green's function for stress given in Equations (A17)-(A19). We need to consider the existence of singularities for values of ς and ξ equal x and y, respectively, where the Green's function becomes infinite. This only occurs for points (x, y) located inside the inclusion, for which the integral become improper. Thus, we perform the regular bounded integral for (x, y) located outside the inclusion, while for (x, y) located inside the inclusion we solve the improper integral by excluding a neighborhood of the singularity. To generalize the integration of Green's function, we apply an arbitrary coordinate system, as shown in Figure B1. After solving the surface integrals over the triangular and rectangular domains, the solutions are transformed into the coordinate system of Figure 2.1.

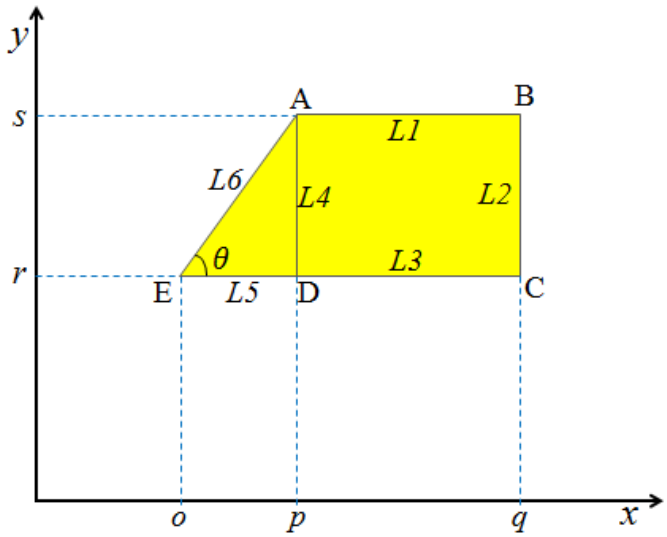

Figure B1: Schematic geometry of triangular and rectangular domains in an arbitary coordinate system

Rectangular Inclusion:

For (x, y) located outside of the rectangle, we calculate the surface integral of the Green's function for horizontal stress $g_{xx}(x, y, \varsigma, \xi)$ using standard techniques and we obtain

$$
\begin{aligned}
G_{xx}^{\text{out}}(x,y) &= \int_r^s \int_p^q g_{xx}(x,y,\varsigma,\xi)\, d\varsigma d\xi \\
&= \int_r^s -\left[\frac{x-\varsigma}{(x-\varsigma)^2+(y-\xi)^2} \right]_p^q d\xi \\
&= \left[\operatorname{atan}\frac{y-\xi}{x-q} - \operatorname{atan}\frac{y-\xi}{x-p} \right]_r^s \\
&= \operatorname{atan}\frac{y-s}{x-q} - \operatorname{atan}\frac{y-s}{x-p} - \operatorname{atan}\frac{y-r}{x-q} + \operatorname{atan}\frac{y-r}{x-p}
\end{aligned}
\quad . \tag{B1}
$$

If (x, y) is located in the rectangle, we need to consider the improper integration of the Green's function. Note that if standard integration (like in Equation (B1)) is applied for such points, the result depends on the order of integration, because Fubini's theorem (DiBenedetto, 2016) does not hold in this case. We solve the improper integral excluding a neighborhood of the singular point (ς, ξ) = (x, y), which makes the integrand function being bounded. We observe that $g_{xx}(x,y,\varsigma,\xi)$ is antisymmetric with respect to the line y - ξ = x - ς, that is, $g_{xx}(x,y,\varsigma,\xi) = -g_{xx}(y,x,\xi,\varsigma)$. This means that the integral is zero for a square domain centered in the singular point, because the contribution from the triangle above the symmetry line cancels with the contribution from the triangle below. Therefore, we can exclude a square neighborhood of any size contained in the domain Ω and centered in the singular point. In the rest of the domain Fubini's theorem holds and we can apply the standard sequential integration (Equation (B1)). For the square domain, the actual contribution is zero while standard integration technique gives π, which can be checked by substituting y - r = x - p = s - y = q - x into Equation (B1). Therefore, we must remove the offending contribution, so that the integral for points inside the inclusion is

$$
G_{xx}^{\text{in}}(x,y) = G_{xx}^{\text{out}}(x,y) - \pi\,. \tag{B2}
$$

Note that this result is independent on the order of integration.

Equations (B1) and (B2) only differ for the last term $-\pi$, which is a result of the improper integral for points located inside the reservoir. We therefore express the surface integral in the general form

$$
G_{xx}(x,y) = \operatorname{atan}\frac{y-r}{x-p} - \operatorname{atan}\frac{y-r}{x-q} - \operatorname{atan}\frac{y-s}{x-p} + \operatorname{atan}\frac{y-s}{x-q} - \pi\delta_\Omega \tag{B3}
$$

with δ_Ω defined in Equation (A21).

There are four singularities at the corners (A, B, C and D) of the rectangular inclusion domain (Figure 2.B1) where the arguments in Equation (B3) become indefinite (i.e., 0/0). The integral is in fact not defined at these points, and it is discontinuous there (different values are obtained when approaching it from one side or the other).

The same procedure can be applied to integrate the Green's function for vertical stress $g_{yy}(x,y,\varsigma,\xi)$. Since $g_{yy}(x,y,\varsigma,\xi) = -g_{xx}(x,y,\varsigma,\xi)$ (see Equations (A17) and (A18)), it follows

$$G_{yy}(x,y) = \int_r^s \int_p^q g_{yy}(x,y,\varsigma,\xi)\, d\varsigma d\xi = -G_{xx}(x,y)\,. \tag{B4}$$

To integrate the Green's function for shear stress $g_{xy}(x,y,\varsigma,\xi)$, we follow the same procedure used to integrate $g_{xx}(x,y,\varsigma,\xi)$. We observe that $g_{xy}(x,y,\varsigma,\xi)$ is antisymmetric with respect to $y - \xi = 0$ or $x - \varsigma = 0$, therefore the integral over a square domain centered in the singular point is 0. We also observe that standard sequential integration technique in this case gives

$$\begin{aligned} G_{xy}(x,y) &= \int_p^q \int_r^s g_{xy}(x,y,\varsigma,\xi)\, d\xi d\varsigma \\ &= \int_p^q \left[\frac{-(x-\varsigma)}{(x-\varsigma)^2 + (y-\xi)^2} \right]_r^s d\varsigma = \frac{1}{2}\left[\ln \frac{(x-\varsigma)^2 + (y-s)^2}{(x-\varsigma)^2 + (y-r)^2} \right]_p^q . \\ &= \frac{1}{2} \ln \frac{\left[(x-q)^2 + (y-s)^2\right]\left[(x-p)^2 + (y-r)^2\right]}{\left[(x-q)^2 + (y-r)^2\right]\left[(x-p)^2 + (y-s)^2\right]} \end{aligned} \tag{B5}$$

Application of Equation (B5) for a square neighborhood of the singular point gives 0, which demonstrates that Equation (B5) is valid for both the cases of (x, y) located outside or inside the inclusion.

In Equation (B5), there are four singularities at the corners A, B, C and D.

Triangular Inclusion:

For the integration over a triangular inclusion, we apply the same technique adopted for the case of the rectangular inclusion. As an example, the integral of the Green's function for horizontal stress is

$$\begin{aligned} G_{xx}(x,y) &= \int_r^s \int_{\xi\cot\theta}^p \frac{(y-\xi)^2 - (x-\varsigma)^2}{\left[(x-\varsigma)^2 + (y-\xi)^2\right]^2} d\varsigma d\xi - \pi\delta_\Omega \\ &= \int_r^s -\left[\frac{x-\varsigma}{(x-\varsigma)^2 + (y-\xi)^2} \right]_{\xi\cot\theta}^p d\xi - \pi\delta_\Omega \quad , \\ &= \left[\operatorname{atan} \frac{y-\xi}{x-p} \right]_r^s + \int_r^s \frac{x - \xi\cot\theta}{(x-\xi\cot\theta)^2 + (y-\xi)^2} d\xi - \pi\delta_\Omega \end{aligned} \tag{B6}$$

where the last term $-\pi\delta_\Omega$ takes into account the effect of the improper integral for

points located inside the inclusion. The integration of the second term in the right-hand side of Equation (B6) is non-trivial and a potential solution can be obtained by the following transformation

$$\begin{aligned} x-\xi\cot\theta = &[(x-\xi\cot\theta)\cos^2\theta+(y-\xi)\sin\theta\cos\theta] \\ &+[(x-\xi\cot\theta)\sin^2\theta-(y-\xi)\sin\theta\cos\theta] \end{aligned}. \tag{B7}$$

Substituting Equation (B7) into Equation (B6) and after some derivations, we obtain

$$\begin{aligned} \int_r^s \frac{x-\xi\cot\theta}{\left(x-\xi\cot\theta\right)^2+\left(y-\xi\right)^2}d\xi = &-\frac{\sin\theta\cos\theta}{2}\left[\ln\left[\left(x-\xi\cot\theta\right)^2+\left(y-\xi\right)^2\right]\right]_r^s \\ &-\sin^2\theta\left[\operatorname{atan}\frac{(x-\xi\cot\theta)\cot\theta+(y-\xi)}{x-y\cot\theta}\right]_r^s \end{aligned}. \tag{B8}$$

The final expression of the integration of the Green's function for horizontal stress over a triangular inclusion domain is

$$\begin{aligned} G_{xx}(x,y) = &\operatorname{atan}\frac{y-s}{x-p}-\operatorname{atan}\frac{y-r}{x-p}-\frac{\sin\theta\cos\theta}{2}\ln\frac{f_2(x,y,s)}{f_2(x,y,r)}, \\ &-\left[f_1(x,y,s)-f_1(x,y,r)\right]\sin^2\theta-\pi\delta_\Omega \end{aligned} \tag{B9}$$

where functions f_1 and f_2 are

$$f_1(x,y,\hat{y}) = \operatorname{atan}\frac{(x-\hat{y}\cot\theta)\cot\theta+(y-\hat{y})}{x-y\cot\theta}, \tag{B10}$$

$$f_2(x,y,\hat{y}) = \left(x-\hat{y}\cot\theta\right)^2+\left(y-\hat{y}\right)^2. \tag{B11}$$

Similarly, integrations of the Green's function for the vertical and shear stress components over a triangular inclusion domain are

$$G_{yy}(x,y) = \int_r^s\int_{\xi\cot\theta}^p g_{yy}(x,y,\varsigma,\xi)\,d\varsigma d\xi = -G_{xx}(x,y), \tag{B12}$$

$$\begin{aligned} G_{xy}(x,y) &= \int_r^s\int_{\xi\cot\theta}^p g_{xy}(x,y,\varsigma,\xi)\,d\varsigma d\xi \\ &= \left[f_1(x,y,s)-f_1(x,y,r)\right]\sin\theta\cos\theta \\ &\quad -\frac{\sin^2\theta}{2}\ln\frac{f_2(x,y,s)}{f_2(x,y,r)}+\frac{1}{2}\ln\frac{f_3(x-p,y-s)}{f_3(x-p,y-r)} \end{aligned}, \tag{B13}$$

where function f_3 is

$$f_3(x-\hat{x},y-\hat{y}) = (x-\hat{x})^2+(y-\hat{y})^2, \tag{B14}$$

The singularities are located at the three corners A, D and E in this case.

Trapezoidal Inclusion:

We apply the superposition principle and obtain the integrations of the Green's

function for the stress components over a trapezoid as the combination of the above integrals for rectangular and triangular inclusions

$$\begin{aligned} G_{xx}(x,y) &= \int_r^s \int_{\xi\cot\theta}^{p} g_{xx}(x,y,\varsigma,\xi)\,d\varsigma d\xi + \int_r^s \int_p^q g_{xx}(x,y,\varsigma,\xi)\,d\varsigma d\xi \\ &= \operatorname{atan}\frac{y-s}{x-q} - \operatorname{atan}\frac{y-r}{x-q} - \frac{\sin\theta\cos\theta}{2}\ln\frac{f_2(x,y,s)}{f_2(x,y,r)} \\ &\quad -\left[f_1(x,y,s) - f_1(x,y,r)\right]\sin^2\theta - \pi\delta_\Omega \end{aligned}, \tag{B15}$$

$$G_{yy}(x,y) = \int_r^s \int_{\xi\cot\theta}^{p} g_{yy}(x,y,\varsigma,\xi)\,d\varsigma d\xi + \int_r^s \int_p^q g_{yy}(x,y,\varsigma,\xi)\,d\varsigma d\xi = -G_{xx}(x,y), \tag{B16}$$

$$\begin{aligned} G_{xy}(x,y) &= \int_r^s \int_{\xi\cot\theta}^{p} g_{xy}(x,y,\varsigma,\xi)\,d\varsigma d\xi + \int_r^s \int_p^q g_{xy}(x,y,\varsigma,\xi)\,d\varsigma d\xi \\ &= \left[f_1(x,y,s) - f_1(x,y,r)\right]\sin\theta\cos\theta \\ &\quad -\frac{\sin^2\theta}{2}\ln\frac{f_2(x,y,s)}{f_2(x,y,r)} + \frac{1}{2}\ln\frac{f_3(x-q,y-s)}{f_3(x-q,y-r)} \end{aligned}. \tag{B17}$$

Note that the last term in Equation (B15) is a consequence of having improper integrals either for the rectangle or the triangle, i.e., (x, y) falls within the rectangle or the triangle. In Equations (B15)-(B17), the singularities are located at the four corners A, B, C and E of the trapezoid.

Application into a specific coordinate system:

For a permeable fault, pore pressure changes at both sides of the fault during fluid injection or production and thus, the inclusion is composed by two trapezoids. The analytical expressions of integration of the Green's function for the stress components in the general coordinate system is transformed into the coordinate system of Figure 2.1 such as

$$\begin{aligned} G_{xx}(x,y) &= \int_a^{-b} \int_{\xi\cot\theta}^{-b\cot\theta} g_{xx}(x,y,\varsigma,\xi)\,d\varsigma d\xi + \int_a^{-b} \int_{-b\cot\theta}^{-c} g_{xx}(x,y,\varsigma,\xi)\,d\varsigma d\xi \\ &\quad + \int_{-a}^{b} \int_{\xi\cot\theta}^{b\cot\theta} g_{xx}(x,y,\varsigma,\xi)\,d\varsigma d\xi + \int_{-a}^{b} \int_{b\cot\theta}^{d} g_{xx}(x,y,\varsigma,\xi)\,d\varsigma d\xi \\ &= \int_a^{-b} \int_{\xi\cot\theta}^{-c} g_{xx}(x,y,\varsigma,\xi)\,d\varsigma d\xi + \int_{-a}^{b} \int_{\xi\cot\theta}^{d} g_{xx}(x,y,\varsigma,\xi)\,d\varsigma d\xi \\ &= \operatorname{atan}\frac{y+b}{x+c} - \operatorname{atan}\frac{y-a}{x+c} + \operatorname{atan}\frac{y-b}{x-d} - \operatorname{atan}\frac{y+a}{x-d} \\ &\quad -\left[f_1(x,y,-b) - f_1(x,y,a) + f_1(x,y,b) - f_1(x,y,-a)\right]\sin^2\theta \\ &\quad -\frac{\sin\theta\cos\theta}{2}\ln\frac{f_2(x,y,-b)\,f_2(x,y,b)}{f_2(x,y,a)\,f_2(x,y,-a)} - \pi\delta_\Omega \end{aligned}, \tag{B18}$$

$$G_{yy}(x,y) = \int_a^{-b} \int_{\xi\cot\theta}^{-c} g_{yy}(x,y,\varsigma,\xi)\,d\varsigma d\xi + \int_{-a}^{b} \int_{\xi\cot\theta}^{d} g_{yy}(x,y,\varsigma,\xi)\,d\varsigma d\xi = -G_{xx}(x,y), \tag{B19}$$

$$
\begin{aligned}
G_{xy}(x,y) &= \int_a^{-b}\int_{\xi\cot\theta}^{-c} g_{xy}(x,y,\varsigma,\xi)\,d\varsigma d\xi + \int_{-a}^{b}\int_{\xi\cot\theta}^{d} g_{xy}(x,y,\varsigma,\xi)\,d\varsigma d\xi \\
&= \left[f_1(x,y,-b) - f_1(x,y,a) + f_1(x,y,b) - f_1(x,y,-a)\right]\sin\theta\cos\theta \\
&\quad -\frac{\sin^2\theta}{2}\ln\frac{f_2(x,y,-b)\,f_2(x,y,b)}{f_2(x,y,a)\,f_2(x,y,-a)} + \frac{1}{2}\ln\frac{f_3(x+c,y+b)\,f_3(x-d,y-b)}{f_3(x+c,y-a)\,f_3(x-d,y+a)}
\end{aligned}
\quad . \tag{B20}
$$

If c and d have finite value, the inclusion represents a finite reservoir and there are eight singularities for the solution: the four corners P1, P2, P3 and P4 located on the fault (Figure 2.1) and the four corners on the outer boundary of the faulted reservoir. If $c = d = \infty$, the reservoir is infinite and there are only the four singularities located on the fault.

For a vertical fault ($\theta = 90°$), such integral solutions read

$$
\begin{aligned}
G_{xx}(x,y) &= -G_{yy}(x,y) \\
&= \int_{-b}^{a}\int_{-c}^{0} g_{xx}(x,y,\varsigma,\xi)\,d\varsigma\,d\xi + \int_{-a}^{b}\int_{0}^{d} g_{xx}(x,y,\varsigma,\xi)\,d\varsigma d\xi \\
&= \operatorname{atan}\frac{y-a}{x} - \operatorname{atan}\frac{y-a}{x+c} - \operatorname{atan}\frac{y+b}{x} + \operatorname{atan}\frac{y+b}{x+c} \\
&\quad + \operatorname{atan}\frac{y-b}{x-d} - \operatorname{atan}\frac{y-b}{x} - \operatorname{atan}\frac{y+a}{x-d} + \operatorname{atan}\frac{y+a}{x} - \pi\delta_\Omega
\end{aligned}
\quad , \tag{B21}
$$

$$
\begin{aligned}
G_{xy}(x,y) &= \int_{-c}^{0}\int_{-b}^{a} g_{xy}(x,y,\varsigma,\xi)\,d\xi d\varsigma + \int_{0}^{d}\int_{-a}^{b} g_{xy}(x,y,\varsigma,\xi)\,d\xi d\varsigma \\
&= \frac{1}{2}\ln\frac{f_3(x,y-a)\,f_3(x+c,y+b)\,f_3(x-d,y-b)\,f_3(x,y+a)}{f_3(x,y+b)\,f_3(x+c,y-a)\,f_3(x-d,y+a)\,f_3(x,y-b)}
\end{aligned}
\quad , \tag{B22}
$$

and for a zero offset fault in which $a = b$, we have

$$
\begin{aligned}
G_{xx}(x,y) &= -G_{yy}(x,y) \\
&= \operatorname{atan}\frac{y+b}{x+c} - \operatorname{atan}\frac{y-a}{x+c} + \operatorname{atan}\frac{y-b}{x-d} - \operatorname{atan}\frac{y+a}{x-d} - \pi\delta_\Omega
\end{aligned}
\quad , \tag{B23}
$$

$$
G_{xy}(x,y) = \frac{1}{2}\ln\frac{f_3(x+c,y+b)\,f_3(x-d,y-b)}{f_3(x+c,y-a)\,f_3(x-d,y+a)} . \tag{B24}
$$

C. Induced stress on the fault plane

The expression for normal and tangential stress on the fault plane can be found by transforming the main coordinate system into a coordinate system placed on the fault and oriented along it. We first operate the translation, thus the horizontal and vertical integral solutions of the Green's function for the stress components on the fault plane are evaluated by setting $x = y\cot\theta$ in Equations (B18)-(B20), such that

$$\begin{aligned} G_{xx}(y\cot\theta, y) &= -G_{yy}(y\cot\theta, y) \\ &= -\frac{\pi}{2}\left[\operatorname{sgn}(y+b) - \operatorname{sgn}(y-a) + \operatorname{sgn}(y-b) - \operatorname{sgn}(y+a)\right]\sin^2\theta \\ &\quad + \operatorname{atan}\frac{y+b}{y\cot\theta + c} - \operatorname{atan}\frac{y-a}{y\cot\theta + c} + \operatorname{atan}\frac{y-b}{y\cot\theta - d} \\ &\quad - \operatorname{atan}\frac{y+a}{y\cot\theta - d} - \frac{\sin\theta\cos\theta}{2}\ln\frac{f_4(y,b)}{f_4(y,a)} - \pi\delta_\Omega \end{aligned}, \tag{C1}$$

$$\begin{aligned} G_{xy}(y\cot\theta, y) &= \frac{\pi}{2}\left[\operatorname{sgn}(y+b) - \operatorname{sgn}(y-a) + \operatorname{sgn}(y-b) - \operatorname{sgn}(y+a)\right]\sin\theta\cos\theta \\ &\quad + \frac{1}{2}\ln\frac{f_3(y\cot\theta + c, y+b)\, f_3(y\cot\theta - d, y-b)}{f_3(y\cot\theta + c, y-a)\, f_3(y\cot\theta - d, y+a)} - \frac{\sin^2\theta}{2}\ln\frac{f_4(y,b)}{f_4(y,a)} \end{aligned}, \tag{C2}$$

where sgn(•) is the sign function defined as 1 if (•) > 0, 0 if (•) = 0 or -1 if (•) <0, and function f_4 is

$$f_4(y, \hat{y}) = \left(y + \hat{y}\right)^2 \left(y - \hat{y}\right)^2. \tag{C3}$$

Substituting Equations (C1) and (C2) into Equation (2.1) yields the *x*-*y* planar induced stress along the fault plane. Subsequently, applying the stress transformation with axis rotation to transform the coordinate system, one can obtain the expression of induced normal $\sigma_n(y\cot\theta, y)$ and tangential $\tau(y\cot\theta, y)$ stress components along a fault plane with an arbitrary dip angle. Considering the sign convention and geometry adopted here, such stress transformation equations are

$$\sigma_n(y\cot\theta, y) = \frac{\sigma_{xx} + \sigma_{yy}}{2} + \frac{\sigma_{xx} - \sigma_{yy}}{2}\cos(2\theta + \pi) + \sigma_{xy}\sin(2\theta + \pi), \tag{C4}$$

$$\tau(y\cot\theta, y) = -\frac{\sigma_{xx} - \sigma_{yy}}{2}\sin(2\theta + \pi) + \sigma_{xy}\cos(2\theta + \pi). \tag{C5}$$

Substituting Equations (C1), (C2) and (2.1) into Equations (C4) and (C5) and normalizing by the scaling parameter *C* (Equation (2.2)), the dimensionless induced normal $\overline{\sigma}_n(y\cot\theta, y)$ and tangential $\overline{\tau}(y\cot\theta, y)$ stress components along the fault plane are

$$\begin{aligned}\bar{\sigma}_n(y\cot\theta, y) &= (G_{xx}-\pi\delta_\Omega)\sin^2\theta + (G_{yy}-\pi\delta_\Omega)\cos^2\theta - 2G_{xy}\sin\theta\cos\theta \\ &= -\frac{\pi}{2}\left[\mathrm{sgn}(y+b)-\mathrm{sgn}(y-a)+\mathrm{sgn}(y-b)-\mathrm{sgn}(y+a)\right]\sin^2\theta \\ &\quad -\cos 2\theta\left(\mathrm{atan}\frac{y+b}{y\cot\theta+c}-\mathrm{atan}\frac{y-a}{y\cot\theta+c}+\mathrm{atan}\frac{y-b}{y\cot\theta-d}\right. \\ &\quad \left.-\mathrm{atan}\frac{y+a}{y\cot\theta-d}-\pi\delta_\Omega\right)+\frac{\sin 2\theta}{4}\ln\frac{f_4(y,b)}{f_4(y,a)} \\ &\quad -\frac{\sin 2\theta}{2}\ln\frac{f_3(y\cot\theta+c,y+b)\,f_3(y\cot\theta-d,y-b)}{f_3(y\cot\theta+c,y-a)\,f_3(y\cot\theta-d,y+a)}-\pi\delta_\Omega\end{aligned} \quad , \tag{C6}$$

$$\begin{aligned}\bar{\tau}(y\cot\theta, y) &= \sin\theta\cos\theta\left[(G_{xx}-\pi\delta_\Omega)-(G_{yy}-\pi\delta_\Omega)\right]-G_{xy}(\cos^2\theta-\sin^2\theta) \\ &= -\frac{\pi}{4}\left[\mathrm{sgn}(y+b)-\mathrm{sgn}(y-a)+\mathrm{sgn}(y-b)-\mathrm{sgn}(y+a)\right]\sin 2\theta \\ &\quad +\sin 2\theta\left(\mathrm{atan}\frac{y+b}{y\cot\theta+c}-\mathrm{atan}\frac{y-a}{y\cot\theta+c}+\mathrm{atan}\frac{y-b}{y\cot\theta-d}\right. \\ &\quad \left.-\mathrm{atan}\frac{y+a}{y\cot\theta-d}-\pi\delta_\Omega\right)-\frac{\sin^2\theta}{2}\ln\frac{f_4(y,b)}{f_4(y,a)} \\ &\quad -\frac{\cos 2\theta}{2}\ln\frac{f_3(y\cot\theta+c,y+b)\,f_3(y\cot\theta-d,y-b)}{f_3(y\cot\theta+c,y-a)\,f_3(y\cot\theta-d,y+a)}\end{aligned} \quad , \tag{C7}$$

where $G_{ij}(y\cot\theta, y)$ is shorten into G_{ij} for convenience, and the four corners P1, P2, P3 and P4 on the fault plane are singularities (Figure 2.1). To simplify Equations (B18)-(B20) into Equations (C1) and (C2), we apply the general rule of taking the right limit, i.e., the limit that the argument approaches the fault from its right-hand side, as the value of the fault plane. Thus, the segment P1-P2 belongs to the inclusion, while the segment P3-P4 belongs to the surroundings for a permeable fault in the above equations.

In particular, for a vertical fault ($\theta = 90°$), we obtain

$$\begin{aligned}\bar{\sigma}_n(0, y) &= G_{xx}(0, y)-\pi\delta_\Omega \\ &= \frac{\pi}{2}\left[\mathrm{sgn}(y-a)-\mathrm{sgn}(y+b)-\mathrm{sgn}(y-b)+\mathrm{sgn}(y+a)\right] \\ &\quad +\mathrm{atan}\frac{y+b}{c}-\mathrm{atan}\frac{y-a}{c}-\mathrm{atan}\frac{y-b}{d}+\mathrm{atan}\frac{y+a}{d}-2\pi\delta_\Omega\end{aligned} \quad , \tag{C8}$$

$$\begin{aligned}\bar{\tau}(0, y) &= G_{xy}(0, y) \\ &= \frac{1}{2}\ln\frac{f_3(c,y+b)\,f_3(d,y-b)}{f_3(c,y-a)\,f_3(d,y+a)}-\frac{1}{2}\ln\frac{f_4(y,b)}{f_4(y,a)}\end{aligned} \quad , \tag{C9}$$

and for a zero offset fault, we have

$$\bar{\sigma}_n(y\cot\theta, y) = -\cos 2\theta\left(\operatorname{atan}\frac{y+b}{y\cot\theta+c} - \operatorname{atan}\frac{y-a}{y\cot\theta+c}\right.$$
$$\left. + \operatorname{atan}\frac{y-b}{y\cot\theta-d} - \operatorname{atan}\frac{y+a}{y\cot\theta-d} - \pi\delta_\Omega\right) \quad , \qquad \text{(C10)}$$
$$-\frac{\sin 2\theta}{2}\ln\frac{f_3(y\cot\theta+c, y+b)\, f_3(y\cot\theta-d, y-b)}{f_3(y\cot\theta+c, y-a)\, f_3(y\cot\theta-d, y+a)} - \pi\delta_\Omega$$

$$\bar{\tau}(y\cot\theta, y) = \sin 2\theta\left(\operatorname{atan}\frac{y+b}{y\cot\theta+c} - \operatorname{atan}\frac{y-a}{y\cot\theta+c}\right.$$
$$\left. + \operatorname{atan}\frac{y-b}{y\cot\theta-d} - \operatorname{atan}\frac{y+a}{y\cot\theta-d} - \pi\delta_\Omega\right) \quad . \qquad \text{(C11)}$$
$$-\frac{\cos 2\theta}{2}\ln\frac{f_3(y\cot\theta+c, y+b)\, f_3(y\cot\theta-d, y-b)}{f_3(y\cot\theta+c, y-a)\, f_3(y\cot\theta-d, y+a)}$$

D. Supplementary Information for Chapter 2

Two sections are included in this Appendix. Section D1 contains the detailed comparison between our analytical solution and the numerical solution of the fully coupled finite element code CODE_BRIGHT (Olivella et al., 1994; 1996) for both permeable and impermeable fault with a dip angle 60°(Text D1 and Figures D1-D6). Section D2 presents the analytical results of induced stress for a vertical permeable fault (Text D2 and Figures D7-D9).

Text D1: Detailed comparison between our analytical solution and CODE_BRIGHT for an inclined displaced fault

For verification purposes of the analytical solution, we compare in the main text (Figure 2.2) the horizontal and vertical total stress as well as the shear stress along the fault resulting from our analytical solution and the numerical results obtained with CODE_BRIGHT. Here, we present a more detailed comparison of the results, showing the contour plots and the line diagrams on induced horizontal, vertical and shear stress components in Figures D1-D6. Each figure includes four parts, (a) is the results of the analytical solution developed in the main text, (b) is the simulated results of CODE_BRIGHT, (c) and (d) are the comparisons between the analytical solution and CODE_BRIGHT at the lines x = 0 m, x = 100 m, and y = 0 m, y = 150 m, respectively. To show the features clearly, we plot both the analytical and numerical results focusing on a rectangle of 800 m by 600 m centered in the fault. Figures D1-D3 show the results for a permeable fault, and Figures D4-D6 display the results for an impermeable fault. Figures D1-D6 clearly show that the analytical results are almost identical to the numerical results, only the maximum and minimum values have a little difference because the corners are singularities for the analytical solution, which leads to an infinite stress (for representation purposes, the infinite stress is cut off to a finite value), while there is no singularity for numerical solution. Additionally, the discrete nature of the numerical solution also contributes to such discrepancies. Thus, the absolute maximum and minimum values in the numerical results are always smaller than those of the analytical results.

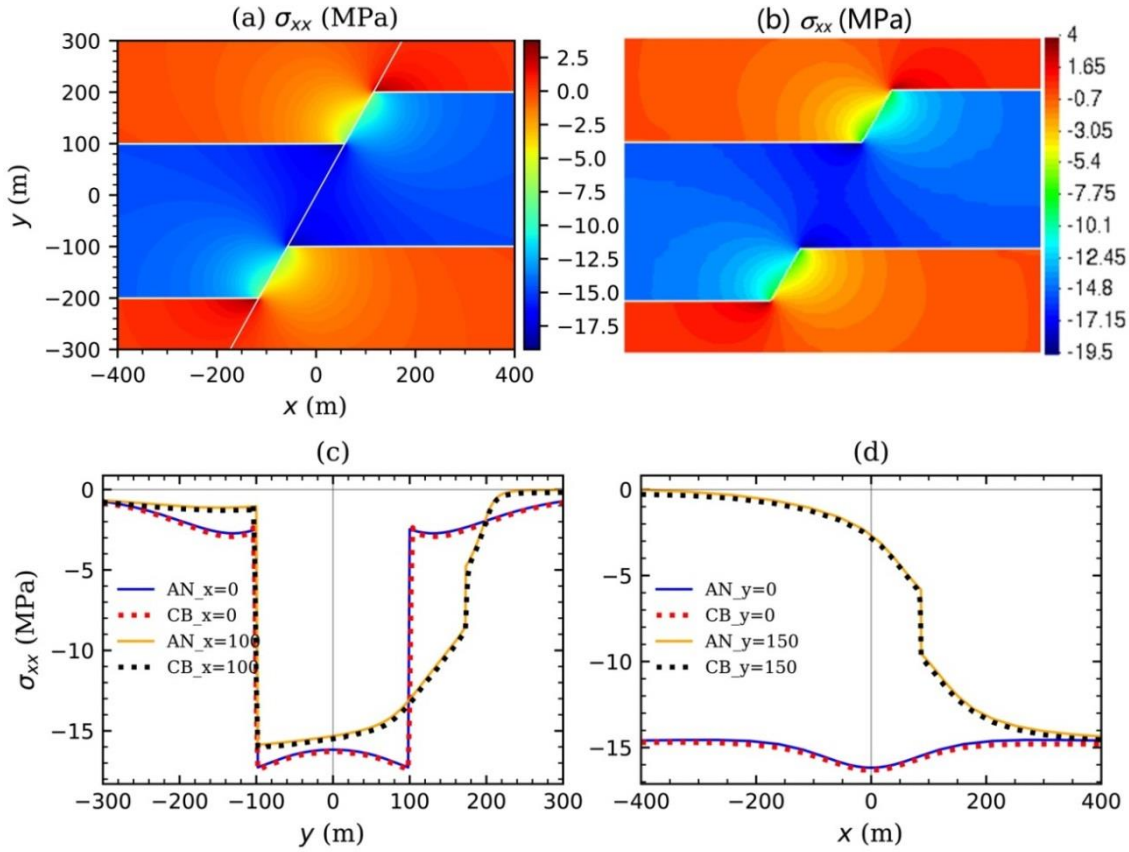

Figure D1. Detailed comparison of the induced horizontal stress for a permeable fault between (a) the analytical solution (AN) and (b) the numerical results of CODE_BRIGHT (CB), as well as the specific comparison of them at the lines (c) $x = 0$ and $x = 100$ m, and (d) $y = 0$ and $y = 150$ m. The reservoir geometry and the fault are indicated by the white lines in (a).

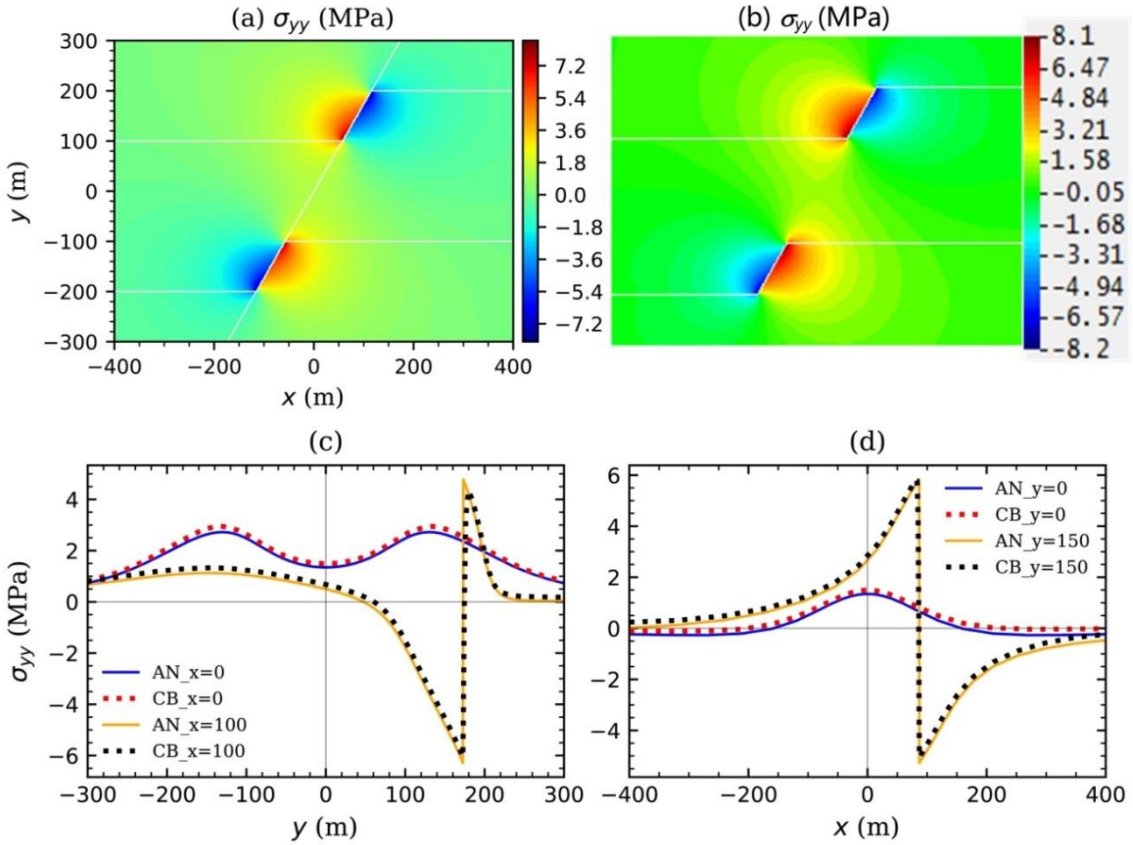

Figure D2. Detailed comparison of the induced vertical stress for a permeable fault between (a) the analytical solution (AN) and (b) the numerical results of CODE_BRIGHT (CB), as well as the specific comparison of them at the lines (c) x = 0 and x = 100 m, and (d) y = 0 and y = 150 m. The reservoir geometry and the fault are indicated by the white lines in (a).

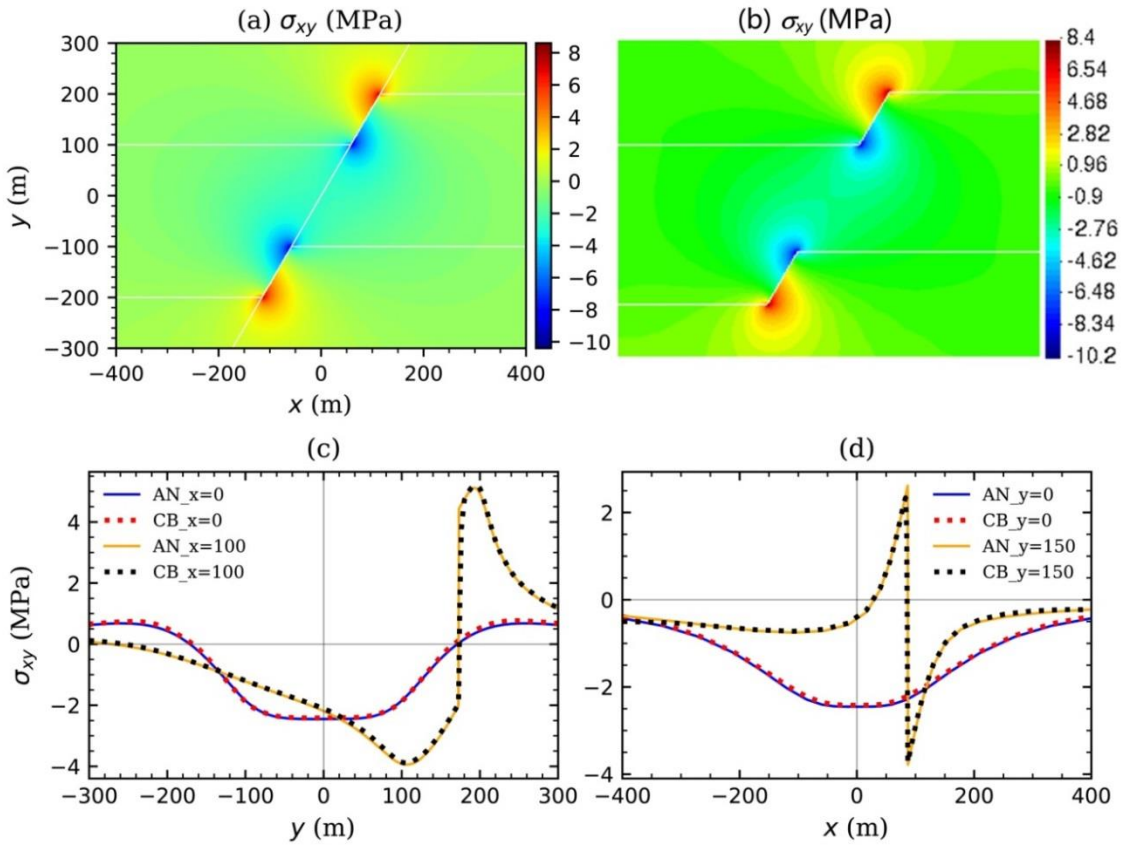

Figure D3. Detailed comparison of the induced shear stress for a permeable fault between (a) the analytical solution (AN) and (b) the numerical results of CODE_BRIGHT (CB), as well as the specific comparison of them at the lines (c) x = 0 and x = 100 m, and (d) y = 0 and y = 150 m. The reservoir geometry and the fault are indicated by the white lines in (a).

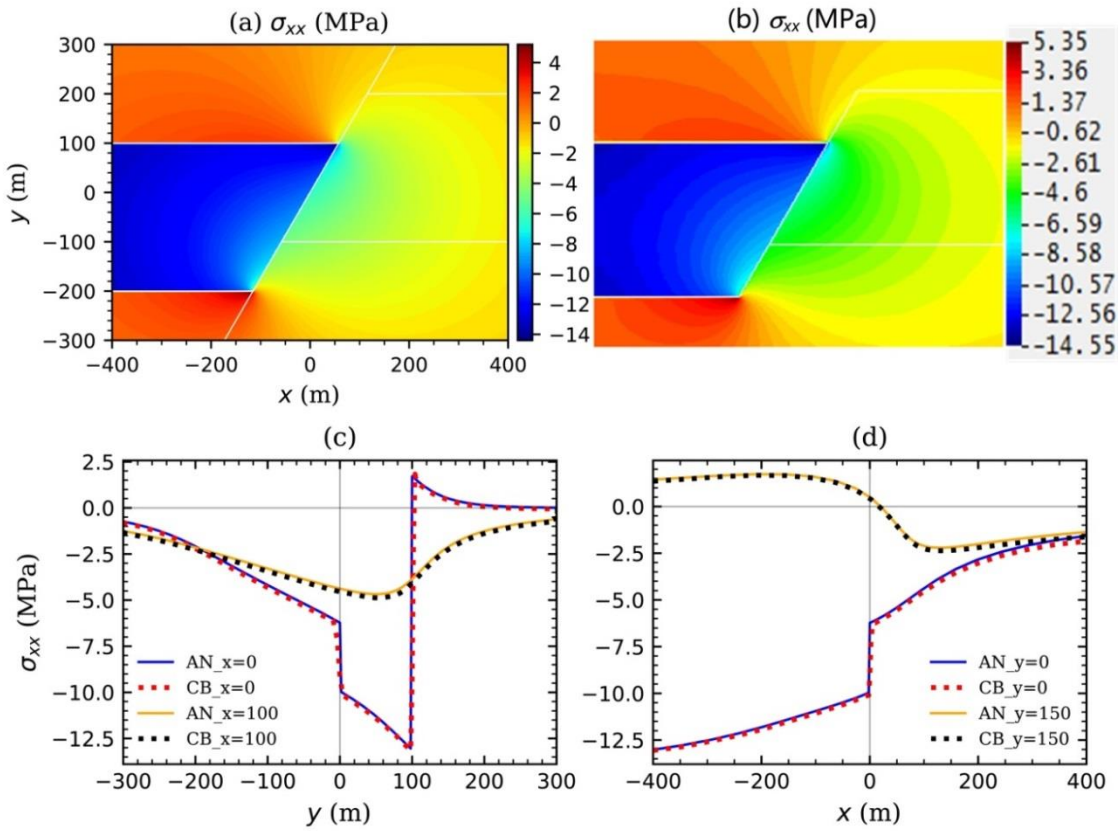

Figure D4. Detailed comparison of the induced horizontal stress for an impermeable fault between (a) the analytical solution (AN) and (b) the numerical results of CODE_BRIGHT (CB), as well as the specific comparison of them at the lines (c) x = 0 and x = 100 m, and (d) y = 0 and y = 150 m. The reservoir geometry and the fault are indicated by the white lines in (a).

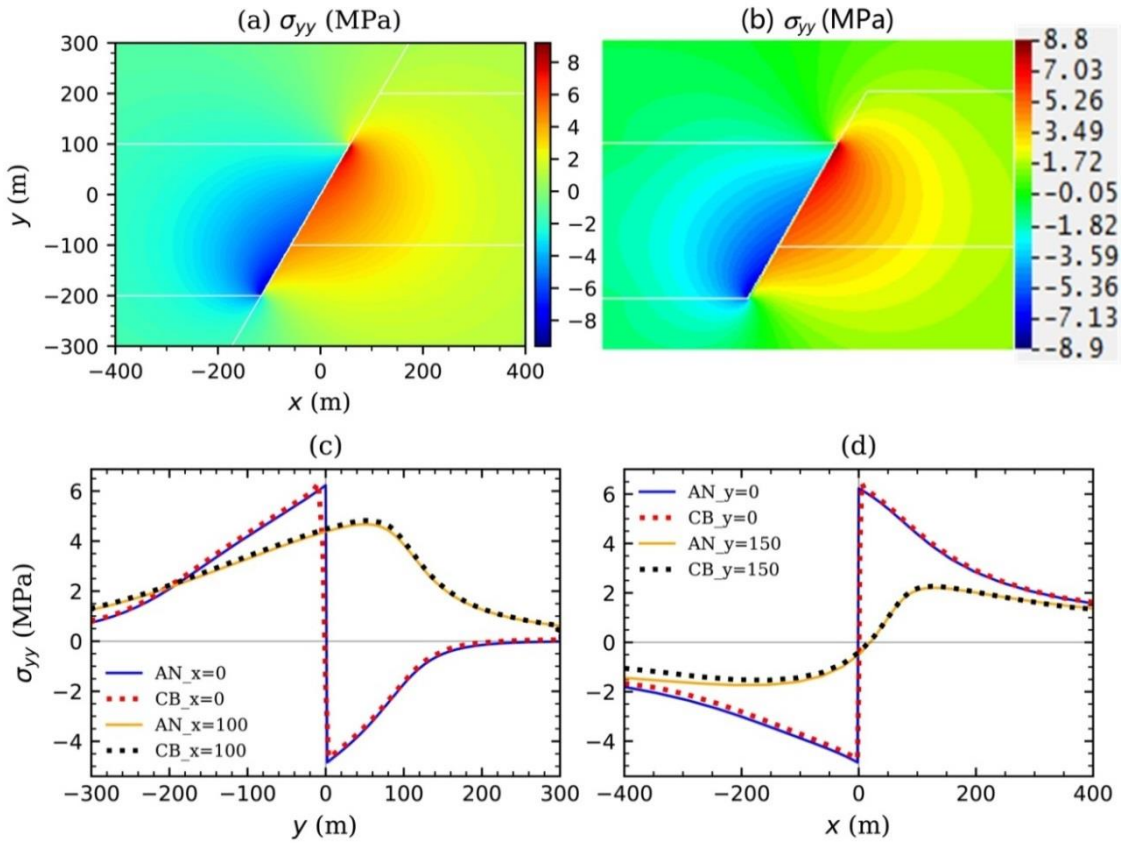

Figure D5. Detailed comparison of the induced vertical stress for an impermeable fault between (a) the analytical solution (AN) and (b) the numerical results of CODE_BRIGHT (CB), as well as the specific comparison of them at the lines (c) x = 0 and x = 100 m, and (d) y = 0 and y = 150 m. The reservoir geometry and the fault are indicated by the white lines in (a).

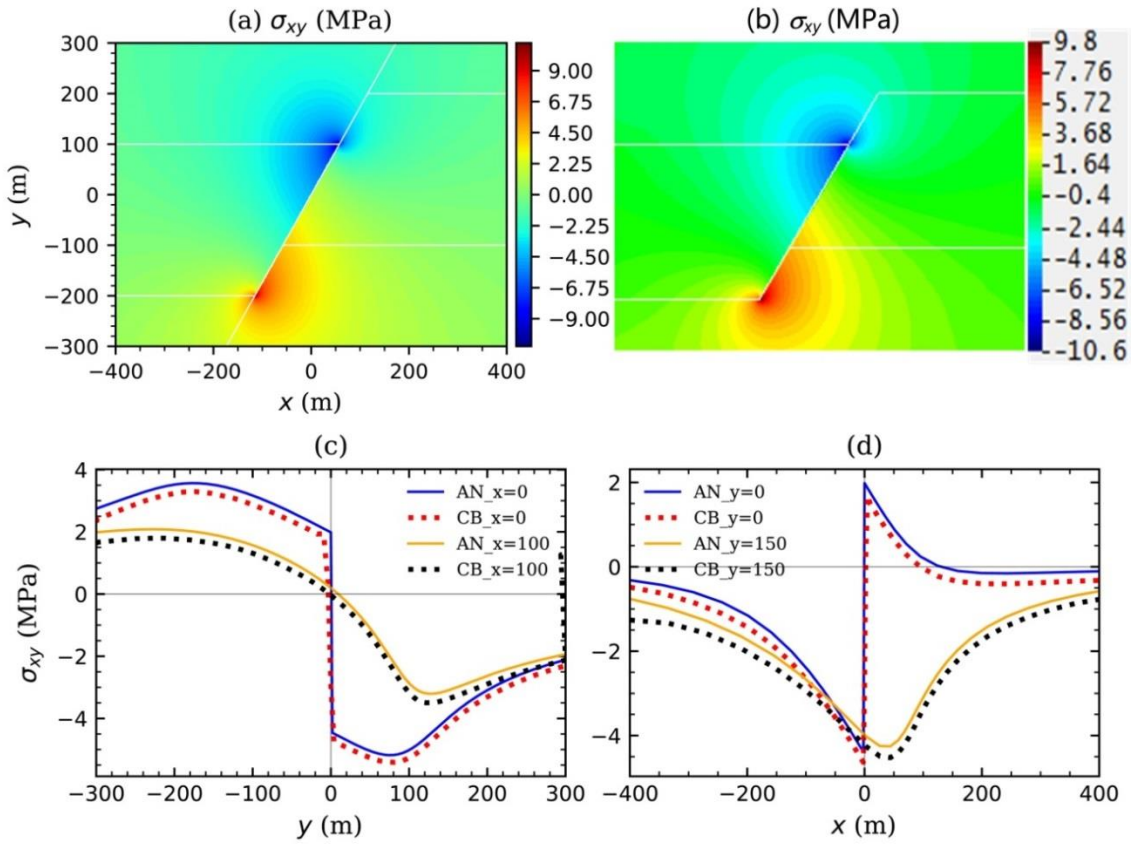

Figure D6. Detailed comparison of the induced shear stress for an impermeable fault between (a) the analytical solution (AN) and (b) the numerical results of CODE_BRIGHT (CB), as well as the specific comparison of them at the lines (c) $x = 0$ and $x = 100$ m, and (d) $y = 0$ and $y = 150$ m. The reservoir geometry and the fault are indicated by the white lines in (a).

Text D2: Analytical results for a vertical permeable fault

We plot the analytical results for a vertical permeable fault, which aims at comparing our solution with the results of Jansen et al. (2019). Using the same example as Jansen et al. (2019), we find that Figures D7-D9 in this Appendix are identical to Figures 6-8 in Jansen et al. (2019). Thus, the analytical solution developed in this work is verified again by comparing it with an existing analytical solution.

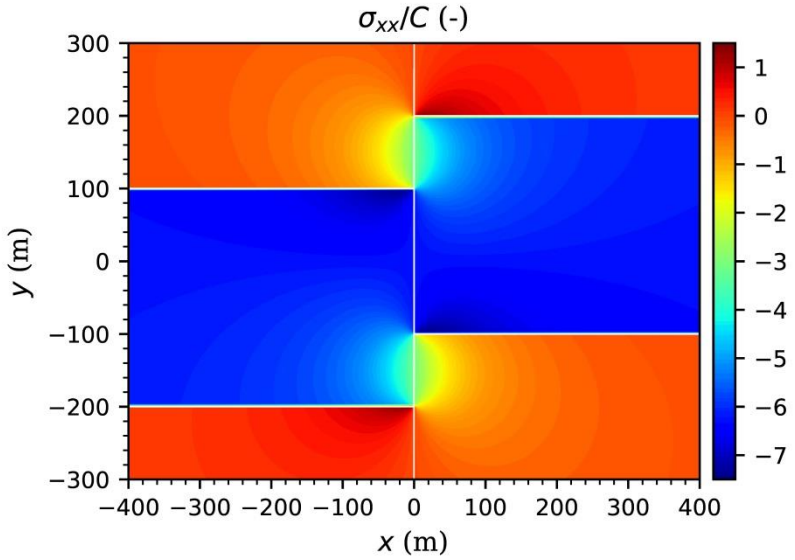

Figure D7. Dimensionless induced horizontal stress for a vertical permeable fault calculated using our analytical solution. The scaling parameter *C* is 2.36 MPa for the parameter values listed in Table 1. The reservoir geometry and the fault are indicated by the white lines.

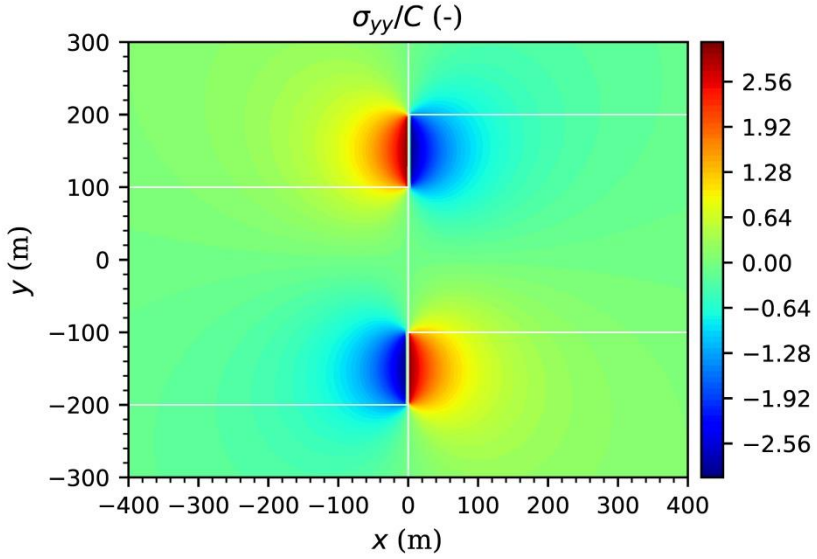

Figure D8. Dimensionless induced vertical stress for a vertical permeable fault calculated using our analytical solution. The scaling parameter *C* is the same as in Figure D7. The reservoir geometry and the fault are indicated by the white lines.

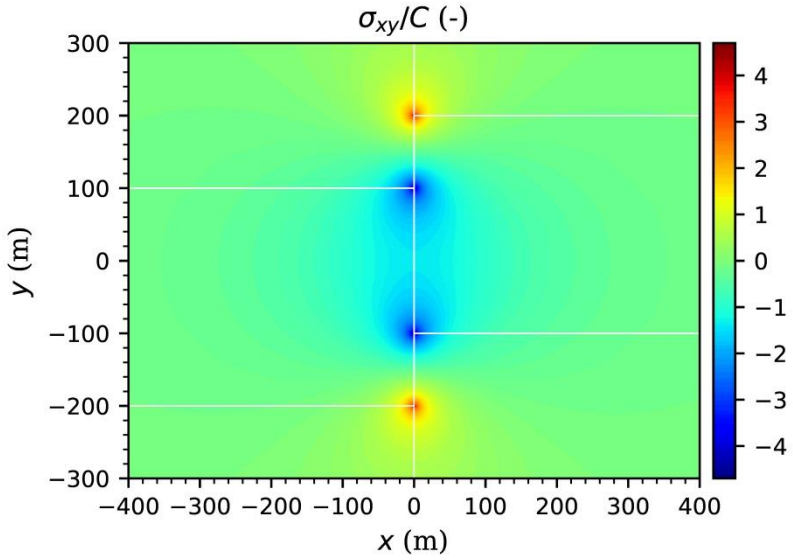

Figure D9. Dimensionless induced shear stress for a vertical permeable fault calculated using our analytical solution. The scaling parameter *C* is the same as in Figure D7. The reservoir geometry and the fault are indicated by the white lines.

E. Poroelastic displacement due to fluid injection/depletion in a half space

We derive the solution for poroelastic displacement based on Eshelby's inclusion theory (Eshelby, 1957) and Green's function under point force (Mindlin, 1936; Segall, 2010). We treat the reservoir as an inclusion when a uniform pore pressure variation Δp occurs in the reservoir due to fluid injection/depletion. Once re-welding the inclusion to its surrounding matrix and applying the restoring force in opposite direction (to remove the restoring force), a displacement field $u_i(x, y, z)$ is generated inside and outside the inclusion (detailed imaginary steps of the inclusion theory can be found in Jansen *et al*., 2019; Rudnicki, 2011; Segall, 2010)

$$u_i(x, y, z) = \alpha \Delta p \iint_{\Gamma} \tilde{\mathbf{g}}_i(x, y, z, \varsigma, \xi, \psi) \cdot \mathbf{n}_{\Gamma}(\varsigma, \xi, \psi)\, d\Gamma, \tag{E1}$$

where α is Biot's coefficient, $\mathbf{n}_{\Gamma}$ is the unit normal vector pointing outward from the boundary (Γ) of the inclusion, *x*, *y* and *z* are the Cartesian coordinates, ς, ξ, ψ are the coordinate values on Γ, and

$$\tilde{\mathbf{g}}_i(x, y, z, \varsigma, \xi, \psi) = \left[\tilde{\mathrm{g}}_{i\varsigma}(x, y, z, \varsigma, \xi, \psi), \tilde{\mathrm{g}}_{i\xi}(x, y, z, \varsigma, \xi, \psi), \tilde{\mathrm{g}}_{i\psi}(x, y, z, \varsigma, \xi, \psi) \right]^T, \tag{E2}$$

where $\tilde{\mathrm{g}}_{ij}(x, y, z, \varsigma, \xi, \psi)$ means Green's function tensor, a fundamental solution representing the displacement in the *i*-direction at point (x, y, z) under a unit body force in the *j*-direction at point (ς, ξ, ψ) in elasticity (Mindlin, 1936; Segall, 2010), subscripts *i* and *j* are free indexes with $i \in (x, y, z)$ and $j \in (\varsigma, \xi, \psi)$ in the three dimensional (3D) Cartesian space. The point source (ς, ξ, ψ) is a center of dilatation/contraction that consists of three mutually orthogonal double forces without moment (Mindlin, 1936). Pore pressure shows the same property as the center of dilatation in mechanics, which establishes the theoretical basis of representing the former by the latter.

Applying Gauss's divergence theorem in Equation (E1) transforms the surface integral into a volume integral

$$u_i(x, y, z) = \alpha \Delta p \iiint_{\Omega} \nabla \cdot \tilde{\mathbf{g}}_i(x, y, z, \varsigma, \xi, \psi)\, d\Omega, \tag{E3}$$

where Ω denotes the inclusion domain, and now ς, ξ, ψ mean the coordinate values

inside the domain Ω.

For a plane-strain problem, Equation (E3) can be reduced into a two-dimensional (2D) version

$$u_i(x,y) = \alpha\Delta p \iint_{\Omega} \frac{\partial \tilde{g}_{i\varsigma}(x,y,\varsigma,\xi)}{\partial \varsigma} + \frac{\partial \tilde{g}_{i\xi}(x,y,\varsigma,\xi)}{\partial \xi} d\Omega . \tag{E4}$$

For the sake of simplification, Jansen et al. (2019) and Wu et al. (2021a) adopted a full-space version of Green's function to develop an analytical solution for induced stress. It is valid for the stress analysis around faults buried at depth. However, an upward/downward motion of the overburden will accommodate the vertical displacement (Richard et al., 1995; Rowan et al., 2004), and thus, the displacement distribution is more sensitive to the free-surface effects than the stress. We here apply a half-space Green's function, which was first solved by Mindlin (1936), to derive the closed-form solution for displacement. A related 2D version of half-space Green's function can be found in Segall (2010, p.61)

$$\begin{aligned}
\tilde{g}_{x\varsigma}(x,y,\varsigma,\xi) &= \frac{1}{8\pi\mu(1-\nu)}\left[-(3-4\nu)\ln R_1 - [8(1-\nu)^2-(3-4\nu)]\ln R_2 - \frac{(y-\xi)^2}{R_1^2}\right. \\
&\quad \left. - \frac{(3-4\nu)(y+\xi)^2 + 2y\xi}{R_2^2} + \frac{4y\xi(y+\xi)^2}{R_2^4}\right] \\
\tilde{g}_{y\varsigma}(x,y,\varsigma,\xi) &= \frac{1}{8\pi\mu(1-\nu)}\left[\frac{(x-\varsigma)(y-\xi)}{R_1^2} + \frac{(3-4\nu)(x-\varsigma)(y-\xi)}{R_2^2} + 4(1-2\nu)(1-\nu)\theta_2\right. \\
&\quad \left. - \frac{4y\xi(y+\xi)(x-\varsigma)}{R_2^4}\right] \\
\tilde{g}_{x\xi}(x,y,\varsigma,\xi) &= \frac{1}{8\pi\mu(1-\nu)}\left[\frac{(x-\varsigma)(y-\xi)}{R_1^2} + \frac{(3-4\nu)(x-\varsigma)(y-\xi)}{R_2^2} - 4(1-2\nu)(1-\nu)\theta_2\right. \\
&\quad \left. + \frac{4y\xi(y+\xi)(x-\varsigma)}{R_2^4}\right] \\
\tilde{g}_{y\xi}(x,y,\varsigma,\xi) &= \frac{1}{8\pi\mu(1-\nu)}\left[-(3-4\nu)\ln R_1 - [8(1-\nu)^2-(3-4\nu)]\ln R_2 - \frac{(x-\varsigma)^2}{R_1^2}\right. \\
&\quad \left. - \frac{(3-4\nu)(x-\varsigma)^2 - 2y\xi}{R_2^2} - \frac{4y\xi(x-\varsigma)^2}{R_2^4}\right] ,
\end{aligned} \tag{E5}$$

where μ and ν are the shear modulus and Poisson's ratio, respectively, x and y have the same setting as the one shown in Figure 3.1, and

$$R_1^2 = (x-\varsigma)^2 + (y-\xi)^2 , \tag{E6}$$

$$R_2^2 = (x-\varsigma)^2 + (y+\xi)^2 , \tag{E7}$$

$$\theta_2 = \text{atan}\frac{x-\varsigma}{y+\xi}. \tag{E8}$$

Note that the 2D version of Green's function is dimensionless as it is obtained by integrating the 3D version with respect to the out-of-plane dimension, while the latter has dimension of 1/m.

Substituting Equation (E5) into Equation (E4) yields

$$u_i(x,y) = \frac{(1-2\nu)\alpha\Delta p}{2\pi(1-\nu)\mu}\iint_\Omega g_i(x,y,\varsigma,\xi)d\Omega = \eta\frac{\Delta p}{\mu}\frac{G_i(x,y)}{\pi}, \tag{E9}$$

where $\eta = \frac{\alpha(1-2\nu)}{2(1-\nu)}$ is the poroelastic coefficient (Detournay and Cheng, 1993), and

displacement function tensor $g_i(x,y,\varsigma,\xi)$ is

$$g_x(x,y,\varsigma,\xi) = \frac{x-\varsigma}{2R_1^2} + \frac{(3-4\nu)(x-\varsigma)}{2R_2^2} - \frac{2y(y+\xi)(x-\varsigma)}{R_2^4}, \tag{E10}$$

$$g_y(x,y,\varsigma,\xi) = \frac{y-\xi}{2R_1^2} - \frac{(3-4\nu)(y+\xi)}{2R_2^2} + \frac{y[(x-\varsigma)^2-(y+\xi)^2]}{R_2^4}. \tag{E11}$$

The displacement function describes the displacement gradient at point (*x*, *y*) in response to a unit center of dilatation/contraction at point source in physics. It is identical to the one shown in Segall (1985, Equation C8 in Appendix C), while the latter is derived from Melan's results (Melan, 1932). Such consistency benchmarks our previous mathematical manipulations. The first term in the right-hand side of Equations (E10) and (E11) just corresponds to the full-space version of displacement function, and other two terms describe the effects of free surface. For the sake of convenience in solving the above surface integral $G_i(x,y)$, we abbreviate these three terms as $g\mathrm{I}_x, g\mathrm{II}_x, g\mathrm{III}_x$ for Equation (E10), respectively, and $g\mathrm{I}_y, g\mathrm{II}_y, g\mathrm{III}_y$ for Equation (E11), respectively. All the variables/parameters adopted in this Appendix will keep the same physical meaning when we use them in the following Appendices F-J.

F. Closed-form integral solution of displacement function in a half space for two basic elements of inclusion: a rectangle and a triangle

We here present the mathematical derivations of the surface integral of Equation (E9) for the two basic elements of inclusion domain: a rectangle and a triangle, by following the idea of Wu et al. (2021a). For a complicated inclusion domain, one can achieve it by the principle of superposition. The integrand function is the displacement function given in Equations (E10) and (E11). We need to consider the existence of singularities for values of ς and ξ equal to x and y, respectively, where the displacement function becomes infinite/undefined. This only occurs for points (x, y) located inside the inclusion, for which the integral becomes improper. Thus, we perform the regular bounded integral for (x, y) located outside the inclusion, while for (x, y) located inside the inclusion we solve the improper integral by excluding a neighborhood of the singularity. To generalize the integration of the displacement function, we apply a general coordinate system as shown in Figure F1. Once we have the integral solution, its application only requires transforming the general coordinates to specific ones as illustrated in Section 3.2.2 of the Thesis.

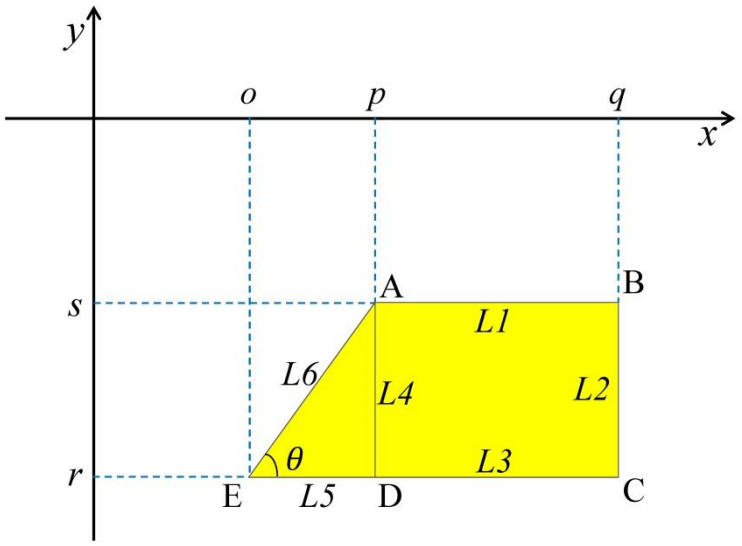

Figure F1: Schematic geometry of triangular and rectangular domains in a general coordinate system

Rectangular Inclusion:

For (x, y) located outside of the rectangle, we calculate the surface integral of horizontal displacement function $g_x(x, y, \varsigma, \xi)$ using standard techniques and we obtain

$$G_x^{\text{Rec, out}}(x,y) = \int_p^q \int_r^s g_x(x,y,\varsigma,\xi) d\xi d\varsigma = \int_p^q \int_r^s (g\text{I}_x + g\text{II}_x + g\text{III}_x) d\xi d\varsigma \\ = G\text{I}_x^{\text{Rec, out}}(x,y) + G\text{II}_x^{\text{Rec, out}}(x,y) + G\text{III}_x^{\text{Rec, out}}(x,y) \quad , \tag{F1}$$

where the upper and lower limits *o*, *p*, *q*, *r*, and *s* are the general coordinates shown in Figure B1, and

$$G\text{I}_x^{\text{Rec, out}}(x,y) = \int_p^q \int_r^s g\text{I}_x d\xi d\varsigma = \int_p^q \int_r^s \frac{x-\varsigma}{2R_1^2} d\xi d\varsigma \\ = \frac{-1}{2} \int_p^q \text{atan} \frac{y-\xi}{x-\varsigma}\bigg|_r^s d\varsigma = \frac{-1}{2} \int_p^q \left(\text{atan} \frac{y-s}{x-\varsigma} - \text{atan} \frac{y-r}{x-\varsigma} \right) d\varsigma \quad , \tag{F2}$$

$$G\text{II}_x^{\text{Rec, out}}(x,y) = \int_p^q \int_r^s g\text{II}_x d\xi d\varsigma = \int_p^q \int_r^s \frac{(3-4\nu)(x-\varsigma)}{2R_2^2} d\xi d\varsigma \\ = \frac{3-4\nu}{2} \int_p^q \text{atan} \frac{y+\xi}{x-\varsigma}\bigg|_r^s d\varsigma = \frac{3-4\nu}{2} \int_p^q \left(\text{atan} \frac{y+s}{x-\varsigma} - \text{atan} \frac{y+r}{x-\varsigma} \right) d\varsigma \quad , \tag{F3}$$

$$G\text{III}_x^{\text{Rec, out}}(x,y) = \int_p^q \int_r^s g\text{III}_x d\xi d\varsigma = \int_p^q \int_r^s -\frac{2y(y+\xi)(x-\varsigma)}{R_2^4} d\xi d\varsigma \\ = \int_p^q \frac{y(x-\varsigma)}{(x-\varsigma)^2 + (y+\xi)^2}\bigg|_r^s d\varsigma = -\frac{y}{2} \ln \frac{(y+s)^2 + (x-\varsigma)^2}{(y+r)^2 + (x-\varsigma)^2}\bigg|_p^q \quad . \tag{F4}$$

By integrating by parts,

$$G\text{I}_x^{\text{Rec, out}}(x,y) = \frac{-1}{2} \Bigg\{ \varsigma \left(\text{atan} \frac{y-s}{x-\varsigma} - \text{atan} \frac{y-r}{x-\varsigma} \right) + x \left(\text{atan} \frac{x-\varsigma}{y-s} - \text{atan} \frac{x-\varsigma}{y-r} \right) \\ - \frac{y-s}{2} \ln \left[(y-s)^2 + (x-\varsigma)^2 \right] + \frac{y-r}{2} \ln \left[(y-r)^2 + (x-\varsigma)^2 \right] \Bigg\} \Bigg|_p^q \quad , \tag{F5}$$

$$G\text{II}_x^{\text{Rec, out}}(x,y) = \frac{3-4\nu}{2} \Bigg\{ \varsigma \left(\text{atan} \frac{y+s}{x-\varsigma} - \text{atan} \frac{y+r}{x-\varsigma} \right) + x \left(\text{atan} \frac{x-\varsigma}{y+s} - \text{atan} \frac{x-\varsigma}{y+r} \right) \\ - \frac{y+s}{2} \ln \left[(y+s)^2 + (x-\varsigma)^2 \right] + \frac{y+r}{2} \ln \left[(y+r)^2 + (x-\varsigma)^2 \right] \Bigg\} \Bigg|_p^q \quad . \tag{F6}$$

To save space, we do not unfold the final expressions in Equations (F4)-(F6), which can be obtained by replacing ς with *q* and *p*, and then subtracting the latter from the former.

If (*x*, *y*) is located within the rectangle, we need to consider the improper integration of the displacement function. Note that if the standard integration (like in Equations (F2)-(F6)) is applied for such a case, the result depends on the order of integration, because Fubini's theorem does not hold in this case. We solve the improper integral (Courant & John, 1989) excluding a neighborhood of the singular point (ς, ξ) = (*x*, *y*),

which makes the integrand function being bounded. We observe that $g_x(x,y,\varsigma,\xi)$ is antisymmetric with respect to the line $x - \varsigma = 0$, i.e., $g_x(x,y,\varsigma,\xi) = -g_x(\varsigma,y,x,\xi)$.

This mean that the integral is zero for a square domain centered in the singular point, because the contribution from the triangle above the symmetry line cancels with the contribution from the triangle below. Therefore, we can exclude a square neighborhood of any size contained in the domain Ω and centered in the singular point. In the rest of the domain, Fubini's theorem holds and we can apply the standard sequential integration (Equations (F2)-(F6)). For the excluded square domain, the actual contribution is zero while the standard integration technique gives $-\pi x$, which can be checked by substituting $x - p = q - x = 0^+$ (or 0^-) into Equations (F4)-(F6). Therefore, we must remove this redundant contribution resulting from the standard integration in the excluded square domain, so that the integral for points inside the inclusion is

$$G_x^{\text{Rec, in}}(x,y) = G_x^{\text{Rec, out}}(x,y) + \pi x\,. \tag{F7}$$

Note that this result is independent on the order of integration.

Equations (F1) and (F7) only differ for the last term πx, which is a result of the improper integral for points located inside the reservoir. We therefore express the integral solution of horizontal displacement function in the general form

$$G_x^{\text{Rec}}(x,y) = G_x^{\text{Rec, out}}(x,y) + \pi x \delta_\Omega\,, \tag{F8}$$

where δ_Ω is the modified Kronecker delta, which equals 1 if $(x,y) \in \Omega$ and 0 if $(x,y) \notin \Omega$.

There are four singularities for the integral solution (Equation (F8)) at the corners (A, B, C and D) of the rectangular inclusion domain (Figure B1) where some arguments in Equation (F5) become indefinite, i.e., 0/0. The integral is in fact not defined at these points, and it is discontinuous there (different values are obtained when approaching it from one side or the other).

The same procedure can be applied to integrate the vertical displacement function $g_y(x,y,\varsigma,\xi)$, which reads,

$$\begin{aligned} G_y^{\text{Rec, out}}(x,y) &= \int_r^s \int_p^q g_y(x,y,\varsigma,\xi)\,d\varsigma\,d\xi = \int_r^s \int_p^q (g\text{I}_y + g\text{II}_y + g\text{III}_y)\,d\varsigma\,d\xi \\ &= G\text{I}_y^{\text{Rec, out}}(x,y) + G\text{II}_y^{\text{Rec, out}}(x,y) + G\text{III}_y^{\text{Rec, out}}(x,y) \end{aligned}, \tag{F9}$$

where,

$$
\begin{aligned}
G\mathrm{I}_y^{\mathrm{Rec,\,out}}(x,y) &= \int_r^s\int_p^q g\mathrm{I}_y\,d\varsigma d\xi = \int_r^s\int_p^q \frac{y-\xi}{2R_1^2}\,d\varsigma d\xi \\
&= \frac{-1}{2}\left\{\xi(\operatorname{atan}\frac{x-q}{y-\xi}-\operatorname{atan}\frac{x-p}{y-\xi})+y(\operatorname{atan}\frac{y-\xi}{x-q}-\operatorname{atan}\frac{y-\xi}{x-p})\right. \\
&\quad \left.-\frac{x-q}{2}\ln\left[(y-\xi)^2+(x-q)^2\right]+\frac{x-p}{2}\ln\left[(y-\xi)^2+(x-p)^2\right]\right\}\Bigg|_r^s
\end{aligned}
\quad , \tag{F10}
$$

$$
\begin{aligned}
G\mathrm{II}_y^{\mathrm{Rec,\,out}}(x,y) &= \int_r^s\int_p^q g\mathrm{II}_y\,d\varsigma d\xi = \int_r^s\int_p^q -\frac{(3-4\nu)(y+\xi)}{2R_2^2}\,d\varsigma d\xi \\
&= \frac{3-4\nu}{2}\left\{\xi(\operatorname{atan}\frac{x-q}{y+\xi}-\operatorname{atan}\frac{x-p}{y+\xi})-y(\operatorname{atan}\frac{y+\xi}{x-q}-\operatorname{atan}\frac{y+\xi}{x-p})\right. \\
&\quad \left.+\frac{x-q}{2}\ln\left[(y+\xi)^2+(x-q)^2\right]-\frac{x-p}{2}\ln\left[(y+\xi)^2+(x-p)^2\right]\right\}\Bigg|_r^s
\end{aligned}
\quad , \tag{F11}
$$

$$
\begin{aligned}
G\mathrm{III}_y^{\mathrm{Rec,\,out}}(x,y) &= \int_r^s\int_p^q g\mathrm{III}_y\,d\varsigma d\xi = \int_r^s\int_p^q \frac{y[(x-\varsigma)^2-(y+\xi)^2]}{R_2^4}\,d\varsigma d\xi \\
&= \int_r^s \frac{y(x-\varsigma)}{(x-\varsigma)^2+(y+\xi)^2}\Bigg|_p^q d\xi = y\left(\operatorname{atan}\frac{y+\xi}{x-q}-\operatorname{atan}\frac{y+\xi}{x-p}\right)\Bigg|_r^s .
\end{aligned}
\tag{F12}
$$

For (x, y) located in the rectangle, it becomes improper integral. We solve it with the same method adopted for the horizontal component. We observe that although there is no uniform antisymmetric line for $g_y(x,y,\varsigma,\xi)$, $g\mathrm{I}_y$ is antisymmetric with respect to the line $y-\xi=0$, i.e., $g\mathrm{I}_y(x,y,\varsigma,\xi)=-g\mathrm{I}_y(x,\xi,\varsigma,y)$, and $g\mathrm{II}_y$ and $g\mathrm{III}_y$ are bounded. This means that we only need to consider the improper integration for $g\mathrm{I}_y$. Therefore, we similarly exclude a square neighborhood of any size contained in the domain Ω and centered in the singular point. In the rest of the domain, Fubini's theorem holds and we can apply the standard sequential integration (Equations (F10)-(F12)). For the excluded square domain, the actual contribution is zero while the standard integration technique for $g\mathrm{I}_y$ gives $-\pi y$, which can be checked by substituting y - r = s – y = 0^+ (or 0^-) into Equation (F10). Therefore, we must remove this redundant contribution, so that the integral for points inside the inclusion is

$$
G_y^{\mathrm{Rec,\,in}}(x,y) = G_y^{\mathrm{Rec,\,out}}(x,y)+\pi y\,. \tag{F13}
$$

Equations (F9) and (F13) only differ for the last term πy, thus, the general form for the integral solution of vertical displacement function is

$$
G_y^{\mathrm{Rec}}(x,y) = G_y^{\mathrm{Rec,\,out}}(x,y)+\pi y\delta_\Omega\,. \tag{F14}
$$

There are also four singularities for the integral solution (Equation (F14)) of vertical displacement function at the corners (A, B, C and D) of the rectangular inclusion domain where some arguments in Equation (F10) become indefinite, i.e., 0/0. The integral is not defined at these points, and it is discontinuous there.

Triangular Inclusion:

For the integration over a triangular inclusion, we apply the same technique adopted for the case of a rectangular inclusion. The integral of the horizontal displacement function is

$$\begin{aligned} G_x^{\text{Tri, out}}(x,y) &= \int_o^p \int_r^{(\varsigma-o)\tan\theta+r} g_x(x,y,\varsigma,\xi)\,d\xi\,d\varsigma \\ &= GI_x^{\text{Tri, out}}(x,y) + GII_x^{\text{Tri, out}}(x,y) + GIII_x^{\text{Tri, out}}(x,y) \end{aligned}, \tag{F15}$$

where,

$$\begin{aligned} GI_x^{\text{Tri, out}}(x,y) &= \int_o^p \int_r^{(\varsigma-o)\tan\theta+r} \frac{x-\varsigma}{2R_1^2}\,d\xi\,d\varsigma = \frac{-1}{2}\int_o^p \operatorname{atan}\frac{y-\xi}{x-\varsigma}\Bigg|_r^{(\varsigma-o)\tan\theta+r} d\varsigma \\ &= \frac{-1}{2}\int_o^p \left(\operatorname{atan}\frac{y_{\text{I}}-\varsigma\tan\theta}{x-\varsigma} - \operatorname{atan}\frac{y-r}{x-\varsigma}\right) d\varsigma \\ &= \frac{-1}{2}\left[\left(\varsigma\operatorname{atan}\frac{y_{\text{I}}-\varsigma\tan\theta}{x-\varsigma}\right)\Bigg|_o^p - \int_o^p \frac{(y_{\text{I}}-x\tan\theta)\varsigma}{(x-\varsigma)^2+(y_{\text{I}}-\varsigma\tan\theta)^2}d\varsigma\right. \\ &\quad \left. - \int_o^p \operatorname{atan}\frac{y-r}{x-\varsigma}d\varsigma\right] \end{aligned}, \tag{F16}$$

$$\begin{aligned} GII_x^{\text{Tri, out}}(x,y) &= \int_o^p \int_r^{(\varsigma-o)\tan\theta+r} \frac{(3-4\nu)(x-\varsigma)}{2R_2^2}\,d\xi\,d\varsigma = \frac{3-4\nu}{2}\int_o^p \operatorname{atan}\frac{y+\xi}{x-\varsigma}\Bigg|_r^{(\varsigma-o)\tan\theta+r} d\varsigma \\ &= \frac{3-4\nu}{2}\int_o^p \left(\operatorname{atan}\frac{y_{\text{II}}+\varsigma\tan\theta}{x-\varsigma} - \operatorname{atan}\frac{y+r}{x-\varsigma}\right) d\varsigma \\ &= \frac{3-4\nu}{2}\left[\left(\varsigma\operatorname{atan}\frac{y_{\text{II}}+\varsigma\tan\theta}{x-\varsigma}\right)\Bigg|_o^p - \int_o^p \frac{(y_{\text{II}}+x\tan\theta)\varsigma}{(x-\varsigma)^2+(y_{\text{II}}+\varsigma\tan\theta)^2}d\varsigma\right. \\ &\quad \left. - \int_o^p \operatorname{atan}\frac{y+r}{x-\varsigma}d\varsigma\right] \end{aligned} \tag{F17}$$

,

$$
\begin{aligned}
GIII_x^{\text{Tri, out}}(x,y) &= \int_o^p \int_r^{(\varsigma-o)\tan\theta+r} -\frac{2y(y+\xi)(x-\varsigma)}{R_2^4} d\xi d\varsigma \\
&= \int_o^p \frac{y(x-\varsigma)}{(x-\varsigma)^2+(y+\xi)^2}\Bigg|_r^{(\varsigma-o)\tan\theta+r} d\varsigma \\
&= \int_o^p \frac{y(x-\varsigma)}{(x-\varsigma)^2+(y_{\text{III}}+\varsigma\tan\theta)^2} - \frac{y(x-\varsigma)}{(x-\varsigma)^2+(y+r)^2} d\varsigma
\end{aligned}, \tag{F18}
$$

where $y_{\text{I}} = y + o\tan\theta - r$, $y_{\text{II}} = y - o\tan\theta + r$, and $y_{\text{III}} = y_{\text{II}}$.

Integration of the last term in the right-hand side of Equations (F16)-(F18) is similar to the one for a rectangular inclusion, while the second term of Equations (F16) and (F17) and the first term of Equation (F18) are non-trivial. A potential solution for the second term of Equation (F16) can be obtained by the following transformation

$$
\begin{aligned}
(x-\varsigma)^2+(y_{\text{I}}-\varsigma\tan\theta)^2 &= (x-\varsigma)^2+[y_{\text{I}}-x\tan\theta+(x-\varsigma)\tan\theta]^2 \\
&= \left\{(y_{\text{I}}-x\tan\theta)^2+[(y_{\text{I}}-\varsigma\tan\theta)\tan\theta+(x-\varsigma)]^2\right\}\cos^2\theta
\end{aligned}. \tag{F19}
$$

Substituting Equation (F19) into Equation (F16) and after some derivations, we obtain

$$
\int_o^p \frac{(y_{\text{I}}-x\tan\theta)\varsigma}{(x-\varsigma)^2+(y_{\text{I}}-\varsigma\tan\theta)^2} d\varsigma = \int_o^p \frac{(1+\tan^2\theta)(y_{\text{I}}-x\tan\theta)\varsigma}{(y_{\text{I}}-x\tan\theta)^2+[(y_{\text{I}}-\varsigma\tan\theta)\tan\theta+(x-\varsigma)]^2} d\varsigma . \tag{F20}
$$

We further make the transformation

$$
\varsigma = [(\varsigma-x)-(y_{\text{I}}-x\tan\theta)\sin\theta\cos\theta]+[x+(y_{\text{I}}-x\tan\theta)\sin\theta\cos\theta]. \tag{F21}
$$

Substituting Equation (F21) into Equation (F20) and after some derivations, we obtain

$$
\begin{aligned}
\text{Equation (F20)} &= \int_o^p \frac{(y_{\text{I}}-x\tan\theta)[(\varsigma-x)-(y_{\text{I}}-\varsigma\tan\theta)\tan\theta]}{(y_{\text{I}}-x\tan\theta)^2+[(y_{\text{I}}-\varsigma\tan\theta)\tan\theta+(x-\varsigma)]^2} d\varsigma \\
&\quad + \int_o^p \frac{(x+y_{\text{I}}\tan\theta)(y_{\text{I}}-x\tan\theta)}{(y_{\text{I}}-x\tan\theta)^2+[(y_{\text{I}}-\varsigma\tan\theta)\tan\theta+(x-\varsigma)]^2} d\varsigma \\
&= \frac{y_{\text{I}}-x\tan\theta}{2(1+\tan^2\theta)} \ln\left[(y_{\text{I}}-x\tan\theta)^2+[(y_{\text{I}}-\varsigma\tan\theta)\tan\theta+(x-\varsigma)]^2\right]\Big|_o^p \\
&\quad - \frac{x+y_{\text{I}}\tan\theta}{1+\tan^2\theta} \operatorname{atan}\frac{(y_{\text{I}}-\varsigma\tan\theta)\tan\theta+(x-\varsigma)}{y_{\text{I}}-x\tan\theta}\Bigg|_o^p
\end{aligned}. \tag{F22}
$$

Substituting Equation (F22) into Equation (F16), we finally get

$$
\begin{aligned}
GI_x^{\text{Tri, out}}(x,y) &= \frac{-1}{2}\Bigg\{\varsigma\left(\operatorname{atan}\frac{y_{\text{I}}-\varsigma\tan\theta}{x-\varsigma} - \operatorname{atan}\frac{y-r}{x-\varsigma}\right) + \frac{y-r}{2}\ln\left[(y-r)^2+(x-\varsigma)^2\right] \\
&\quad - \frac{y_{\text{I}}-x\tan\theta}{2(1+\tan^2\theta)}\ln\left[(y_{\text{I}}-x\tan\theta)^2+[(y_{\text{I}}-\varsigma\tan\theta)\tan\theta+(x-\varsigma)]^2\right] \\
&\quad + \frac{x+y_{\text{I}}\tan\theta}{1+\tan^2\theta}\operatorname{atan}\frac{(y_{\text{I}}-\varsigma\tan\theta)\tan\theta+(x-\varsigma)}{y_{\text{I}}-x\tan\theta} - x\operatorname{atan}\frac{x-\varsigma}{y-r}\Bigg\}\Bigg|_o^p
\end{aligned}. \tag{F23}
$$

Similarly, applying the following transformations for the similar term of Equations (F17) and (F18), respectively,

$$(x-\varsigma)^2+(y_{\mathrm{II}}+\varsigma\tan\theta)^2=(x-\varsigma)^2+[y_{\mathrm{II}}+x\tan\theta+(\varsigma-x)\tan\theta]^2$$
$$=\left\{(y_{\mathrm{II}}+x\tan\theta)^2+[(y_{\mathrm{II}}+\varsigma\tan\theta)\tan\theta+(\varsigma-x)]^2\right\}\cos^2\theta \quad \text{(F24)}$$

,

$$(x-\varsigma)^2+(y_{\mathrm{III}}+\varsigma\tan\theta)^2=\left\{(y_{\mathrm{III}}+x\tan\theta)^2+[(y_{\mathrm{III}}+\varsigma\tan\theta)\tan\theta+(\varsigma-x)]^2\right\}\cos^2\theta, \quad \text{(F25)}$$

leads to

$$\int_o^p\frac{(y_{\mathrm{II}}+x\tan\theta)\varsigma}{(x-\varsigma)^2+(y_{\mathrm{II}}+\varsigma\tan\theta)^2}d\varsigma=\int_o^p\frac{(1+\tan^2\theta)(y_{\mathrm{II}}+x\tan\theta)\varsigma}{(y_{\mathrm{II}}+x\tan\theta)^2+[(y_{\mathrm{II}}+\varsigma\tan\theta)\tan\theta+(\varsigma-x)]^2}d\varsigma, \quad \text{(F26)}$$

$$\int_o^p\frac{y(x-\varsigma)}{(x-\varsigma)^2+(y_{\mathrm{III}}+\varsigma\tan\theta)^2}d\varsigma=\int_o^p\frac{-y(1+\tan^2\theta)(\varsigma-x)}{(y_{\mathrm{III}}+x\tan\theta)^2+[(y_{\mathrm{III}}+\varsigma\tan\theta)\tan\theta+(\varsigma-x)]^2}d\varsigma. \quad \text{(F27)}$$

Further substituting the following transformations

$$\varsigma=[(\varsigma-x)+(y_{\mathrm{II}}+x\tan\theta)\sin\theta\cos\theta]+[x-(y_{\mathrm{II}}+x\tan\theta)\sin\theta\cos\theta], \quad \text{(F28)}$$

$$\varsigma-x=[(\varsigma-x)+(y_{\mathrm{III}}+x\tan\theta)\sin\theta\cos\theta]-(y_{\mathrm{III}}+x\tan\theta)\sin\theta\cos\theta, \quad \text{(F29)}$$

into Equations (F26) and (F27), respectively, gives

$$\text{Equation (F26)}=(y_{\mathrm{II}}+x\tan\theta)\int_o^p\frac{(y_{\mathrm{II}}+\varsigma\tan\theta)\tan\theta+(\varsigma-x)+(x-y_{\mathrm{II}}\tan\theta)}{(y_{\mathrm{II}}+x\tan\theta)^2+[(y_{\mathrm{II}}+\varsigma\tan\theta)\tan\theta+(\varsigma-x)]^2}d\varsigma$$
$$=\frac{y_{\mathrm{II}}+x\tan\theta}{2(1+\tan^2\theta)}\ln\left[(y_{\mathrm{II}}+x\tan\theta)^2+[(y_{\mathrm{II}}+\varsigma\tan\theta)\tan\theta+(\varsigma-x)]^2\right]\Big|_o^p, \quad \text{(F30)}$$
$$+\frac{x-y_{\mathrm{II}}\tan\theta}{1+\tan^2\theta}\operatorname{atan}\frac{(y_{\mathrm{II}}+\varsigma\tan\theta)\tan\theta+(\varsigma-x)}{y_{\mathrm{II}}+x\tan\theta}\Big|_o^p$$

$$\text{Equation (F27)}=-y\int_o^p\frac{(y_{\mathrm{III}}+\varsigma\tan\theta)\tan\theta+(\varsigma-x)-(y_{\mathrm{III}}+x\tan\theta)\tan\theta}{(y_{\mathrm{III}}+x\tan\theta)^2+[(y_{\mathrm{III}}+\varsigma\tan\theta)\tan\theta+(\varsigma-x)]^2}d\varsigma$$
$$=\frac{-y\cos^2\theta}{2}\ln\left[(y_{\mathrm{III}}+x\tan\theta)^2+[(y_{\mathrm{III}}+\varsigma\tan\theta)\tan\theta+(\varsigma-x)]^2\right]\Big|_o^p. \quad \text{(F31)}$$
$$+y\sin\theta\cos\theta\operatorname{atan}\frac{(y_{\mathrm{III}}+\varsigma\tan\theta)\tan\theta+(\varsigma-x)}{y_{\mathrm{III}}+x\tan\theta}\Big|_o^p$$

Finally, substituting Equations (F30) and (F31) into Equations (F17) and (F18), respectively, reads

$$GII_x^{\text{Tri, out}}(x,y)=\frac{3-4v}{2}\left\{\varsigma(\operatorname{atan}\frac{y_{\text{II}}+\varsigma\tan\theta}{x-\varsigma}-\operatorname{atan}\frac{y+r}{x-\varsigma})+\frac{y+r}{2}\ln\left[(y+r)^2+(x-\varsigma)^2\right]\right.$$
$$-\frac{y_{\text{II}}+x\tan\theta}{2(1+\tan^2\theta)}\ln\left[(y_{\text{II}}+x\tan\theta)^2+[(y_{\text{II}}+\varsigma\tan\theta)\tan\theta+(\varsigma-x)]^2\right] \quad , \quad \text{(F32)}$$
$$\left.-\frac{x-y_{\text{II}}\tan\theta}{1+\tan^2\theta}\operatorname{atan}\frac{(y_{\text{II}}+\varsigma\tan\theta)\tan\theta+(\varsigma-x)}{y_{\text{II}}+x\tan\theta}-x\operatorname{atan}\frac{x-\varsigma}{y+r}\right\}\Bigg|_o^p$$

$$GIII_x^{\text{Tri, out}}(x,y)=\left\{y\sin\theta\cos\theta\operatorname{atan}\frac{(y_{\text{III}}+\varsigma\tan\theta)\tan\theta+(\varsigma-x)}{y_{\text{III}}+x\tan\theta}\right.$$
$$\frac{-y\cos^2\theta}{2}\ln\left[(y_{\text{III}}+x\tan\theta)^2+[(y_{\text{III}}+\varsigma\tan\theta)\tan\theta+(\varsigma-x)]^2\right]. \quad \text{(F33)}$$
$$\left.+\frac{y}{2}\ln\left[(y+r)^2+(x-\varsigma)^2\right]\right\}\Bigg|_o^p$$

Applying the same procedure for the vertical displacement function yields

$$G_y^{\text{Tri, out}}(x,y)=\int_r^s\int_{(\xi-r)\cot\theta+o}^{p}g_y(x,y,\varsigma,\xi)d\varsigma d\xi$$
$$=GI_y^{\text{Tri, out}}(x,y)+GII_y^{\text{Tri, out}}(x,y)+GIII_y^{\text{Tri, out}}(x,y) \quad , \quad \text{(F34)}$$

where,

$$GI_y^{\text{Tri, out}}(x,y)=\int_r^s\int_{(\xi-r)\cot\theta+o}^{p}\frac{y-\xi}{2R_1^2}d\varsigma d\xi=\frac{-1}{2}\int_r^s\operatorname{atan}\frac{x-\varsigma}{y-\xi}\Bigg|_{(\xi-r)\cot\theta+o}^{p}d\xi$$
$$=\frac{1}{2}\left[\left(\xi\operatorname{atan}\frac{x_{\text{I}}-\xi\cot\theta}{y-\xi}\right)\Bigg|_r^s-\int_r^s\frac{(x_{\text{I}}-y\cot\theta)\xi}{(y-\xi)^2+(x_{\text{I}}-\xi\cot\theta)^2}d\xi\right., \quad \text{(F35)}$$
$$\left.-\int_r^s\operatorname{atan}\frac{x-p}{y-\xi}d\xi\right]$$

$$GII_y^{\text{Tri, out}}(x,y)=\int_r^s\int_{(\xi-r)\cot\theta+o}^{p}-\frac{(3-4v)(y+\xi)}{2R_2^2}d\varsigma d\xi=\frac{3-4v}{2}\int_r^s\operatorname{atan}\frac{x-\varsigma}{y+\xi}\Bigg|_{(\xi-r)\cot\theta+o}^{p}d\xi$$
$$=-\frac{3-4v}{2}\left[\left(\xi\operatorname{atan}\frac{x_{\text{II}}-\xi\cot\theta}{y+\xi}\right)\Bigg|_r^s+\int_r^s\frac{(x_{\text{II}}+y\cot\theta)\xi}{(y+\xi)^2+(x_{\text{II}}-\xi\cot\theta)^2}d\xi\right. \quad , \quad \text{(F36)}$$
$$\left.-\int_r^s\operatorname{atan}\frac{x-p}{y+\xi}d\xi\right]$$

$$GIII_y^{\text{Tri, out}}(x,y) = \int_r^s \int_{(\xi-r)\cot\theta+o}^{p} \frac{y[(x-\varsigma)^2-(y+\xi)^2]}{R_2^4} d\varsigma d\xi$$

$$= \int_r^s \frac{y(x-\varsigma)}{(x-\varsigma)^2+(y+\xi)^2}\Bigg|_{(\xi-r)\cot\theta+o}^{p} d\xi \quad , \tag{F37}$$

$$= y\,\text{atan}\frac{y+\xi}{x-p}\Bigg|_r^s - \int_r^s \frac{y(x_{\text{III}}-\xi\cot\theta)}{(x_{\text{III}}-\xi\cot\theta)^2+(y+\xi)^2} d\xi$$

where $x_{\text{I}} = x + r\cot\theta - o$, $x_{\text{II}} = x_{\text{I}}$, and $x_{\text{III}} = x_{\text{I}}$.

For the second term in the right-hand side of Equations (F35) and (F36), we apply

$$(y-\xi)^2 + (x_{\text{I}}-\xi\cot\theta)^2 = \left\{(x_{\text{I}}-y\cot\theta)^2 + [(x_{\text{I}}-\xi\cot\theta)\cot\theta + (y-\xi)]^2\right\}\sin^2\theta, \tag{F38}$$

$$(y+\xi)^2 + (x_{\text{II}}-\xi\cot\theta)^2 = \left\{(x_{\text{II}}+y\cot\theta)^2 + [(x_{\text{II}}-\xi\cot\theta)\cot\theta - (y+\xi)]^2\right\}\sin^2\theta, \tag{F39}$$

which leads to

$$\int_r^s \frac{(x_{\text{I}}-y\cot\theta)\xi}{(y-\xi)^2+(x_{\text{I}}-\xi\cot\theta)^2} d\xi = \int_r^s \frac{(1+\cot^2\theta)(x_{\text{I}}-y\cot\theta)\xi}{(x_{\text{I}}-y\cot\theta)^2+[(x_{\text{I}}-\xi\cot\theta)\cot\theta+(y-\xi)]^2} d\xi, \tag{F40}$$

$$\int_r^s \frac{(x_{\text{II}}+y\cot\theta)\xi}{(y+\xi)^2+(x_{\text{II}}-\xi\cot\theta)^2} d\xi = \int_r^s \frac{(1+\cot^2\theta)(x_{\text{II}}+y\cot\theta)\xi}{(x_{\text{II}}+y\cot\theta)^2+[(x_{\text{II}}-\xi\cot\theta)\cot\theta-(y+\xi)]^2} d\xi. \tag{F41}$$

Making transformations $\xi = [(\xi-y)-(x_{\text{I}}-y\cot\theta)\sin\theta\cos\theta] + [y+(x_{\text{I}}-y\cot\theta)\sin\theta\cos\theta]$ and $\xi = [(\xi+y)-(x_{\text{II}}+y\cot\theta)\sin\theta\cos\theta] - [y-(x_{\text{II}}+y\cot\theta)\sin\theta\cos\theta]$ for Equations (F40) and (F41), respectively, and then taking the results into Equations (F35) and (F36), respectively, we obtain

$$GI_y^{\text{Tri, out}}(x,y) = \frac{1}{2}\Bigg\{\xi\left(\text{atan}\frac{x_{\text{I}}-\xi\cot\theta}{y-\xi} - \text{atan}\frac{x-p}{y-\xi}\right) + \frac{x-p}{2}\ln\left[(y-\xi)^2+(x-p)^2\right]$$

$$-\frac{x_{\text{I}}-y\cot\theta}{2(1+\cot^2\theta)}\ln\left[(x_{\text{I}}-y\cot\theta)^2+[(x_{\text{I}}-\xi\cot\theta)\cot\theta+(y-\xi)]^2\right] \quad , \tag{F42}$$

$$+\frac{y+x_{\text{I}}\cot\theta}{1+\cot^2\theta}\text{atan}\frac{(x_{\text{I}}-\xi\cot\theta)\cot\theta+(y-\xi)}{x_{\text{I}}-y\cot\theta} - y\,\text{atan}\frac{y-\xi}{x-p}\Bigg\}\Bigg|_r^s$$

$$GII_y^{\text{Tri, out}}(x,y) = \frac{4v-3}{2}\Bigg\{\xi\left(\text{atan}\frac{x_{\text{II}}-\xi\cot\theta}{y+\xi} - \text{atan}\frac{x-p}{y+\xi}\right) - \frac{x-p}{2}\ln\left[(y+\xi)^2+(x-p)^2\right]$$

$$+\frac{x_{\text{II}}+y\cot\theta}{2(1+\cot^2\theta)}\ln\left[(x_{\text{II}}+y\cot\theta)^2+[(x_{\text{II}}-\xi\cot\theta)\cot\theta-(y+\xi)]^2\right] \quad . \tag{F43}$$

$$-\frac{-y+x_{\text{II}}\cot\theta}{1+\cot^2\theta}\text{atan}\frac{(x_{\text{II}}-\xi\cot\theta)\cot\theta-(y+\xi)}{x_{\text{II}}+y\cot\theta} + y\,\text{atan}\frac{y+\xi}{x-p}\Bigg\}\Bigg|_r^s$$

For the last term in the right-hand side of Equation (F37), a further derivation gives

$$\int_r^s \frac{y(x_{\mathrm{III}}-\xi\cot\theta)}{(x_{\mathrm{III}}-\xi\cot\theta)^2+(y+\xi)^2}d\xi = \frac{-y}{2\cot\theta}\ln\left[(x_{\mathrm{III}}-\xi\cot\theta)^2+(y+\xi)^2\right]\Big|_r^s + \frac{y}{\cot\theta}\int_r^s \frac{y+\xi}{(x_{\mathrm{III}}-\xi\cot\theta)^2+(y+\xi)^2}d\xi \quad \text{(F44)}$$

The last term in the right-hand side of Equation (F44) is similar to the second term of Equation (F36), we thus follow similar transformations and take the results into Equation (F44). Finally substituting all the derived equations into Equation (F37) reads

$$\begin{aligned} G\mathrm{III}_y^{\mathrm{Tri,\,out}}(x,y) = \Bigg\{ & \frac{y}{2\cot\theta}\ln\left[(x_{\mathrm{III}}-\xi\cot\theta)^2+(y+\xi)^2\right] \\ & -\frac{y\sin^2\theta}{2\cot\theta}\ln\left[(x_{\mathrm{III}}+y\cot\theta)^2+[(x_{\mathrm{III}}-\xi\cot\theta)\cot\theta-(y+\xi)]^2\right]. \\ & +y\sin^2\theta\,\mathrm{atan}\frac{(x_{\mathrm{III}}-\xi\cot\theta)\cot\theta-(y+\xi)}{x_{\mathrm{III}}+y\cot\theta}+y\,\mathrm{atan}\frac{y+\xi}{x-p}\Bigg\}\Bigg|_r^s \end{aligned} \quad \text{(F45)}$$

For points located inside the inclusion, the improper integral still gives an extra term πx and πy for the horizontal and vertical components of the displacement function, respectively. Thus, the general form of the integral solution for a triangular inclusion is

$$G_x^{\mathrm{Tri}}(x,y) = G_x^{\mathrm{Tri,\,out}}(x,y) + \pi x\delta_\Omega, \quad \text{(F46)}$$

$$G_y^{\mathrm{Tri}}(x,y) = G_y^{\mathrm{Tri,\,out}}(x,y) + \pi y\delta_\Omega. \quad \text{(F47)}$$

The singularities of the integral solution (Equations (F46) and (F47)) for a triangular inclusion are located at the three corners A, D and E of the triangle where some arguments in Equations (F23) and (F42) become indefinite, i.e., 0/0. The integral is not defined in these points.

G. Closed-form versions of Geertsma's solution and our solution for vertical displacement along the vertical reservoir center line

The initial version of Geertsma's solution (Geertsma, 1973) is expressed in the form of elliptic integrals. We here provide two closed-form versions for its vertical displacement along the vertical reservoir center line to compare with our plane-strain solution. The first one is an approximate version obtained by assuming a vertically concentrated compaction at the horizontal reservoir center line (Fjær et al., 2008),

$$u_y^{\text{Geertsma v1}}(0,y)=\frac{1}{2}C_{\text{m}}h\alpha\Delta p\left[3-4\nu+\frac{D+y}{|D+y|}-\frac{D+y}{\sqrt{(D+y)^2+R^2}}+\frac{(3-4\nu)(-D+y)}{\sqrt{(-D+y)^2+R^2}}-\frac{2R^2y}{[(-D+y)^2+R^2]^{3/2}}\right], \tag{G1}$$

where h, D, R are the thickness, depth, and radius of the disk-shaped reservoir, respectively, and $C_{\text{m}}=\frac{(1-2\nu)}{2(1-\nu)\mu}=\frac{\eta}{\alpha\mu}$ is the uniaxial reservoir compaction coefficient defined in Geertsma (1973). We have transformed the solution to the setting shown in Figure 3.2.

The approximate version however cannot provide good results for points inside the reservoir. We improve the approximate solution to an exact one

$$\begin{aligned}u_y^{\text{Geertsma v2}}(0,y)=\frac{1}{2}C_{\text{m}}\alpha\Delta p\Bigg\{&(3-4\nu)h+\begin{cases}-h, & \text{if } y\le -D-h/2\\ h, & \text{if } y\ge -D+h/2\\ 2y+2D, & \textit{otherwise}\end{cases}\\&+\left[\sqrt{(-D+h/2-y)^2+R^2}-\sqrt{(-D-h/2-y)^2+R^2}\right]\\&+(3-4\nu)\left[\sqrt{(-D+h/2+y)^2+R^2}-\sqrt{(-D-h/2+y)^2+R^2}\right]\\&-2y\left[\frac{-D+h/2+y}{\sqrt{(-D+h/2+y)^2+R^2}}-\frac{-D-h/2+y}{\sqrt{(-D-h/2+y)^2+R^2}}\right]\Bigg\}.\end{aligned} \tag{G2}$$

For the setting of Figure 3.2B, the inclusion is a simple rectangular domain. For the special center line, our plane-strain solution thus reduces to

$$u_y(0,y)=\frac{\eta\Delta p}{\pi\mu}\left\{\left[(-D+h/2)\operatorname{atan}\frac{R}{y+D-h/2}-(-D-h/2)\operatorname{atan}\frac{R}{y+D+h/2}\right.\right.$$
$$\left.+y\left(\operatorname{atan}\frac{y+D-h/2}{R}-\operatorname{atan}\frac{y+D+h/2}{R}\right)-\frac{R}{2}\ln\frac{(y+D-h/2)^2+R^2}{(y+D+h/2)^2+R^2}\right]$$
$$+(3-4\nu)\left[-(-D+h/2)\operatorname{atan}\frac{R}{y-D+h/2}+(-D-h/2)\operatorname{atan}\frac{R}{y-D-h/2}\right. \quad \text{(G3)}$$
$$\left.\left.+y\left(\operatorname{atan}\frac{y-D+h/2}{R}-\operatorname{atan}\frac{y-D-h/2}{R}\right)-\frac{R}{2}\ln\frac{(y-D+h/2)^2+R^2}{(y-D-h/2)^2+R^2}\right]\right.$$
$$\left.-2y\left(\operatorname{atan}\frac{y-D+h/2}{R}-\operatorname{atan}\frac{y-D-h/2}{R}\right)+\pi y\delta_\Omega\right\}$$

H. Closed-form version of Segall's solution and our solution for ground displacement

The initial version of Segall's solution (Segall, 1985) is a semi-analytical one. It was simplified into a closed-form version for ground displacement (Segall, 1989). We here rewrite the approximate version by taking the pore pressure change instead of the pore fluid content as the primary variable based on the illustration of Segall (1989), which reads, under the setting shown in Figure 3.2B,

$$u_x^{\text{Segall: approximate}}(x,0)=\frac{\eta\Delta p}{\pi\mu}h(1-v)\ln\frac{D^2+(x+R)^2}{D^2+(x-R)^2}, \tag{H1}$$

$$u_y^{\text{Segall: approximate}}(x,0)=\frac{\eta\Delta p}{\pi\mu}2h(1-v)(\operatorname{atan}\frac{x+R}{D}-\operatorname{atan}\frac{x-R}{D}). \tag{H2}$$

Note that Equations (7a) and (7b) of Segall (1989) lose a minus, we have corrected them here.

When focusing on the ground displacement for a rectangular inclusion, our solution can be reduced as

$$\begin{aligned}u_x(x,0)=\frac{\eta\Delta p}{\pi\mu}2(1-v)\Bigg\{&R(\operatorname{atan}\frac{h/2-D}{x-R}+\operatorname{atan}\frac{D+h/2}{x-R}+\operatorname{atan}\frac{h/2-D}{x+R}+\operatorname{atan}\frac{D+h/2}{x+R})\\&+x(\operatorname{atan}\frac{x-R}{-D+h/2}+\operatorname{atan}\frac{x-R}{D+h/2}-\operatorname{atan}\frac{x+R}{-D+h/2}-\operatorname{atan}\frac{x+R}{D+h/2})\\&-\frac{-D+h/2}{2}\ln\frac{(-D+h/2)^2+(x-R)^2}{(-D+h/2)^2+(x+R)^2}-\frac{D+h/2}{2}\ln\frac{(D+h/2)^2+(x-R)^2}{(D+h/2)^2+(x+R)^2}\Bigg\}\end{aligned}, \tag{H3}$$

$$\begin{aligned}u_y(x,0)=\frac{\eta\Delta p}{\pi\mu}2(1-v)\Bigg\{&(-D+h/2)(\operatorname{atan}\frac{x-R}{-D+h/2}-\operatorname{atan}\frac{x+R}{-D+h/2})\\&-(D+h/2)(\operatorname{atan}\frac{x-R}{D+h/2}-\operatorname{atan}\frac{x+R}{D+h/2})\\&+\frac{x-R}{2}\ln\frac{(-D+h/2)^2+(x-R)^2}{(D+h/2)^2+(x-R)^2}-\frac{x+R}{2}\ln\frac{(-D+h/2)^2+(x+R)^2}{(D+h/2)^2+(x+R)^2}\Bigg\}\end{aligned}. \tag{H4}$$

I. Approximate version of our integral solution for displacement function in a half space

We show the approximate version of the surface integral presented in Appendix F by assuming a vertically concentrated contraction/dilatation at the horizontal reservoir center instead of a distributed one throughout the entire reservoir in vertical direction. For a rectangular inclusion, the approximate version is

$$G_x^{\mathrm{Rec}}(x,y)=\frac{h}{4}\ln\frac{(y+D)^2+(x-p)^2}{(y+D)^2+(x-q)^2}+\frac{h(3-4\nu)}{4}\ln\frac{(y-D)^2+(x-p)^2}{(y-D)^2+(x-q)^2} +hy(y-D)\left[\frac{1}{(y-D)^2+(x-p)^2}-\frac{1}{(y-D)^2+(x-q)^2}\right], \tag{I1}$$

$$G_y^{\mathrm{Rec}}(x,y)=\frac{h}{2}(\operatorname{atan}\frac{x-p}{y+D}-\operatorname{atan}\frac{x-q}{y+D})+\frac{h(3-4\nu)}{2}(\operatorname{atan}\frac{x-q}{y-D}-\operatorname{atan}\frac{x-p}{y-D}) +hy\left[\frac{x-q}{(y-D)^2+(x-q)^2}-\frac{x-p}{(y-D)^2+(x-p)^2}\right]. \tag{I2}$$

For a triangular inclusion, we have

$$G_x^{\mathrm{Tri}}(x,y)=\frac{h}{4}\ln\frac{(y+D)^2+(x-\bar{x}_{op})^2}{(y+D)^2+(x-p)^2}+\frac{h(3-4\nu)}{4}\ln\frac{(y-D)^2+(x-\bar{x}_{op})^2}{(y-D)^2+(x-p)^2} +hy(y-D)\left[\frac{1}{(y-D)^2+(x-\bar{x}_{op})^2}-\frac{1}{(y-D)^2+(x-p)^2}\right], \tag{I3}$$

$$G_y^{\mathrm{Tri}}(x,y)=\frac{h}{2}(\operatorname{atan}\frac{x-\bar{x}_{op}}{y+D}-\operatorname{atan}\frac{x-p}{y+D})+\frac{h(3-4\nu)}{2}(\operatorname{atan}\frac{x-p}{y-D}-\operatorname{atan}\frac{x-\bar{x}_{op}}{y-D}) +hy\left[\frac{x-p}{(y-D)^2+(x-p)^2}-\frac{x-\bar{x}_{op}}{(y-D)^2+(x-\bar{x}_{op})^2}\right], \tag{I4}$$

where $\bar{x}_{op}=(h\cot\theta)/2+o$ is the middle point of *o* and *p*. We do not need to consider the problem of improper integration because the integral variable ξ has been replaced by constant *D* during the integration with respect to ξ. The lateral boundaries at the depth of the reservoir center are the singularities of the solution in this case.

For a trapezoidal inclusion or the one in Figure 3.1, a similar solution can be obtained by combining Equations (I1)-(I4) as illustrated in Section 3.2.2. We should adopt two different reservoir depths for the left and right reservoir compartments, respectively, instead of the previous uniform depth for the combined inclusion in Figure 3.1 because the horizontal reservoir center has been displaced by faults. For the left reservoir compartment, the real depth is *D*+(*b*-*a*)/2, and it is *D*-(*b*-*a*)/2 for the right one.

J. Supplementary Information for Chapter 3

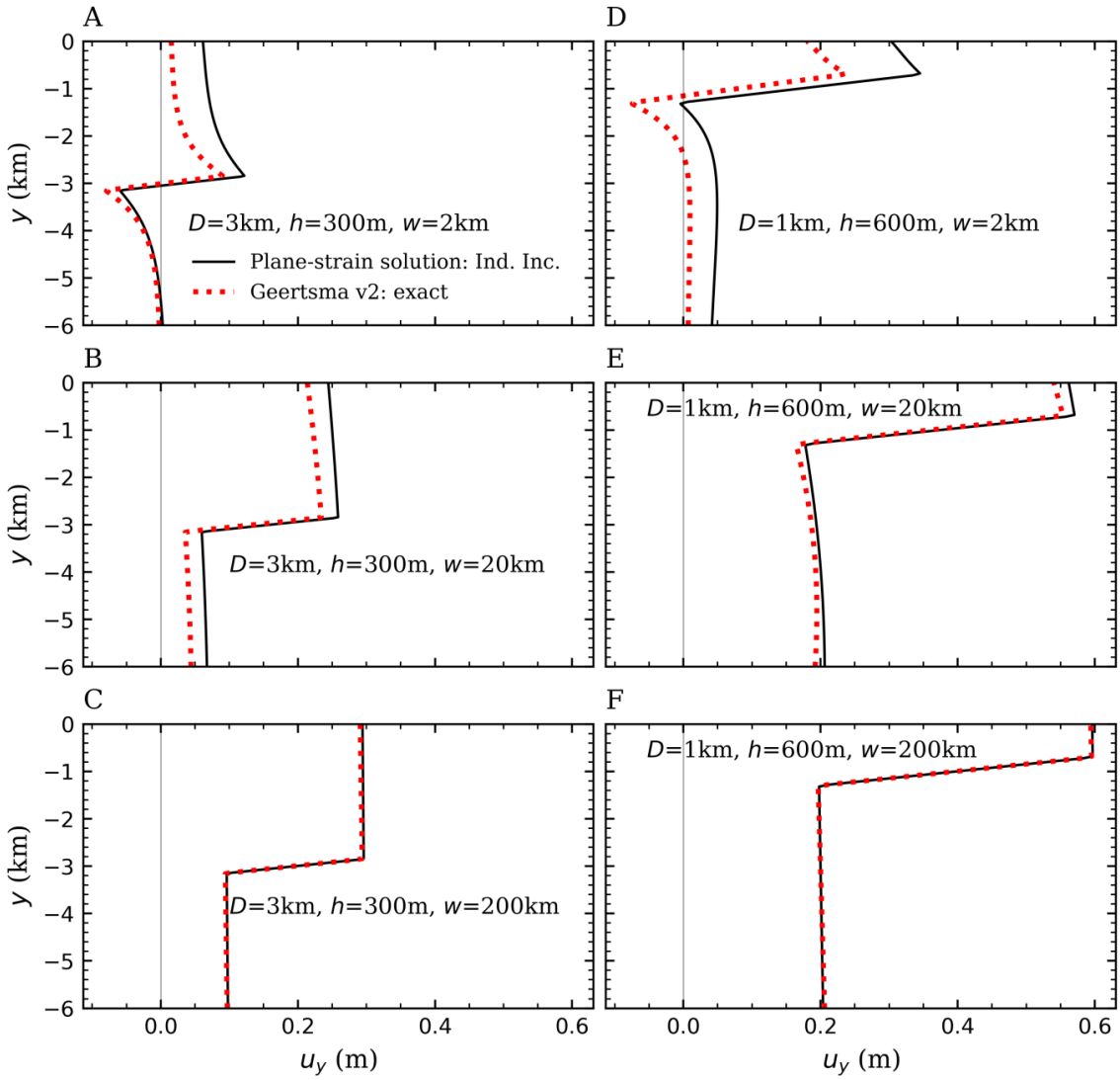

Figure J1: Comparison of vertical poroelastic displacement along the vertical reservoir center line between our 2D plane-strain solution and the 3D Geertsma's solution under various reservoir-geometrical conditions. The legend is shown in (A): the black solid and the red dotted lines represent our plane-strain solution evaluated with an individual inclusion (Ind. Inc.) and the exact version (v2) of Geertsma's solution, respectively.

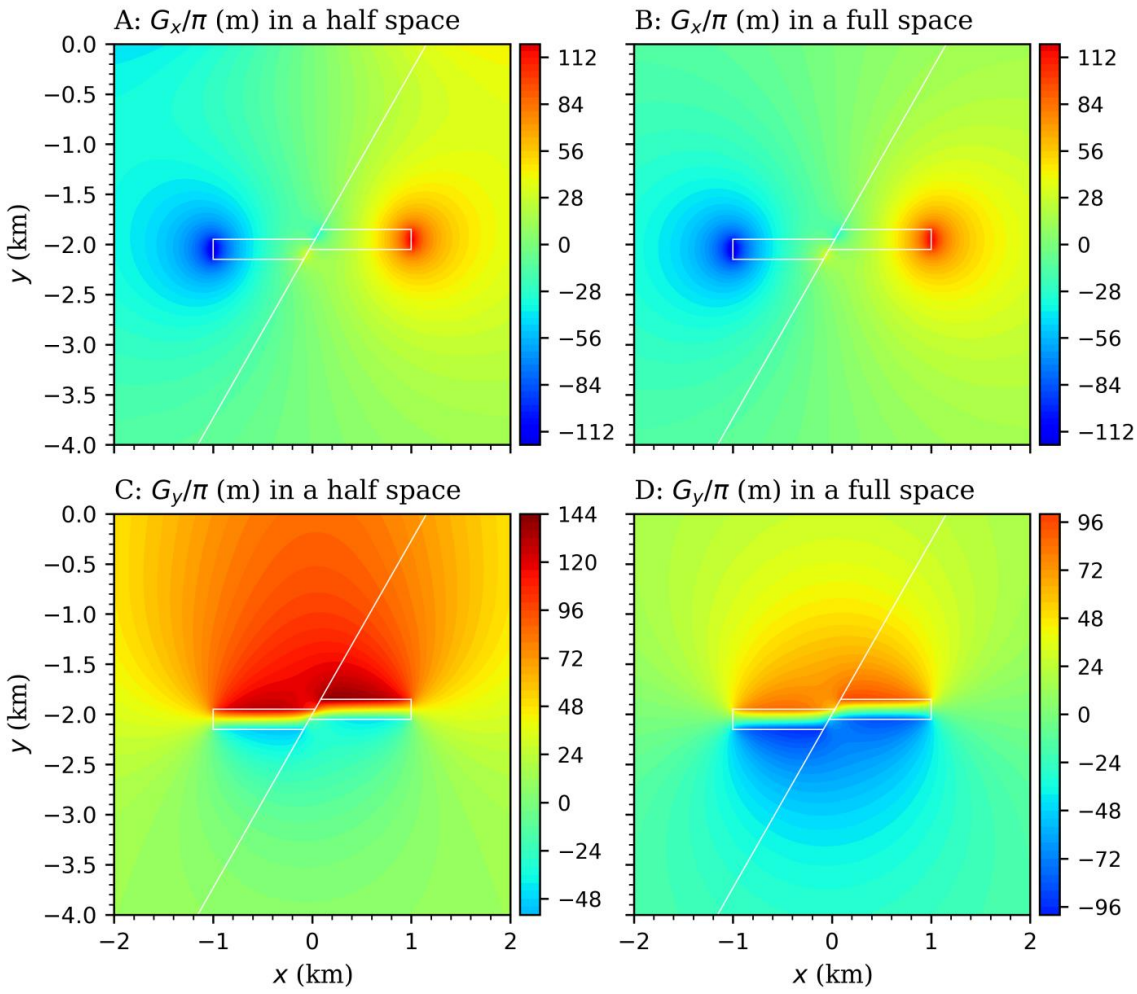

Figure J2: Horizontal (A and B) and vertical (C and D) components of the scaled poroelastic displacement for a permeable fault in a half space (A and C) and in a full space (B and D). Displacement is scaled by $\eta\Delta p / \mu$ with a value shown in Section 4.1. A, B, C, and D have the same color scale but the range of the legends is adapted to the values shown in each case. The reservoir geometry and the fault are indicated by the white lines.

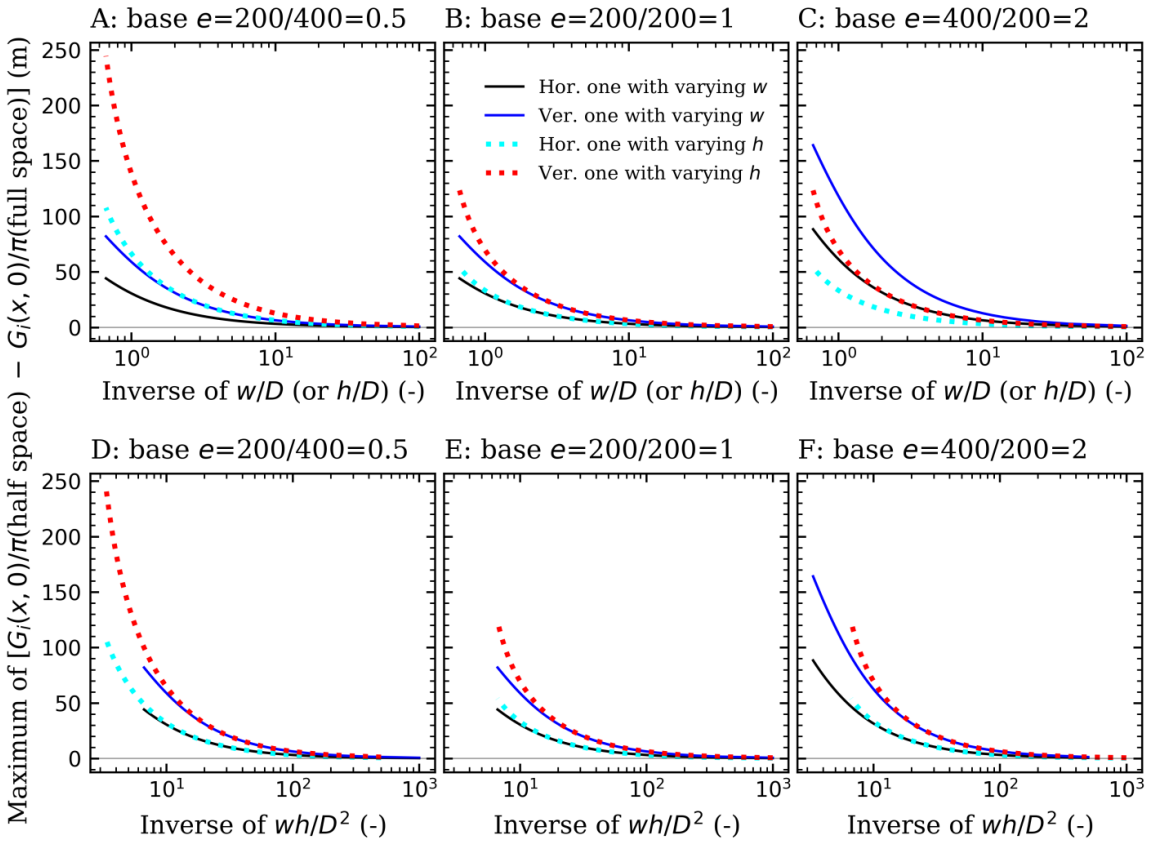

Figure J3: Maximum difference of the scaled horizontal (Hor.) and vertical (Ver.) ground displacement components between the solution in a half space and in a full space as a function of the inverse of w/D or h/D (Figures 10A-10C), and of the inverse of wh/D^2 (D, E, and F) for a rectangular reservoir with three comparative base values of aspect ratio e. Displacement is scaled by $\eta\Delta p / \mu$ with a value shown in Section 4.1. The legend is shown in B. The base values of reservoir thickness and width for each base-case scenario are included in the title of each subfigure. All the results associated with either varying w or h from 20 m to 3 km are included in this semi-log plotting, which aims at presenting the potential full-profile of the maximum difference with either varying w or h.

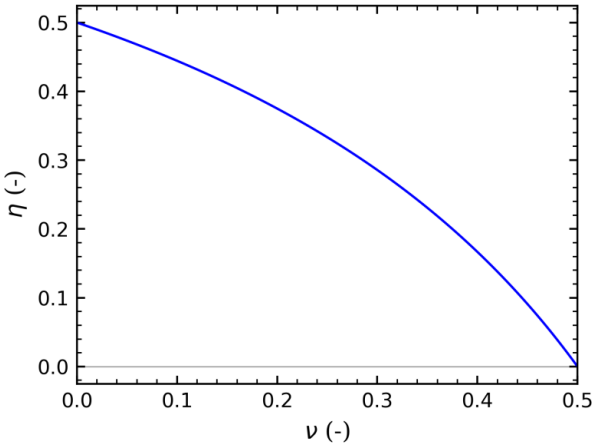

Figure J4: Poroelastic coefficient η as a function of Poisson's ratio ν with a unit value of Biot's coefficient. The value of Poisson's ratio ranges from 0 to 0.5 for real materals.

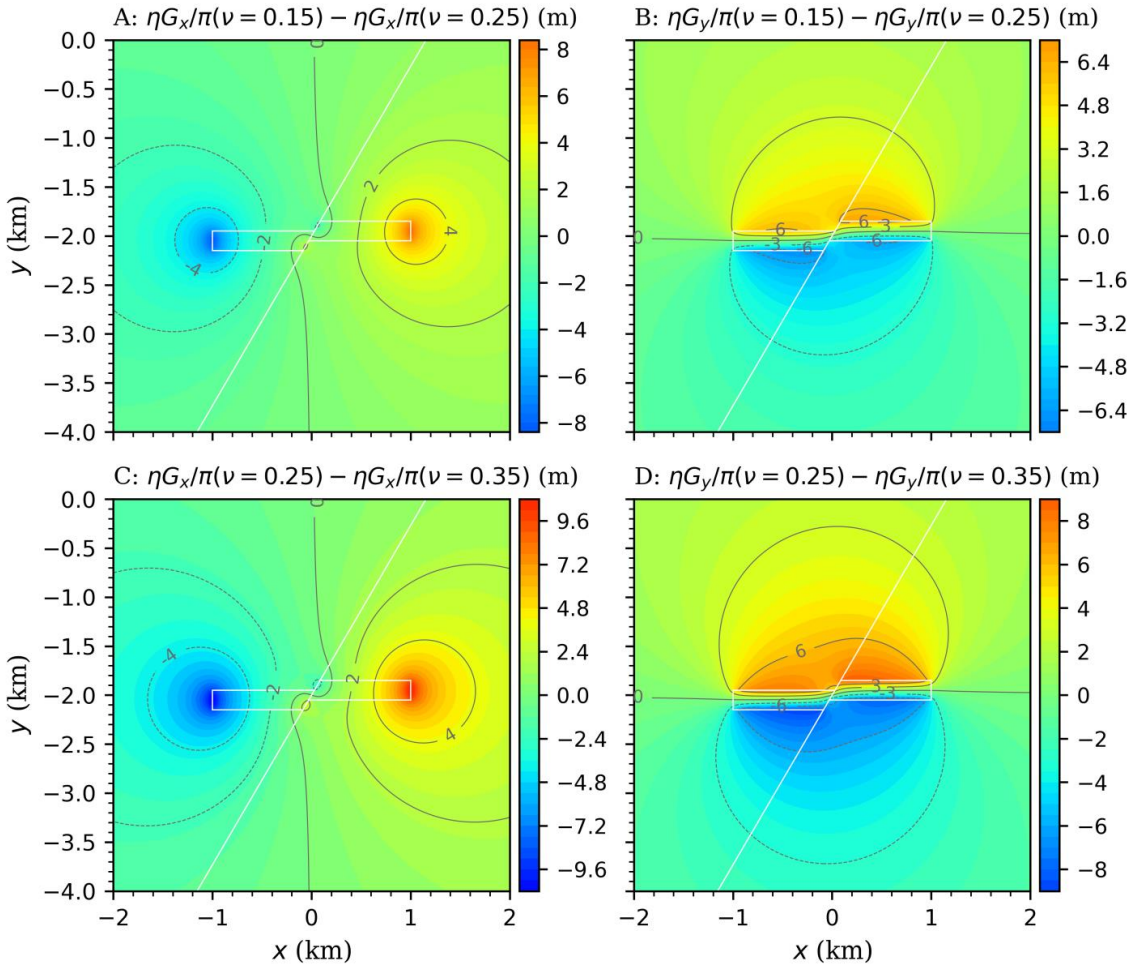

Figure J5: Difference of $\eta G_i / \pi$ between the cases of $\nu = 0.15$ and $\nu = 0.25$ (A and B), and between the cases of $\nu = 0.25$ and $\nu = 0.35$ (C and D) for a permeable fault in a full space. A, B, C, and D have the same color scale as Figure 11 but the range of the legends is adapted to the values shown in each case. The reservoir geometry and the fault are indicated by the white lines. We take the base-case study in Section 4.1 as an example.

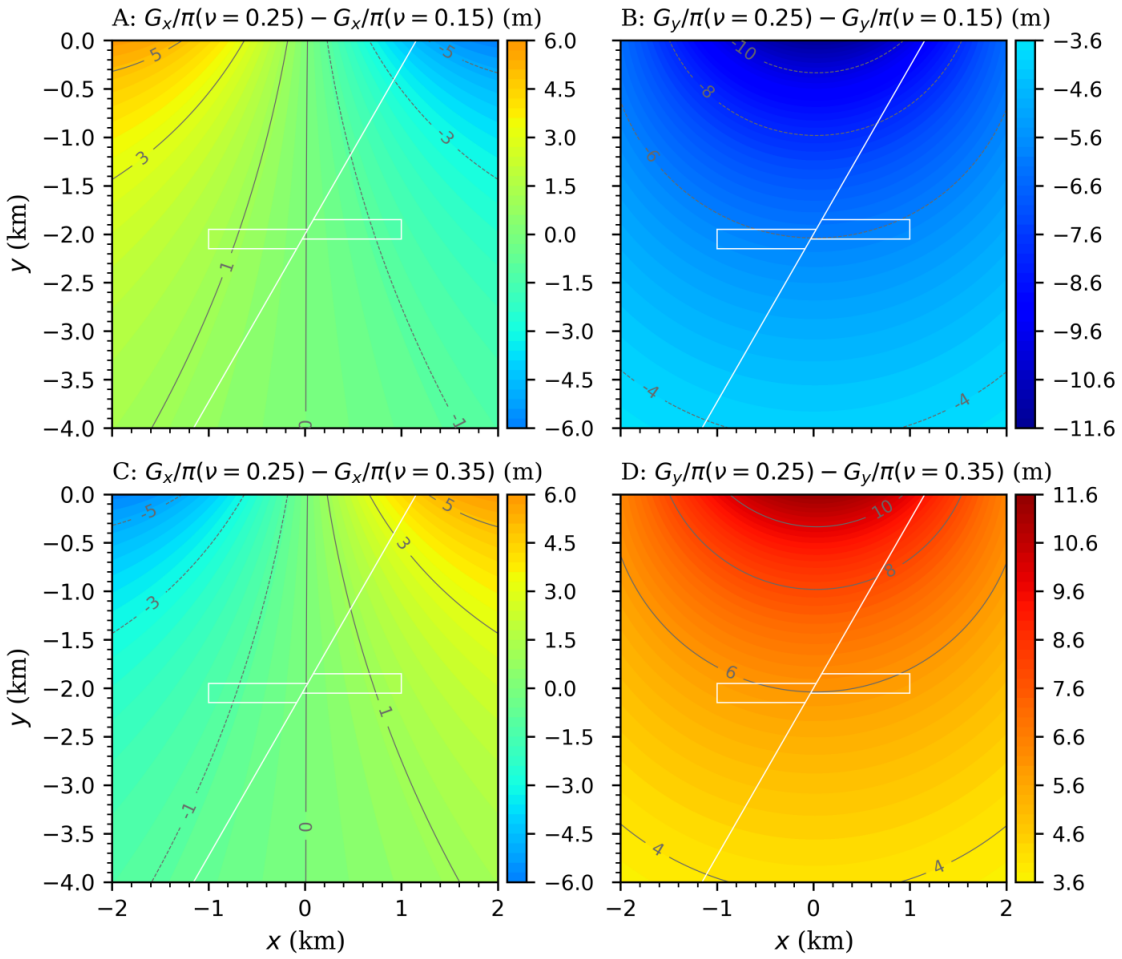

Figure J6: Difference of the reservoir geometry factor G_i / π between the cases of $\nu = 0.25$ and $\nu = 0.15$ (A and B), and between the cases of $\nu = 0.25$ and $\nu = 0.35$ (C and D) for a permeable fault in a half space. A, B, C, and D have the same color scale but the range of the legends is adapted to the values shown in each case. The reservoir geometry and the fault are indicated by the white lines. We take the base-case study in Section 4.1 as an example.

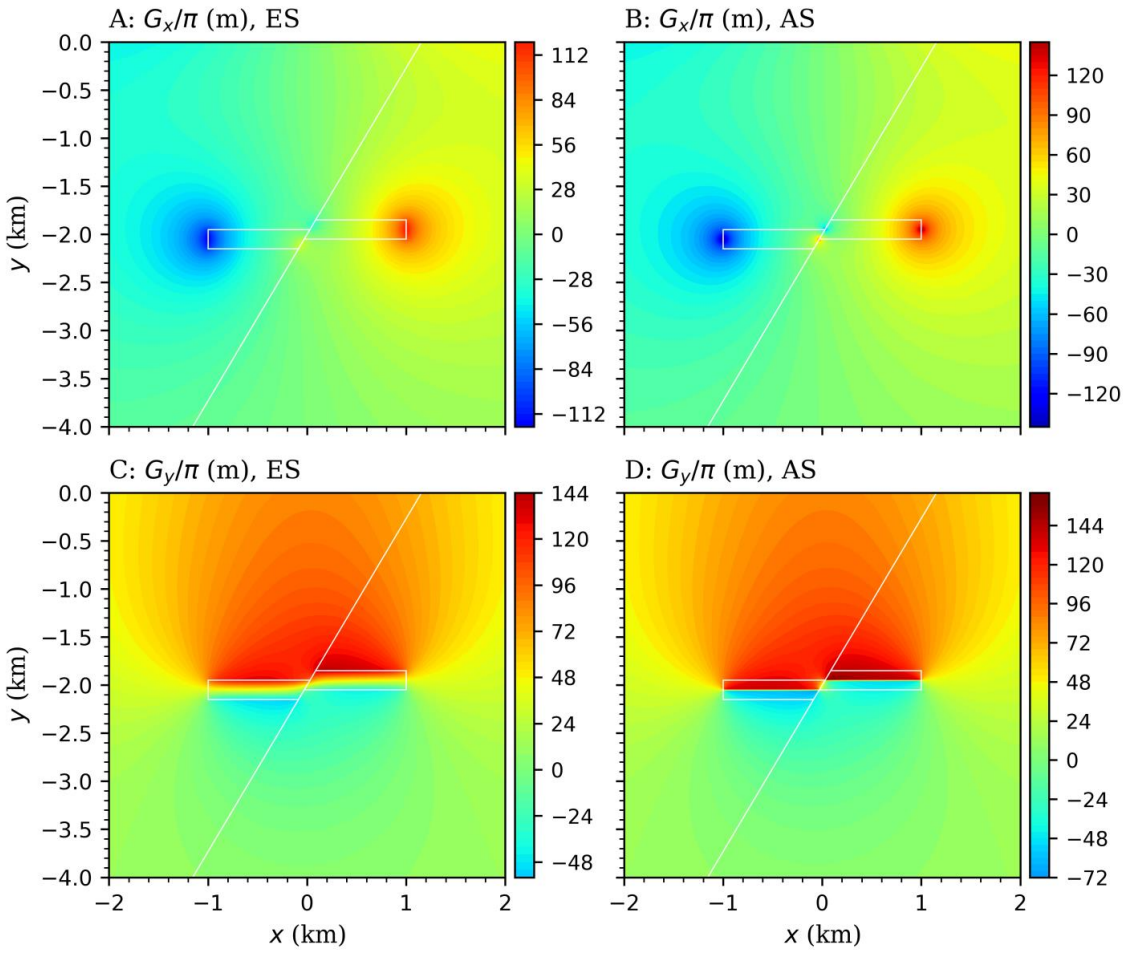

Figure J7: Comparison of the scaled horizontal (A and B) and vertical (C and D) displacement components between our exact solution (ES, A and C) and approximate solution (AS, B and D) for the zone of interest. A, B, C, and D have the same color scale but the range of the legends is adapted to the values shown in each case. Displacement is scaled by $\eta\Delta p / \mu$ with a value shown in Section 4.1 (we take the base-case study in Section 4.1 as an example). The reservoir geometry and the fault are indicated by the white lines.

K. Supplementary Information for Chapter 5

Text K1: Cases of fault shear strength variations due to fluid injection

In the chapter 5, we consider three factors that vary the frictional shear strength inside the slipping fault patch. To compare the role of each factor, we divide the shear strength variations into four cases, with the quasi-static elastic equilibrium equation for each case listed below.

Case A: only the role of overpressure is considered. We take it as the base case for comparison. We can get a similar equation to Equation (5.4) as

$$\frac{\tau^{\mathrm{b}}}{\tau_{\mathrm{p}}}-\frac{\mu^{*}}{2\pi\tau_{\mathrm{p}}}\int_{-a}^{a}\frac{d\delta(s)/ds}{x-s}ds=1-\frac{\alpha\Delta p(x,t)}{\sigma_0'}, \tag{K1}$$

where $\mu^{*}=\mu$ for mode III and $\mu^{*}=\mu/(1-\nu)$ for mode II, and μ is the shear modulus, ν is Poisson's ratio, α is Biot's coefficient, a is the crack half-length, x and t denote the spatial and temporal variables, respectively, and $1/(x\text{-}s)$ is a simple Cauchy-type kernel of singular integral. $\delta(x)$ is the slip, $\Delta p(x,t)$ means the pore pressure changes, τ^{b} is the background shear stress (loading), $\tau_{\mathrm{p}}=f_{\mathrm{p}}\sigma_0'$ denotes the peak shear strength where f_{p} is the static friction coefficient and $\sigma_0'=\sigma_0-\alpha p_0$ denotes the initial effective normal stress.

Case B: this case adds the poroelastic stress (poroelastic effects) to Case A, obtaining

$$\frac{\tau^{\mathrm{b}}+\Delta\tau(x,t)}{\tau_{\mathrm{p}}}-\frac{\mu^{*}}{2\pi\tau_{\mathrm{p}}}\int_{-a}^{a}\frac{d\delta(s)/ds}{x-s}ds=1-\frac{\alpha\Delta p(x,t)-\Delta\sigma(x,t)}{\sigma_0'}, \tag{K2}$$

where $\Delta\tau(x,t)$ and $\Delta\sigma(x,t)$ are the tangential and normal components of poroelastic stress.

Case C: this case adds the slip-weakening effects to Case A, it is the one considered by Garagash and Germanovich (2012), resulting in

$$\frac{\tau^{\mathrm{b}}}{\tau_{\mathrm{p}}}-\frac{\mu^{*}}{2\pi\tau_{\mathrm{p}}}\int_{-a}^{a}\frac{d\delta(s)/ds}{x-s}ds=\left[1-\frac{\delta(x)}{\delta_{\mathrm{w}}}\right]\left[1-\frac{\alpha\Delta p(x,t)}{\sigma_0'}\right],\quad 0\le\delta(x)<\delta_{\mathrm{w}}, \tag{K3}$$

where $\delta_{\mathrm{w}}=f_{\mathrm{p}}/w$ means the slip-weakening scale in which w is the linear decreasing rate of friction coefficient.

Case D: the latter case adds both the poroleastic and slip-weakening effects to Case A, which yields Equation (5.4).

Text K2: Surface integral of Green's function for a rectangle inclusion

The derivations of surface integral G_{ij} of Green's function for evaluating the poroelastic stress are introduced in the chapter 2. For a rectangle inclusion, the three components of surface integral read

$$G_{yy}(x,y) = -G_{xx}(x,y) = \operatorname{atan}\frac{x-x_1}{y-y_1} - \operatorname{atan}\frac{x-x_2}{y-y_1} - \operatorname{atan}\frac{x-x_1}{y-y_2} + \operatorname{atan}\frac{x-x_2}{y-y_2}, \tag{K4}$$

$$G_{xy}(x,y) = \frac{1}{2}\ln\frac{\left[\left(x-x_2\right)^2+\left(y-y_2\right)^2\right]\left[\left(x-x_1\right)^2+\left(y-y_1\right)^2\right]}{\left[\left(x-x_2\right)^2+\left(y-y_1\right)^2\right]\left[\left(x-x_1\right)^2+\left(y-y_2\right)^2\right]}, \tag{K5}$$

where x and y are the Cartesian coordinates, x_1, x_2, y_1, and y_2 are the left, right, bottom, and top boundaries of the rectangle inclusion, respectively.

Text K3: Benchmark of the Gauss-Chebyshev quadrature

We adopt the problem scenario of Garagash and Germanovich (2012) to benchmark the Gauss-Chebyshev quadrature applied to solve the singular integral equations. In their work, Garagash and Germanovich (2012) investigated the one dimensional fault slip problem due to fluid injection into the fault zone with only longitudinal permeability under a constant overpressure at injection well,

$$\Delta p(x,t) = \Delta p_{\text{well}} \cdot Erfc\left|\xi\right|, \qquad \xi = x/\sqrt{4D_{\text{h}}t} = \frac{\bar{x}\cdot\bar{a}}{\sqrt{\bar{t}}}, \tag{K6}$$

where Δp_{well} is the constant overpressure at the injection well and ξ is a spatiotemporal variable, D_{h} is the hydraulic diffusivity.

The previous case C is in agreement with the assumptions of Garagash and Germanovich (2012), hence, substituting Equation (K6) into Equation (K3) and reformatting the result in a dimensionless form read

$$-\frac{1}{2\pi\bar{a}}\int_{-1}^{1}\frac{d\bar{\delta}(\bar{s})/d\bar{s}}{\bar{x}-\bar{s}}d\bar{s} = 1-\bar{\tau}^{\text{b}} - \left[1-\bar{\delta}(\bar{x})\right]\alpha\Delta\bar{p}_{\text{well}}Erfc\left(\frac{\left|\bar{x}\right|\cdot\bar{a}}{\sqrt{\bar{t}}}\right) - \bar{\delta}(\bar{x}), \tag{K7}$$

where the variables with an overbar denote their dimensionless form, in particular, $\bar{a} = a/a_{\text{w}}$, $\bar{\delta} = \delta/\delta_{\text{w}}$, $\bar{x} = x/a$ ($\bar{s} = s/a$ as well), $\bar{t} = 4D_{\text{h}}t/a_{\text{w}}^2$, $\bar{\tau}^{\text{b}} = \tau^{\text{b}}/\tau_{\text{p}}$, and $\Delta\bar{p}_{\text{well}} = \Delta p_{\text{well}}/\sigma_0'$ in which $a_{\text{w}} = \delta_{\text{w}}\mu^*/\tau_{\text{p}}$ denotes the characteristic patch length.

Applying the Gauss-Chebyshev quadrature (see details in Section 5.2.3 of the Thesis) to solve Equation (K7), we obtain

$$-\frac{1}{2\pi\bar{a}}\sum_{j=1}^{n}w_j\frac{F(\bar{s}_j)}{\bar{x}_i-\bar{s}_j} = 1-\bar{\tau}^{\text{b}} - \left[1-\bar{\delta}(\bar{x}_i)\right]\alpha\Delta\bar{p}_{\text{well}}Erfc\left(\frac{\left|\bar{x}_i\right|\cdot\bar{a}}{\sqrt{\bar{t}}}\right) - \bar{\delta}(\bar{x}_i). \tag{K8}$$

We here take Biot's coefficient as 1 because Garagash and Germanovich (2012) does

not consider Biot's effect. We can solve the unknowns of Equation (K8) given the normalized background shear loading $\tau^{\mathrm{b}}/\tau_{\mathrm{P}}$ and the normalized overpressure $\Delta p_{\mathrm{well}}/\sigma_0'$ for an arbitrary injection time. Then, we can evaluate the distribution of normalized slip and shear stress along the crack plane. In the benchmark problem, we compare these distributions with the results of Garagash and Germanovich (2012) for three instants of normalized injection time under $\tau^{\mathrm{b}}/\tau_{\mathrm{P}} = 0.75$ and $\Delta p_{\mathrm{well}}/\sigma_0' = 0.5$ (Figure K1), showing an excellent agreement.

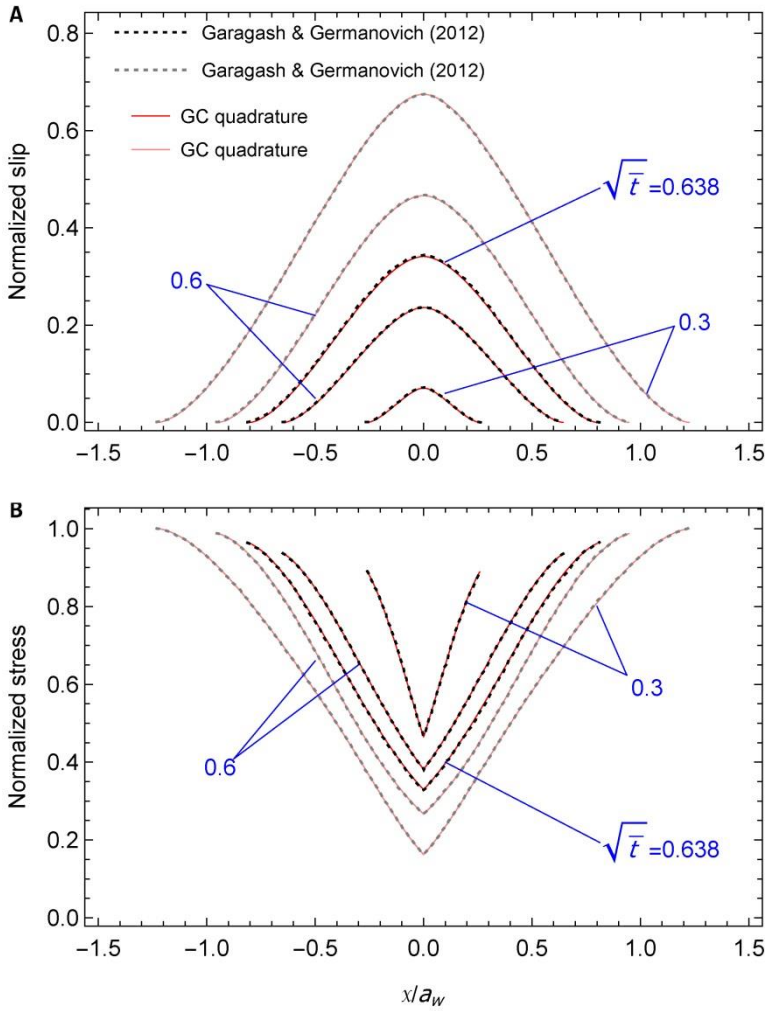

Figure K1: Distribution of the normalized (A) slip and (B) shear stress along the crack plane for the case of normalized overpressure equals 0.5 and of normalized shear loading equals 0.75 at the instants of the square root of normalized time equals 0.3, 0.6, and 0.638. Solid and dotted lines denote the results of the Gauss-Chebyshev quadrature and Garagash and Germanovich (2012), respectively; red and black lines represent the physically meaningful distribution, while pink and gray lines correspond to the physically meaningless one associated with the crack growth under the meaningless reversal of pore pressure diffusion.

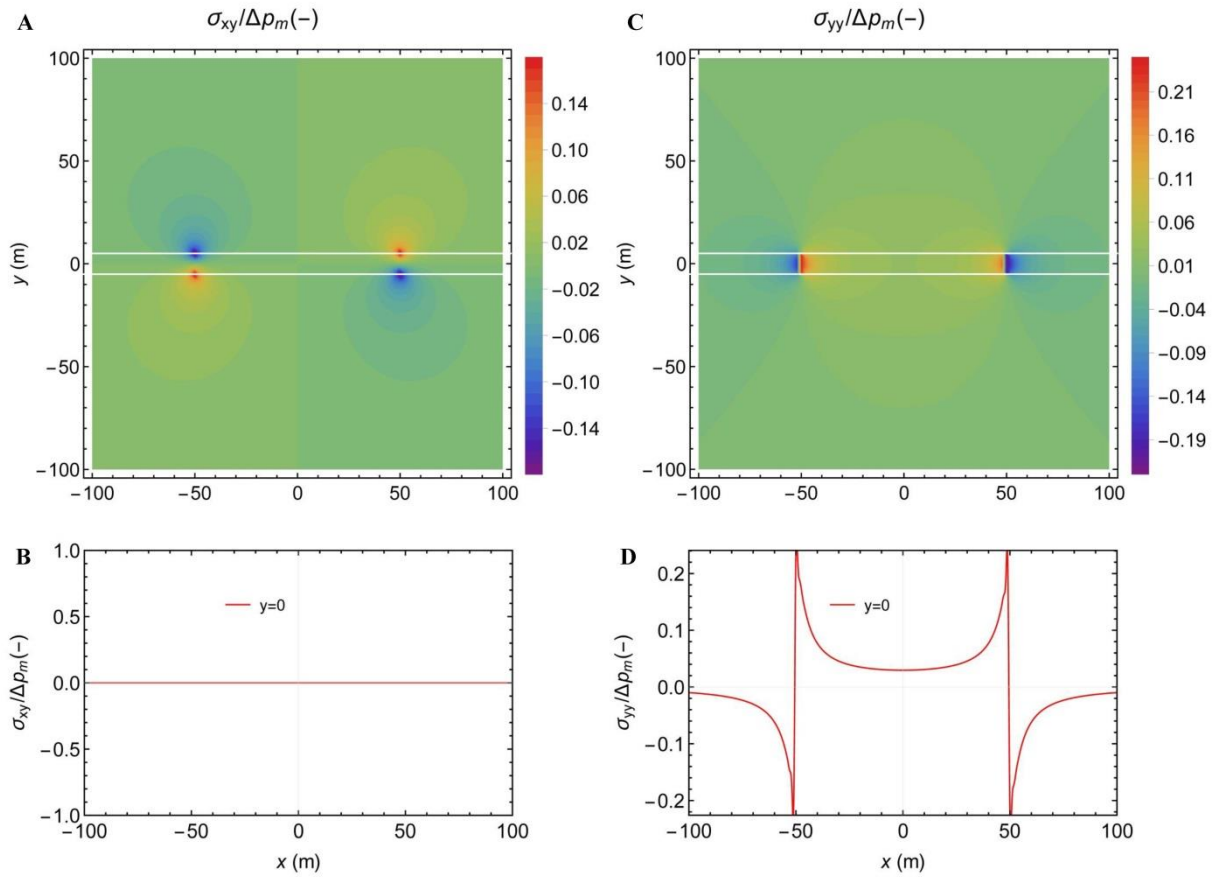

Figure K2: Distribution of scaled poroelastic stress components $\Delta\sigma_{xy}$ (A and B) and $\Delta\sigma_{yy}$ (C and D) in two dimensional *x*-*y* plane (A and C) and on the fault plane (y = 0, B and D). Poroelastic stress is evaluated with Equations (5.14), (K4) and (K4) and scaled by the mean pore pressure Δp_{m} of the pressurized inclusion, i.e., the results are independent of the mean pore pressure, under given values of $\alpha = 0.7$ and $\nu = 0.25$. The size of inclusion is 100 m in the *x* direction by 10 m in the *y* direction.

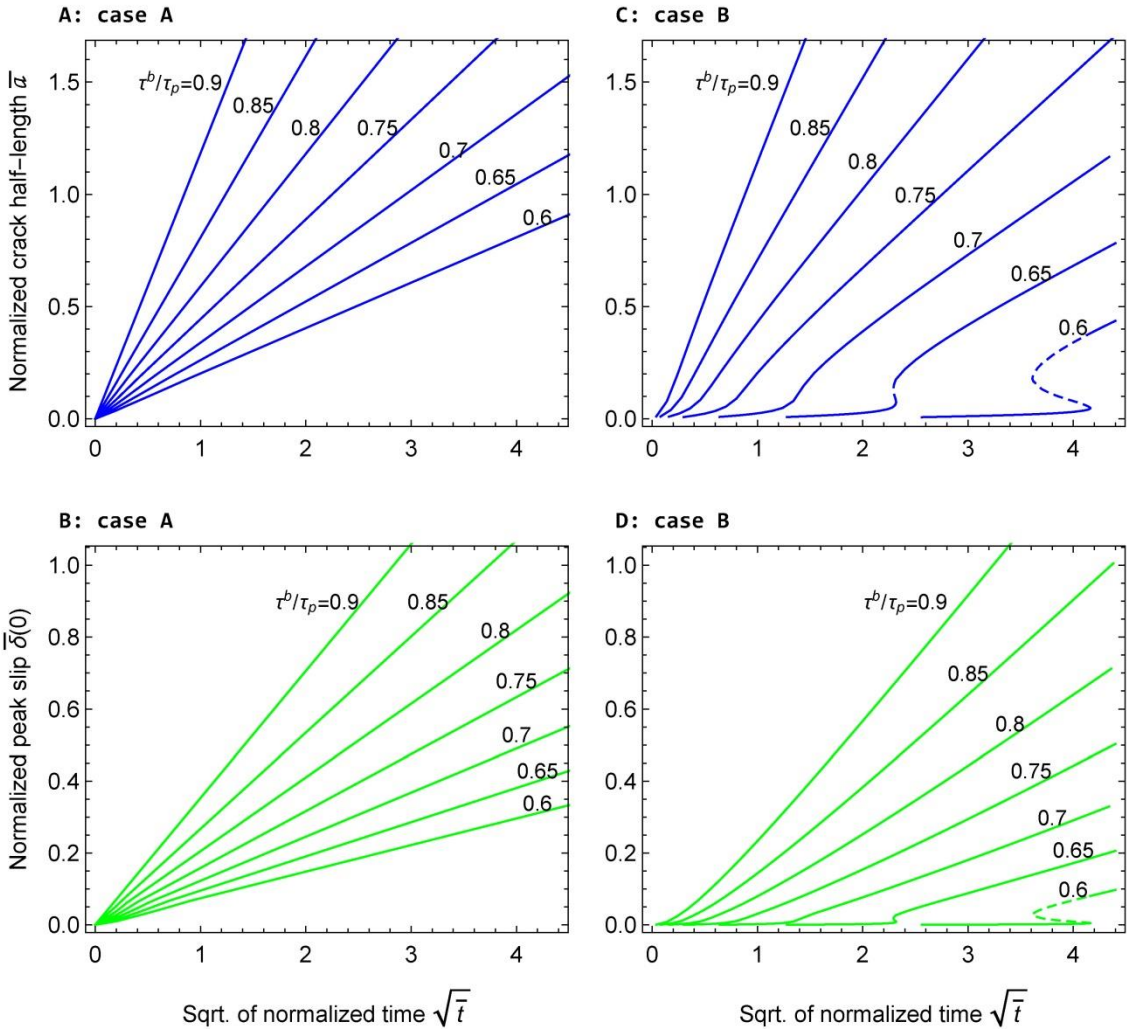

Figure K3: Evolution of the normalized crack half-length (A and C) and the normalized peak slip (i.e., the slip at the crack center) (B and D) of cases A (only pore pressure changes are considered) (A and B) and B (pore pressure changes and poroelastic effects are considered) (C and D) under the normalized volumetric injection rate of 0.9 and various values of the background stress. Solid and dashed parts of the lines correspond to the crack growth under physically meaningful advance and meaningless reversal of the pore pressure diffusion, respectively. The quasi-static fault slip never transits to dynamic rupture in case A, in which, the crack length and peak slip are proportional to the square root of normalized time. There is one nucleation point of dynamic rupture in case B for relatively small values of background shear loading. This dynamic rupture, which we denominate as poroelasticity-dominant, will arrest and turn to quasi-static slip again. These two phenomena are expected because the unabated dynamic crack propagation only occurs for the slip-weakening faults.

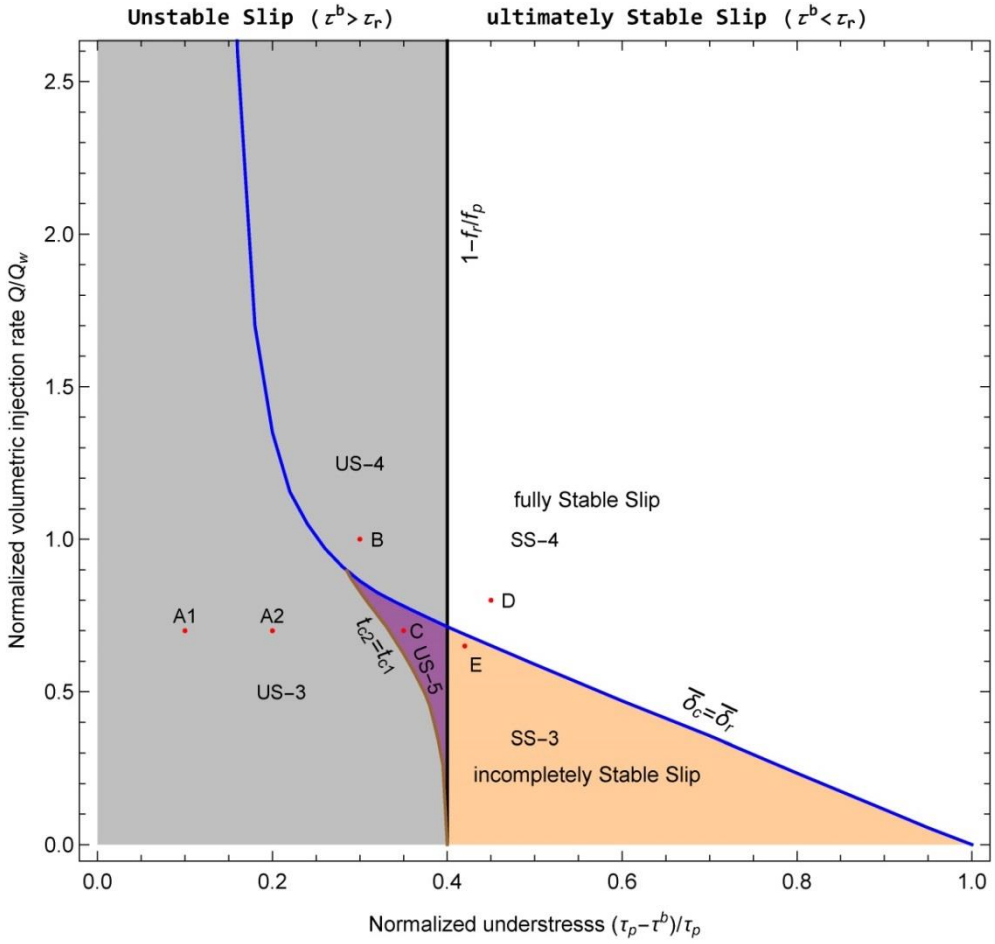

Figure K4: Map of slip regimes for case C (considering pore pressure changes and slip-weakening effects) in the normalized space of fault understress and injection rate. The black line separates the map as unstable slip (US) and ultimately stable slip (SS) regimes. The blue line separates the map where the nucleation/re-nucleation is and is not affected by residual friction f_r, respectively, which is evaluated from the solution with an unlimited slip-weakening law, i.e., without f_r. The brown line cuts out a sub-regime that indicates that the new re-nucleation, caused by the ending of slip weakening of a local patch, is and is not physically meaningful, respectively, which is evaluated with the limited slip-weakening law $f_\mathrm{r}/f_\mathrm{p} = 0.6$. US-3: slip-weakening-dominant unstable slip regime, with one nucleation point, caused by slip-weakening effects and not affected by f_r; US-4: slip-weakening-dominant unstable slip regime with a residual friction-delayed nucleation point; US-5: cut from the regime US-3, with one more re-nucleation point, caused by the ending of slip weakening, in addition to the one of US-3, not affected by f_r. SS-4: slip-weakening-dominant ultimately stable slip regime without nucleation, which is removed by f_r; SS-3: slip-weakening-dominant ultimately stable slip regime with one nucleation point, not affected by f_r. Here we extend the upper limit of normalized injection rate to the same one as in Figure 5 for comparison, while the potential tensile failure is not considered. The typical evolution of the normalized crack half-length and peak slip for each slip regime is shown in Figure S5. US-3, US-4, US-5, SS-4, and SS-3 just correspond to the slip regimes 2a, 3, 2b, 4, and 2c in Figure 11 of Garagash and Germanovich (2012), respectively.

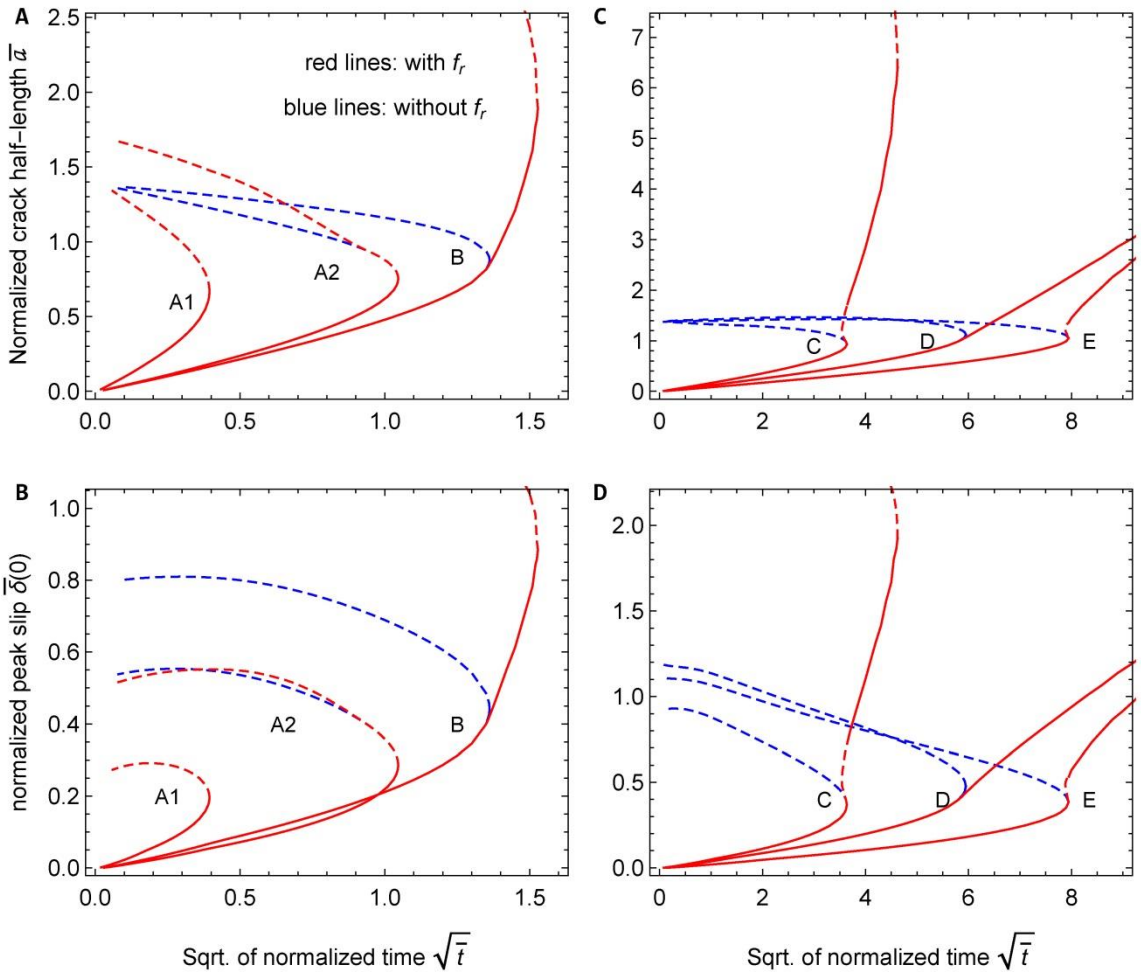

Figure K5: Typical evolution of the normalized crack half-length (A and C) and peak slip (B and D) for case C (considering pore pressure changes and slip-weakening effects) with (red lines) and without (blue lines) the residual friction for each slip regime. Solid and dashed parts of the lines correspond to the crack growth under physically meaningful advance and meaningless reversal of the pore pressure diffusion, respectively. The location of points A1-E is shown in Figure K4.

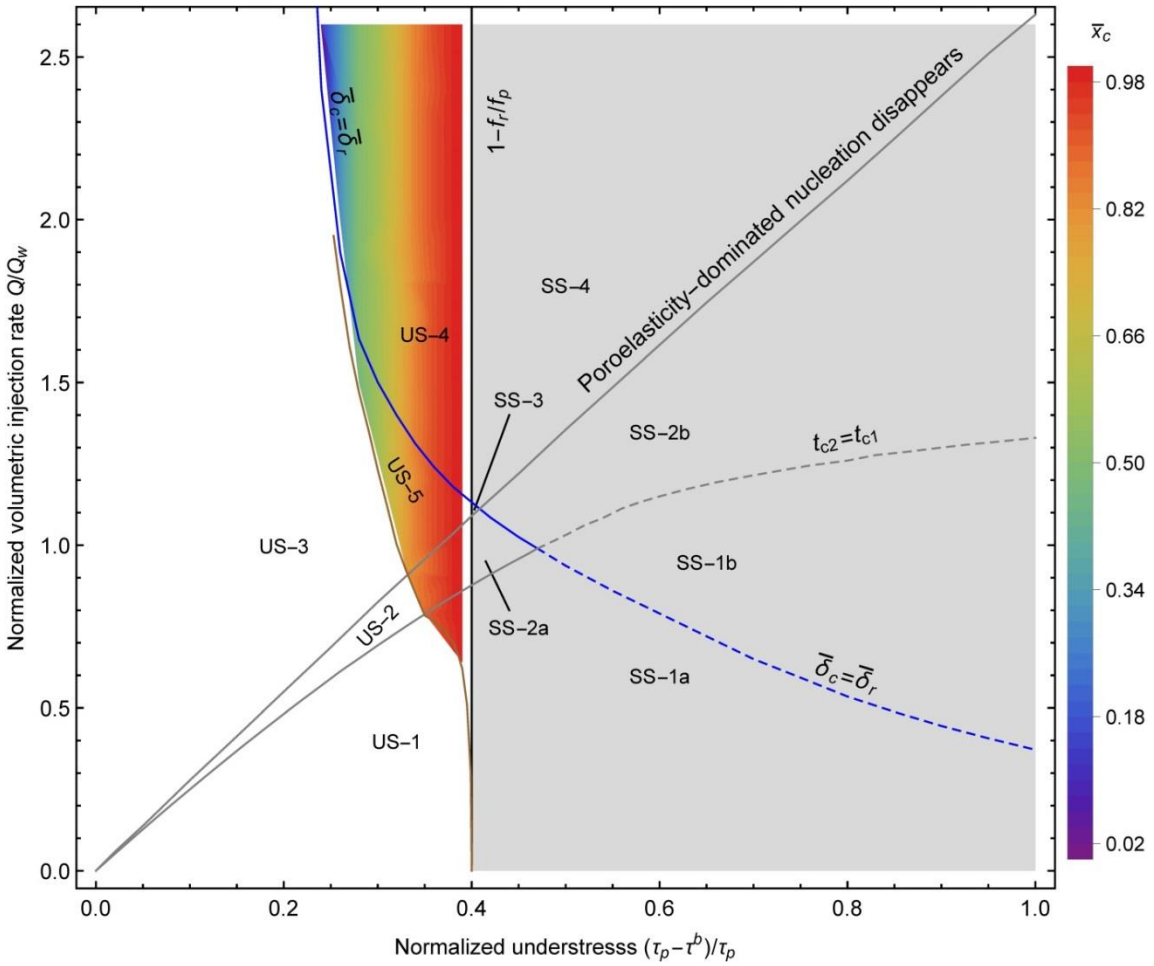

Figure K6: Distribution of normalized half-length $\bar{x}_c$ of the mature slip-weakening patch under case D (pore pressure changes and both poroelastic and slip-weakening effects are considered) in the normalized space of fault understress and volumetric injection rate. x_c is scaled by the crack half-length *a*. The previous three types of boundaries as well as the abbreviation of each slip regime shown in Figure 5.5 are also plotted here as a background for comparison.

References

Ahmadi, H., Lotfollahi-Yaghin, M. A., Yong-Bo, S. and Aminfar, M. H. (2012). Parametric study and formulation of outer-brace geometric stress concentration factors in internally ring-stiffened tubular KT-joints of offshore structures. *Applied Ocean Research*, 38, 74-91.

Alian, H., Konforty, S., Ben-Simon, U., Klein, R., Tur, M. and Bortman, J., 2019. Bearing fault detection and fault size estimation using fiber-optic sensors. *Mechanical Systems and Signal Processing*, 120, pp.392-407.

Ampuero, J.P. and Rubin, A.M., 2008. Earthquake nucleation on rate and state faults–Aging and slip laws. *Journal of Geophysical Research: Solid Earth*, 113(B1).

Araya, M.C. and Biggs, J. 2020. Episodic ground deformation associated with geothermal energy production at the Guayabo Caldera, Costa Rica. *Journal of Volcanology and Geothermal Research*. 407:107110.

Atkinson, G.M., Eaton, D.W. and Igonin, N., 2020. Developments in understanding seismicity triggered by hydraulic fracturing. *Nature Reviews Earth & Environment*, 1(5), pp.264-277.

Azad, M., Garagash, D.I. and Satish, M., 2017. Nucleation of dynamic slip on a hydraulically fractured fault. *Journal of Geophysical Research: Solid Earth*, 122(4), pp.2812-2830.

Bachu, S., Bonijoly, D., Bradshaw, J., Burruss, R., Holloway, S., Christensen, N.P. and Mathiassen, O.M., 2007. CO2 storage capacity estimation: Methodology and gaps. *International journal of greenhouse gas control*, 1(4), pp.430-443.

Bagheri-Gavkosh, M., Hosseini, S.M., Ataie-Ashtiani, B., Sohani, Y., Ebrahimian, H., … Ashrafi, S. 2021. Land subsidence: A global challenge. *Science of The Total Environment*. 778:146193.

Bai, B., Li, X., Wu, H., Wang, Y. and Liu, M. (2017). A methodology for designing maximum allowable wellhead pressure for CO_2 injection: application to the Shenhua CCS demonstration project, China. *Greenhouse Gases: Science and Technology*. 7(1): 158–181 doi:10.1002/ghg.1640

Bandilla, K. W. and Celia, M. A. (2017). Active pressure management through brine production for basin‐wide deployment of geologic carbon sequestration. *International Journal of Greenhouse Gas Control*, 61, 155-167

Bao, X. and Eaton, D.W., 2016. Fault activation by hydraulic fracturing in western Canada. *Science*, 354(6318), pp.1406-1409.

Barla, G. 1972. Stresses around a single underground opening near a traction-free surface. *International Journal of Rock Mechanics and Mining Sciences &*

Geomechanics Abstracts. 9(1):103–126.

Barry, D. A., Parlange, J. Y., & Li, L. (2000). Approximation for the exponential integral (Theis well function). *Journal of Hydrology*, 227(1-4), 287-291.

Ben-Zion, Y., and Sammis, C. G., 2003. Characterization of fault zones. *Pure and Applied Geophysics*, 160, 677-715.

Bernabe, Y. (1986). The effective pressure law for permeability in Chelmsford granite and Barre granite. *In International Journal of Rock Mechanics and Mining Sciences & Geomechanics Abstracts*. Vol. 23(3): 267-275

Bethmann, F., Ollinger, D., & Tormann, T., 2019. Seismicity analysis with spatial or temporal relation to the deep geothermal project in Pohang during 2016/2017. Geo-Energie Suisse AG, Zürich, Switzerland.

Bhattacharya, P., and Viesca, R. C., 2019. Fluid-induced aseismic fault slip outpaces pore-fluid migration. *Science*, 364(6439), 464-468.

Bilby, B. A., and Eshelby, J. D., 1968. Dislocations and theory of fracture, in Fracture, An Advanced Treatise, vol. 1, edited by H. Liebowitz, pp.99– 182, Academic, San Diego, Calif.

Bourne, S.J. 2003. Contrast of elastic properties between rock layers as a mechanism for the initiation and orientation of tensile failure under uniform remote compression. *Journal of Geophysical Research: Solid Earth*. 108(B8).

Bourne, S. J. and Oates, S. J. (2017). Extreme threshold failures within a heterogeneous elastic thin sheet and the spatial-temporal development of induced seismicity within the Groningen gas field. *J. Geoph. Res. Solid Earth*, 122, 10,299-10, 32. https://doi.org/ 10.1002/2017JB014356.

Bourne, S.J., Oates, S.J., Bommer, J.J., Dost, B., van Elk, J. and Doornhof, D., 2015. A Monte Carlo method for probabilistic hazard assessment of induced seismicity due to conventional natural gas production. *Bulletin of the Seismological Society of America*, 105(3), pp.1721-1738.

Boyet, A., De Simone, S., Ge, S. and Vilarrasa, V., 2023. Poroelastic stress relaxation, slip stress transfer and friction weakening controlled post-injection seismicity at the Basel Enhanced Geothermal System. *Communications Earth & Environment*, 4(1), p.104.

Budhu, M. 2011. Earth Fissure Formation from the Mechanics of Groundwater Pumping. *International Journal of Geomechanics*. 11(1):1–11.

Buijze, L., van den Bogert, P.A., Wassing, B.B., Orlic, B. and ten Veen, J., 2017. Fault reactivation mechanisms and dynamic rupture modelling of depletion-induced seismic events in a Rotliegend gas reservoir. *Netherlands Journal of Geosciences*, 96(5), pp.s131-s148.

Buijze, L., Van den Bogert, P.A.J., Wassing, B.B.T. and Orlic, B., 2019. Nucleation and arrest of dynamic rupture induced by reservoir depletion. *Journal of Geophysical*

Research: Solid Earth, 124(4), pp.3620-3645.

Brown, M.R. and Ge, S., 2018. Small earthquakes matter in injection‐induced seismicity. *Geophysical Research Letters*, 45(11), pp.5445-5453.

Byerlee, J.D., Brace, W.F., 1968. Stick slip, stable sliding, and earthquakes—Effect of rock type, pressure, strain rate, and stiffness. *J. Geophys. Res.* 1896-1977 73, 6031–6037. https://doi.org/10.1029/JB073i018p06031

Caine, J. S., Evans, J. P. and Forster, C. B. (1996). Fault zone architecture and permeability structure. *Geology*, 24(11), 1025-1028.

Cappa, F. and Rutqvist, J., 2012. Seismic rupture and ground accelerations induced by CO2 injection in the shallow crust. *Geophysical Journal International*, 190(3), pp.1784-1789.

Cappa, F., Scuderi, M.M., Collettini, C., Guglielmi, Y. and Avouac, J.P., 2019. Stabilization of fault slip by fluid injection in the laboratory and in situ. *Science advances*, 5(3), p.eaau4065.

Castelletto, N., Gambolati, G. and Teatini, P. (2013). Geological CO_2 sequestration in multi‐compartment reservoirs: Geomechanical challenges. *Journal of Geophysical Research: Solid Earth*, 118(5), 2417-2428.

Catalli, F., Meier, M.A. and Wiemer, S., 2013. The role of Coulomb stress changes for injection‐induced seismicity: The Basel enhanced geothermal system. *Geophysical Research Letters*, 40(1), pp.72-77.

Catalli, F., Rinaldi, A.P., Gischig, V., Nespoli, M. and Wiemer, S., 2016. The importance of earthquake interactions for injection‐induced seismicity: Retrospective modeling of the Basel Enhanced Geothermal System. *Geophysical Research Letters*, 43(10), pp.4992-4999.

Chang, K.W. and Segall, P., 2016. Injection‐induced seismicity on basement faults including poroelastic stressing. *Journal of Geophysical Research: Solid Earth*, 121(4), pp.2708-2726.

Chang, K.W., Yoon, H., Kim, Y. and Lee, M.Y., 2020. Operational and geological controls of coupled poroelastic stressing and pore-pressure accumulation along faults: Induced earthquakes in Pohang, South Korea. *Scientific reports*, 10(1), pp.1-12.

Chang, K. W., & Yoon, H., 2021. Mitigating injection-induced seismicity along basement faults by extraction: Application to 2016–2018 Pohang earthquakes. *Journal of Geophysical Research: Solid Earth*, 126, e2020JB021486. https://doi.org/10.1029/2020JB021486

Cheng, Y., Liu, W., Xu, T., Zhang, Y., Zhang, X., Xing, Y., Feng, B. and Xia, Y., 2023. Seismicity induced by geological CO2 storage: A review. *Earth-Science Reviews*, p.104369.

Chiaramonte, L., White, J.A., Hao, Y. 2013. Probabilistic Risk Assessment of

Mechanical Deformation due to CO2 Injection in a Compartmentalized Reservoir. 47th US Rock Mechanics / Geomechanics Symposium, San Francisco, CA, USA, 23-26 June 2013. ARMA 13-577

Choi, J. H., Ko, K., Gihm, Y. S., Cho, C. S., Lee, H., Song, S. G., ... & Lee, S. R., 2019. Surface deformations and rupture processes associated with the 2017 M w 5.4 Pohang, Korea, earthquake. *Bulletin of the Seismological Society of America*, 109(2), 756-769.

Ciardo, F. and Lecampion, B., 2019. Effect of dilatancy on the transition from aseismic to seismic slip due to fluid injection in a fault. *Journal of Geophysical Research: Solid Earth*, 124(4), pp.3724-3743.

Ciardo, F. and Rinaldi, A.P., 2022. Impact of injection rate ramp-up on nucleation and arrest of dynamic fault slip. *Geomechanics and Geophysics for Geo-Energy and Geo-Resources*, 8(1), p.28.

Cocco, M. and Rice, J.R., 2002. Pore pressure and poroelasticity effects in Coulomb stress analysis of earthquake interactions. *Journal of Geophysical Research: Solid Earth*, 107(B2), pp.ESE-2.

Cooper Jr, H. H., & Jacob, C. E., 1946. A generalized graphical method for evaluating formation constants and summarizing well‐field history. *Eos, Transactions American Geophysical Union*, 27(4), 526-534.

Cornet, F.H., 2016. Seismic and aseismic motions generated by fluid injections. *Geomech. Energy Environ*. 5, 42–54. https://doi.org/10.1016/j.gete.2015.12.003

Courant, R., and John, F., 1989. Introduction to calculus and analysis volume II. New York, NY: Springer-Verlag. https://doi. org/10.1007/978-1-4613-8958-3

Crews, J.B. and Cooper, C.A. 2014. Transient pore pressure response to confining stress excursions in Berea sandstone flooded with an aqueous solution of CO2. *Water Resources Research*. 50(6):4775–4786.

Deng, F., Dixon, T.H. and Xie, S. 2016. Surface Deformation and Induced Seismicity Due to Fluid Injection and Oil and Gas Extraction in Western Texas. *Journal of Geophysical Research: Solid Earth*. 125(5):e2019JB018962.

Del Potro, R. and Diez, M. (2015). Induced seismicity in underground gas storage - the case of castor, offshore ne spain. *77th EAGE Conference and Exhibition - Workshops*, Jun 2015, Volume 2015, p.1 - 3

Deichmann, N. and Giardini, D. (2009). Earthquakes induced by the stimulation of an enhanced geothermal system below Basel (Switzerland). *Seismological Research Letters*, 80(5), 784-798.

De Simone, S., Carrera, J. and Vilarrasa, V., 2017. Superposition approach to understand triggering mechanisms of post-injection induced seismicity. *Geothermics*, 70, pp.85-97.

De Simone, S., Vilarrasa, V., Carrera, J., Alcolea, A. and Meier, P., 2013. Thermal

coupling may control mechanical stability of geothermal reservoirs during cold water injection. *Physics and Chemistry of the Earth, Parts A/B/C*, 64, pp.117-126.

Detournay, E. and Cheng, A.H.-D., 1993. "Fundamentals of poroelasticity," Chapter 5 in Comprehensive Rock Engineering: Principles, Practice and Projects, Vol. II, Analysis and Design Method, ed. C. Fairhurst, Pergamon Press, pp. 113-171

DiBenedetto, E. (2016). Real Analysis 2nd edition, *Birkhäuser Advanced Texts: Basler Lehrbücher*, Boston: Birkhäuser. DOI 10.1007/978-1-4939-4005-9

Douma, L.A.N.R., Regelink, J.A., Bertotti, G., Boersma, Q.D. and Barnhoorn, A. 2019. The mechanical contrast between layers controls fracture containment in layered rocks. *Journal of Structural Geology*. 127:103856.

Doyle, T.C. and Ericksen, J.L. 1956. Nonlinear Elasticity. In: H.L. Dryden and Th. von Kármán, eds. Vol. 4. *Advances in Applied Mechanics*. Elsevier. pp. 53–115.

Dublanchet, P., 2019. Fluid driven shear cracks on a strengthening rate-and-state frictional fault. *Journal of the Mechanics and Physics of Solids*, 132, p.103672.

Du, J. and Olson, J.E. 2001. A poroelastic reservoir model for predicting subsidence and mapping subsurface pressure fronts. *Journal of Petroleum Science and Engineering*. 30(3):181–197.

Duverger, C., Godano, M., Bernard, P., Lyon‐Caen, H. and Lambotte, S. (2015). The 2003–2004 seismic swarm in the western Corinth rift: Evidence for a multiscale pore pressure diffusion process along a permeable fault system. *Geophysical Research Letters*, 42(18), 7374-7382.

Dziewonski, A.M. and Anderson, D.L. 1981. Preliminary reference Earth model. *Physics of the Earth and Planetary Interiors*. 25(4):297–356.

Ellsworth, W. L., 2013. Injection-induced earthquakes. *Science*, 341(6142), 1225942.

Elsworth, D., Spiers, C.J. and Niemeijer, A.R., 2016. Understanding induced seismicity. *Science*, 354(6318), pp.1380-1381.

Ellsworth, W.L. and Beroza, G.C., 1995. Seismic evidence for an earthquake nucleation phase. *Science*, 268(5212), pp.851-855.

Ellsworth, W. L., Giardini, D., Townend, J., Ge, S., and Shimamoto, T., 2019. Triggering of the Pohang, Korea, Earthquake (Mw 5.5) by Enhanced Geothermal System Stimulation. *Seismological Research Letters*, 90(5), 1844-1858.

Emter, D., 1997. Tidal triggering of earthquakes and volcanic events. *Tidal Phenomena*, 66, 293–309.

Erdogan, F., Gupta, G.D., 1972. On the numerical solution of singular integral equations. *Q. Appl. Math.* 289, 288–291.

Erdogan, F., Gupta, G.D., Cook, T.S., 1973. Numerical solution of singular integral equations. In: Sih, G.C. (Ed.), Methods of Analysis and Solutions of Crack Problems, Mechanics of Fracture Series. *NoordhoffInt.Pub*.,pp.368–425.

Eshelby, J. D., 1957. The determination of the elastic field of an ellipsoidal inclusion and related problems. Proceedings of the Royal Society London. *Series A. Mathematical and Physical Sciences*, 241, 376–396. http://dx.doi.org/10.1098/rspa.1957.0133

Evans, K.F., Zappone, A., Kraft, T., Deichmann, N. and Moia, F., 2012. A survey of the induced seismic responses to fluid injection in geothermal and CO2 reservoirs in Europe. *Geothermics*, 41, pp.30-54.

Eyre, T. S., Eaton, D. W., Garagash, D. I., Zecevic, M., Venieri, M., Weir, R., and Lawton, D. C., 2019. The role of aseismic slip in hydraulic fracturing–induced seismicity. *Science advances*, 5(8), eaav7172.

Eyre, T.S., Samsonov, S., Feng, W., Kao, H. and Eaton, D.W., 2022. InSAR data reveal that the largest hydraulic fracturing-induced earthquake in Canada, to date, is a slow-slip event. *Scientific reports*, 12(1), p.2043.

Fan, Z., Eichhubl, P. and Gale, J.F., 2016. Geomechanical analysis of fluid injection and seismic fault slip for the Mw4. 8 Timpson, Texas, earthquake sequence. *Journal of Geophysical Research: Solid Earth*, 121(4), pp.2798-2812.

Farkas, M. P., Hofmann, H., Zimmermann, G., Zang, A., Bethmann, F., Meier, P., ... & Josephson, N. (2021). Hydromechanical analysis of the second hydraulic stimulation in well PX-1 at the Pohang fractured geothermal reservoir, South Korea. *Geothermics*, 89, 101990.

Fjær, E., Holt, R.M., Horsrud, P., Raaen, A.M. and Risnes, R. 2008. Chapter 12 Reservoir geomechanics. In: E. Fjær, R.M. Holt, P. Horsrud, A.M. Raaen, and R. Risnes, eds. Vol. 53. (Petroleum Related Rock Mechanics 2nd Edition). *Developments in Petroleum Science*. Elsevier. pp. 391–433.

Foulger, G.R., Wilson, M.P., Gluyas, J.G., Julian, B.R. and Davies, R.J., 2018. Global review of human-induced earthquakes. *Earth-Science Reviews*, 178, pp.438-514.

Freed, A.M., 2005. Earthquake triggering by static, dynamic, and postseismic stress transfer. *Annu. Rev. Earth Planet. Sci.*, 33, pp.335-367.

Fu, J., Yang, J., Yan, L. and Abbas, S.M. 2015. An analytical solution for deforming twin-parallel tunnels in an elastic half plane: AN ANALYTICAL SOLUTION FOR DEFORMING TWIN TUNNELS. *International Journal for Numerical and Analytical Methods in Geomechanics*. 39(5):524–538.

Galis, M., Ampuero, J.P., Mai, P.M. and Cappa, F., 2017. Induced seismicity provides insight into why earthquake ruptures stop. *Science Advances*, 3(12), p.eaap7528.

Galis, M., Pelties, C., Kristek, J., Moczo, P., Ampuero, J.P. and Mai, P.M., 2015. On the initiation of sustained slip-weakening ruptures by localized stresses. *Geophysical Journal International*, 200(2), pp.890-909.

Galis, M., Ampuero, J. P., Mai, P. M. and Kristek, J., 2019. Initiation and arrest of earthquake ruptures due to elongated overstressed regions. *Geophysical Journal International*, 217(3), 1783-1797.

Gan, W. and Frohlich, C., 2013. Gas injection may have triggered earthquakes in the Cogdell oil field, Texas. *Proceedings of the National Academy of Sciences*, 110(47), pp.18786-18791.

Galloway, D.L. and Burbey, T.J. 2011. Review: Regional land subsidence accompanying groundwater extraction. *Hydrogeology Journal*. 19(8):1459–1486.

Garagash, D. I., 2021. Fracture mechanics of rate-and-state faults and fluid injection induced slip. *Philosophical Transactions of the Royal Society A*, 379(2196), 20200129.

Garagash, D. I., and Germanovich, L. N., 2012. Nucleation and arrest of dynamic slip on a pressurized fault. *Journal of Geophysical Research: Solid Earth*, 117(B10).

Garagash, D.I. and Rudnicki, J.W., 2003. Shear heating of a fluid‐saturated slip‐weakening dilatant fault zone 1. Limiting regimes. *Journal of Geophysical Research: Solid Earth*, 108(B2).

Ge, S. and Saar, M.O., 2022. Induced Seismicity During Geoenergy Development—A Hydromechanical Perspective. *Journal of Geophysical Research: Solid Earth*, 127(3), p.e2021JB023141.

Geertsma, J. 1973. Land Subsidence Above Compacting Oil and Gas Reservoirs. *Journal of Petroleum Technology*. 25(06):734–744.

Géraud, Y., Diraison, M., and Orellana, N. 2006. Fault zone geometry of a mature active normal fault: a potential high permeability channel (Pirgaki fault, Corinth rift, Greece). Tectonophysics, 426(1-2), 61-76.Gilluly, J. and Grant, U.S. 1949. SUBSIDENCE IN THE LONG BEACH HARBOR AREA, CALIFORNIA. *GSA Bulletin*. 60(3):461–530.

Ghassemi, A., Tarasovs, S. and Cheng, A.D., 2007. A 3-D study of the effects of thermomechanical loads on fracture slip in enhanced geothermal reservoirs. *International Journal of Rock Mechanics and Mining Sciences*, 44(8), pp.1132-1148.

Gischig, V.S., 2015. Rupture propagation behavior and the largest possible earthquake induced by fluid injection into deep reservoirs. *Geophysical Research Letters*, 42(18), pp.7420-7428.

Gischig, V.S. and Wiemer, S., 2013. A stochastic model for induced seismicity based on non-linear pressure diffusion and irreversible permeability enhancement. *Geophysical Journal International*, 194(2), pp.1229-1249.

Goebel, T.H.W., Weingarten, M., Chen, X., Haffener, J. and Brodsky, E.E., 2017. The 2016 Mw5. 1 Fairview, Oklahoma earthquakes: Evidence for long-range poroelastic triggering at> 40 km from fluid disposal wells. *Earth and Planetary Science Letters*, 472, pp.50-61.

Goodier, J.N. 1937. XCVII. On the integration of the thermo-elastic equations. *The London, Edinburgh, and Dublin Philosophical Magazine and Journal of Science*. 23(157):1017–1032.

Grigoli, F., Cesca, S., Priolo, E., Rinaldi, A.P., Clinton, J.F., Stabile, T.A., Dost, B., Fernandez, M.G., Wiemer, S. and Dahm, T., 2017. Current challenges in monitoring, discrimination, and management of induced seismicity related to underground industrial activities: A European perspective. *Reviews of Geophysics*, 55(2), pp.310-340.

Grigoli, F., Cesca, S., Rinaldi, A.P., Manconi, A., Lopez-Comino, J.A., Clinton, J.F., Westaway, R., Cauzzi, C., Dahm, T. and Wiemer, S., 2018. The November 2017 M w 5.5 Pohang earthquake: A possible case of induced seismicity in South Korea. *Science*, 360(6392), pp.1003-1006.

Grilli, S.T., Harris, J.C., Tajalli Bakhsh, T.S., Masterlark, T.L., Kyriakopoulos, C., … Shi, F. 2013. Numerical Simulation of the 2011 Tohoku Tsunami Based on a New Transient FEM Co-seismic Source: Comparison to Far- and Near-Field Observations. *Pure and Applied Geophysics*. 170(6):1333–1359.

Guglielmi, Y., Cappa, F., Avouac, J.P., Henry, P. and Elsworth, D., 2015. Seismicity triggered by fluid injection–induced aseismic slip. *Science*, 348(6240), pp.1224-1226.

Hanks, T. C., and Kanamori, H., 1979. A moment magnitude scale. *Journal of Geophysical Research: Solid Earth*, 84(B5), 2348-2350.

Hansen, O., Gilding, D., Nazarian, B., Osdal, B., Ringrose, P., Kristoffersen, J. B., ... and Hansen, H., 2013. Snøhvit: The history of injecting and storing 1 Mt CO2 in the fluvial Tubåen Fm. *Energy Procedia*, 37, 3565-3573.

Häring, M. O., Schanz, U., Ladner, F. and Dyer, B. C., 2008. Characterisation of the Basel 1 enhanced geothermal system. *Geothermics*, 37(5), 469–495.

Haug, C., Nuchter, J.-A. and Henk, A., 2018. Assessment of geological factors potentially affecting production-induced seismicity in North German gas fields. *Geomechanics for Energy and the Environment*, 16, 15-31. https://doi.org/10.1016/j.gete.2018.04.002.

Karvounis, D. C., Gischig, V. S. and Wiemer, S., 2014. Towards a real-time forecast of induced seismicity for enhanced geothermal systems. In *Shale Energy Engineering 2014: Technical Challenges, Environmental Issues and Public Policy* (pp. 246-255).

Harrison, R.L., 2010, January. Introduction to monte carlo simulation. In AIP conference proceedings (Vol. 1204, No. 1, pp. 17-21). *American Institute of Physics*.

Hazzard, J.F. and Young, R.P., 2004. Dynamic modelling of induced seismicity. *International journal of rock mechanics and mining sciences*, 41(8), pp.1365-1376.

Healy, J.H., Rubey, W.W., Griggs, D.T. and Raleigh, C.B., 1968. The denver earthquakes. *Science*, 161(3848), pp.1301-1310.

Hofmann, H., Zimmermann, G., Farkas, M., Huenges, E., Zang, A., Leonhardt, M., ...

& Kim, K. Y. (2019). First field application of cyclic soft stimulation at the Pohang Enhanced Geothermal System site in Korea. *Geophysical Journal International*, 217(2), 926-949.

Hoteit, H., Fahs, M. and Soltanian, M.R., 2019. Assessment of CO2 injectivity during sequestration in depleted gas reservoirs. *Geosciences*, 9(5), p.199.

Hubbert, M.K. and Rubey, W.W., 1959. Role of fluid pressure in mechanics of overthrust faulting: I. Mechanics of fluid-filled porous solids and its application to overthrust faulting. *Geological Society of America Bulletin*, 70(2), pp.115-166.

IEA (International Energy Agency)., 2011. World Energy Outlook 2011. OECD/IEA, Paris.

IEA (International Energy Agency)., 2020. Energy Technology Perspectives 2020, Special Report on Carbon Capture Utilisation and Storage. OECD/IEA, Paris.

Jacquey, A.B. and Viesca, R.C., 2023. Nucleation and Arrest of Fluid‐Induced Aseismic Slip. *Geophysical Research Letters*, 50(4), p.e2022GL101228.

Jaeger, J. C., Cook, N. G., & Zimmerman, R., 2007. Fundamentals of rock mechanics, 4th ed. Blackwell Publishing.

Jachens, R.C. and Holzer, T.L. 1982. Differential compaction mechanism for earth fissures near Casa Grande, Arizona. *GSA Bulletin*. 93(10):998–1012.

Jansen, J.D., Singhal, P. and Vossepoel, F.C., 2019. Insights from closed‐form expressions for injection‐and production‐induced stresses in displaced faults. *Journal of Geophysical Research: Solid Earth*, 124(7), pp.7193-7212.

Jayeoba, A., Mathias, S.A., Nielsen, S., Vilarrasa, V. and Bjørnarå, T.I. 2019. Closed-form equation for subsidence due to fluid production from a cylindrical confined aquifer. *Journal of Hydrology*. 573:964–969.

Jeanne, P., Rutqvist, J., Dobson, P.F., Walters, M., Hartline, C. and Garcia, J., 2014. The impacts of mechanical stress transfers caused by hydromechanical and thermal processes on fault stability during hydraulic stimulation in a deep geothermal reservoir. *International Journal of Rock Mechanics and Mining Sciences*, 72, pp.149-163.

Jha, B. and Juanes, R. (2014). Coupled multiphase flow and poromechanics: a computational model of pore pressure effects on fault slip and earthquake triggering. *Water Resources Research*, 50(5), 3776-3808.

Ji, Y., Zhuang, L., Wu, W., Hofmann, H., Zang, A., & Zimmermann, G., 2021. Cyclic Water Injection Potentially Mitigates Seismic Risks by Promoting Slow and Stable Slip of a Natural Fracture in Granite. Rock Mechanics and Rock Engineering, 1-17.

Johnson, P.A. and Rasolofosaon, P.N.J. 1996. Nonlinear elasticity and stress-induced anisotropy in rock. *Journal of Geophysical Research: Solid Earth*. 101(B2):3113–3124.

Juncu, D., Árnadóttir, Th., Geirsson, H., Guðmundsson, G.B., Lund, B., … Michalczewska, K. 2020. Injection-induced surface deformation and seismicity at the Hellisheidi geothermal field, Iceland. *Journal of Volcanology and Geothermal Research*. 391:106337.

Juncu, D., Árnadóttir, Th., Hooper, A. and Gunnarsson, G. 2017. Anthropogenic and natural ground deformation in the Hengill geothermal area, Iceland. *Journal of Geophysical Research: Solid Earth*. 122(1):692–709.

Juanes, R., Castiñeira, D., Fehler, M. C., Hager, B. H., Jha, B., Shaw, J. H. and Plesch, A., 2017. *Coupled flow and geomechanical modeling and assessment of induced seismicity, at the Castor underground gas storage project*. Final report.

Juanes, R., Hager, B.H. and Herzog, H.J., 2012. No geologic evidence that seismicity causes fault leakage that would render large-scale carbon capture and storage unsuccessful. *Proceedings of the National Academy of Sciences*, 109(52), pp.E3623-E3623.

Kanamori, H., 1977. The energy release in great earthquakes. *Journal of Geophysical Research*, 82(20), 2981-2987.

Kang, S., Kim, B., Bae, S., Lee, H., & Kim, M., 2019. Earthquake-induced ground deformations in the low-seismicity region: A case of the 2017 M5. 4 Pohang, South Korea, earthquake. *Earthquake Spectra*, 35(3), 1235-1260.

Kang, J.Q., Zhu, J.B. and Zhao, J., 2019. A review of mechanisms of induced earthquakes: from a view of rock mechanics. *Geomechanics and Geophysics for Geo-Energy and Geo-Resources*, 5(2), pp.171-196.

Keranen, K.M. & Weingarten, M., 2018. Induced Seismicity. *Annual Review of Earth and Planetary Sciences*. 46(1):149–174.

Ketelaar, V., van Leijen, F., Marinkovic, P. and Hanssen, R. 2006. On the use of point target characteristics in the estimation of low subsidence rates dues to gas extraction in Groningen, The Netherlands. In: null A. Arnaud & null J. Mallorqui, eds. Frascati, Italy: ESA Publications Division. pp. http://earth.esa.int/workshops/fringe05/proceedings/toc_clean.html Date of access: 21 Mar. 2023.

Kim, H., Xie, L., Min, K. B., Bae, S., & Stephansson, O., 2017. Integrated in situ stress estimation by hydraulic fracturing, borehole observations and numerical analysis at the EXP-1 borehole in Pohang, Korea. *Rock Mechanics and Rock Engineering*, 50(12), 3141-3155.

Kim, K. H., Ree, J. H., Kim, Y., Kim, S., Kang, S. Y., & Seo, W., 2018. Assessing whether the 2017 Mw 5.4 Pohang earthquake in South Korea was an induced event. *Science*, 360(6392), 1007-1009.

Kim, K.H., Seo, W., Han, J., Kwon, J., Kang, S.Y., Ree, J.H., Kim, S. & Liu, K., 2020. The 2017 ML 5.4 Pohang earthquake sequence, Korea, recorded by a dense seismic network. *Tectonophysics*, 774, p.228306.

King, G.C., Stein, R.S. and Lin, J., 1994. Static stress changes and the triggering of earthquakes. *Bulletin of the Seismological Society of America*, 84(3), pp.935-953.

Kivi, I. R., Boyet, A., Wu, H., Walter, L., Hanson-Hedgecock, S., Parisio, F., and Vilarrasa, V., 2022a. Global physics-based database of injection-induced seismicity [Dataset], https://doi.org/10.20350/digitalCSIC/14813

Kivi, I.R., Pujades, E., Rutqvist, J. and Vilarrasa, V., 2022b. Cooling-induced reactivation of distant faults during long-term geothermal energy production in hot sedimentary aquifers. *Scientific reports*, 12(1), p.2065.

Kivi, I. R., Boyet, A., Wu, H., Walter, L., Hanson-Hedgecock, S., Parisio, F. and Vilarrasa, V., 2023. Global physics-based database of injection-induced seismicity. *Earth System Science Data Discussions*, [preprint], https://doi.org/10.5194/essd-2022-448, accepted.

Kokusho, T., Ishizawa, T. and Nishida, K., 2009. Travel distance of failed slopes during 2004 Chuetsu earthquake and its evaluation in terms of energy. *Soil Dynamics and Earthquake Engineering*, 29(7), pp.1159-1169.

Korean Government Commission. 2019. "Summary report of the Korean Government Commission on relations between the 2017 Pohang earthquake and EGS project". Geological Society of Korea, Seoul, South Korea, https://doi.org/10.22719/KETEP-20183010111860.

Kruszewski, M., Hofmann, H., Alvarez, F.G., Bianco, C., Haro, A.J., Garduño, V.H., Liotta, D., Trumpy, E., Brogi, A., Wheeler, W. and Bastesen, E., 2021. Integrated stress field estimation and implications for enhanced geothermal system development in Acoculco, Mexico. *Geothermics*, 89, p.101931.

Kwiatek, G., Saarno, T., Ader, T., Bluemle, F., Bohnhoff, M., Chendorain, M., Dresen, G., Heikkinen, P., Kukkonen, I., Leary, P. and Leonhardt, M., 2019. Controlling fluid-induced seismicity during a 6.1-km-deep geothermal stimulation in Finland. *Science Advances*, 5(5), p.eaav7224.

Kwon, S., Xie, L., Park, S., Kim, K. I., Min, K. B., Kim, K. Y., ... & Lee, T. J., 2019. Characterization of 4.2-km-deep fractured granodiorite cores from Pohang Geothermal Reservoir, Korea. *Rock Mechanics and Rock Engineering*, 52(3), 771-782.

Langenbruch, C. and Zoback, M.D., 2016. How will induced seismicity in Oklahoma respond to decreased saltwater injection rates?. *Science advances*, 2(11), p.e1601542.

Lee, C.F., Zhang, J.M. and Zhang, Y.X. 1996. Evolution and origin of the ground fissures in Xian, China. *Engineering Geology*. 43(1):45–55.

Lee, K.K., Ellsworth, W.L., Giardini, D., Townend, J., Ge, S., Shimamoto, T., Yeo, I.W., Kang, T.S., Rhie, J., Sheen, D.H. & Chang, C., 2019. Managing injection-induced seismic risks. *Science*, 364(6442), pp.730-732.

Lee, T. J., Y. Song, D.-W. Park, J. Jeon, and W. S. Yoon, 2015. Three dimensional

geological model of Pohang EGS pilot site, Korea, paper presented at Proc. of the World Geothermal Congress, Melbourne, Australia, 19–25 April 2015.

Lehner, F.K. 2019. *An analysis of depletion-induced fault stressing-new closed-form analytical solutions*. (Scientific Report SR.19.01549). NAM and Shell Global Solutions International B.V. http://www.nam.nl/feiten-en-cijfers/onderzoeksrapporten.html.

Lele, S., Hsu, S.-Y., Garzon, J., DeDontney, N., Searles, K., Gist, G., . . . Dale, B. (2016). Geomechanical modeling to evaluate production-induced seismicity at Groningen field. *In Proc. Abu Dhabi International Petroleum Exhibition and Conference*. https://doi.org/10.2118/183554-MS. (7-10 Nov., Abu Dhabi, UAE)

Lemoine, A., Briole, P., Bertil, D., Roullé, A., Foumelis, M., … Hoste Colomer, R. 2020. The 2018–2019 seismo-volcanic crisis east of Mayotte, Comoros islands: seismicity and ground deformation markers of an exceptional submarine eruption. *Geophysical Journal International*. 223(1):22–44.

Lim, H., Deng, K., Kim, Y.H., Ree, J.-H., Song, T.-R. A., & Kim, K.-H., 2020. The 2017 Mw 5.5 Pohang earthquake, South Korea, and poroelastic stress changes associated with fluid injection. *Journal of Geophysical Research: Solid Earth*, 124, e2019JB019134.

Lisle, R.J. and Srivastava, D.C., 2004. Test of the frictional reactivation theory for faults and validity of fault-slip analysis. *Geology*, 32(7), pp.569-572.

Loesch, E. and Sagan, V. 2018. SBAS Analysis of Induced Ground Surface Deformation from Wastewater Injection in East Central Oklahoma, USA. *Remote Sensing*. 10(2):283.

Love, A.E.H. (1944) *A treatise on the mathematical theory of elasticity*. 4th edn. New York. NY: Dover Publications

Majer, E.L., Baria, R., Stark, M., Oates, S., Bommer, J., Smith, B. and Asanuma, H., 2007. Induced seismicity associated with enhanced geothermal systems. *Geothermics*, 36(3), pp.185-222.

Makhnenko, R. Y. and Labuz, J. F. (2015). Dilatant hardening of fluid‐saturated sandstone. *Journal of Geophysical Research: Solid Earth*, 120(2), 909-922.

Makhnenko, R. Y., & Labuz, J. F., 2016. Elastic and inelastic deformation of fluid-saturated rock. *Philosophical Transactions of the Royal Society A: Mathematical, Physical and Engineering Sciences*, 374(2078), 20150422.

Marone, C., 1998. Laboratory-derived friction laws and their application to seismic faulting. *Annual Review of Earth and Planetary Sciences*, 26(1), pp.643-696.

Masoudian, M.S., Afrapoli, M.A.H., Tasalloti, A. and Marshall, A.M., 2019. A general framework for coupled hydro-mechanical modelling of rainfall-induced instability in unsaturated slopes with multivariate random fields. *Computers and Geotechnics*, 115, p.103162.

Mathias, S. A., Hardisty, P. E., Trudell, M. R. and Zimmerman, R. W. . (2009). Screening and selection of sites for CO_2 sequestration based on pressure buildup. *International Journal of Greenhouse Gas Control*, 3(5), 577-585.

McGarr, A., 2014. Maximum magnitude earthquakes induced by fluid injection. *Journal of Geophysical Research: solid earth*, 119(2), pp.1008-1019.

McGarr, A., Simpson, D., Seeber, L. and Lee, W., 2002. Case histories of induced and triggered seismicity. *International Geophysics Series*, 81(A), pp.647-664.

McTigue, D.F., 1986. Thermoelastic response of fluid‐saturated porous rock. *Journal of Geophysical Research: Solid Earth*, 91(B9), pp.9533-9542.

Mehrabian, A. and Abousleiman, Y.N. 2015. Geertsma's subsidence solution extended to layered stratigraphy. *Journal of Petroleum Science and Engineering*. 130:68–76.

Mindlin, R.D. 1936. Force at a Point in the Interior of a Semi-Infinite Solid. *Physics*. 7(5):195–202.

Mindlin, R.D. and Cheng, D.H. 1950a. Thermoelastic Stress in the Semi-Infinite Solid. *Journal of Applied Physics*. 21(9):931–933.

Mindlin, R.D. and Cheng, D.H. 1950b. Nuclei of Strain in the Semi-Infinite Solid. *Journal of Applied Physics*. 21(9):926–930.

Morita, N., Whitfill, D.L., Nygaard, O. and Bale, A. 1989. A Quick Method To Determine Subsidence, Reservoir Compaction, and In-Situ Stress Induced by Reservoir Depletion. *Journal of Petroleum Technology*. 41(01):71–79.

Morris, A., Ferrill, D.A. and Henderson, D.B., 1996. Slip-tendency analysis and fault reactivation. *Geology*, 24(3), pp.275-278.

Mura, T. (1987). *Micromechanics of defects in solids*, 2nd ed. Martinus Nijho Publishers, Dordrecht.

Muskhelishvili, N.I., 1953. Singular integral equations: boundary problems of function theory and their application to mathematical physics. Edited by Radok, J.R.M. Noordhoff Publishing, Groningen, The Netherlands.

Nagel, N.B. 2001. Compaction and subsidence issues within the petroleum industry: From wilmington to ekofisk and beyond. *Physics and Chemistry of the Earth, Part A: Solid Earth and Geodesy*. 26(1):3–14.

NAM. (2016). *Winningsplan Groningen gasveld* (Tech. Rep.). Nederlandse Aardolie Maatschappij. http://www.nam.nl/gas-en-oliewinning/groningen-gasveld/winningsplan-groningen-gasveld.html.

Neely, J. S., Salditch, L., Spencer, B. D., and Stein, S., 2023. A More Realistic Earthquake Probability Model Using Long‐Term Fault Memory. *Bulletin of the Seismological Society of America*, doi.org/10.1785/0120220083

Nguyen, T.K., Pouya, A. and Rohmer, J., 2015. Integrating damage zone

heterogeneities based on stochastic realizations of fracture networks for fault stability analysis. *International Journal of Rock Mechanics and Mining Sciences*, 80, pp.325-336.

Nordbotten, J. M., Celia, M. A. andBachu, S. (2005). Injection and storage of CO_2 in deep saline aquifers: analytical solution for CO_2 plume evolution during injection. *Transp Porous Media*, 58: 339–360.

Ohnaka, M., 1992. Earthquake source nucleation: a physical model for short-term precursors. *Tectonophysics*, 211(1-4), pp.149-178.

Ohnaka, M., 1996. Nonuniformity of the constitutive law parameters for shear rupture and quasistatic nucleation to dynamic rupture: a physical model of earthquake generation processes. *Proceedings of the National Academy of Sciences,* 93(9), pp.3795-3802.

Ohnaka, M., 2000. A physical scaling relation between the size of an earthquake and its nucleation zone size. *Pure and applied geophysics,* 157(11), 2259-2282.

Ohnaka, M., 2013. The physics of rock failure and earthquakes. Cambridge University Press, New York, U.S.A.

Ohnaka, M. and Kuwahara, Y., 1990. Characteristic features of local breakdown near a crack-tip in the transition zone from nucleation to unstable rupture during stick-slip shear failure. *Tectonophysics*, 175(1-3), pp.197-220.

Okada, Y. 1985. Surface deformation due to shear and tensile faults in a half-space. *Bulletin of the Seismological Society of America*. 75(4):1135–1154.

Okada, Y. 1992. Internal deformation due to shear and tensile faults in a half-space. *Bulletin of the Seismological Society of America*. 82(2):1018–1040.

Olivella, S., Carrera, J., Gens, A. and Alonso, E. E. (1994). Nonisothermal multiphase flow of brine and gas through saline media. *Transport in porous media*, 15(3), 271-293.

Olivella, S., Gens, A., Carrera, J. and Alonso, E. E. (1996). Numerical formulation for a simulator (CODE_BRIGHT) for the coupled analysis of saline media. *Engineering computations*, 13(7), 87-112.

Orlic, B. and Wassing, B. (2013). A study of stress change and fault slip in producing gas reservoirs overlain by elastic and viscoelastic caprocks. *Rock Mech. Rock Eng.*, 46, 421-435. https://doi.org/10.1007/s00603-012-0347-6.

Orlic, B., Wassing, B. and Geel, C. (2013). Field scale geomechanical modeling for prediction of fault stability during underground gas storage operations in a depleted gas field in the Netherlands. *In 47th US Rock Mechanics / Geome-chanics Symposium*. (Paper ARMA-13-300. 23-26 June, San Francisco, USA)

Ortiz-Zamora, D. and Ortega-Guerrero, A. 2010. Evolution of long-term land subsidence near Mexico City: Review, field investigations, and predictive

simulations. *Water Resources Research*. 46(1).

Pan, E., Amadei, B. and Kim, Y.I. 1998. 2-D BEM analysis of anisotropic half-plane problems—application to rock mechanics. *International Journal of Rock Mechanics and Mining Sciences*. 35(1):69–74.

Park, S., Xie, L., Kim, K. I., Kwon, S., Min, K. B., Choi, J., ... & Song, Y. (2017). First hydraulic stimulation in fractured geothermal reservoir in Pohang PX-2 well. *Procedia Engineering*, 191, 829-837.

Park, S., Kim, K. I., Xie, L., Yoo, H., Min, K. B., Kim, M., ... & Meier, P. (2020). Observations and analyses of the first two hydraulic stimulations in the Pohang geothermal development site, South Korea. *Geothermics*, 88, 101905.

Parsons, T. (2008). Monte Carlo method for determining earthquake recurrence parameters from short paleoseismic catalogs: Example calculations for California. *Journal of Geophysical Research: Solid Earth*, 113(B3).

Passey, Q.R., Bohacs, K.M., Esch, W.L., Klimentidis, R. and Sinha, S. 2010. From Oil-Prone Source Rock to Gas-Producing Shale Reservoir – Geologic and Petrophysical Characterization of Unconventional Shale-Gas Reservoirs. In: OnePetro.

Pearson, C., 1981. The relationship between microseismicity and high pore pressures during hydraulic stimulation experiments in low permeability granitic rocks. *Journal of Geophysical Research: Solid Earth*, 86(B9), pp.7855-7864.

Peng, Z. and Gomberg, J., 2010. An integrated perspective of the continuum between earthquakes and slow-slip phenomena. *Nature geoscience*, 3(9), pp.599-607.

Peng, J., Xu, J., Ma, R. and Wang, F. 2016. Characteristics and mechanism of the Longyao ground fissure on North China Plain, China. *Engineering Geology*. 214:136–146.

Peška, P., & Zoback, M. D. (1995). Compressive and tensile failure of inclined well bores and determination of in situ stress and rock strength. *Journal of Geophysical Research: Solid Earth*, 100(B7), 12791-12811.

Piris Casasnovas, G., 2022. Evaluation of reservoir potential and induced seismicity of deep geothermal systems. PhD thesis, Universitat Autònoma de Barcelona

Plúa, C., Vu, M.N., Seyedi, D.M. and Armand, G., 2021. Effects of inherent spatial variability of rock properties on the thermo-hydro-mechanical responses of a high-level radioactive waste repository. *International Journal of Rock Mechanics and Mining Sciences*, 145, p.104682.

Poland, J.F. and Davis, G.H. 1969. Land Subsidence Due to Withdrawal of Fluids. In: D.J. Varnes and G. Kiersch, eds. Vol. 2. *Reviews in Engineering Geology*. Geological Society of America. pp. 0.

Pollitz, F.F. 1996. Coseismic Deformation From Earthquake Faulting On A Layered Spherical Earth. *Geophysical Journal International*. 125(1):1–14.

Power, W.L., Tullis, T.E., Brown, S.R., Boitnott, G.N. and Scholz, C.H., 1987. Roughness of natural fault surfaces. *Geophysical Research Letters*, 14(1), pp.29-32.

Pratt, W.E. and Johnson, D.W. 1926. Local Subsidence of the Goose Creek Oil Field. *The Journal of Geology*. 34(7, Part 1):577–590.

Raleigh, C.B., Healy, J.H. and Bredehoeft, J.D., 1976. An experiment in earthquake control at Rangely, Colorado. *Science*, 191(4233), pp.1230-1237.

Rathnaweera, T.D., Wu, W., Ji, Y. and Gamage, R.P., 2020. Understanding injection-induced seismicity in enhanced geothermal systems: From the coupled thermo-hydro-mechanical-chemical process to anthropogenic earthquake prediction. *Earth-science reviews*, 205, p.103182.

Raychaudhuri, S. (2008). Introduction to monte carlo simulation. In 2008 Winter simulation conference (pp. 91-100). *IEEE*.

Raziperchikolaee, S. and Mishra, S., 2020. Statistical based hydromechanical models to estimate poroelastic effects of CO2 injection into a closed reservoir. *Greenhouse Gases: Science and Technology*, 10(1), pp.176-195.

Reasenberg, P. A., and R. W. Simpson. (1992). Response of regional seismicity to the static stress change produced by the Loma Prieta earthquake, *Science* 255, no. 5052, 1687–1690, doi: 10.1126/science.255.5052.1687.

Reyes Canales, M. and Van der Baan, M., 2021. Forecasting of induced seismicity rates from hydraulic fracturing activities using physics-based models for probabilistic seismic hazard analysis: A case study. *Pure and Applied Geophysics*, 178(2), pp.359-378.

Ricco, C., Petrosino, S., Aquino, I., Del Gaudio, C. and Falanga, M. 2019. Some Investigations on a Possible Relationship between Ground Deformation and Seismic Activity at Campi Flegrei and Ischia Volcanic Areas (Southern Italy). *Geosciences*. 9(5):222.

Rice, J. R., 1980. The mechanics of earthquake rupture, in Physics of the Earth's Interior, edited by A. M. Dziewonski and E. Boschi, pp. 555– 649, Ital. Phys. Soc./North-Holland, New York, 1980.

Rice, J.R., 1983. Constitutive Relations for Fault Slip and Earthquake Instabilities. *Pure Appl. Geophys*., Contributions to Current Research in Geophysics 121, 443–475. https://doi.org/10.1007/978-3-0348-6608-8_7

Rice, J. R., 2006. Heating and weakening of faults during earthquake slip. *Journal of Geophysical Research: Solid Earth*, 111(B5).

Rice, J.R. and Cleary, M.P. 1976. Some basic stress diffusion solutions for fluid-saturated elastic porous media with compressible constituents. *Reviews of Geophysics*. 14(2):227.

Rice, J.R. and Ruina, A.L., 1983. Stability of Steady Frictional Slipping. *J. Appl. Mech.*

50, 343–349. https://doi.org/10.1115/1.3167042

Rice, J.R., Sammis, C.G. and Parsons, R., 2005. Off-fault secondary failure induced by a dynamic slip pulse. *Bulletin of the Seismological Society of America*, 95(1), pp.109-134.

Richard, P.D., Naylor, M.A. and Koopman, A. 1995. Experimental models of strike-slip tectonics. *Petroleum Geoscience*. 1(1):71–80.

Rinaldi, A.P. and Rutqvist, J. 2013. Modeling of deep fracture zone opening and transient ground surface uplift at KB-502 CO2 injection well, In Salah, Algeria. *International Journal of Greenhouse Gas Control*. 12:155–167.

Ripperger, J., Ampuero, J.P., Mai, P.M. and Giardini, D., 2007. Earthquake source characteristics from dynamic rupture with constrained stochastic fault stress. *Journal of Geophysical Research: Solid Earth*, 112(B4).

Rivière, J., Shokouhi, P., Guyer, R.A. and Johnson, P.A. 2015. A set of measures for the systematic classification of the nonlinear elastic behavior of disparate rocks. *Journal of Geophysical Research: Solid Earth*. 120(3):1587–1604.

Robinson, K. 1951. Elastic Energy of an Ellipsoidal Inclusion in an Infinite Solid. *Journal of Applied Physics*. 22(8):1045–1054.

Roering, J.J., Cooke, M.L. and Pollard, D.D. 1997. Why blind thrust faults do not propagate to the Earth's surface: Numerical modeling of coseismic deformation associated with thrust-related anticlines. *Journal of Geophysical Research: Solid Earth*. 102(B6):11901–11912.

Rohmer, J., Pluymakers, A. and Renard, F., 2016. Mechano-chemical interactions in sedimentary rocks in the context of CO2 storage: Weak acid, weak effects?. *Earth-Science Reviews*, 157, pp.86-110.

Rowan, M.G., Peel, F.J. and Vendeville, B.C. 2004. Gravity-driven Fold Belts on Passive Margins. 157–182. http://archives.datapages.com/data/specpubs/memoir82/CHAPTER9/CHAPTER9.HTM *Date of access*: 24 Mar. 2023.

Rubin, A.M. and Ampuero, J.P., 2005. Earthquake nucleation on (aging) rate and state faults. *Journal of Geophysical Research: Solid Earth*, 110(B11).

Rubinstein, J.L. and Mahani, A.B., 2015. Myths and facts on wastewater injection, hydraulic fracturing, enhanced oil recovery, and induced seismicity. *Seismological Research Letters*, 86(4), pp.1060-1067.

Rudnicki, J.W. 1999. Alteration of Regional Stress By Reservoirs And Other Inhomogeneities: Stabilizing Or Destabilizing? In: OnePetro. https://onepetro.org/isrmcongress/proceedings-abstract/CONGRESS99/All-CONGRESS99/168935 Date of access: 10 Mar. 2023.

Rudnicki, J.W., 2002. Eshelby transformations, pore pressure and fluid mass changes and subsidence. *In Second Biot Conference on Poromechanics (Poromechanics II)*,

Grenoble, France, August (pp. 26-28).

Rudnicki, J.W. 2011. Eshelby's Technique for Analyzing Inhomogeneities in Geomechanics. In: Y.M. Leroy and F.K. Lehner, eds. (CISM Courses and Lectures). *Mechanics of Crustal Rocks*. Vienna: Springer. pp. 43–72.

Rudnicki, J.W. and Chen, C.H., 1988. Stabilization of rapid frictional slip on a weakening fault by dilatant hardening. *Journal of Geophysical Research: Solid Earth*, 93(B5), pp.4745-4757.

Rudziński, Ł., Mirek, K. and Mirek, J. 2019. Rapid ground deformation corresponding to a mining-induced seismic event followed by a massive collapse. *Natural Hazards*. 96(1):461–471.

Rutqvist, J. and Stephansson, O., 2003. The role of hydromechanical coupling in fractured rock engineering. *Hydrogeology Journal*, 11, pp.7-40.

Rutqvist, J., Birkholzer, J., Cappa, F., & Tsang, C. F., 2007. Estimating maximum sustainable injection pressure during geological sequestration of CO2 using coupled fluid flow and geomechanical fault-slip analysis. *Energy Conversion and Management*, 48(6), 1798–1807.

Rutqvist, J., Birkholzer, J.T. and Tsang, C.-F. 2008. Coupled reservoir–geomechanical analysis of the potential for tensile and shear failure associated with CO2 injection in multilayered reservoir–caprock systems. *International Journal of Rock Mechanics and Mining Sciences*. 45(2):132–143.

Rutqvist, J., Rinaldi, A.P., Cappa, F., Jeanne, P., Mazzoldi, A., Urpi, L., Guglielmi, Y. and Vilarrasa, V., 2016. Fault activation and induced seismicity in geological carbon storage–Lessons learned from recent modeling studies. *Journal of Rock Mechanics and Geotechnical Engineering*, 8(6), pp.789-804.

Rutqvist, J., Vasco, D.W. and Myer, L. 2010. Coupled reservoir-geomechanical analysis of CO2 injection and ground deformations at In Salah, Algeria. *International Journal of Greenhouse Gas Control*. 4(2):225–230.

Sáez, A., Lecampion, B., Bhattacharya, P. and Viesca, R.C., 2022. Three-dimensional fluid-driven stable frictional ruptures. *Journal of the Mechanics and Physics of Solids*, 160, p.104754.

Sacks, I. S., Linde, A. T., Suyehiro, S. and Snoke, J. A. (1978). Slow earthquakes and stress redistribution. *Nature*, 275(5681), 599-602.

Scholz, C.H. 1968. Microfracturing and the inelastic deformation of rock in compression. *Journal of Geophysical Research (1896-1977)*. 73(4):1417–1432.

Scholz, C.H., Wyss, M., Smith, S.W., 1969. Seismic and aseismic slip on the San Andreas Fault. *J. Geophys. Res.* 1896-1977 74, 2049–2069. https://doi.org/10.1029/JB074i008p02049

Schultz, R., Skoumal, R.J., Brudzinski, M.R., Eaton, D., Baptie, B. and Ellsworth, W., 2020. Hydraulic fracturing‐induced seismicity. *Reviews of Geophysics*, 58(3),

p.e2019RG000695.

Segall, P. 1985. Stress and subsidence resulting from subsurface fluid withdrawal in the epicentral region of the 1983 Coalinga Earthquake. *Journal of Geophysical Research: Solid Earth*. 90(B8):6801–6816.

Segall, P. 1989. Earthquakes triggered by fluid extraction. *Geology*. 17(10):942–946.

Segall, P. 1992. Induced stresses due to fluid extraction from axisymmetric reservoirs. *Pure and Applied Geophysics*, 139(3–4), 535–560. https://doi.org/10.1007/BF00879950

Segall, P. 2010. Earthquake and Volcano Deformation. *Earthquake and Volcano Deformation*. Princeton University Press.

Segall, P. and Rice, J.R., 1995. Dilatancy, compaction, and slip instability of a fluid‐infiltrated fault. *Journal of Geophysical Research: Solid Earth*, 100(B11), pp.22155-22171.

Segall, P., Grasso, J.-R. and Mossop, A. 1994. Poroelastic stressing and induced seismicity near the Lacq gas field, southwestern France. *Journal of Geophysical Research: Solid Earth*. 99(B8):15423–15438.

Segall, P., Rubin, A.M., Bradley, A.M. and Rice, J.R., 2010. Dilatant strengthening as a mechanism for slow slip events. *Journal of Geophysical Research: Solid Earth*, 115(B12).

Shapiro, S. A. and Dinske, C., 2009. Fluid‐induced seismicity: Pressure diffusion and hydraulic fracturing. *Geophysical Prospecting*, 57(2), 301-310.

Shirzaei, M., Ellsworth, W.L., Tiampo, K.F., González, P.J. and Manga, M., 2016. Surface uplift and time-dependent seismic hazard due to fluid injection in eastern Texas. *Science*, 353(6306), pp.1416-1419.

Simpson, D.W., Leith, W.S. and Scholz, C.H., 1988. Two types of reservoir-induced seismicity. *Bulletin of the Seismological Society of America*, 78(6), pp.2025-2040.

Soh, I., Chang, C., Lee, J., Hong, T. K., & Park, E. S. (2018). Tectonic stress orientations and magnitudes, and friction of faults, deduced from earthquake focal mechanism inversions over the Korean Peninsula. *Geophysical Journal International*, 213(2), 1360-1373.

Soltanzadeh, H., 2009. *Geomechanical analysis of caprock integrity.* University of Saskatchewan, Saskatoon, Canada

Soltanzadeh, H. and Hawkes, C.D. 2008. Semi-analytical models for stress change and fault reactivation induced by reservoir production and injection. *Journal of Petroleum Science and Engineering*. 60(2):71–85.

Soltanzadeh, H. and Hawkes, C., 2009. Assessing fault reactivation tendency within and surrounding porous reservoirs during fluid production or injection. *Int. J. Rock Mech. Mining Sci.*, 46, 1-7. https://doi.org/10.1016/j.ijrmms.2008.03.008.

Song, S. G., & Lee, H. (2019). Static slip model of the 2017 M w 5.4 Pohang, South Korea, earthquake constrained by the InSAR data. *Seismological Research Letters*, 90(1), 140-148.

Stein, R.S., 1999. The role of stress transfer in earthquake occurrence. *Nature*, 402(6762), pp.605-609.

Steketee, J.A. 1958a. On volterra's dislocations in a semi-infinite elastic medium. *Canadian Journal of Physics*. 36(2):192–205.

Steketee, J.A. 1958b. Some geophysical applications of the elasticity theory of dislocations. *Canadian Journal of Physics*. 36(9):1168–1198.

Strack, O.E. and Verruijt, A. 2002. A complex variable solution for a deforming buoyant tunnel in a heavy elastic half-plane. *International Journal for Numerical and Analytical Methods in Geomechanics*. 26(12):1235–1252.

Sun, W. 2014. Recent advances of computing coseismic deformations in theory and applications. *Earthquake Science*. 27(2):217–227.

Teatini P., Castelletto, N., Ferronato, M., Gambolati, G., Janna, C., Cairo, E., Marzorati, D., Colombo, D., Ferretti, A., Bagliani, A., and Bottazzi. F. 2011. Geomechanical response to seasonal gas storage in depleted reservoirs: A case study in the Po River basin, Italy. *Journal of Geophysical Research*. 116, F02002.

Terakawa, T., Miller, S. A. and Deichmann, N., 2012. High fluid pressure and triggered earthquakes in the enhanced geothermal system in Basel, Switzerland. *Journal of Geophysical Research: Solid Earth*, 117(B7).

Terakawa, T., Seo, W., Kim, K.-H., & Ree, J.-H., 2020. Three-dimensional pore fluid pressures in source region of 2017 Pohang earthquake inferred from earthquake focal mechanisms. *Geophysical Research Letters*, 47, e2019GL085964. https://doi.org/10.1029/2019GL085964

Theis, C.V., 1935. The relation between the lowering of the piezometric surface and the rate and duration of discharge of a well using ground‐water storage. *Eos, Transactions American Geophysical Union*, 16(2), pp.519-524.

Thienen-Visser, K. van and Fokker, P.A. 2017. The future of subsidence modelling: compaction and subsidence due to gas depletion of the Groningen gas field in the Netherlands. *Netherlands Journal of Geosciences*. 96(5):s105–s116.

Toda, S., Stein, R.S. and Lin, J., 2011. Widespread seismicity excitation throughout central Japan following the 2011 M= 9.0 Tohoku earthquake and its interpretation by Coulomb stress transfer. *Geophysical Research Letters*, 38(7).

Toda, S., Stein, R.S., Richards‐Dinger, K. and Bozkurt, S.B., 2005. Forecasting the evolution of seismicity in southern California: Animations built on earthquake stress transfer. *Journal of Geophysical Research: Solid Earth*, 110(B5).

Townend, J., & Zoback, M. D. (2000). How faulting keeps the crust strong. *Geology*, 28(5), 399-402.

Tseng, P. H., & Lee, T. C. (1998). Numerical evaluation of exponential integral: Theis well function approximation. *Journal of Hydrology*, 205(1-2), 38-51.

Uenishi, K., and Rice, J.R., 2003. Universal nucleation length for slip-weakening rupture instability under nonuniform fault loading, *J. Geophys. Res.*, 108(B1), 2042, doi:10.1029/2001JB001681, 2003.

Van den Ende, M., Scuderi, M.M., Cappa, F. and Ampuero, J.P., 2020. Extracting microphysical fault friction parameters from laboratory and field injection experiments. *Solid Earth*, 11(6), pp.2245-2256.

van der Baan, M., 2021. Earthquakes triggered by underground fluid injection modelled for a tectonically active oil field. *Nature*, Vol: 595, pp.655-656

Van den Bogert, P., 2015. *Impact of various modelling options on the onset of fault slip and fault slip response using 2-dimensional finite-element modelling*. Restricted report No. SR.15.11455. https://nam-feitenencijfers.data-app.nl/download/rapport/604ef59b-5ac5-4770-93b1-e501c87da3a9?open=true.

Van der Elst, N.J., Page, M.T., Weiser, D.A., Goebel, T.H. and Hosseini, S.M., 2016. Induced earthquake magnitudes are as large as (statistically) expected. *Journal of Geophysical Research: Solid Earth*, 121(6), pp.4575-4590.

Van Wees, J., Buijze, L., Van Thienen-Visser, K., Nepveu, M., Wassing, B., Orlic, B., and Fokker, P. 2014. Geomechanics response and induced seismicity during gas field production in the Netherlands. *Geothermics*, 52, 206-219. https://doi.org/10.1016/j.geothermics.2014.05.004.

Van Wees, J., Fokker, P., Van Thienen-Visser, K., Wassing, B., Osinga, S., Orlic, B., . . . Pluymaekers, M. (2017). Geomechanical models for induced seismicity in the Netherlands: inferences from simplified analytical, finite element and rupture model approaches. *Netherl. J. Geosc.*, 96 (5), S183-S202.https://doi.org/10.1017/njg.2017.38.

Verruijt, A. 1998. Deformations of an elastic half plane with a circular cavity. *International Journal of Solids and Structures*. 35(21):2795–2804.

Verruijt, A. and Booker, J.R. 1996. Surface settlements due to deformation of a tunnel in an elastic half plane. *Géotechnique*. 46(4):753–756.

Viesca, R. C., and Garagash, D. I., 2015. Ubiquitous weakening of faults due to thermal pressurization. *Nature Geoscience*, 8(11), 875-879.

Viesca, R. C., and Garagash, D. I., 2018. Numerical methods for coupled fracture problems. *Journal of the Mechanics and Physics of Solids*, 113, 13-34.

Viesca, R. C., 2021. Self-similar fault slip in response to fluid injection. *Journal of Fluid Mechanics*, 928.

Vilarrasa, V. and Carrera, J., 2015. Geologic carbon storage is unlikely to trigger large earthquakes and reactivate faults through which CO2 could leak. *Proceedings of*

the National Academy of Sciences, 112(19), pp.5938-5943.

Vilarrasa, V., Bolster, D., Olivella, S. and Carrera, J. 2010. Coupled hydromechanical modeling of CO2 sequestration in deep saline aquifers. *International Journal of Greenhouse Gas Control*. 4(6):910–919.

Vilarrasa, V., Carrera, J., & Olivella, S. (2013). Hydromechanical characterization of CO2 injection sites. *International Journal of Greenhouse Gas Control*, 19, 665-677.

Vilarrasa, V., Carrera, J., Olivella, S., Rutqvist, J. and Laloui, L., 2019. Induced seismicity in geologic carbon storage. *Solid Earth*, 10(3), pp.871-892.

Vilarrasa, V., De Simone, S., Carrera, J. and Villaseñor, A., 2021. Unraveling the causes of the seismicity induced by underground gas storage at Castor, Spain. *Geophysical Research Letters*, 48(7), p.e2020GL092038.

Vilarrasa, V., De Simone, S., Carrera, J., and Villaseñor, A., 2022. Multiple induced seismicity mechanisms at Castor underground gas storage illustrate the need for thorough monitoring. *Nature Communications*, 13, 3447

Vilarrasa, V., Makhnenko, R. and Gheibi, S. 2016. Geomechanical analysis of the influence of CO2 injection location on fault stability. *Journal of Rock Mechanics and Geotechnical Engineering*. 8(6):805–818.

Villaseñor, A., Herrmann, R. B., Gaite, B. and Ugalde, A. (2020). Fault reactivation by gas injection at an underground gas storage off the east coast of Spain. *Solid Earth*, 11(1), 63-74.

Walsh, J. B. (2002). Subsidence above a planar reservoir, *J. Geophys. Res.*,107(B9), 2202, doi:10.1029/2001JB000606.

Wang, H.F. 2000. Theory of Linear Poroelasticity with Applications to Geomechanics and Hydrogeology. *Princeton University Press*.

Wang, L., Bai, B., Li, X., Liu, M., Wu, H. and Hu, S. (2016). An analytical model for assessing stability of pre-existing faults in caprock caused by fluid injection and extraction in a reservoir. *Rock Mechanics and Rock Engineering*, 49(7), 2845-2863.

Wang, R., Lorenzo-Martín, F. and Roth, F. 2006. PSGRN/PSCMP—a new code for calculating co- and post-seismic deformation, geoid and gravity changes based on the viscoelastic-gravitational dislocation theory. *Computers & Geosciences*. 32(4):527–541.

Wang, Y., Feng, G., Li, Z., Xu, W., Zhu, J., … Qiao, X. 2022. Retrieving the displacements of the Hutubi (China) underground gas storage during 2003–2020 from multi-track InSAR. *Remote Sensing of Environment*. 268:112768.

Wassing, B. B. T., Gan, Q., Candela, T., & Fokker, P. A. (2021). Effects of fault transmissivity on the potential of fault reactivation and induced seismicity: Implications for understanding induced seismicity at Pohang EGS. *Geothermics*,

91, 101976.

Wawersik, W.R. and Brace, W.F., 1971. Post-failure behavior of a granite and diabase. *Rock mechanics*, 3, pp.61-85.

Wawersik, W.R. and Fairhurst, C.H., 1970. A study of brittle rock fracture in laboratory compression experiments. *International Journal of Rock Mechanics and Mining Sciences & Geomechanics Abstracts*, 7(5), pp.561-575

Westaway, R., & Burnside, N. M. (2019). Fault "corrosion" by fluid Injection: A potential cause of the November 2017 5.5 Korean Earthquake. *Geofluids*, 2019.

Wong, T.F., 1982. Shear fracture energy of Westerly granite from post‐failure behavior. *Journal of Geophysical Research: Solid Earth*, 87(B2), pp.990-1000.

Woo, J. U., Kim, M., Sheen, D. H., Kang, T. S., Rhie, J., Grigoli, F., Ellsworth, W. L. & Giardini, D. (2019). An in-depth seismological analysis revealing a causal link between the 2017 MW 5.5 Pohang earthquake and EGS project. *Journal of Geophysical Research: Solid Earth*, 124(12), 13060-13078.

Wright, T.J., Elliott, J.R., Wang, H. and Ryder, I. 2013. Earthquake cycle deformation and the Moho: Implications for the rheology of continental lithosphere. *Tectonophysics*. 609:504–523.

Wu, H. and Vilarrasa, V., 2019. Numerical and analytical solutions to assess induced seismicity. *Workshop Quo Vadis Hydrogeology Group UPC-CSIC*, Sant Fruitós del Bages, Spain, 25-26 June 2019

Wu, H., Bai, B., Li, X., Gao, S., Liu, M. andWang, L., 2016. An explicit integral solution for pressure buildup during CO2 injection into infinite saline aquifers. *Greenhouse Gas: Science and Technology*, 6(5): 633-647. DOI: 10.1002/ghg.1601

Wu, H., Bai, B., Li, X., 2018. An advanced analytical solution for pressure buildup during CO_2 injection into infinite saline aquifers: The role of compressibility. *Advances in Water Resources*, 112: 95-105. DOI: 10.1016/j.advwatres.2017.12.010

Wu, H., Vilarrasa, V., De Simone, S., Saaltink, M. and Parisio, F., 2020a. A novel analytical solution to assess induced seismicity potential. *Seminar cycle in Hydrogeology and Geochemistry*, Barcelona, Spain, 8 Oct. 2020

Wu, H., Vilarrasa, V., De Simone, S., Saaltink, M. and Parisio, F., 2020b. Assessment of the induced seismicity potential in pressurized and depleted reservoirs: the role of fault permeability. *International Conference on Coupled Processes in Fractured Geological Media: Observation, Modeling, and Application (CouFrac 2020)*, Seoul Korea, 11-13 Nov. 2020

Wu, H., Vilarrasa, V., De Simone, S., Saaltink, M. and Parisio, F., 2020c. A novel analytical solution to assess induced seismicity in pressurized and depleted reservoirs. *AGU Fall Meeting 2020*, Online Everywhere, 1-17 Dec. 2020

Wu, H., Vilarrasa, V., De Simone, S., Saaltink, M. and Parisio, F., 2021a. Analytical

Solution to Assess the Induced Seismicity Potential of Faults in Pressurized and Depleted Reservoirs. Journal of Geophysical Research: Solid Earth. 126(1):e2020JB020436. https://doi.org/10.1029/2020JB020436

Wu, H., Vilarrasa, V., De Simone, S., Saaltink, M. and Parisio, F., 2021b. Verification of an analytical solution for poroelastic stress changes due to reservoir pressurization/depletion. *12th Workshop of CODE_BRIGHT Users*. Barcelona, Spain, 22 Sep. 2021

Wu, H., Vilarrasa, V. and Parisio, F., 2021c. Uncertainty analysis on the potential triggering mechanisms of the Pohang Mw5.5 earthquake. *Seminar cycle in Hydrogeology and Geochemistry*. Barcelona, Spain, 21 Oct. 2021

Wu, H., Vilarrasa, V. and Parisio, F., 2021d. Uncertainty analysis on the potential triggering mechanisms of the Pohang M_w5.5 earthquake. *AGU Fall Meeting 2021*, Online Everywhere, 11-17 Dec. 2021

Wu, H., Vilarrasa, V. and Parisio, F., 2022. Poroelasticity effects on the transient fault rupture during fluid injection. *Seminar cycle in Hydrogeology and Geochemistry*. Barcelona, Spain, 01 Dec. 2022

Wu, H., Parisio, F. and Vilarrasa, V., 2023a. Poroelastic effects on the nucleation process of dynamic fault rupture during fluid injection. *Submitted*.

Wu, H., Rutqvist, J. and Vilarrasa, V., 2023b. Analytical solution to quickly assess ground displacement for a pressurized or depleted deep reservoir intersected by a fault in a half space. *Submitted*.

Wu, H., Alcolea, A., Parisio, F., Meier, P., Carrera, J., Olivella, S., Saaltink, M. and Vilarrasa, V., 2023c. Stochastic poromechanical analysis of induced seismicity – application to Pohang Mw5.5 earthquake. *In preparation.*

Wu, H., Xie, J. and Vilarrasa, V., 2023d. Risk assessment and mitigation of induced seismicity for geo-energy related applications at the basin scale, *Galileo Conference: Solid Earth and Geohazards in the Exascale Era*, Barcelona, Spain, 23–26 May 2023, GC11-solidearth-27, https://doi.org/10.5194/egusphere-gc11-solidearth-27.

Yeo, I. W., Brown, M. R. M., Ge, S., & Lee, K. K. (2020). Causal mechanism of injection-induced earthquakes through the Mw5.5 Pohang earthquake case study. *Nature communications*, 11(1), 1-12.

Yoo, H. (2018). Numerical modeling of hydraulic stimulation at a fractured geothermal reservoir. Master thesis, Seoul, Seoul National University. Retrieved from ‘http://s‐space.snu.ac.kr/bitstream/10371/141462/1/000000150962.pdf’.

Yoo, H., Park, S., Xie, L., Kim, K. I., Min, K. B., Rutqvist, J., & Rinaldi, A. P. (2021). Hydro-mechanical modeling of the first and second hydraulic stimulations in a fractured geothermal reservoir in Pohang, South Korea. *Geothermics*, 89, 101982.

Zang A., Yoon J.S., Stephansson O., Heidbach O. (2013). Fatigue hydraulic fracturing by cyclic reservoir treatment enhances permeability and reduces induced

seismicity. *Geophys J Int* 195(2):1282–1287. https ://doi.org/10.1093/gji/ggt301.993

Zang, A., Zimmermann, G., Hofmann, H., Stephansson, O., Min, K. B., & Kim, K. Y. (2019). How to reduce fluid-injection-induced seismicity. Rock Mechanics and Rock Engineering, 52(2), 475-493.

Zbinden, D., Rinaldi, A.P., Urpi, L. and Wiemer, S., 2017. On the physics-based processes behind production-induced seismicity in natural gas fields. *Journal of Geophysical Research: Solid Earth*. 122(5):3792–3812.

Zbinden, D., Rinaldi, A.P., Diehl, T. and Wiemer, S., 2020. Hydromechanical Modeling of Fault Reactivation in the St. Gallen Deep Geothermal Project (Switzerland): Poroelasticity or Hydraulic Connection? *Geophysical Research Letters*. 47(3):e2019GL085201.

Zhang, M., Ge, S., Yang, Q. and Ma, X., 2021. Impoundment‐Associated Hydro‐Mechanical Changes and Regional Seismicity Near the Xiluodu Reservoir, Southwestern China. *Journal of Geophysical Research: Solid Earth*, 126(9), p.e2020JB021590.

Zhang, Y., Person, M., Rupp, J., Ellett, K., Celia, M.A., Gable, C.W., Bowen, B., Evans, J., Bandilla, K., Mozley, P. and Dewers, T., 2013. Hydrogeologic controls on induced seismicity in crystalline basement rocks due to fluid injection into basal reservoirs. *Groundwater*, 51(4), pp.525-538.

Zhou, Q., Birkholzer, J. T., Tsang, C. F. and Rutqvist, J. (2008). A method for quick assessment of CO_2 storage capacity in closed and semi-closed saline formations. *International Journal of Greenhouse Gas Control*, 2(4), 626–639

Zoback, M. D., 2010. Reservoir geomechanics. Cambridge University Press.

Zoback, M. D., & Gorelick, S. M., 2012. Earthquake triggering and large-scale geologic storage of carbon dioxide. *Proceedings of the National Academy of Sciences*, 109(26), 10164-10168.